UNIVERSITY OF SOUTHAMPTON

FACULTY OF ENGINEERING, SCIENCE AND MATHEMATICS

Optoelectronics Research Centre

Distributed optical-fibre sensors for monitoring mechanical strain and disturbance

by

Justin Peter William Hayward

Thesis for the degree of Doctor of Philosophy

September 2005

UNIVERSITY OF SOUTHAMPTON

ABSTRACT

ENGINEEERING SCIENCE & MATHEMATICS

OPTOELECTRONICS RESEARCH CENTRE

Doctor of Philosophy

DISTRIBUTED OPTICAL FIBRE SENSORS FOR MONITORING MECHANICAL STRAIN AND DISTURBANCE

by Justin Peter William Hayward

This thesis reports work carried out to develop an optical sensor capable of detecting disturbance of optical fibre cables, for application in protection of telecommunications infrastructure. Initially, three types of sensor were investigated, however after preliminary experimental and theoretical work it was decided to concentrate on a novel coherent-optical time-domain reflectometer (C-OTDR).

The operation of the C-OTDR has been investigated theoretically, using various models to describe coherent scattering in the optical fibre. The assumptions used in the models were applied to a numerical simulation of coherent scattering, obtaining results in good agreement with theoretical predictions and experimental measurements. Having developed a clear explanation of the sensor's operation, a detailed noise analysis is carried out, enabling the limiting factors to be identified and minimised.

The design and development of a portable sensor system is then described, and the results from a number of field trials are presented. Seeking to explain unexpected observations during these trials, a detailed experimental and theoretical analysis of the limits due to optical non-linearity was carried out, showing that the pulse power is limited by the need to prevent spectral broadening due to self-phase modulation, which adds noise to the sensor output.

Applying the findings of these investigations, further field trials and laboratory tests were carried out with improved experimental C-OTDR sensors. By optimising the pulse power and carefully controlling the noise sources, it has been possible to demonstrate operation at longer ranges, with superior spatial resolution, than has been reported for other sensors of this type.

Poor wandering ones!

Though ye have surely strayed,

Take heart of grace,

Your steps retrace,

Poor wandering ones!

The Pirates of Penzance

W. S. Gilbert

Contents

Declaration of Authorship

I, Justin Peter William Hayward, declare that the thesis entitled "Distributed optical-fibre sensors for monitoring mechanical strain and disturbance" and the work presented in it are my own. I confirm that:

- this work was done wholly or mainly while in candidature for a research degree at this University;

- where any part of this thesis has previously been submitted for a degree or any other qualification at this University or any other institution, this has been clearly stated;

- where I have consulted the published work of others, this is always clearly attributed;

- where I have quoted from the work of others, the source is always given. With the exception of such quotations, this thesis is entirely my own work;

- I have acknowledged all main sources of help;

- where the thesis is based on work done by myself jointly with others, I have made clear exactly what was done by others and what I have contributed myself;

- parts of this work have been published as:

  Hayward, J. P. W*., et al.* "*Direct monitoring of fibre extension by correlation-based coherent optical time-domain reflectometry"*, in *OFS-17*, 2005, Bruges, Belgium: SPIE.

Signed: ……..

Date:……..……

Acknowledgements

"Time flies when you're having fun", so the saying goes, and four years have certainly flown by; it seems like no time since the notion of writing my thesis was a distant dream.

At this juncture, I must mention a few people for easing my progress to this point:

Firstly, thanks to Professor John Dakin, my supervisor for the past four years and a source of innumerable ideas and advice.

Many thanks also to Dr Stuart "Stu" Russell –whose patient advice, encouragement and knowledge have been indispensable throughout my time in the ORC, and whose perceptive comments have been a great help in the preparation of this thesis.

Thanks also to Eleanor Tarbox for kindly reading through my draft thesis, for her useful suggestions and eye for typographical detail.

I would like to acknowledge the support of EPSRC and Radiodetection Ltd, who sponsored part of this work.

A mention must go to my colleagues, and friends, the inimitable Andrew, Barry and Bob; their unique combination of Jalfrezi and Cobra-fuelled wit and wisdom has made the past four years infinitely more enjoyable.

I would like to thank Joachim Boudet for his contributions to the P-OTDR investigation. Thanks are due also to Ed Weatherby, for helping to build some of the experimental equipment and for many enjoyable nights in the Dolphin, and to Andy Webb, for allowing me to take over the winding machine for a whole week, without once complaining.

Postgraduate research can be a stressful activity at times and without the relaxation of making music my life would be much poorer – so thanks to all the members of the University Symphony Orchestra, the Winchester Symphony Orchestra and, of course, the Southampton University Concert band, who have provided a vent for my frustrations, and been the cause of a fair few, over the past years.

Finally, a very special thanks to Nicky, who has remained a model of patience, for putting up with my obscure working hours, cleaning the bathroom – even though it was *my* turn! - and for putting up with me on the days when it seemed like everything had gone wrong. I couldn't have done it without you.

Table of Abbreviations

AC	Alternating Current
ADC	Analogue-to-Digital Converter
AM	Amplitude Modulation
AOM	Acousto-Optic Modulator
ASE	Amplified Spontaneous Emission
AST	Acoustic Signalling Tool
AU	Arbitrary Units (Assumed to be linear)
BPF	Band-Pass Filter
C-OTDR	Coherent Optical Time-Domain Reflectomet-er/ry
CW	Continuous Wave
DAC	Digital-to-Analogue Converter
DC	Direct Current
DCM	Delay and Cross-Multiply
DDS	Direct Digital Synthesiser
DFB	Distributed Feedback
DOP	Degree of Polarisation
DSP	Digital Signal Process-or/ing
EDFA	Erbium-Doped-Fibre Amplifier
FBG	Fibre Bragg Grating
FFT	Fast Fourier Transform
FM	Frequency Modulation
FPGA	Field-Programmable Gate Array
FTAS	Fibre Threat Alerting System
FUT	Fibre Under Test
FWHM	Full Width at Half Maximum
FWM	Four-Wave Mixing
GUI	Graphical User Interface
HPF	High-Pass Filter
LED	Light-Emitting Diode
LPF	Low-Pass Filter
OFDR	Optical Frequency-Domain Reflectomet-er/ry
OPL	Optical Path Length

ORC	Optoelectronics Research Centre
OSA	Optical Spectrum Analyser
OTDR	Optical Time-Domain Reflectomet-er/ry
PC	Personal Computer
PCB	Printed Circuit Board
PDF	Probability Density Function
PM	Phase Modulation
PSU	Power Supply Unit
RF	Radio Frequency
S&H	Sample-and-Hold
SBS	Stimulated Brillouin Scattering
SD	Standard Deviation
SMF	Single-Mode Fibre
SNR	Signal-to-Noise Ratio
SONET	Synchronous Optical Network
SOP	State of Polarisation
SPM	Self-Phase Modulation
SRS	Stimulated Raman Scattering
TIA	Transimpedance Amplifier
TTL	Transistor-Transistor Logic
UoS	University of Southampton
WDM	Wavelength Division Multiplex-er/ing
wrt	with respect to
XPM	Cross-Phase Modulation

Chapter 1 Introduction

In this chapter the motivation behind the research presented in this thesis is introduced and the history of the project is outlined. Following a brief introduction to optical-fibre sensing techniques, a brief analysis of the advantages and disadvantages of various sensors is presented; highlighting those most suitable for the current work. Finally, the structure of the remainder of the thesis is outlined.

1.1. Background

1.1.1. Optical-Fibre Communications

Communication using light is as old as civilisation itself, using coded flashes from a mirrored surface to reflect sunlight, or more recently artificial light sources. The use of beacons for sending information over long distances formed a crude communications network, later superseded by the large semaphore towers along the coast for long-range communication during the Napoleonic wars.

The first "modern" communication system was the electric telegraph, which was rapidly deployed by the expanding railway industry for communications purposes. From 1852, telegraph signals were used by the Great Western Railway for synchronising clocks along its rail network, particularly the London to Plymouth line, avoiding timetabling errors due to the difference in solar time encountered on the East-West running route which could amount to 20 minutes [1]. The development of the analogue telephone followed, and with it complex networks allowing a user to communicate directly with one of a large number of other users, with the signal being routed through a number of exchanges.

Interest in using light for communication was rekindled in the early 1960s by the invention of the laser, the low beam-divergence and high power densities now possible opening up the possibilities for free-space optical communications. The transmission properties of the atmosphere, however, limit such systems to short-range operation, and as a result the use of free-space optical communication systems over long distances has remained relatively rare except for specialised applications [2].

During the 1960s attempts were made to overcome the problems with free-space communications by developing systems based on gas-filled or evacuated pipes with series of lenses to maintain the beam shape [3]. Although transmission losses as low as 1 dB / km were obtained, the engineering challenges of making such a system suitable for real-world application meant that the concept was soon replaced by the rapidly developing glass fibre [4].

The breakthrough for optical communications came in 1966 when Kao and Hockham and, independently, Werts, proposed fabricating a glass waveguide to confine the light, avoiding atmospheric degradation of the signal [5]. Early fibres had very poor transmission properties with losses of the order 1000 dB / km, very much larger than the copper-based coaxial cables used for high-speed communications at the time which

could achieve losses of 5 dB / km. By the mid 1980s, manufacturing techniques had improved significantly, and fibres were commercially available with losses of less than 0.4 dB / km in the 1300 nm low-loss window and below 0.25 dB / km in the 1550 nm window: approaching the fundamental scattering limit. These developments paved the way for the widespread deployment of optical-fibre technology for long-distance communication. With the development of the erbium-doped-fibre amplifier repeater, all-optical links over any terrestrial distance became possible [6]. As a result of these innovations, modern long-haul communication systems are now almost completely reliant on fibre-optic links.

1.1.2. Motivation

In communications systems, fibres are typically installed in armoured cables, which may contain up to 100 fibres. A single WDM channel in a fibre link typically operates at a data rate of 10 Gb / s and each fibre typically carries 64 channels. Considering this, a cable containing 10 fibres can transmit over 2×10^{16} bits per hour, equivalent to around half a billion megabytes of data! This phenomenal data rate means that, for the communications company, each cable represents a significant source of revenue and, in the event of a cable failure, the potential for significant loss of revenue and negative impact on customer satisfaction.

Luckily, link failures are rare in practice. Intensive research and development has led to modern optical components with median lifetimes of 25 years or more [5]. Similarly, fibre cables rarely fail spontaneously in the field and, where faults do occur, for example due to failure of splices etc, normally only one fibre within a cable is affected, minimising disruption. The most common cause of catastrophic premature failure of deployed cable is accidental damage from “dig-ups” [7, 8]. Lightning damage of steel-armoured cables is also relatively common, causing particular problems, since the damage often leaves no visual evidence above ground, making visual location of the fault difficult.

To prevent accidental damage to cables, the USA, and many other countries, implement “call before you dig” policies, where contractors needing to excavate must contact a central registry of underground utilities who, free of charge, arrange for the utility companies to mark the location of their services, minimising the danger of accidental damage. Making use of this facility is a legal requirement in most US states; nonetheless, unauthorised excavation still occurs, leading to unexpected damage to

cables. Such damage can be very difficult to repair. In some situations sufficient spare cable may be available to pull the cable break into an existing access point and splice, but often pulling the cable through is not possible and the break must be bridged, requiring new splice enclosures and excavations: expensive in terms of man-hours, complexity and, most importantly, fibre down time.

There is therefore a demand for a technology that would allow threats to fibre cables to be detected and identified, before damage is caused to the cable. Given the extent of the deployed fibre network (by 2000, over 300 million kilometres [9] had been installed world-wide, enough to wrap 23 thousand times around the Earth's equator), conventional monitoring systems such as CCTV surveillance, patrol by security personnel etc are not feasible.

1.1.3. Project History

Seeking to address this weak link in the communications system, Radiodetection, a company manufacturing network support equipment, approached the ORC, establishing the long-running Fibre Threat Alerting System (FTAS) research project aiming to produce an optical sensor which, coupled with suitable signal processing systems, could monitor the acoustic vibration along a fibre link, signalling an alarm in the case of a threat (e.g. an unexpected mechanical digger) being identified, allowing preventative action to be taken before fibre damage occurs.

The initial work carried out within the collaboration led to the development of a novel Sagnac sensor [10-12]. This system had extremely high sensitivity, allowing detection of very small-strain disturbances, but poor spatial discrimination of particular sections of fibre, particularly in the presence of substantial acoustic background noise. Furthermore, two dedicated fibres are required in the cable with a link at the far end to form a loop.

Work was also carried out to investigate the feasibility of using the principle of Optical Time-Domain Reflectometry (OTDR), already extensively applied to the measurement of loss and reflection, to monitor the fibre with improved spatial resolution relative to the Sagnac technology. In this technique pulses of light are launched into the fibre, allowing spatial discrimination using time-of-flight techniques, analogous to RADAR and LIDAR. The author joined the ORC in 2001, concentrating primarily on developing the OTDR approach to develop a sensor to fulfil the

requirements of cable protection applications. Work on this technology, and some related areas, forms the bulk of this thesis.

1.1.4. Aims

In summary, the project aim was to develop an optical fibre sensor technology, for cable protection applications. In order to be successful, the sensor must have the capability to:

- Operate on a single, standard telecommunications single-mode fibre, as found in installed telecommunications networks;
- Detect the acoustic disturbances corresponding to a threat to the cable;
- Locate a disturbance unambiguously with resolution <100 m, giving sufficiently accurate location so allow the source of a disturbance to be observed from the indicated location;
- Operate at a range of 40 km, the typical repeater separation for installed fibres, with sufficient SNR to allow a threat to be observed;
- Operate with access to a single end of the fibre only, allowing operation on a broken fibre and minimising installation costs.

1.1.5. Other Applications

Although the project aims described above, due to the nature of industrial collaboration, had a specific goal in the field of telecommunications network security, a sensor meeting these requirements could obviously find application in a large number of other fields. These include:

- Perimeter security: prisons, air-fields and other applications where long-length perimeters must be continuously monitored;
- Monitoring the location of vehicles on roads or rails;
- Seismic monitoring over long distances (many tens of kilometres);
- Structural vibration monitoring in buildings, bridges, tunnels, dams etc;
- Pipe-line monitoring, both for leak identification which is important economically and for safety and environmental reasons, and security where pipelines are at risk from theft or sabotage.

Since optical sensors are complex, and have high unit cost, the most promising applications are those where their long-range capability allows many discrete sensors to

be replaced by a single distributed sensor, reducing the overall cost of installation. Since an audio output is easily analysed, the potential for automated signal identification is much better than for more conventional image-based systems, where an operator is usually required to interpret the images obtained.

1.2. Optical Fibre Sensors

Optical Fibre sensors are divisible into two distinct categories: extrinsic sensors, in which conventional optical sensors are interrogated via an optical-fibre link; and intrinsic sensors, where the fibre itself forms the sensor, as required for the cable protection application of interest here. In the latter case, various external parameters: strain, temperature, electromagnetic fields, etc, modify the properties of light propagating through the fibre. The fibre may be of a standard type, or specifically designed for high sensitivity to the parameter of interest. In many applications the mechanical design of the fibre layout is also important, for example in fibre hydrophones, the fibre is wound on cylindrical mandrels to increase the total phase signal, and in micro-bend sensors the fibre is tightly bent so that any small changes in profile give a large change in the bending loss.

The advantages of optical fibre over copper-based systems in communications are mirrored in the field of sensors. Signals in fibre are virtually immune to electromagnetic interference and none is generated. Optical systems are generally considered to be intrinsically safe in volatile or explosive atmospheres. Although this is generally true, in the case of very high optical powers, or in flammable atmospheres, it is possible to generate enough heat to cause an explosion or fire in the event of fibre breakage [13]. Finally, the extremely low attenuation of fibre, which can be as small as 0.2 dB / km, compared to 5 dB / km for copper conductors [14], can allow operation over long ranges with relatively modest performance degradation.

Distributed optical fibre strain sensors can generally be split into two groups. The first containing the standard interferometers: the Michelson [14], the Mach-Zehnder [14] and the Sagnac [15], while the second groups together those sensors which operate using the principle of optical time-domain reflectometry (OTDR) [16], these are discussed in Sections 1.3 and 1.4 respectively.

1.3. Conventional Interferometer Sensors

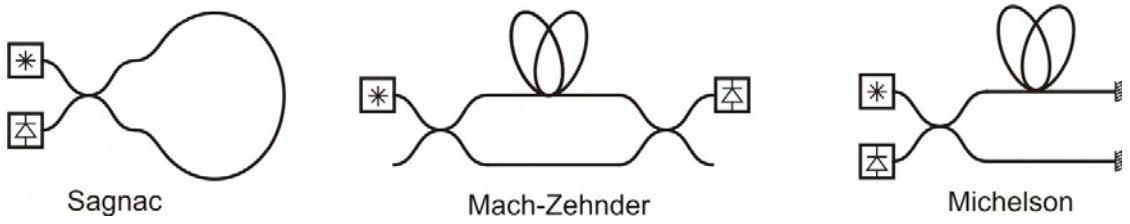

Figure 1.3.1

The three principal interferometer architectures discussed in the text. In the Sagnac, light which has counter-propagated around the loop interferes; in the Mach-Zehnder the light is split between two paths, one of which is the sensing fibre; and in the Michelson light reflected from the sensing and reference arms is interfered at the photo-detector.

In the Sagnac interferometer [15, 17], light from the source passes around the loop, in both directions, before interfering at the photo-detector. When an external perturbation generates a time-varying phase disturbance, away from the mid-point of the loop, the light arriving at the detector from each direction has passed through a different total optical path length (OPL), so information about the disturbance is contained in the intensity of the resulting interference. Novel methods have been developed to enable location of phase disturbances [10-12], however the accuracy of the location is severely degraded where the acoustic background noise is high, since the decoded signal results from the integral of the phase disturbances around the entire loop.

The Mach-Zehnder interferometer operates by combining light which has passed through two independent fibres. A phase disturbance, acting on one fibre, will vary the phase difference between the two arms, modulating the intensity resulting from the interference, allowing the phase disturbance to be identified. A disturbance may be located by forming two, counter-propagating interferometers, at different wavelengths, and using time-of-flight comparison to deduce the location [18]. However, this method is unreliable in situations where the sum of the acoustic background, over the whole sensor, is comparable to the signal of interest, or where there are multiple disturbances. Other methods proposed to allow location of disturbances involve combining the Sagnac and Mach-Zehnder techniques [19], however these still become unreliable where more than one disturbance occurs concurrently or within a short time scale.

The Michelson interferometer [14] is similar to the Mach-Zehnder but, in this case, the light passes through two independent arms, with reflectors at the far ends, one of which is the sensing arm, the other the reference. The resulting interference is modulated by the variation of the phase accumulated by the light reflected from each arm. Again, the acoustic background noise is integrated along the fibre length and no reliable means of locating a disturbance is available.

Thus, although conventional interferometric sensors are very sensitive, their application to cable-protection applications is limited by the integration of the signals over the whole gauge length. This is obviously a severe draw-back where the signal of interest may be a small disturbance at one specific location on a deployed fibre, which may pass under roads, through buildings and other noisy environments. Even very small phase disturbances, when integrated over a fibre of many kilometres in length will rapidly exceed the size of even a very large disturbance with small spatial extent. From the preceding discussion, it is clear that, to obtain the disturbance location performance set out in Section 1.1.4, an alternative type of sensor must be sought.

1.4. Optical Time-Domain Reflectometry

1.4.1. Rayleigh Scattering

Rayleigh scattering refers to the scattering of light by particles which, typically, have dimensions less than a tenth of the wavelength of the light. The strength of the scattering is strongly dependent on the wavelength, λ, and the scattering angle, θ, being proportional to $\lambda^{-4} \sin^2 \theta$ [20].

The strong dependence on wavelength leads to the so-called Tyndall effect where, in a medium containing only small scattering particles, blue light is scattered more strongly than longer-wavelength red light. It is this effect which leads to the blue appearance of the sky, varying with angle relative to the incident light from the sun [21]. Similarly, when viewing the sun near the horizon, the light passes through a much greater length of atmosphere than when the sun is high in the sky, and the angle of viewing is small, so the sun is reddened as the blue wavelengths are more strongly attenuated by scattering.

As glass cools below its melting temperature during manufacture, it retains the amorphous structure of the molten phase. As a result, the structure of glass retains some of the thermodynamically induced fluctuations in density corresponding to the melt temperature. Such frozen-in fluctuations are not present in crystals but can occur in amorphous glass, due to the large freedom of relative orientation allowed by the tetrahedral structure of silica. These density fluctuations lead to microscopically-sized regions where the refractive index varies from the mean value, giving rise to scattering of light propagating in the glass [2, 20]. Where the physical dimensions of the fluctuation is of the order of a tenth of the wavelength of light, or smaller, Rayleigh scattering occurs. Larger discontinuities, where the change in refractive index is small, such that the accumulated phase delay is less than a quarter of a wavelength compared to the bulk index, give rise to Rayleigh-Gans scattering which is behaviourally similar to Rayleigh scattering. From now on these will be grouped together as "Rayleigh scattering".

1.4.2. Rayleigh Scattering in Optical Fibres

The attenuation of optical fibres is fundamentally limited by the Rayleigh scattering due to the refractive index fluctuations frozen into the glass. Modern fibre manufacturing techniques can reduce scattering from other sources, such as impurities and mechanical defects, to negligible levels [2, 5]. Rayleigh scattering causes

attenuation of light passing along an optical fibre through two mechanisms. A small fraction of light is backscattered: where scattered light is reflected back towards the source and re-captured by the fibre and directed back towards the source. The main contribution is from light scattering at angles which are too large, relative to the fibre axis, for the light to undergo total-internal reflection in the fibre, instead the light leaks out through the cladding.

A theoretical analysis of Rayleigh backscattering in single-mode optical fibre was first given, using a wave-optics approach, by Brinkmeyer [22]. The analysis was later generalised, for arbitrary refractive index profiles and loss distributions, by Hartog and Gold [23], the two approaches agreeing for a Gaussian mode-profile.

For a rectangular pulse, of temporal duration τ and power P_0, launched into a single-mode fibre at $t = 0$, the backscattered power returned to the launch end of the fibre $P_B(t)$, can be shown [22] to be given by:

$$P_B(t) = \tfrac{1}{2}\alpha_s v_g \tau S P_0 e^{-2\alpha v_g t}, \qquad 1.4.1$$

where α_s is the Rayleigh scattering constant, α is the attenuation coefficient, v_g is the group velocity of light in the core and S is the fraction of the scattered light which is recaptured by the fibre in the reverse direction. For a step-index single-mode fibre, with core and cladding refractive indices of n_1 and n_2 are the respectively, S is approximately constant:

$$0.21\frac{n_1^2 - n_2^2}{n_1^2} \le S \le 0.24\frac{n_1^2 - n_2^2}{n_1^2}. \qquad 1.4.2$$

Typical values of the refractive indices, for silica fibres at 1550 nm, are $n_1 = 1.46$ and $n_2 = 1.44$ [2]. Taking these values and assuming a mid-point coefficient of $(0.21 + .024)/2$ gives $S = 0.0063$, which varies by only a few percent for graded-index fibres [22].

Noting that the total attenuation, α, and scattering coefficient, α_s, may vary with z, it is clear that the power backscattered from a point is directly related to the forward-propagating optical power at that point and to the local scattering coefficient. Therefore, by launching a pulse of light into a fibre and monitoring the backscattered light as a function of time, information about the spatial distribution of optical

attenuation and reflection can be extracted using 1.4.1. This forms the basis of the powerful technique of Optical Time-Domain Reflectometry.

1.4.3. Optical Time-Domain Reflectometry (OTDR)

Optical Time-Domain Reflectometry (OTDR), shown schematically in Figure 1.4.1, was first demonstrated in 1976 by Barnoski & Jensen [16], who used the technique in an experiment to measure the attenuation characteristics of a 360 m long multi-mode fibre. Using a pulsed gallium-arsenide injection laser, they launched a 200 ns pulse into the fibre and, by averaging the Rayleigh backscatter over many pulses, they were able to measure the attenuation coefficient to an accuracy of ± 0.05 dB / km. Prior to their invention, measurements of the distribution of fibre attenuation were only possible using the destructive "cut back" method.

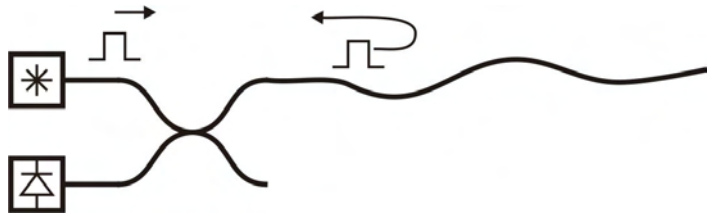

Figure 1.4.1

The principle of optical time-domain reflectometry. Pulses of light are launched into the fibre and scattering reflects some light back to the source. Since the propagation velocity is known, the range from which the received light was backscattered can be calculated.

The OTDR technique gained rapid acceptance for use in multi-mode fibres, but its application to single-mode fibre (SMF) was slower to gain pace. This was primarily due to the challenges presented by the reduced backscatter power, resulting from the low index change compared to multi-mode fibre, and the increased difficulty of coupling into SMF with much reduced core diameter relative to multimode fibre [24]. These issues were gradually overcome and, by the early 1980s, OTDR of SMF at long-wavelengths from 1.0 μm to 1.8 μm was well established [24-26]. OTDR has subsequently been developed into a sensitive and sophisticated technique for characterising optical fibres, with numerous review articles detailing the many advances in the field, for example [26-28], and commercial instruments are available from a number of manufacturers.

One area of research was in launching coherent light into the fibre to allow coherent detection, where the backscattered light is interfered with frequency-shifted light from the same source, giving an electrical carrier at the difference frequency allowing high-sensitivity detection [29, 30]. This technique became known as coherent-OTDR (C-OTDR). For the purposes of this thesis, any OTDR launching pulses derived from a coherent source will be known as C-OTDR. A problem observed with the highly-coherent light required for C-OTDR was that of "coherence" or "fading" noise. This is the phenomenon where, due to the interference of the backscattered light from many, randomly-located, scattering sites, the backscatter trace from a single pulse is no longer the smooth decay predicted by 1.4.1, instead giving a noise-like signal [31, 32]. For loss and reflection measurements this could be overcome by averaging the backscatter signal over a number of wavelengths or polarisation states [30, 33].

1.4.4. OTDR Strain Sensors

It was rapidly realised that the technique of OTDR could be used, not only to characterise optical fibres, but to realise long-range distributed sensors by monitoring suitable parameters of the backscattered light modulated by the variable of interest. Most simply, micro-bend sensors use specially constructed fibre assemblies to introduce bending loss to the sensing fibre, which can be monitored using a standard OTDR. The need to control the fibre geometry, to obtain sufficient sensitivity, makes the method more suitable for point measurements rather than truly distributed sensors [14].

The technique of Polarisation-OTDR, monitoring the polarisation of the backscattered light to detect externally induced changes in birefringence, was first proposed by Rogers [34, 35]. The technique was quickly applied to measuring the birefringence of optical fibres [36] but has seen little use in general sensing applications, partly because of the complex processing required to eliminate cross talk, although a distributed pressure sensor, relying on a custom-made holey fibre to increase the modulation of the birefringence, has been recently reported [37].

Most successful have been the various sensors based on variants of C-OTDR which monitor the phase of the backscattered light, via a number of optical architectures that allow interferometric interrogation, allowing phase disturbances, induced by external perturbations to the fibre, to be observed.

The most simple of these C-OTDR sensors launch a single coherent pulse and monitor changes in the resulting backscatter trace with time [38-42], which varies with

phase disturbance since the self-interference pattern of the pulse is modified. Another technique incorporates a Mach-Zehnder interferometer in the C-OTDR receiver and, by launching two pulses, effectively synthesises a Mach-Zehnder interferometer, moving along the fibre with the pulses [43]. In a similar technique, self-heterodyne OTDR, proposed by Dakin and Lamb [44], two pulses are launched, at different frequencies, generating a carrier, with phase modulation from any disturbance occurring between the pulses, when the resulting backscatter interferes at the optical receiver. A similar method, demonstrated by Wooler and Crickmore [45], uses partially reflective fibre Bragg gratings to increase the signal above the level due to Rayleigh scattering, but otherwise applying the same principle.

Closely related to the OTDR, is the technique of frequency-modulated continuous-wave sensing, also referred to as optical frequency-domain reflectometry (OFDR). Instead of launching short pulses, light is launched continuously at swept frequency and the backscatter monitored, with the measurement range defined by the frequency of the backscattered light [46]. OFDR has shown promise for high-resolution, accurate characterisation of short (~1 km) fibres, however practical limitations on the frequency excursion suggest that they are unlikely to be suitable for high-resolution strain sensing over tens of kilometres.

In addition to the Rayleigh scattering-based sensors, OTDR sensors can be implemented which monitor the light backscattered by one, or both, of the non-linear scattering mechanisms, Raman scattering and Brillouin scattering [14, 47]. The light scattered by these processes is significantly lower in intensity than the Rayleigh scattering, making the detection more challenging than in Rayleigh-based systems. Nonetheless Raman-based sensors have proven very successful for temperature measurements [48], however Raman-based techniques are not of interest for vibration sensing as the Raman scattering exhibits no strain dependence [14].

Brillouin scattering leads to backscattered light which is shifted in frequency by around 10 GHz, with a line-width of ~100 MHz [14]. The exact value of the Brillouin shift is temperature and strain dependent, allowing a change in these parameters to be observed by measuring changes in the frequency of the backscattered light. OTDR-type sensors based on Brillouin scattering generally fall into two groups: Brillouin-OTDR (B-OTDR) [49], where a pulse is launched from one end of the fibre and the scattered light analysed; and Brillouin-optical time-domain analysis (B-OTDA) where the

modulation of a CW beam due to Brillouin scattering resulting from a counter-propagating probe pulse is observed [14, 47].

The main drawback of Brillouin-based sensors for dynamic strain measurement is that to measure the strain-induced change in Brillouin shift of ~ 50 MHz / με [14], significant averaging is required because the bandwidth of the Brillouin scattered light is ~ 100 MHz. Typically the averaging is over many million samples, taking several minutes to acquire [49]. Some techniques have been reported which avoid the need for long-term averaging giving sampling rates ~(1- 10) Hz [50, 51], however these are not truly distributed and can only operate at a small number of points simultaneously. As a result, Brillouin-based strain sensors are not suitable for applications where acoustic-frequency signals are of interest.

1.5. Discussion

From the brief outline of the various available sensor technologies in the preceding sections, summarised in the table of Figure 1.5.1 (overleaf), it is clear that the conventional interferometric sensors are unlikely to meet the requirements described in Section 1.1.4. Although methods for locating disturbances exist, they are invariably unreliable in the presence of significant background noise. A further subtle difference should be noted between the interferometric schemes for locating a disturbance and the OTDR method: in the former, an observed signal may be located, whereas, in the latter, it is possible to interrogate a given location, regardless of the magnitude of signals at other locations and the presence, or otherwise, of a significant signal at the location of interest.

For cable protection the OTDR-based sensors are clearly most suitable. Brillouin-based sensors were rejected, based on the limited measurement bandwidth, as were techniques using Raman scattering, as it is insensitive to strain.

Thus, the sensor technologies based on OTDR using Rayleigh scattering appear to be the most suitable for cable-protection applications. OFDR sensing would be unlikely to allow long-range (40 km) sensing with the required high resolution (~ 100 m or less).

Therefore, the remaining techniques, identified as promising for fibre protection, were those based on C-OTDR, and P-OTDR. Of the many C-OTDR techniques available, the one considered particularly interesting was the self-heterodyne OTDR because the mode of operation allowed the benefits of coherent detection, high receiver sensitivity and the possibility of linear demodulation of the interference, along with the possibility of spatial resolutions of < 100 m, as required in the target specification of section 1.1.4. The P-OTDR was considered promising as any perturbation of the fibre is likely to cause modulation of the birefringence and sensitivities capable of observing the effect of resting a mass of ~10 g on the fibre have been predicted [35]. Having reached these conclusions, initial investigations into these technologies were carried out (described in Chapter 2), before performing more detailed analysis of the scheme that showed the most initial promise.

Scattering Mechanism	Backscatter Power wrt Rayleigh	Technique	Single Ended?	Bandwidth	Comments
Rayleigh	0 dB	"Normal" OTDR	Y	DC – kHz	Attenuation change likely to be small so bandwidth limited by averaging
		Micro-bend OTDR	Y	DC – kHz	Improved strain resolution but needs custom cable.
		P-OTDR	Y	DC – kHz	Theoretically very sensitive [35] but complex signal analysis to avoid cross talk.
		C-OTDR	Y	DC – kHz	Several methods to extract strain signal, generally interferometric so sensitive but non-linear.
		OFDR	Y	DC – kHz	(Range / Resolution) limited by practical frequency sweep.
Raman	-30 dB [47]	N/A	Y	DC / ~10 Hz	Raman shift is not strain-dependent and scattered light is incoherent so no way to extract strain
Brillouin	-20 dB [14] (better for stimulated)	B-OTDR	Y	DC	Brillouin bandwidth ~ 100 MHz [14] so need averaging times ~ minutes [52] to resolve small changes in Brillouin shift. Linear response to strain.
		B-OTDA	N	DC	Access required to each end of fibre, increased power if stimulated but still limited by need to average to observe change in Brillouin shift

Figure 1.5.1

Comparison of OTDR-type technologies for strain sensing.

1.6. Thesis Outline

The chronology of the work behind this thesis, and the interconnection of the various elements, is shown schematically in the flow diagram Figure 1.6.1. The work was clearly influenced by the industrial collaboration, which provided the main focus of the project – acoustic vibration sensing for fibre-cable protection; most notably in the production of a series of prototype systems which were used during extensive field trials, which were made possible by the close links with the industrial sponsor. This strong involvement from the sponsors was pivotal in defining the direction of the work and the practical experience gained by applying the technology in real-life situations provided the focus and motivation necessary to make a number of important observations, which lead to significant follow up work. An important benefit was that the experimental equipment produced was considerably more robustly engineered, and the signal processing systems more complex and powerful, than may have been possible in a purely academic environment, providing significant benefit to the research.

The rest of the thesis details this work. Chapter 2 describes the initial experiments, carried out to investigate the approaches considered promising, as discussed in the previous section. Following this work, it was decided to concentrate on the most promising technique, the theory of which is considered in detail in Chapter 3, before the potential performance is analysed in Chapter 4. The practical investigation was boosted at this stage by the construction of a portable prototype system, in collaboration with Radiodetection, allowing field trials to be carried out to investigate the performance of the system in an installed-fibre environment. The design and subsequent trials of the prototype are described in Chapter 5.

The results of these field trials suggested that the models, developed in Chapter 4 describing the noise performance, required revision. Chapter 6 describes the laboratory investigation and theoretical analysis required to explain the observations made during the field trials described in Chapter 5, explaining the disparity with the predictions from Chapter 3. Having developed an improved understanding of the factors limiting the performance of the sensor, improved experimental designs were implemented and tested, described in Chapter 7.

The main part of the thesis ends with Chapter 8, where the conclusions from the work are discussed along with the potential for future work. The possible future work includes further investigation into a novel sensor concept, following on from a brief

preliminary investigation carried out in parallel to the main work which resulted in a successful poster presentation at OFS-17 in Bruges [53].

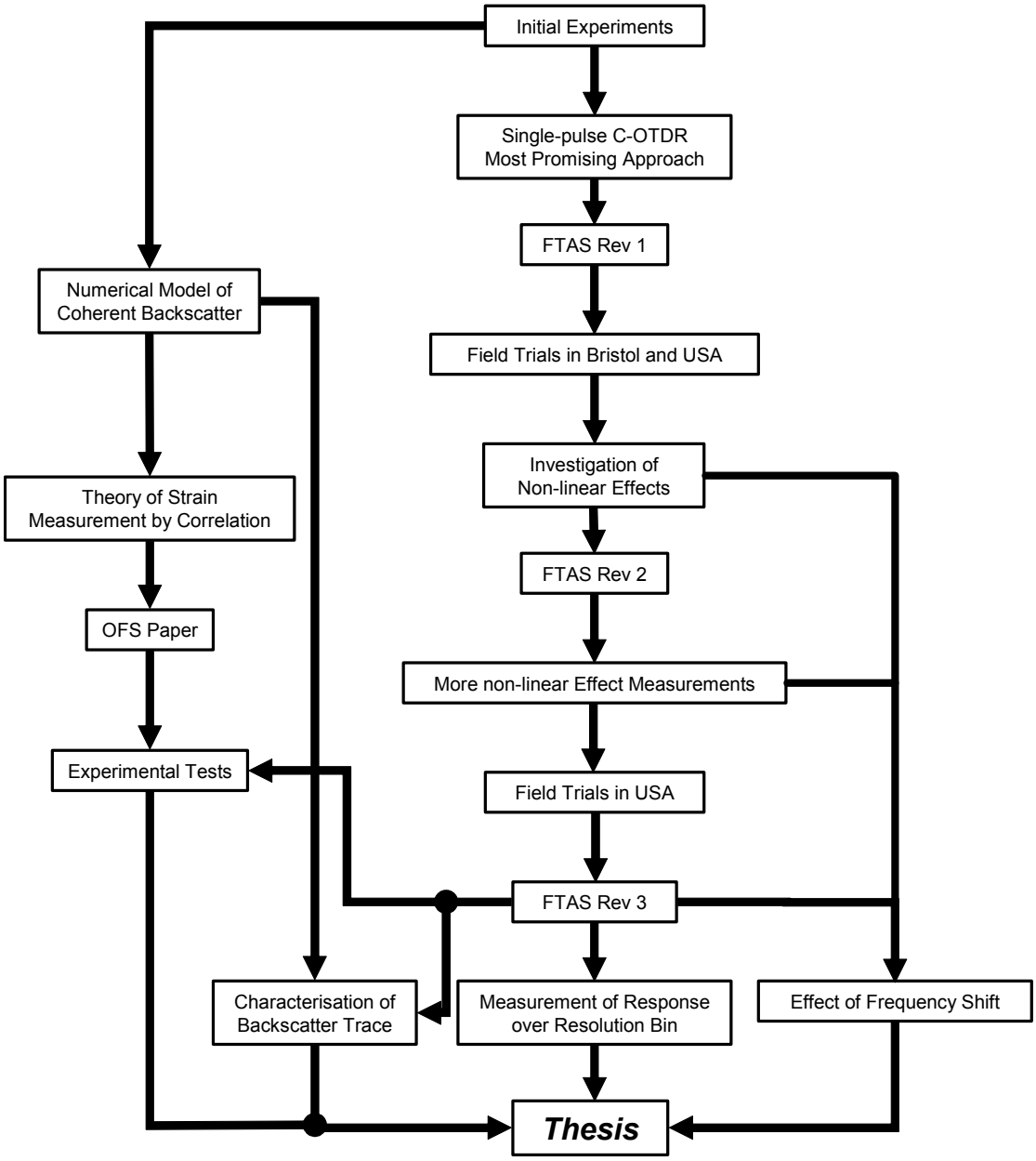

Figure 1.6.1

Approximate representation of chronological flow of the work presented in this thesis, showing the relationship of the Fibre Threat Alerting System (FTAS) project to the more exploratory investigation of strain measurement by correlation of the backscatter trace.

1.7. Summary of Experimental Systems

As explained in the previous section, the work carried out for the purposes of this thesis involved experimentation with a large number of sensor systems. For reference these are summarised in the table below (Figure 1.7.1), with an indication of the chapter where their use is described.

Experimental System	Uses / Features	Chapter
Self-heterodyne C-OTDR	Initial testing in laboratory	2
C-OTDR (Lab)	Initial testing in laboratory	2
P-OTDR	Initial testing in laboratory	2
FTAS Rev 1.0	Initial tests in different environments	5
FTAS Rev 1.1	Field trials on deployed telecommunications cable; Investigation into non-linear effects	5 6
FTAS Rev 2	Incorporated digital signal processing; Extensive field trials	7
FTAS Rev 3	Added split detection scheme; Used for proof-of-principle experiments into strain measurement using correlation.	7 8 & [53]

Figure 1.7.1

Summary of the experimental systems which were designed, manufactured and used during the preparation of this thesis.

Chapter 2 Preliminary Experiments

In the previous chapter, three approaches, for developing an OTDR-based sensor, for telecommunications cable protection, were identified as attractive for further investigation. In this chapter the evaluation of each approach is described, using brief analysis and some initial experiments, to determine the potential benefits and limiting factors of each technique.

2.1. Self-Heterodyne C-OTDR

2.1.1. Introduction

The first of the approaches to be investigated was the self-heterodyne C-OTDR. Following a brief description of the theory describing the operation of the sensor, the initial experimental system and the results obtained are described. An improved optical architecture and demodulation technique are then explained, and the potential for successful demodulation is investigated.

2.1.2. Theory

As discussed in the previous chapter, the self-heterodyne C-OTDR was proposed as a method of strain sensing by Dakin & Lamb [44]. The principle of operation is illustrated in Figure 2.1.1. Two pulses of light derived from the same coherent source, having angular frequency, ω_0, are frequency shifted, by ω_1 and ω_2 respectively, and launched into the fibre, as shown. Since the light is from the same coherent source, the electric field of each pulse can be written as:

$$\begin{aligned} E_{1-Forward} &= E_0 \exp\{i[(\omega_0+\omega_1)t - kz]\}; \\ E_{2-Forward} &= E_0 \exp\{i[(\omega_0+\omega_2)t - kz]\}. \end{aligned} \qquad 2.1.1$$

Some of the light will undergo Rayleigh backscattering, as shown in Figure 2.1.1. Consider the light scattered from each of the pulses, which are at locations z_1 and z_2 respectively, located either side of a phase time-varying disturbance, $\phi(t)$. The electric field at the detector due to the backscattered light from each pulse can be written as:

$$\begin{aligned} E_1 &= E_0 R \exp\{i[(\omega_0+\omega_1)t - 2kz_1 + 2\phi(t)]\} \\ E_2 &= E_0 R \exp\{i[(\omega_0+\omega_2)t - 2kz_2]\} \end{aligned} \qquad 2.1.2$$

where R is the fraction of the light returned to the detector, taking into account the efficiency of Rayleigh scattering and the attenuation of the fibre. It has been assumed that the phase disturbance varies sufficiently slowly that its value has not changed significantly in the time between the forward propagating pulse and the backscattered light passing through the disturbed region.

Taking the intensity at the detector:

$$I(t) = < (E_1 + E_2)^* (E_1 + E_2) >, \qquad 2.1.3$$

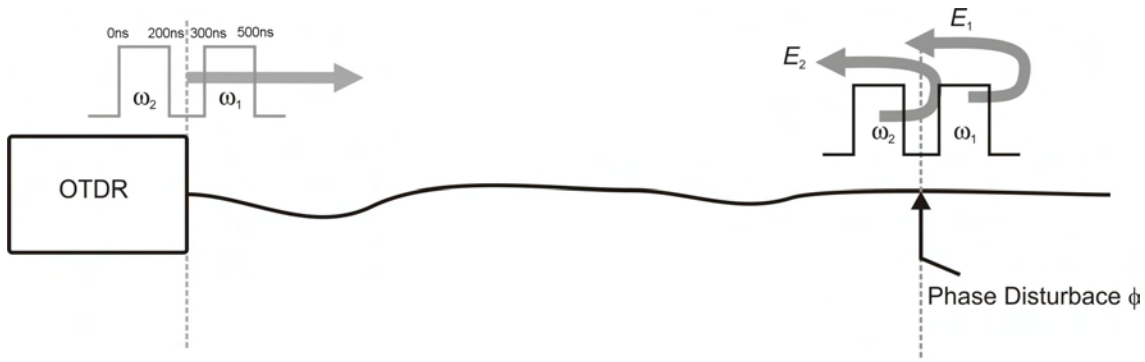

Figure 2.1.1

Principle of the two-pulse self-heterodyne C-OTDR, showing typical timings used in practice. Two pulses are launched at different frequencies, causing the backscatter interference at the photo-detector to generate an RF carrier, at the difference frequency, which is phase modulated by the time-varying phase disturbance, $\phi(t)$.

where * represents the complex conjugate and <…> is the time average over many optical cycles, substitution gives:

$$I(t) = 2E_0^2 R^2 \left[1 + \cos\{(\omega_1 - \omega_2)t - 2k(z_2 - z_1) + 2\phi(t)\}\right]., \qquad 2.1.4$$

Writing the differences as $\omega_1 - \omega_2 = \omega_C$ and $k(z_2 - z_1) = \phi_0$ and substituting $2E_0^2 R^2 = I_0$, the resulting intensity can be written as:

$$I(t) = I_0 \left[1 + \cos\{\omega_C t - 2\phi_0 + 2\phi(t)\}\right], \qquad 2.1.5$$

which is a carrier, of angular frequency ω_C, with phase modulation [6] of twice the phase disturbance $\phi(t)$. Thus, by gating the backscattered light, such that the light received is from pulses either side of the disturbance, and demodulating the PM signal, the phase disturbance may be decoded.

2.1.3. First Experimental Realisation

The first practical realisation of the self-heterodyne C-OTDR is shown in Figure 2.1.2. Pulses of light were generated by switching a CW source with an acousto-optic modulator (AOM), which also frequency-shifts the light. Thus by driving the AOM at a different frequency for each of the two pulses per cycle, the required difference in optical frequencies could be obtained. Before being launched into the fibre, the pulses were amplified by an erbium-doped fibre amplifier (EDFA), increasing the backscattered power. The backscattered light was directed either straight to the receiver, or amplified by a second EDFA before detection.

Having outlined the operation, a more detailed description of the optical architecture, shown in Figure 2.1.2, is given. CW light was generated by a fibre DFB laser (SPI HN01-1550.116) with a specified maximum line-width of 30 kHz, pumped at 975 nm at approximately 90 mW. The CW output was pulsed by an AOM (Gooch & Housego M080-2J-F2S) driven at 85.35 MHz for the 1st pulse and 73.65 MHz for the 2nd, giving a difference frequency of 10.7 MHz. The RF drive for the AOM was generated by independent free-running DDSs (Analog Devices AD9852) built into evaluation boards produced by the manufacturer. The RF was filtered to remove harmonics of the desired frequency and pulsed by RF switches (Mini-Circuits ZYSW-2-50DR), controlled from the FPGA sequencer (PCB by Radiodetection), and combined using an impedance-matched combiner (Mini-Circuits ZFRSC-42) before amplification by a power amplifier (Mini-Circuits ZHL-5W) to drive the AOM. An EDFA then amplified the two pulses, with a second AOM (Gooch & Housego M110-2J-F2S) blocking the out-of-pulse ASE.

An optical circulator (by Foci) directed the pulses into the fibre under test (FUT) and routed the backscattered light, initially directly to the receiver (Theoptics TA10, 30 MHz bandwidth), and later to the receiver via an EDFA. This second, pre-detection, EDFA was built to increase the optical signal to give a stronger carrier, requiring less electrical amplification to reach a given carrier power. The EDFA performance was considered satisfactory at the time; however, in retrospect, the characteristics were less than optimal, which was found when the amplifier was subsequently rebuilt. The ASE from the pre-detection EDFA was removed by an all-fibre filter using a fibre Bragg grating (FBG) (HiWave HWT-FBG-1550-95). The receiver output was gated by

another RF switch, determining the range of the section of fibre under interrogation, and the output passed to the demodulator.

With the optical architecture described a 10.7 MHz carrier was generated, and when a disturbance was applied to the fibre, using a modified loud speaker cone, small sidebands at the corresponding frequency could be observed either side of the carrier. It was also noted that the amplitude of the carrier was unstable, due to coherent fading noise as observed in coherent OTDR for loss and reflection measurement [31]. This intensity modulation, due the disturbance modifying the relative phases between the discrete scattering sites in the fibre, meant that the carrier spectrum also had a component at the disturbance frequency.

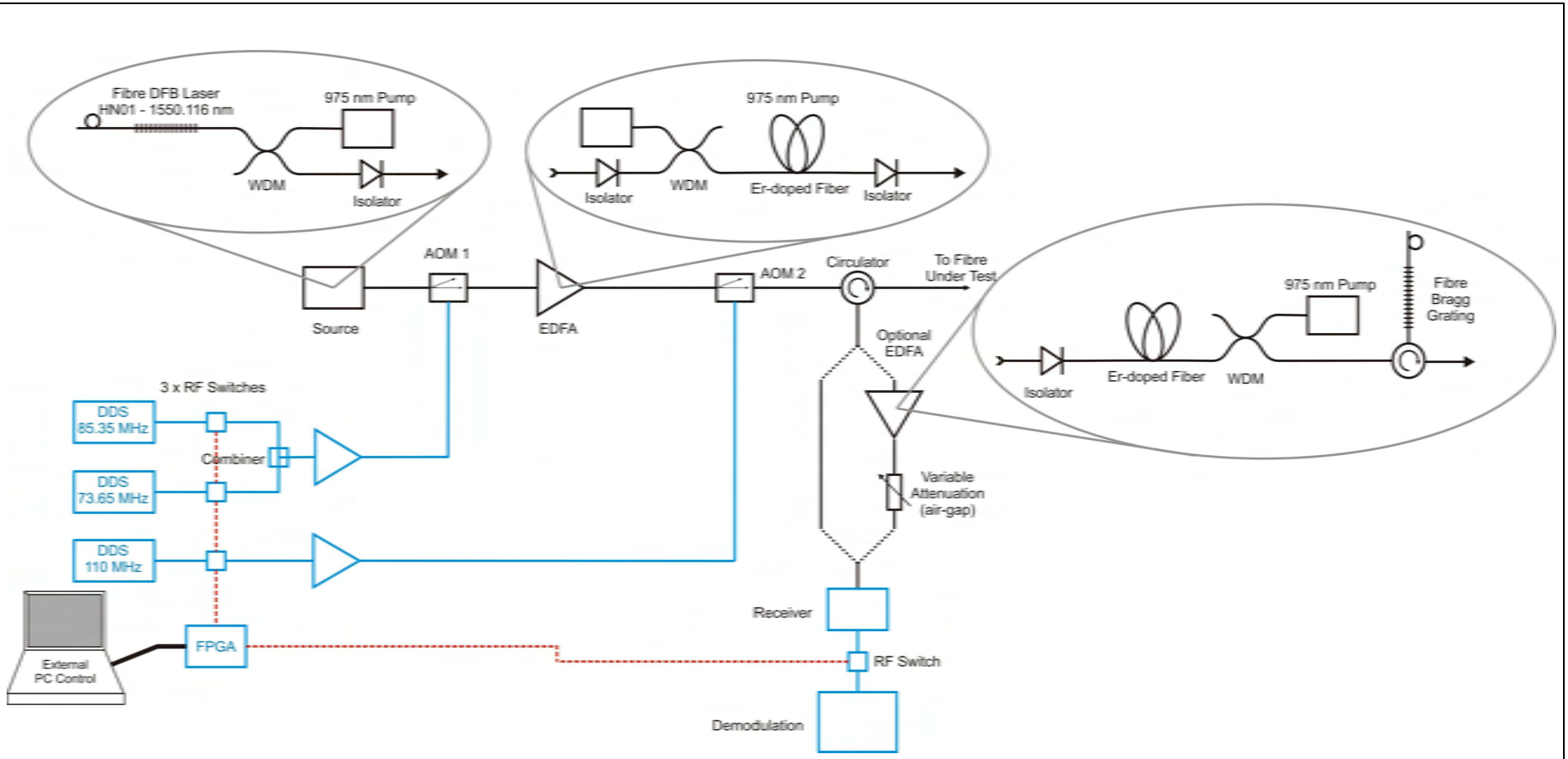

Figure 2.1.2

Optical and schematic control architecture for the initial two-pulse self-heterodyne sensor system. The pre-detection EDFA increased the carrier power at the receiver, reducing the level of electrical amplification required before the demodulation system.

2.1.4. Delay and Cross-Multiply Demodulator

In order to extract the signal from the carrier some form of demodulator was required. The main issue considered likely to cause problems was separating a true demodulation effect from the effects due to feed-through of the undesirable random amplitude modulation of the carrier, due to the coherence noise. As a first iteration it was decided to construct a simple delay and cross-multiply (DCM) demodulator.

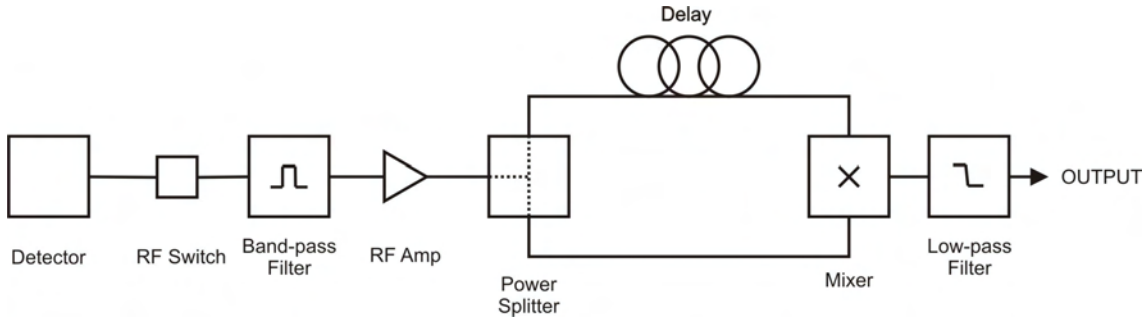

Figure 2.1.3

Schematic of the Delay and Cross-Multiply (DCM) demodulator. The RF amplifier was an attempt to obtain sufficient power into the mixer to achieve limiting, causing the output to be independent of the carrier amplitude.

The implementation of the DCM demodulator is illustrated in Figure 2.1.3. To understand its operation, assume the phase modulation of the carrier is of the form $\phi(t) = \Phi\cos(\omega_m t)$. The phase difference, $\Delta\phi(t)$, between the carrier reaching the mixer via the direct and delayed routes is:

$$\Delta\phi(t) = \int_0^{\tau} \frac{d\phi}{dt}\, dt\,. \qquad 2.1.6$$

When τ, the propagation time through the delay, is small compared to the period of the signal, i.e. $\tau << 2\pi/\omega_m$, the differential can be assumed to be constant over the period of integration, giving:

$$\Delta\phi(t) = \tau \cdot \frac{d\phi}{dt}\,. \qquad 2.1.7$$

At the mixer, where the carrier is now AC coupled, since it lies after the band-pass filter, then if the power is sufficient the mixer inputs will limit the signal, in effect generating a square wave with the same zero-crossings as the input. For simplicity of analysis, assume that this limiting action of the mixer sets the value to be high

(valued 1) where the carrier is positive and low (valued 0) when the carrier is negative. The mixer output is the product of the two inputs, which means that by low-pass filtering the output, effectively giving the time average, gives a signal proportional to the phase difference between the inputs.

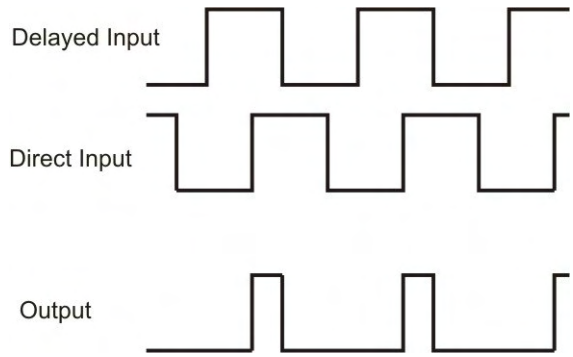

Figure 2.1.4

Schematic illustration of the relationship between the limited mixer inputs and outputs. Low-pass filtering the output give the time average, which is proportional to the phase difference between the two inputs.

By inspection of Figure 2.1.4, and assuming that, with no modulation, the inputs are in quadrature, the output for a single-frequency signal is given by:

$$V_{Out}(t) = 1 - \frac{2\Delta\phi(t)}{\pi}. \qquad 2.1.8$$

Substituting for the phase this becomes:

$$V_{Out}(t) = 1 - 2\frac{\omega_m}{\omega_C}\Phi\left(n+\tfrac{1}{2}\right)\cos(\omega_m t). \qquad 2.1.9$$

This result shows that the size of the demodulated signal depends on the size of the phase modulation, the ratio of the modulation frequency to the carrier frequency and the length of the delay.

For a phase modulated signal, 2.1.9 shows that decreasing the carrier frequency will increase the depth of the amplitude modulation at the output. The carrier frequency could not be lowered significantly here, as for successful demodulation a number of complete cycles are required within the width of the gate, setting the spatial resolution.

In the practical implementation, which was as shown in Figure 2.1.3, following the RF switch that provided range-gating, the RF signal was band-pass filtered and amplified. The crystal band-pass filter (Temex TE5030) gave a 3 dB bandwidth of

3.75 kHz, centred at 10.700 MHz. The location of the band-pass filter, after the range-gating, meant that the band-pass filter would not limit the spatial resolution as it would if it was before the range-gating switch. Following the filter, the signal was amplified and divided equally using an impedance-matched resistive splitter (Mini-Circuits ZFSC-2-1W). Coaxial cables were made, arranged to give a difference in length of $\left(n+\frac{1}{2}\right)\cdot\frac{\lambda_{RF}}{2}$, where λ_{RF} is the RF wavelength in the coaxial cable and *n* is an integer, ensuring that with no phase disturbance the signals from the two branches are in quadrature.

For sufficiently large signals (>0 dBm), the mixer (Mini-Circuits ZFM-3) acts as a phase detector [54], the output containing a DC component proportional to the phase difference at the inputs in addition to the 21.4 MHz term which was removed by the low-pass filter, formed from a standard in-line passive filter (Minicircuits LPF-5) giving a 3 dB point of 5 MHz followed by a custom-built active filter giving a 3 dB cut-off at 6 kHz.

For the practical implementation, using a carrier frequency of $\omega_C = 2\pi \times 10.7 = 67.2 \times 10^6$ rad / s, a typical modulation frequency of 200 Hz and a phase disturbance of magnitude 2π rad the resulting modulation depth is $2.3 \times 10^{-4}\left(n+\frac{1}{2}\right)$, so for the maximum feasible delay length of 50 m, giving $n = 11$, the expected modulation depth is 2.6×10^{-3}. To observe this requires the electrical SNR to be greater than 52 dB.

A typical carrier spectrum after amplification and filtering with a Temex crystal filter giving a pass band of ~8 kHz is shown in Figure 2.1.5, considering the total noise in the filter pass-band, the SNR is ~12 dB, ~40 dB lower than the required for demodulation using the DCM technique, suggesting that a more sensitive demodulation method was required.

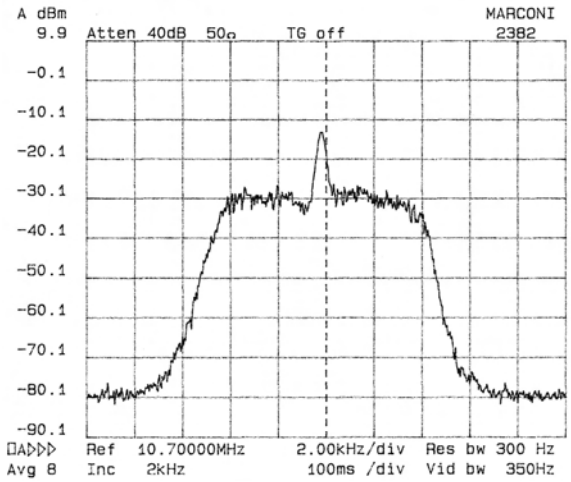

Figure 2.1.5

Typical carrier spectrum after electrical amplification to attempt to obtain saturation in the mixer and filtering with a bandwidth of 8 kHz. *The carrier SNR is ~12 dB, much lower than required for successful demodulation with the DCM scheme.*

2.1.5. Revised Optical Architecture

At this point, with no successful demodulation having been demonstrated, a second practical problem was identified: jitter in the relative timing of the two launch pulses would create phase noise which would swamp the signal of interest.

A simple calculation shows that the phase jitter, $\delta\phi$, corresponding to timing jitter on the delay between the launch of the two pulses δt is given by:

$$\delta\phi = \omega\,\delta t = \frac{2\pi c}{\lambda}\delta t\,. \qquad 2.1.10$$

Thus, to limit the phase noise to $\delta\phi_{Max}$ requires that:

$$\delta t \le \frac{\lambda}{2\pi c}\delta\phi_{Max}\,. \qquad 2.1.11$$

For light at 1550 nm, with the velocity of light $c = 3.0 \times 10^8$ m s^{-1} the maximum jitter for a phase noise of π rad is 5 fs, a level of performance that is unlikely to be achieved by conventional electronics.

To overcome this problem, a different method of producing the two pulses was devised. The modified architecture is shown in Figure 2.2.1. An AOM generated a single pulse from the DFB source which was amplified by the EDFA, before being split into two branches by the 3 dB coupler. Each branch contained another AOM running

continuously to generate the frequency shift. A single AOM could have been used, but it was desired to generate a 10.7 MHz difference frequency, as earlier, to allow use of the same filters. The noise performance could have been improved by gating these AOMs to block out-of-pulse ASE however that measure was not taken here to minimise complexity. The light is recombined at the second 3 dB coupler, with the pulses separated by the length of the delay in the upper branch, 350 m. The sensitive length, defined by the pulse separation, is therefore 350 m, although this could be modified by using an optical delay of different length.

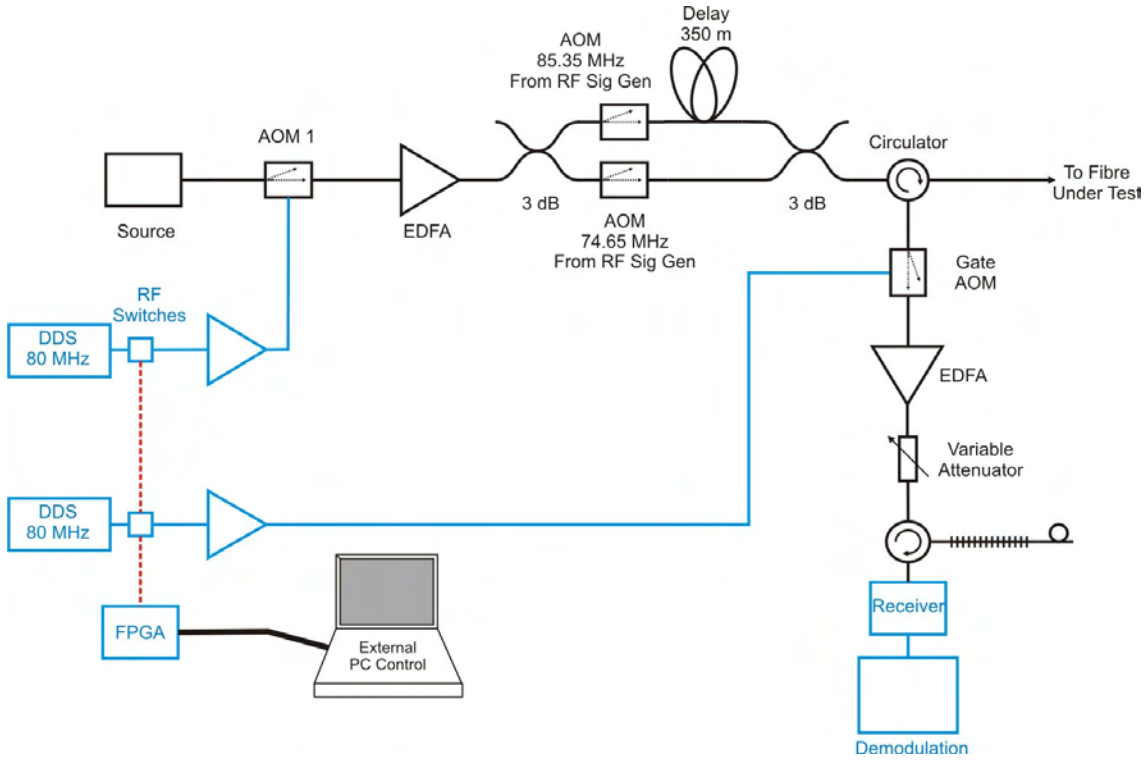

Figure 2.1.6

Modified self-heterodyne C-OTDR system, using a fibre delay to separate a single pulse into two, spatially-separated, frequency-shifted pulse. The stability of the separation is set by the stability of the delay coil. The frequency-shifting AOMs were driven by Marconi RF signal generators with the outputs amplified by linear amplifiers by Mini-Circuits.

The pulses are directed into the FUT by a circulator which routes the backscattered light to a fourth AOM which acts as the range gate, only passing light from the location of interest. A second EDFA amplified the scattered light, the output being filtered to remove out-of-band ASE as before and the signal detected by the Theoptics TA10 receiver.

The filtered received spectrum, having been optically gated with a width of 1 μs (200 m resolution bin) from a range of 6.25 km, where a disturbance at 300 Hz was applied to the fibre using a modified loud speaker, is shown in Figure 2.1.7. The carrier SNR is ~30 dB and sidebands at ±300 Hz are visible approximately 18 dB below the carrier. Despite the promising increase in the relative size of the observed sidebands, the SNR was still below the 52 dB required to observe demodulation using the DCM demodulator, meaning that an improved demodulation system was required.

2.1.6. Improved Demodulator

The DCM demodulator, while simple, had a number of drawbacks. In order for the mixer to act as a phase detector, carrier powers of 0 dBm were required, which means that at the splitter input a power of at least 3 dBm is required at the splitter. While this could be easily achieved on average, it was found almost impossible to amplify the carrier sufficiently that "fading" did not reduce the power below this level, giving amplitude noise on the demodulator output.

To attempt to avoid these problems with the DCM demodulator, an alternative approach to the demodulation was sought. Investigation into commercially available chips revealed that FM receivers are available with external access to the phase detector and limiting stages. It was decided that use of one of these products represented the most promising route forward using a crystal filter to give a large phase shift at the demodulator.

The chip chosen was the SA614 by Phillips. The block diagram of the chip is shown in Figure 2.1.8; a front-end amplifier increases the size of the carrier, after which it was passed, externally, to a limiting amplifier, which converted the phase-modulated sinusoidal waveform to a phase-modulated square waveform. The limiter output is passed internally to one mixer input and is also passed to pin 9. The phase-shifting crystal filter, a Temex TE5030 linked this output to the second mixer input on pin 8 of the SA614. The audio output was taken directly from the mixer on pin 7.

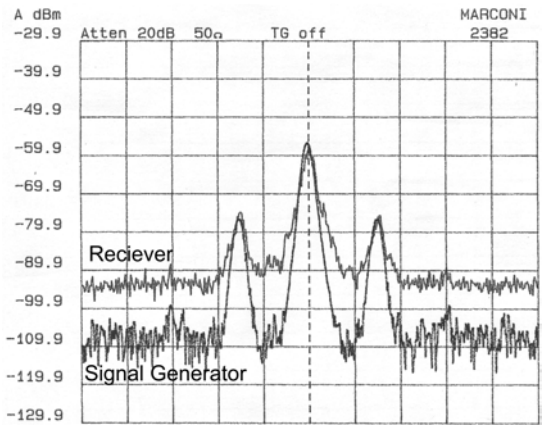

Figure 2.1.7

Received carrier spectrum with 300 Hz *disturbance. The reference at the centre of the plot is 10.700* MHz *and the scale is 200* Hz / div*, the resolution bandwidth was 30* Hz*. The lower plot shows a PM signal with sinusoidal phase modulation of 0.2* rad *amplitude from a signal generator.*

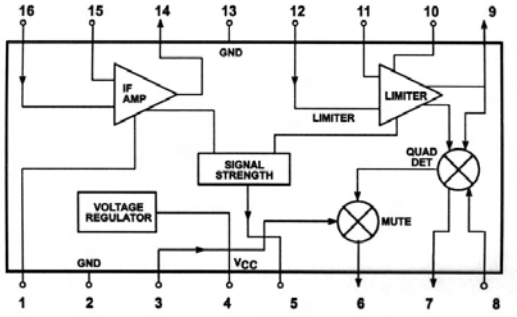

Figure 2.1.8

Block diagram of the SA614 FM demodulator chip [55]. *The filter to induce a frequency-dependent phase shift was located in the signal path from the limiter output on pin 9 to the mixer input on pin 8.*

The phase shift from the filter was measured as a function of frequency using a signal generator and oscilloscope, giving the results shown in Figure 2.1.9, showing that the efficiency is approximately 20 mrad / Hz. The instantaneous frequency, $f(t)$, of a PM waveform is obtained by differentiating the argument of the cosine in 2.1.5:

$$f(t) = \frac{1}{2\pi}\frac{d}{dt}\{\omega_C\, t - 2\phi_0 + 2\phi(t)\} = \frac{\omega_c}{2\pi} + \frac{1}{\pi}\frac{d\phi(t)}{dt}. \qquad 2.1.12$$

Thus, for a sinusoidal modulation at angular frequency f_m and magnitude Φ the peak frequency deviation from the carrier is $\pm 2 f_m \Phi$. For the values considered earlier of 200 Hz and a phase disturbance magnitude of 0.2 rad the resulting frequency excursion is 80 Hz, which should give a phase excursion at the mixer input of 1.8 rad, which should be more than sufficient for demodulation. In practice, despite these improvements to the demodulation sensitivity, demodulation was not observed.

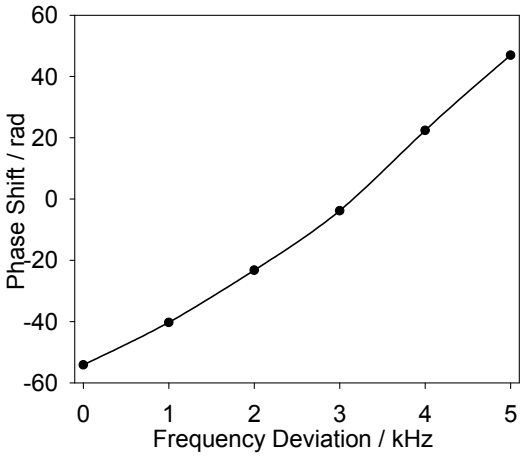

Figure 2.1.9

Phase shift from the Temex TE5030 crystal band-pass filter, measured as a function of the frequency deviation from the nominal pass-band centre at 10.700 MHz*. The efficiency is approximately 20* mrad / Hz*, although it is slightly non-linear.*

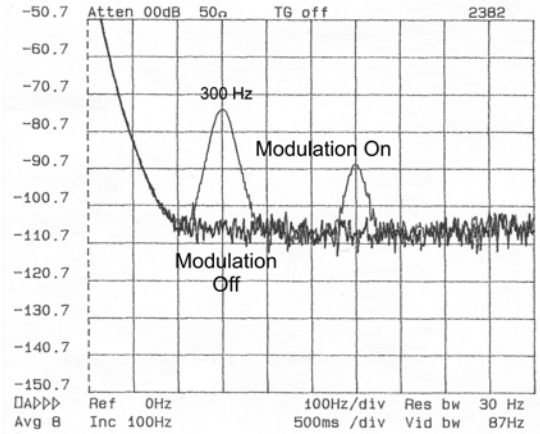

Figure 2.1.10

Demodulator output from the simulated carrier with PM at 300 Hz *with phase amplitude of 0.2* rad*. Note the presence of the second harmonic at 600* Hz *due to the non-linearity of the phase shift induced by the crystal filter.*

To confirm that the demodulator was indeed capable of demodulating the signal, an experiment was devised to test the performance of the demodulator on a signal with the same spectrum as the received carrier, but independently of the optics. The lower plot in Figure 2.1.7 shows the spectrum of a PM signal generated by a signal generator (Marconi 2031) with phase modulation at 300 Hz with 0.2 rad modulation amplitude. The spectrum is identical to the received carrier, except for a lower noise floor. To prove that the received optical signal should allow demodulation, the output from the signal generator was applied to the SA614 demodulator. The demodulator output, shown in Figure 2.1.10, shows that the signal was demodulated with output SNR of approximately 30 dB. The presence of the second harmonic shows the non-linearity of the phase shift due to the filter characteristic shown in Figure 2.1.9.

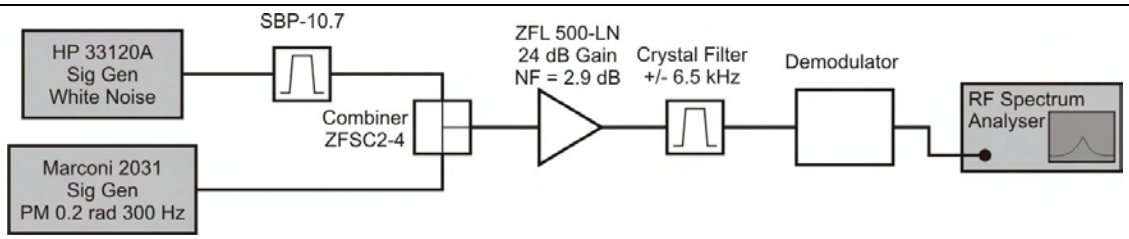

Figure 2.1.11

Experimental arrangement for measuring the performance of the SA614-based demodulator with white noise on the PM carrier.

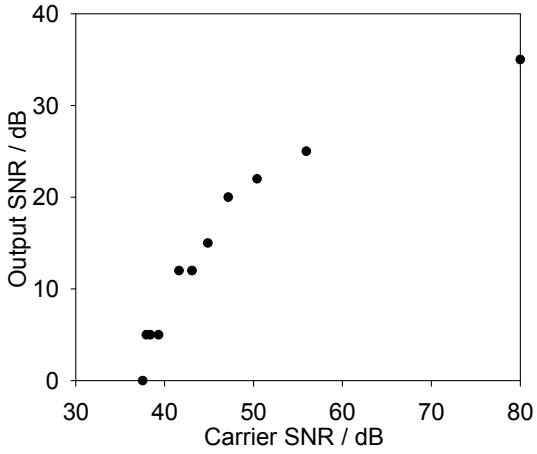

Figure 2.1.12

Measured demodulator output SNR as a function of the carrier SNR for a PM signal at 300 Hz *with 0.2* rad *phase amplitude, with white noise added to reduce the carrier SNR. The output SNR falls to 0* dB *at approximately 38* dB *carrier SNR.*

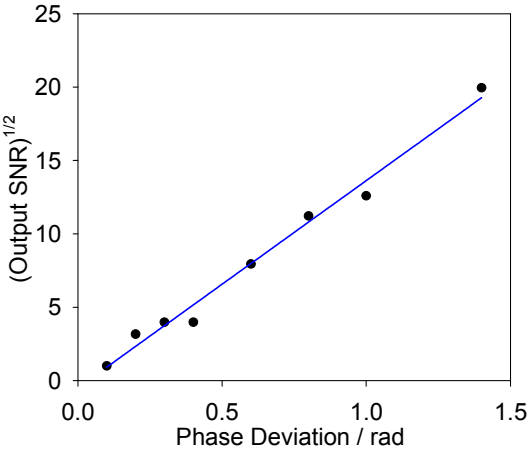

Figure 2.1.13

Square root of the SNR of the demodulated output of the SA614 showing the expected result that the SNR is proportional to the square of the phase deviation. The carrier SNR at the demodulator was ~32 dB.

This quick experiment used a carrier with higher SNR that obtained from the optical experiment. To quantify the required SNR the experiment illustrated in Figure 2.1.11 was carried out. The effect of varying the carrier SNR is shown in Figure 2.1.12 where the phase amplitude of the PM carrier is 0.2 rad, showing that for carrier SNRs below 38 dB the demodulated signal has SNR of less than 0 dB, i.e. it is hidden in the noise. The effect of varying the phase amplitude at constant carrier SNR is shown in Figure 2.1.13, showing that the SNR is proportional to the square of the phase

deviation. This is in agreement with the standard theory [56], which suggests the output SNR, S_{Out}, is related to the carrier SNR, S_{Car}, by:

$$S_{Out} = \Phi^2 \frac{B_{RF}}{2B_m} S_{Car}, \text{ for } S_{Car} >> 1 \qquad 2.1.13$$

where B_{RF} and B_m are the carrier and modulation bandwidths respectively and Φ is the phase deviation. For optimum performance the carrier bandwidth should be limited to twice the modulation bandwidth, the minimum possible.

From Figure 2.1.12 it is clear that to observe the level of phase disturbance applied here, ~0.2 rad, the carrier SNR needs to be in excess of 40 dB compared to the 30 dB observed in Figure 2.1.7, explaining the failure to demodulate the applied signal.

2.1.7. Conclusions

The experiments have shown that a carrier can be generated, and that this appears to carry the signal, but the amplitude noise on the signal due to coherent "fading" has meant that high enough SNRs for demodulation could not be maintained in the simple experiments described.

2.2. Coherent-OTDR (Single Pulse)

2.2.1. Introduction

The performance of the two-pulse self-heterodyning sensor was limited by the statistical variation of the carrier amplitude due to coherent fading and the amplitude modulation induced on the backscatter trace by the disturbance. This acoustic sensitivity of the coherent backscatter trace can be harnessed to produce a disturbance sensor with very simple demodulation [31, 39-41]. The sensor operates by measuring the change in the coherent backscatter intensity from the region of interest, which occurs because the disturbance changes the arrangement of the "frozen-in" scattering sites, altering the resulting intensity when the scattered light interferes at the receiver.

2.2.2. Experimental Realisation

The practical realisation of this simple sensor is shown in Figure 2.2.1. The equipment was virtually unchanged from the more complex experiments described in the previous section, except that only one RF drive was required for the first AOM and this was at the AOM centre frequency, 80 MHz.

The receiver output was sampled by a sample-and-hold (S&H) amplifier. This was based around an Analog Devices AD783 S&H chip, with a small signal bandwidth of 15 MHz, triggered from an external TTL signal from the FPGA sequencer. The output was low-pass filtered by an 8^{th}-order, elliptic, low-pass switched-capacitor filter (Linear Technologies LTC1069-1), giving a cut-off frequency of 3 kHz to reconstruct the signal from the sampled values. Finally, the output was buffered by a 20 dB gain stage.

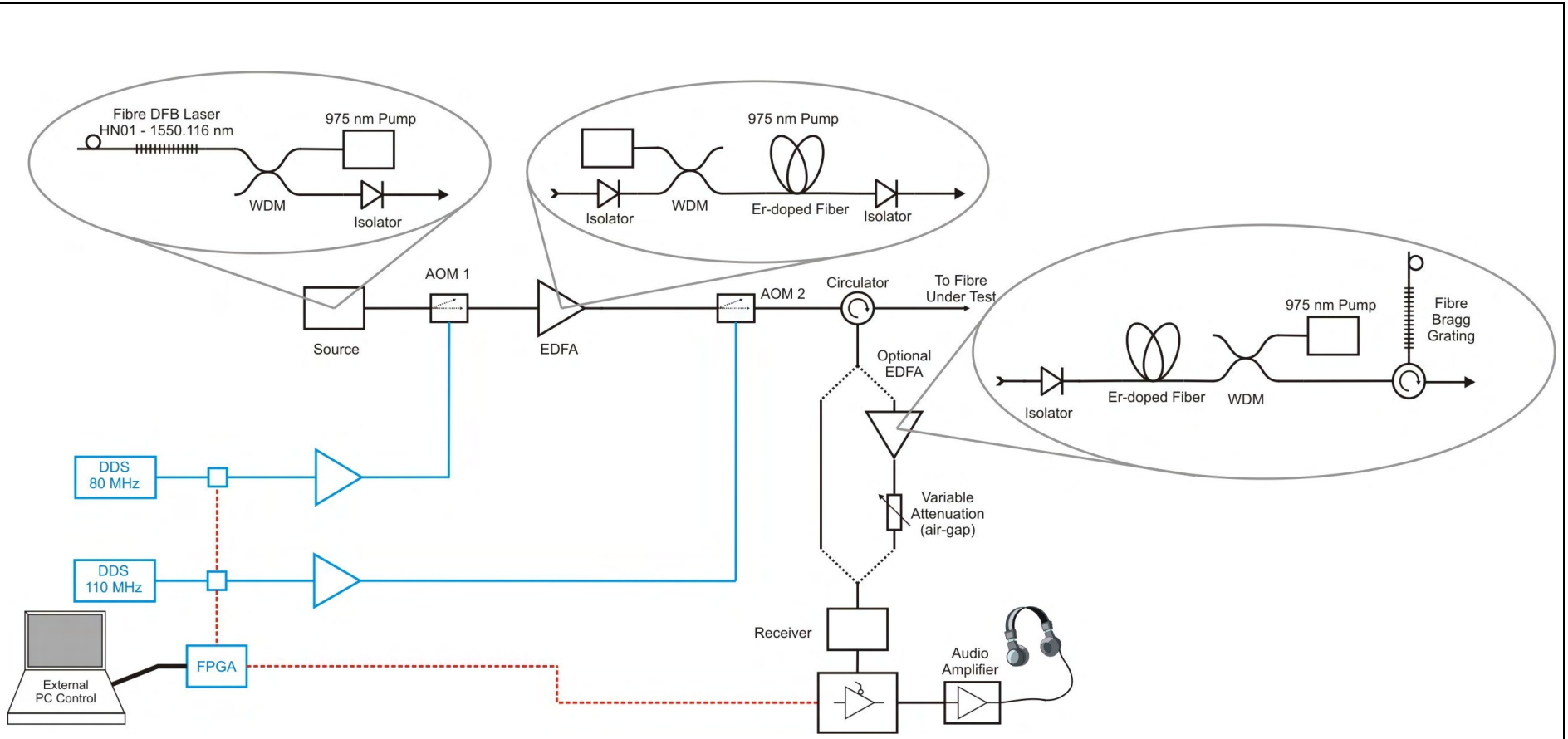

Figure 2.2.1

Optical and schematic control architecture for the initial single-pulse C-OTDR sensor system. The pre-detection EDFA was not used in some early experiments.

The S&H output with a 220 Hz disturbance applied at a range of 6.3 km, is shown in Figure 2.2.2. Under these conditions, the observed SNR at the fundamental is ~20 dB and the second harmonic, due to the non-linearity of the interference, is clearly visible at 440 Hz.

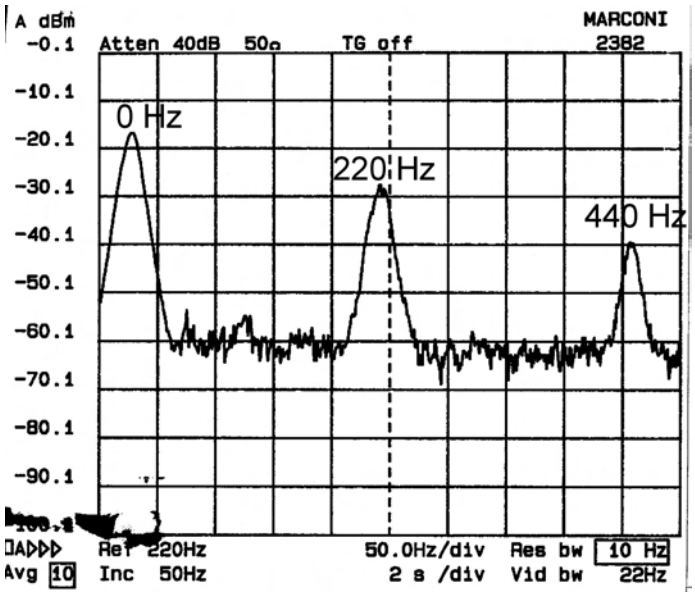

Figure 2.2.2

S&H output without the pre-detection EDFA. The fundamental at 220 Hz *is 30* dB *above the noise floor. Taking into account the noise power over the full 3* kHz *bandwidth, the SNR observed at the fundamental is 20* dB. *The 2nd harmonic can also be clearly seen at 440* Hz*, ~10* dB *below the fundamental.*

2.2.3. Interference with Slow-Varying Strain

To verify that the observed signal was due to interference as believed, and not some other effect, a simple device was constructed to apply a known linear strain to the fibre. The design is shown in Figure 2.2.3. Uncoated, standard 9/125 μm SMF was secured, using epoxy-based adhesive, in a slot approximately 1 mm deep, milled in an aluminium beam, 6.35 mm in thickness and 25.4 mm in height. The beam was supported at both ends against pillars, separated by 310 mm, with a displacement, applied by a micrometer screw, in the centre. As it was glued along the whole length, it is reasonable to expect that the fibre was uniformly stressed. As the fibre bends with the beam there will be some change in birefringence but since the curvature is very small, and the length of fibre is short, this is likely to be small [57].

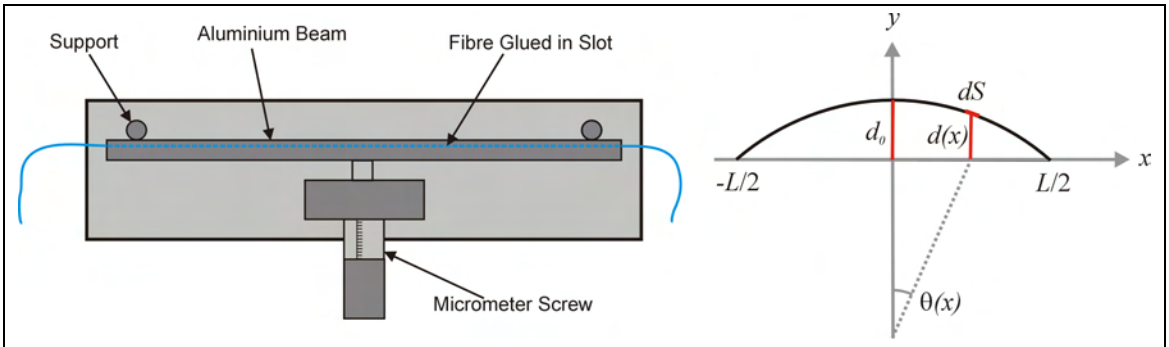

Figure 2.2.3

Simple device for applying a known linear strain to a short length of fibre with minimum change in birefringence and geometry used for analysis.

Since the cross-sectional area of the slot is small in comparison to the overall cross-section of the beam, and the Young's modulus of aluminium is comparable to that of silica, the fibre extension can be calculated by considering the deformation of a beam of solid aluminium.

It can be shown [58] that, for small deflections, the curvature, κ, of a beam, of length L, caused by a displacement d_0 at the centre, $x = 0$, is given by:

$$\kappa(x) = \frac{24 d_0}{L^3} x\,, \qquad 2.2.1$$

defining the shape of the beam when displacement is applied by the screw. The local fibre strain, $\varepsilon(x)$, at a distance, b, from the neutral axis at the beam centre, is therefore:

$$\varepsilon(x) = \frac{24 b x}{L^3} d_0\,. \qquad 2.2.2$$

Re-writing in terms of the optical path length (OPL) and strain sensitivity, S_ε (typically 0.8×10^{-6} [14]), integrating over the whole beam gives the total increase in OPL:

$$\Delta OPL = \frac{6 n b S_\varepsilon}{L} d_0\,. \qquad 2.2.3$$

The device was calibrated using a fibre Mach-Zehnder interferometer, operating at 1550 nm, and measuring the screw deflection required to pass through a given number of fringes. The measured change in OPL, was $\frac{\Delta OPL}{d_0} = (0.054 \pm 0.002)$. This equates to a value of $b = (2.4 \pm 0.1)$ mm, which is close to the expected value of 2.2 mm for the nominal slot depth of 1 mm.

The C-OTDR sensor was connected to the stretcher via a 6 km drum of 125 μm standard coated SMF, with a further 200 m on a separate drum after the stretcher. The receiver output was monitored on an oscilloscope, triggered with the timing pulse that normally triggered the sample-and-hold amplifier. The entire backscatter trace was found to continuously evolve due to thermal drift and acoustic interference. To reduce the rate of change the drums of fibre and the DFB source were acoustically and thermally shielded as far as possible.

On applying a strain with the stretcher, the intensity was seen to oscillate at the region corresponding to the strain, as expected, while the remainder of the trace, before and after the disturbed region, remained stable.

Assuming that the oscillation of the region corresponding to the disturbance is due to interference within the pulse, the phase difference between the two elements will be twice the phase introduced by the strain, so one interference fringe should be observed for every half-wavelength increase of OPL. To verify this experimentally the displacement of the stretcher beam required to pass a number of fringes was measured. The measurements were complicated by the continual drift of the backscatter pattern however, by applying the strain quickly enough the fringes could be made faster than the thermal drift, allowing them to be identified. To mimimise the error, each measurement was repeated three times and the average taken. The results from the Mach-Zehnder measurement were used to convert the applied displacement to the change in OPL.

The results are shown in Figure 2.2.4: the line of best fit, which is forced to have an intercept of zero, has a gradient of of (0.9 ± 0.2) μm / oscillation. This is in agreement with the expected value of 0.775 μm / oscillation, although this is near the lower limit of the estimated standard error, suggesting that some oscillations may have been missed, leading to under-counting; or that the adhesive in the stretcher may slowly creep, affecting the long-term stability. Nonetheless, the results are sufficiently convincing to confirm the mode of sensitivity is interferometric, as observed by Shatalin *et al.* [40].

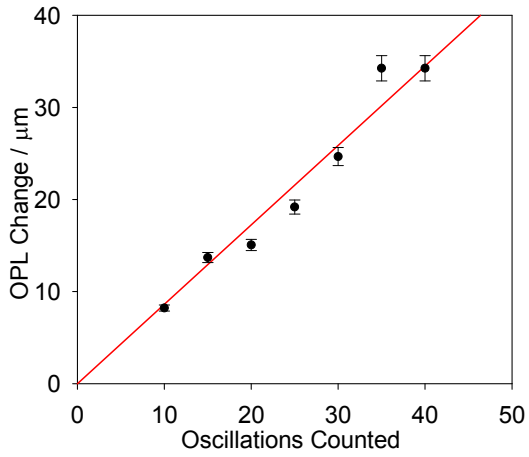

Figure 2.2.4

Change in OPL required to pass through a set number of oscillations monitoring the backscatter trace on an oscilloscope. Forcing the intercept to zero gives a best fit gradient of (0.9 ± 0.2) µm */ oscillation, in agreement with the expected value of 0.775* µm */ oscillation.*

2.2.4. Conclusions

The experiments above have shown that a simple disturbance sensor can be implemented by monitoring variations of the coherent Rayleigh backscatter trace caused by perturbation of the fibre. A simple experiment has confirmed that the mode of modulation is interferometric, and SNRs of ~20 dB have been observed, where the fibre is disturbed directly at a range of 6.3 km, showing that the sensor is capable of fulfilling the requirements set out in Section 1.1.4 at short ranges, however work remains necessary to extend the range of operation to the typical repeater separation of 40 km.

2.3. Polarisation-OTDR (P-OTDR)

2.3.1. Introduction

The aim of the work presented here was to evaluate the feasibility of using P-OTDR for an acoustic-frequency strain sensor with unambiguous location, meeting the requirements laid down in Chapter 1. In the work described, the foundations of this system were laid: measurements of the polarisation evolution along the fibre were made and the effect of altering the fibre geometry investigated.

The work in this section was carried out in collaboration with Joachim Boudet, a final year UoS tripartite student, with the work forming his final-year project [59]. The development of the acquisition and analysis software was entirely his work, making use of some code previously written by Dr Stuart Russell for other applications. My contributions were in the design and construction of new receiver circuits for the polarimeter, optimising the optical set-up and assisting in carrying out the experimental measurements.

Item:	Carried out by:
Construction and optimisation of optics	JPWH / JB
Design and assemble of polarimeter	SR
Design and manufacture of custom TIAs for polarimeter	JPWH / JB
Software development	JB / SR

JB = Joachim Boudet; JPWH = Justin Hayward (Author); SR = Dr Stuart Russell

Figure 2.3.1

Summary of main contributions to P-OTDR experiment

The birefringence of the fibre, and hence the state of polarisation (SOP) of the backscattered light, is modified by the presence of an external disturbance. The expected effect of a cyclic strain on the fibre is to trace a section of an arc on the Poincaré sphere. Joachim Boudet developed an algorithm to decode this variation in the SOP into the strain signal [59] based on a theoretical description of bend-induced birefringence.

2.3.2. Experimental Realisation

The experimental P-OTDR system is shown in Figure 2.3.2. The optical design was similar to the single-pulse C-OTDR system except that the backscattered light was directed to a high-speed polarimeter (Figure 2.3.3) which consists of four optical receivers; each of which is preceded by different polarisation-sensitive filters such that each detector output represents one of the four Stokes parameters used to describe polarised light mathematically. The ASE-blocking AOM was omitted, to increase the launched power, since the polarimeter divides the total optical power received between four detectors, via polarising elements, making higher input powers necessary for acceptable noise performance. The launched power was estimated, by knowledge of the source power, EDFA gain and component losses, to be 250 mW.

In order to monitor the spatial dependence of the SOP it is essential that the spatial resolution is smaller than the beat length of the fibre. If this is not the case then any spatial dependence of the SOP will be averaged away. Typical telecommunications fibre has a beat length of ~(10-60) m [60], so, to a rough approximation, a pulse of length ~1 m would be expected to return light with a degree of polarisation (DOP) $\sim(1-(1/10)) = 90$ %. This requires a receiver bandwidth of ~100 MHz. In practice, using an AOM to switch the light, the minimum pulse width achievable with acceptable attenuation was 20 ns, corresponding to a spatial extent of 4 m, and assuming a beat length of 20 m this should return a DOP of $\sim(1-(4/20)) = 80$ %.

Considerable effort was applied to produce suitable high-speed, high-transimpedance receivers for the polarimeter. The final receiver design used a Maxim 3664 integrated transimpedance amplifier. This IC, designed for communications applications, has an internal transimpedance of 6 kΩ and generates differential outputs designed to drive two 50 Ω transmission lines or a single 100 Ω load. The output was converted to single-ended using a simple differential amplifier, based around the Maxim 4108 op-amp, which has a 400 MHz unity-gain small-signal bandwidth and full-power bandwidth of 300 MHz, corresponding to a spatial resolution of 0.3 m. To prevent oscillations and cross talk between the four channels, each chip was powered using a separate linear regulator.

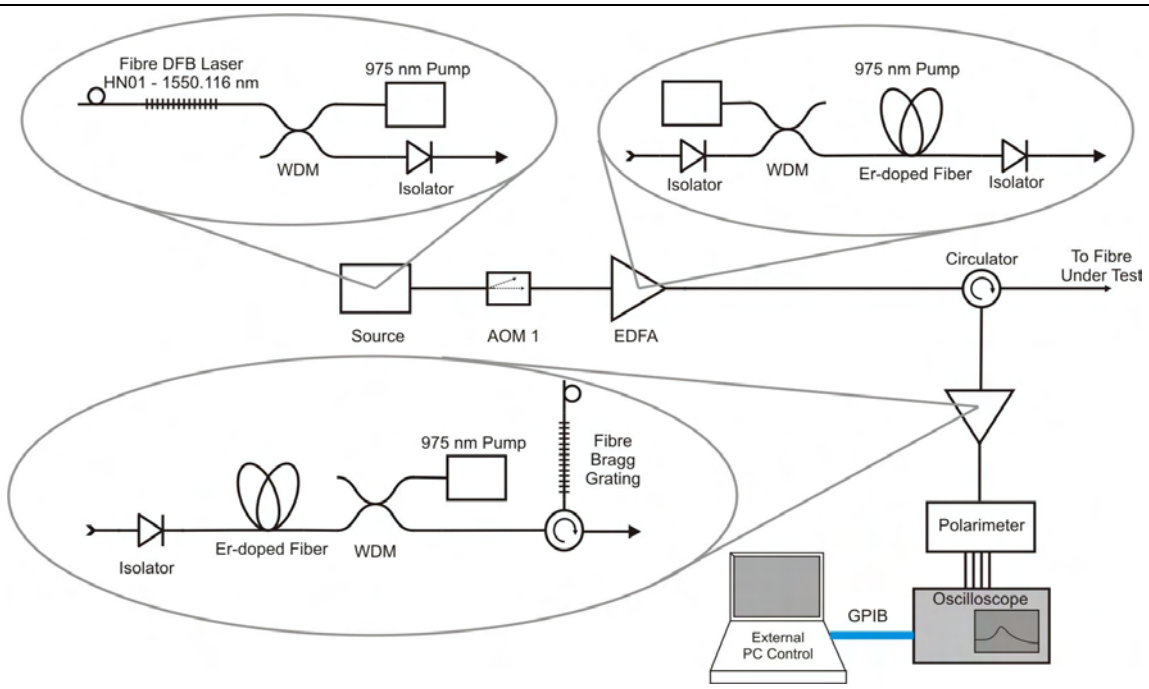

Figure 2.3.2

Experimental P-OTDR. The PC also programmed the FPGA which provided the timing pulses for the oscilloscope trigger and the RF for the AOM.

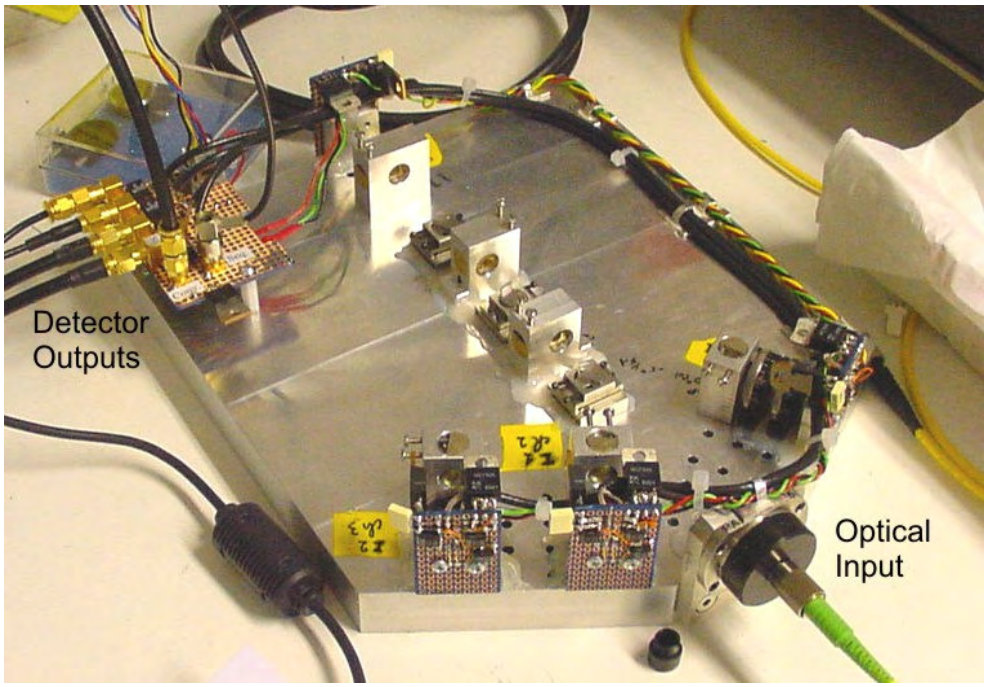

Figure 2.3.3

Custom-built high-speed polarimeter before replacing the TIAs. The four Stokes parameters are extracted by the series of semi-reflecting mirrors and appropriate polarising filters.

The evolution of the backscatter polarisation along the fibre was monitored by using a Tektronics TDS 540 oscilloscope, controlled via a GPIB interface, to acquire the waveforms prior to post-processing. This approach was chosen since none of the alternative acquisition systems, immediately available at the time, gave sufficient analogue bandwidth and sample rate.

Some of the initial results are shown in Figure 2.3.4. The first section of each of the traces shows the effect of bending on the fibre. In the first case, the majority of the fibre was on a reel with the first 5 m unwound. In the second case, approximately 35 m of the fibre was unwound. The reduction in the beat frequency in the latter case is clearly visible: the periodicity is ~5 m in the first case and increasing to ~10 m in the un-reeled case. These are in reasonable agreement with the observations of Galtorossa *et al.* [60] who measured beat lengths of 10 m to 25 m for fibre coiled in the laboratory and 10 m to 60 m in deployed fibre.

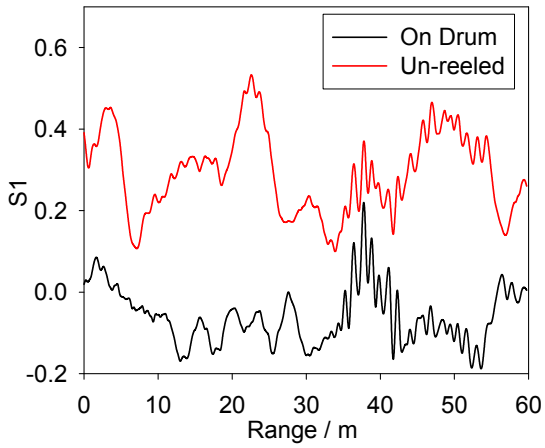

Figure 2.3.4

Normalised S1 over the test fibre on a 150 mm *drum and laid out along the corridor, showing the resulting increase in the beat length in the first 30* m, after [59].

2.3.3. Conclusions

The experimental work described above failed to deliver the performance predicted by Rogers [35], primarily because of the technical challenges relating to accurate measurement of the backscatter SOP in the presence of "coherent fading", and the problem of cumulative cross-talk along the fibre. To continue development of the P-OTDR system there are several areas which would require attention. An acquisition system would be required, that would be capable of synchronously sampling four

channels, with the required analogue bandwidth. In order to locate multiple disturbances, or operate in noisy environments, a more complex signal processing approach would be needed. With simple single-point range gating, points beyond the disturbance will return the same strain signal. This is because birefringence has the same effect on the light regardless of the direction of transit. The detection and location of multiple disturbances would therefore be extremely problematic. The solution is likely to lie in acquiring the SOP from the whole fibre and comparing subsequent sets of data to locate regions where the birefringence is changing. The disturbance is thus located, and after sufficient cycles, the distributed strain signal can be reconstructed over the whole fibre

2.4. Discussion

At this stage, three sensor systems had been investigated, showing varying degrees of promise of fulfilling the specifications, discussed in Chapter 1, for cable protection applications. While all methods have potential, it was desired to focus on one technique to develop it to the highest possible level, allowing testing of the cable-protection concept on installed fibre.

The two-pulse self-heterodyne system should allow linear demodulation of the phase disturbance, although the random amplitude modulation of the coherent backscatter trace and the resulting carrier makes this difficult. With the optical SNR achieved in these early experiments, successful demodulation was not possible with the demodulation techniques attempted in this early work. Improvements of the EDFA and receiver design may have allowed demodulation, however this was un-proven.

The single-pulse C-OTDR system, based on the modulation of the interference, gave output SNRs of 20 dB and has the benefit of simple demodulation, although it is inherently non-linear as it is a randomly biased interferometer.

The investigations into P-OTDR had shown that sensitivity to large changes to the fibre's layout could be observed, but no OTDR measurement of the small, audio-frequency, disturbances of interest was possible. There were also a number of problems foreseen. The most serious drawback of this approach is that signals at a point on the fibre inevitably cross-talk, unpredictably, to all further points on the fibre due to the modulation of the polarisation. Therefore to observe a single point requires complex signal processing, which is likely to sum noise from each location, causing the SNR to reduce rapidly with distance.

One of the main difficulties which would need to be overcome is maintaining sufficient DOP in the scattered light to observe the small changes of birefringence caused by the disturbance. Galtorossa *et al.* [60] measured the birefringence of deployed fibres, finding beat lengths as small as 10 m in some locations. Thus to maintain a 90 % DOP a 1 m pulse would be required. With such narrow pulses there are several technical challenges in detecting the scattered light with sufficient SNR to resolve the variation in SOP.

Sensor	Unambiguous Location	Linear	Demodulation	Optical Complexity	Electronic Complexity	Critical Issue
2-Pulse Self-Heterodyne C-OTDR	Yes, although large high-frequency disturbances may cross-talk	Yes	Un-proven. Requires complex RF circuits or high-speed DSP	Mid	High	Removal of AM from backscatter and obtaining demodulation
Single-Pulse C-OTDR	Yes, although very large disturbances may give cross-talk	No	Direct measurement of intensity	Low	Low	Random response – can be near zero at some locations
P-OTDR	No. Will always need complex signal analysis to remove cross-talk	No	Requires complex optics and high speed detection and post processing	High	Low	Complex signal processing; short pulses required reducing SNR and reduction of SNR due to coherence noise

Figure 2.4.1

Benefits and problems for each of the sensor designs.

These considerations are summarised in the table in Figure 2.4.1. Taking all of the factors into account, it was decided to concentrate on developing the single-pulse C-OTDR as that most suitable for immediate development into a practical system for fibre protection. The P-OTDR technique was rejected since it was considered that the noise performance, with the required narrow pulse and with cumulative degradation from iterative removal of the signals from previous locations to extract signals from the point of interest, would be insufficient to cover ranges of many kilometres. The two-pulse self-heterodyne sensor showed potential as did the single-pulse design. The latter was considered more suitable for development, firstly because the preliminary experiments were more successful, and secondly because similar sensor designs occur relatively infrequently in the literature, making the study of the noise performance and theory of operation more academically interesting than that of the self-heterodyne system which has similarities to a number of fibre-hydrophone sensors which have been extensively analysed in existing work, e.g. [47, 61].

Chapter 3 C-OTDR Theory

In this chapter, the theory of the C-OTDR acoustic sensor is developed. After defining coherence, the scattering of coherent light is discussed before showing how OTDR with coherent light can allow the sensing of phase disturbances. The spatial response characteristics of such a sensor are then analysed, clarifying the link between models that consider only two scattering sources and those that assume a scattering continuum. Having developed a model of the sensor, the implications of birefringence are analysed and discussed. Finally a numerical model of coherent scattering is described, and its results compared to the analytical predictions, made earlier in the chapter, and to experimental data.

3.1. Coherent Rayleigh Backscatter in Optical Fibres

3.1.1. Coherence

In the discussion of Rayleigh scattering in Chapter 1, the coherence properties of the light were not considered. In this section the nature of coherence is briefly discussed before the scattering of coherent light in optical fibres is considered in detail, finally explaining how a phase-sensitive sensor can be simply implemented using the coherent scattering properties of fibre.

Light is considered to be perfectly temporally coherent when the phase at a given moment maintains a deterministic relationship with the phase at *any* other time: a condition that is equivalent to requiring an infinitely narrow spectral line-width. In practice, perfectly coherent light cannot be produced and light from real sources generally exhibits partial coherence. This is characterised by the coherence time, Δt_c, over which the phase maintains a constant relationship. The coherence time is related to the line-width of the source, $\Delta\nu$, by the simple relation $\Delta\nu = 1/\Delta t_c$. Closely related to the coherence time is the longitudinal coherence length, usually referred to simply as the coherence length, $\Delta l_c = c\Delta t_c$, where c is the speed of light in a vacuum, which is the optical-path length, in the direction of propagation, over which the light may be considered to maintain a fixed phase relationship.

Spatial coherence describes the effects of a source which has finite spatial extent. In classical terms, in a source there may be many point radiators, physically separated by more than a wavelength, oscillating in an uncorrelated fashion. The source therefore has low spatial coherence, although each individual oscillator may individually exhibit a high degree of temporal coherence.

Incandescent light sources have low spatial and temporal coherence. The temporal coherence of such a source may be increased by using filters to reduce the line-width; similarly the spatial coherence may be increased by spatial filtering, for example by using a simple pin-hole. In both cases the filtering to modify the coherence properties comes at a severe cost, in terms of wasted power. In contrast, lasers usually exhibit a high degree of temporal and spatial coherence. The temporal coherence is strong due to the narrow line-width, resulting from the high selectivity of the cavity resonances, while the modal structure of the cavity can give strong spatial coherence.

3.1.2. Scattering of Coherent Light in Optical Fibre

When a pulse of temporally coherent light is launched into optical fibre, the resulting backscatter trace does not follow the smooth decay predicted for incoherent scattering, instead the signal varies randomly. This is because each scatter site is randomly located so the coherent light scattered from each site combines interferometrically generating localised maxima and minima in the backscatter trace [62], giving the appearance of the trace shown in Figure 3.1.1. As a hindrance to the operation of a conventional, incoherent, OTDR for attenuation monitoring, this phenomenon became known as "coherence noise" or "fading noise", with many methods being proposed to eliminate it from OTDR traces, e.g. [27, 33, 63].

The probability density function (PDF) of the interference giving a particular intensity, I, from any arbitrary section of fibre, $P(I)$, can be shown [32] to be:

$$P(I) = \frac{I^{(M-1)} \exp(-MI/<I>)}{(M-1)!(<I>/M)^M}, \qquad 3.1.1$$

where $<I>$ is the ensemble average, equivalent to the value that would be expected from incoherent light.

The PDF is plotted in Figure 3.1.2 for various values of the parameter M, which is a measure of the number of degrees of freedom available to the light. For a linearly polarised pulse of temporal duration τ, M is related to the coherence time [27, 32] by $M = \tau / t_c$, i.e. increasing with reducing coherence. If polarisation diversity allows m_t degrees of freedom, i.e. from two orthogonally polarised states, M is increased by a factor κ to $M = \kappa\tau / t_c$, where $1 \le \kappa \le m_t$, the exact value of κ depending on the degree of correlation between the wave in the two states [32]. For perfectly incoherent light, for which $M \to \infty$, the PDF tends to a delta function centred on $<I>$, which is the value predicted by Equation 1.4.1.

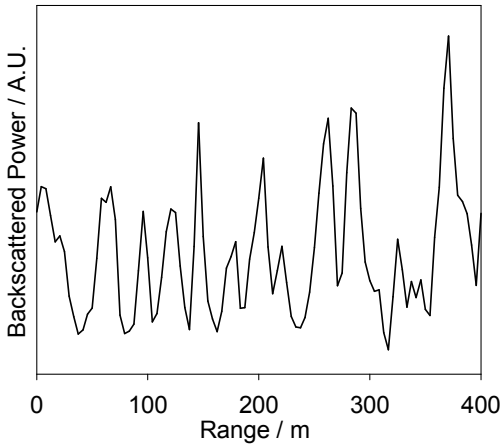

Figure 3.1.1

Experimental coherent backscatter trace from a 40 m *long pulse generated from a CW source of coherence length > 6* km*, sampled at 25* MHz*, corresponding to a pitch of 4.2* m*. The detector bandwidth was 20* MHz*, so the sample rate limits the maximum resolvable frequency components.*

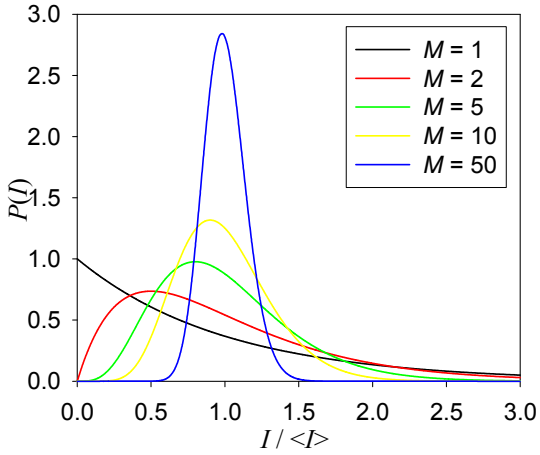

Figure 3.1.2

PDF, of the instantaneous backscattered intensity, I, for various values of the parameter M, where <I> is the ensemble average, giving the deterministic incoherent expected result. When M tends to infinity, i.e. the case of perfectly incoherent light, the PDF is a delta function at I = <I>.

To overcome this effect, in order to carry out accurate characterisation of loss and reflection distributions, requires averaging the backscatter intensity over a number of pulses of different wavelength and / or polarisation [33], effectively synthesising the result from an incoherent, unpolarised source. Mermelstein *et al.* [63] showed that the wavelength diversity must vary the optical frequency by more than $1 / \tau$ to avoid correlation between the backscatter traces, equivalent to the correlation length being equal to the pulse length with averaging over a large number of wavelengths being required to remove the coherence noise completely [33].

Since it is the phase relationship between scattering sites, which are at fixed physical locations within the fibre, that determines the backscatter pattern, the coherent backscatter trace remains stable until an external influence, which may be thermal or mechanical, alters the phase relation between the scatter sites involved in the interference. It was noted that by observing the evolution of the coherent backscatter trace, a simple sensor could be produced [38-42, 64].

3.2. Coherent-OTDR (C-OTDR)

3.2.1. Outline

Having outlined the mode of the sensor's operation, a more rigorous description is now derived in terms of a simple wave optics analysis, generating results that are equivalent to those of Shatalin *et al.* [40] which were derived using statistical techniques. Initially a basic analysis of coherent backscattering is presented in terms of scattering from two discrete scatter sites, and the effect of a phase disturbance on the fibre is analysed, demonstrating the method of sensor operation. The model is then generalised to many scattering sites and it is shown that this is equivalent to the two-site case where a resultant scattering phase is used. The results are used to derive the spatial variation in the sensor response, with the derived response in agreement with the results in the literature [40]. The effect of polarisation is then discussed and its impact on the previous analysis considered. Finally the sensitivity to launch wavelength is considered, explaining the results of Mermelstein *et al.* [63] in terms of a simple analysis of phase.

3.2.2. Backscatter from Two Discrete Scattering Sites

Consider launching a pulse of light, of duration τ, into an optical fibre. Assuming that the coherence time of the source is much longer than the pulse duration, i.e. $t_c >> \tau$, the electric field launched into the fibre, $E_{forward}$, can be written in terms of the distance along the fibre, z, and the time, t, as:

$$E_{forward}(z,t) = E_0 U\left(t - \frac{z}{v_g}\right) e^{-\alpha z/2}\, e^{i(\omega t - kz)}; \qquad U(t) = \begin{cases} 1 & |t| \le \dfrac{\tau}{2} \\ 0 & |t| > \dfrac{\tau}{2} \end{cases} \tag{3.2.1}$$

where v_g is the group velocity, k is the wave-number, α is the attenuation coefficient, ω is the optical angular frequency and $U(t)$ is the pulse electric field envelope.

The light returned to the point of launch, at $z = 0$, due to backscattering from a single scattering site, m, located at z_m, with Rayleigh scattering coefficient R_m is thus described by:

$$E_m(t) = E_0 R_m U\left(t - \frac{2z_m}{v_g}\right) e^{-\alpha z}\, e^{i(\omega t - 2kz_m)}. \tag{3.2.2}$$

Initially consider the case where there are only two scattering sites, located at ranges z_1 and z_2. It is wished to calculate the backscattered intensity received at the point of launch due to scattering when both discrete scatter sites are within the spatial extent of the pulse, as shown in Figure 3.2.1.

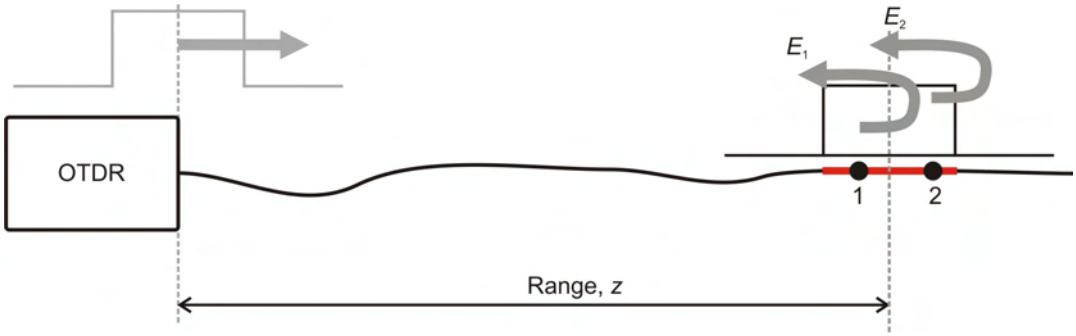

Figure 3.2.1

Simplified model of coherent Rayleigh scattering in optical fibre, considering only two discrete scatter sites.

For simplicity, it is assumed that the scattering coefficient is equal for each site ($R_1 = R_2 = R$), and that since the attenuation over the pulse width is small, the attenuation term may be simplified in terms of the range at the pulse centre, z. The electric field returned to $z = 0$ is therefore:

$$E_{1,2}(t) = E_0 \,\mathrm{Re}^{-\alpha z}\left\{e^{i(\omega t - 2kz_1)} + e^{i(\omega t - 2kz_2)}\right\}, \qquad 3.2.3$$

giving an intensity, $I(t)$, at the detector of:

$$I(t) = \left\langle E^*_{12}(t) E_{12}(t) \right\rangle = 2E_0^2 R^2 e^{-2\alpha z}\left\{1 + \cos\left[2k(z_2 - z_1)\right]\right\}. \qquad 3.2.4$$

Where * denotes the complex conjugate and <…> the time average over an integer number of optical cycles. As discussed earlier, the intensity is determined by the optical phase-separation, $2k(z_2 - z_1)$, of the two scattering sites. It is this dependency of the intensity on the phase-relations between discrete scatter sites which underpins the operation of the C-OTDR acoustic sensor which is the main subject of this thesis.

Now imagine that an external disturbance generates a time-varying phase disturbance, $\phi(t)$, in the region between the two scattering sites. Writing the initial phase due to the site separation as $\phi_0 = 2k(z_2 - z_1)$ and noting that the light scattered from site 2 passes through the phase disturbance twice, the resulting intensity at the launch end of the fibre is:

$$I(t) = 2I_0(z)\{1 + \cos(\phi_0 + 2\phi(t))\}, \quad 3.2.5$$

where $I_0(z) = E_0^2 R^2 e^{-2\alpha z}$. This represents an interferometric signal, with phase bias ϕ_0, which varies with the applied phase $\phi(t)$.

For small disturbances, where $|\phi(t)| << \pi$, by expanding the cosine term in 3.2.5 as a Taylor series, the intensity can be written as:

$$I(t, \phi_0) = 2I_0(z)\{1 + \cos(\phi_0) - 2\sin(\phi_0)\phi(t)\}. \quad 3.2.6$$

Detecting this intensity gives a constant offset of $I_0(z)\{1 + \cos(\phi_0)\}$ with a time-varying modulation of $-4I_0(z)\sin(\phi_0)\phi(t)$. Therefore, by repeatedly sampling the backscatter intensity, the form of phase disturbance can be decoded, although the amplitude will vary with the small-signal sensitivity, *S*:

$$S = \sin(\phi_0). \quad 3.2.7$$

which means the sensitivity can fall to near zero where ϕ_0 takes integer values of π.

For larger phase disturbances, where the amplitude of $\phi(t)$ becomes comparable to $\pi/2$, the response will become non-linear due to the sinusoidal response and for very large disturbances, $> \pi/2$, the interference will pass through many fringes. The result of this non-linearity of the response is that the decoded signal will contain frequency components at harmonics of the fundamental frequency at which the phase disturbance, $\phi(t)$, varies.

The non-deterministic output is the main drawback of a sensor of this type, making quantitative measurement, or even comparison, of strain practically impossible. However, for intrusion sensing and cable protection applications, where the physical parameters of the cable installation may alter the strain transmitted to the fibre unpredictably [45], quantitative strain recovery is less important than high sensitivity and accurate location of time-varying strain signals [39-41].

3.2.3. Generalisation to Multiple Scattering Sites

In reality a pulse will simultaneously interact with many more than the two scattering sites considered in section 3.2.2. In this section the analysis is generalised to consider the scattering from an arbitrary large number, *N*, of scattering sites. As shown in Figure 3.2.2 a phase disturbance $\phi(t)$ acts at a range *z*. The pulse is drawn at time

$t = z/v_g$ and separated into the components before the disturbance, **A**, and those beyond it, **B**. The backscatter of interest is that corresponding to the situation shown in the figure, i.e. that sampled when $t = 2z/v_g$.

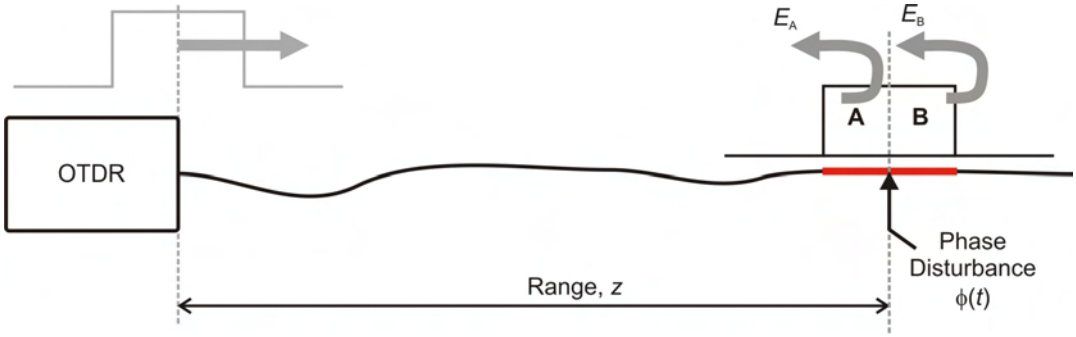

Figure 3.2.2

Improved model for considering the effect of a phase disturbance when scattering occurs at multiple discrete scatter sites.

Let the number of scattering sites in each of the sections **A** and **B** be N_A and N_B respectively. Since the total number of sites is very large, and there is an equal probability of a scatter site existing at any point in the fibre, it is reasonable to assume that, for a pulse of reasonable spatial extent, $N_A = N_B = N/2$.

With no phase disturbance applied, the backscattered field at the detector is simply:

$$E_N(t) = E_0 e^{-\alpha z} \sum_{m=1}^{N} R_m e^{i(\omega t - 2kz_m)}, \qquad 3.2.8$$

where, as in the previous section the attenuation over the duration of the pulse is assumed to be negligible. Taking the phase disturbance into account, by splitting the sum into two components, which is admissible since summation is commutative, i.e.

$$\sum_{n=1}^{N} f(n) = \sum_{n=1}^{m-1} f(n) + \sum_{n=m}^{N} f(n) \quad (1 \le m \le N), \qquad 3.2.9$$

the electric field can be written as:

$$E_N(t,\phi) = E_0 e^{-\alpha z} \left\{ \sum_{m=1}^{N/2} R_m e^{i(\omega t - 2kz_m)} + \sum_{m=N/2+1}^{N} R_m e^{i[(\omega t - 2kz_m) + 2\phi(t)]} \right\}. \qquad 3.2.10$$

To simplify, each summation can be written in terms of R the average scatter coefficient, $R = \frac{1}{N}\sum_{m=1}^{N} R_m$ and resultant relative amplitudes, E_A and E_B, and phases ϕ_A

and ϕ_B which take into account constructive/destructive interference and any variation in R_m between sites in its amplitude. The electric field is written as:

$$E_N(t,\phi) = E_0 e^{-\alpha z} R\left\{E_A e^{i[\omega t - \phi_A]} + E_B e^{i[(\omega t - \phi_B) + 2\phi(t)]}\right\}. \qquad 3.2.11$$

Where the resultant fields are defined by

$$E_A e^{i[\omega t - \phi_A]} = \sum_{m=1}^{N/2} e^{i(\omega t - 2kz_m)}; \quad E_B e^{i[\omega t - \phi_B]} = \sum_{m=N/2+1}^{N} R_m e^{i[\omega t - 2kz_m]}. \qquad 3.2.12$$

Noting that 3.2.11 is equivalent to 3.2.3, the intensity reduces to:

$$I(t,\phi) = I_0(z)\left\{E_A^2 + E_B^2 + 2E_A E_B \cos(\phi_0 + 2\phi(t))\right\}, \qquad 3.2.13$$

where $I_0(z) = E_0^2 R^2 e^{-2\alpha z}$ as previously and $\phi_0 = \phi_B - \phi_A$. This is very similar to the result for two discrete scattering sites (3.2.5), the differences arising from the possibility that E_A and E_B may be unequal which was not considered in the earlier analysis, although for a large overall number of scatter sites it is assumed that $N_A = N_B$, so they may reasonably be expected to have similar magnitudes.

3.2.4. Spatial Response to Point Strain

The analysis so far has considered only the specialised case where a point disturbance acts at the centre of the fibre section from which light is collected at the sampling time. The amplitude of the audio signal decoded from the C-OTDR backscatter will vary depending on the location of the disturbance relative to the nominal sample location. In this section an expression is derived for that variation and the full width at half maximum (FWHM), based on the previous analysis, confirming the results of Shatalin *et al.* [40] derived using the more formal techniques of statistical optics.

It is more convenient to consider the spatial extent of the pulse, which can be written in terms of the group velocity, v_g, and the pulse duration, τ, as $\Lambda = v_g \tau$ which propagates along a fibre, as shown in Figure 3.2.3. The pulse is drawn at time $t = z / v_g$ and the backscatter intensity is sampled at time $2t$, giving a spatial resolution bin of width Λ centred about range z. The point phase disturbance is applied at any point within the resolution bin at a range $(z + z_0)$, as shown in Figure 3.2.3. In the analysis that follows the relative response is calculated as a function of the offset, z_0, from the pulse centre.

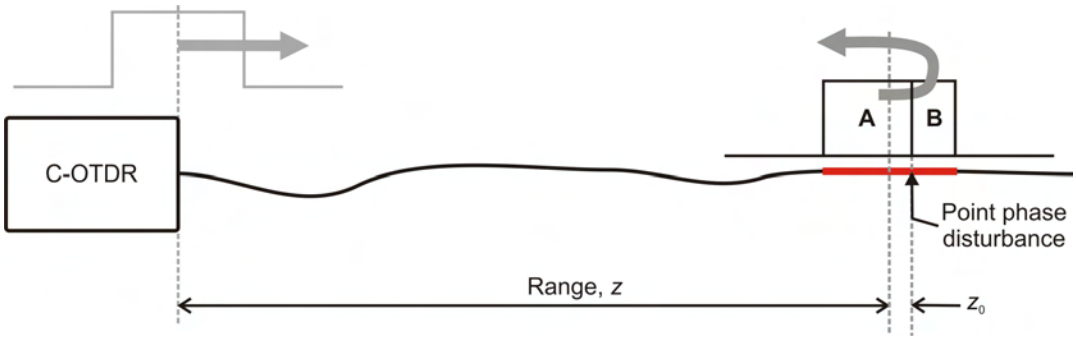

Figure 3.2.3

Model for analysing the spatial response of the C-OTDR sensor. The pulse is launched when $|t| \le \Lambda/2v_g$ *, and is drawn at time* $t = z/v_g$ *. The case is considered where a point phase disturbance is applied at a range* $(z + z_0)$ *as drawn.*

As before, the summation over the *N* scatter sites, enveloped by the pulse, is split into two components and the assumption is made that there is an equal probability of a scatter site existing at any point in the fibre. Thus the number of scattering sites in each of the sections, **A** and **B**, are now given by:

$$N_A = \frac{N}{2}\left(1 + \frac{2z_0}{\Lambda}\right); \quad N_B = \frac{N}{2}\left(1 - \frac{2z_0}{\Lambda}\right). \tag{3.2.14}$$

Equation 3.2.10 therefore becomes:

$$E_N(t,\phi) = E_0 e^{-\alpha z}\left\{\sum_{m=1}^{N_A} R_m e^{i(\omega t - 2kz_m)} + \sum_{m=N_A+1}^{N} R_m e^{i[(\omega t - 2kz_m) + 2\phi(t)]}\right\}. \tag{3.2.15}$$

In exactly the same manner as previously, this can be written in terms of two resultant fields:

$$E_N(t,\phi) = E_0 e^{-\alpha z} R\left\{E_A e^{i[\omega t - \phi_A]} + E_B e^{i[(\omega t - \phi_B) + 2\phi(t)]}\right\}. \tag{3.2.16}$$

Where the resultant fields are similarly defined as:

$$E_A e^{i[\omega t - \phi_A]} = \sum_{m=1}^{N_A} e^{i(\omega t - 2kz_m)}; \quad E_B e^{i[\omega t - \phi_B]} = \sum_{m=N_A+1}^{N} e^{i[\omega t - 2kz_m]}. \tag{3.2.17}$$

Multiplying the electric field with its complex conjugate, the intensity of light at the launch end of the fibre is:

$$I(t,\phi) = I_0(z)\left\{E_A^2 + E_B^2 + 2E_A E_B \cos(\phi_0 + 2\phi(t))\right\}, \tag{3.2.18}$$

where, as before, $I_0(z) = E_0^2 R^2 e^{-2\alpha z}$ and $\phi_0 = \phi_B - \phi_A$. However, in this instance it is expected that E_A and E_B are unequal since they result from summation over different numbers of scattering sites. Since the summation is the coherent addition of waves of random phase, when the number of sites is large the magnitude of the resultant field will be proportional to the square-root of the number of scattering sites, giving

$$E_A = \sqrt{\frac{N_A}{N}}; \quad E_B = \sqrt{\frac{N_B}{N}}. \tag{3.2.19}$$

Substituting into 3.2.18:

$$I(t,\phi) = \frac{I_0(z)}{N}\left\{N_A + N_B + 2\sqrt{N_A N_B}\cos(\phi_0 + 2\phi(t))\right\}. \tag{3.2.20}$$

The relative response of the sensor is best described by the interference visibility [65] which is defined in terms of the maximum and minimum obtainable intensities, I_{Max} and I_{Min}, as:

$$V = \frac{I_{Max} - I_{Min}}{I_{Max} + I_{Min}}. \tag{3.2.21}$$

By inspection of 3.2.20, the visibility of the interference due to the phase disturbance is

$$V(z_0) = \frac{4\sqrt{N_A N_B}}{2(N_A + N_B)} = \sqrt{1 - \left(\frac{2z_0}{\Lambda}\right)^2}, \tag{3.2.22}$$

which is equivalent to the result of Shatalin *et al.* (equation 3, [40]), derived using the principles of statistical optics. This function is plotted in Figure 3.2.4. The FWHM can be found by setting $V(z_0) = \frac{1}{2}$ which occurs for $z_0 = \pm\frac{\sqrt{3}}{4}\Lambda$, giving a FWHM of $\frac{\sqrt{3}}{2}\Lambda = 0.87\Lambda$.

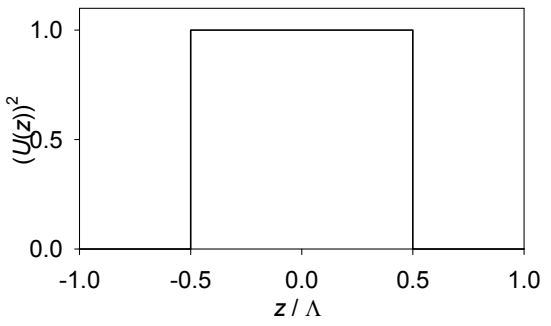

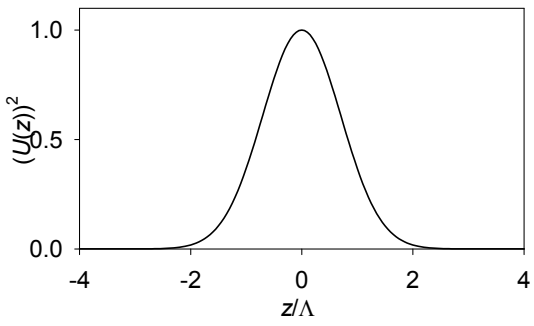

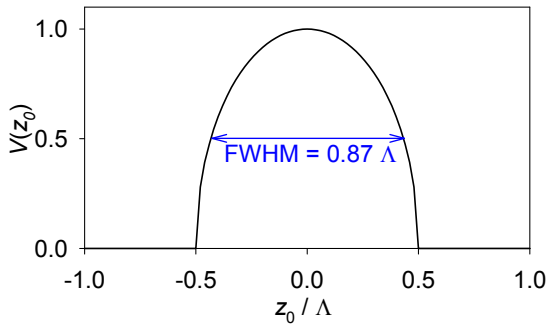

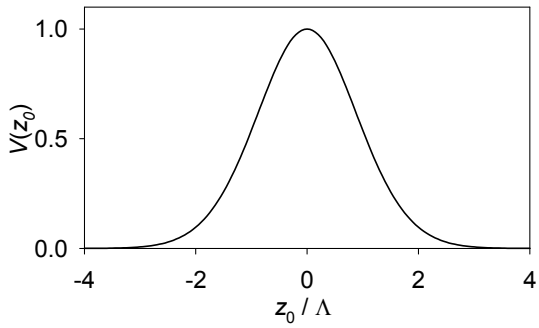

Figure 3.2.4

Theoretical spatial response (bottom) over a single resolution bin centred at $z_0 = 0$ for a rectangular pulse of width Λ (top).

Figure 3.2.5

Theoretical spatial response (bottom) over a single resolution bin centred at $z_0 = 0$ for a pulse with Gaussian intensity envelope with 1/e width of Λ (top).

The analysis above assumed a square pulse, which is an approximation having only limited validity in real systems. The analysis can be readily applied to a pulse of arbitrary shape. If the normalised intensity envelope of the pulse is $U(z)$ then 3.2.17 becomes:

$$E_A e^{i[\omega t-\phi_A]} = \sum_{m=1}^{N_A} U(z_m) e^{i(\omega t-2kz_m)}; \quad E_B e^{i[\omega t-\phi_B]} = \sum_{m=N_A+1}^{N} U(z_m) e^{i[\omega t-2kz_m]}, \qquad 3.2.23$$

effectively weighting the relative field strengths by the electric field envelope. Since $U(z)$ is an arbitrary function it is convenient to re-write the summations in terms of integrals, with the relative field strengths being:

$$E_A = \left[\frac{\int_{-\infty}^{z_0} \left(U(z)\right)^2 dz}{\int_{-\infty}^{\infty} \left(U(z)\right)^2 dz} \right]^{\frac{1}{2}}; \quad E_B = \left[\frac{\int_{z_0}^{\infty} \left(U(z)\right)^2 dz}{\int_{-\infty}^{\infty} \left(U(z)\right)^2 dz} \right]^{\frac{1}{2}}. \qquad 3.2.24$$

Writing the visibility in terms of the electric field magnitudes from each component, E_A and E_B, as:

$$V = \frac{2E_A E_B}{E_A^2 + E_B^2}. \qquad 3.2.25$$

Substitution from 3.2.24 obtains the visibility for a generalised pulse envelope:

$$V(z_0) = 2 \frac{\sqrt{\int_{-\infty}^{z_0} \left(U(z)\right)^2 dz \cdot \int_{z_0}^{\infty} \left(U(z)\right)^2 dz}}{\int_{-\infty}^{\infty} \left(U(z)\right)^2 dz}. \qquad 3.2.26$$

The integrals over space are equivalent to the ensemble averages over all scatter sites in equation (A3) of [40].

Solving 3.2.26 for a pulse with a Gaussian intensity envelope $\left(U(z)\right)^2 = e^{-\left(\frac{z}{\Lambda}\right)^2}$ gives visibility $V(z_0) = \sqrt{1 - \left[\mathrm{erf}(z_0)\right]^2}$, plotted in Figure 3.2.5. As is intuitive, for a non-square pulse the edges of the response fall off more rapidly as the pulse tails carry less energy.

A second assumption made in the analysis above is that the intensity value is sampled instantaneously, implying that the detector has an infinitely narrow impulse response; however a real detector will have a finite impulse response, widening the resolution bin as shown in Figure 3.2.6.

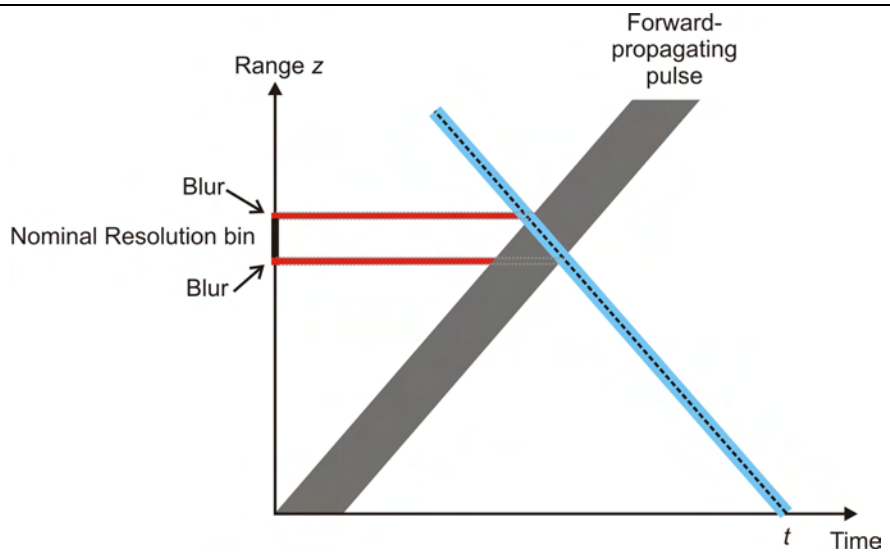

Figure 3.2.6

Widening of spatial response due to finite detector bandwidth. The nominal resolution is the spatial extent of the pulse, the heavy black line on the z-axis. The finite spatial response, indicated by the blue line around the nominal sample point, spreads the response as shown by the horizontal red lines.

Mathematically this effect can be described as the convolution of the spatial impulse response of the detector, $D(z)$, with the visibility, giving an overall response, $V'(z_0)$, of:

$$V'(z_0) = V(z_0) \otimes D(z_0) = \int_{-\infty}^{\infty} V(z_0 - z) D(z) dz \,. \qquad 3.2.27$$

In practice this broadening will partially compensate for the narrowing of the response due to sloping pulse edges. Significant widening of the spatial resolution will only occur where the impulse response approaches the pulse width, which is unlikely where the bandwidth is chosen to be the reciprocal of the pulse duration or larger.

3.2.5. Effect of Polarisation

The discussion above and in [40] ignored the effect of polarisation and fibre birefringence on the coherent backscatter trace. In this section the influence of fibre birefringence on the sensor and the resulting reduction in sensitivity is considered.

In the preceding analysis the light propagating and scattered in the fibre has been described in terms of a single linear polarisation state, which can be fully described by a single scalar quantity. In reality standard SMF will support light of any polarisation,

which can be described as a superposition of waves in two orthogonally polarised modes. If the fibre were perfectly symmetric, then light in one of these modes would maintain constant correlation with light in the other as they propagate along the fibre. In practice, however, small asymmetries in the fibre geometry mean that the propagation varies between each mode. This phenomenon, where the propagation properties are orientation dependent, is birefringence. The inherent birefringence of the fibre can be increased by the physical geometry of the fibre, particularly where it is wound onto small drums or into coils [60].

Mathematically, the electric field, $\mathbf{E}(z,t)$, is divided into two independent, orthogonal components in the *x* and *y* directions, described by the unit vectors $\hat{\mathbf{i}}$ and $\hat{\mathbf{j}}$ respectively:

$$\mathbf{E}(z,t) = \hat{\mathbf{i}}E_x e^{i(\omega t - k_x z)} + \hat{\mathbf{j}}E_y e^{i(\omega t - k_y z + \Phi_0)}, \qquad 3.2.28$$

where the phase Φ_0 is $n\pi$ (n = 0, 1, 2…) for linear polarisation or $n\pi/2$ for circularly polarised light. As the light propagates along the fibre a phase shift between the components is accumulated due to the difference in wave-number. This phase shift, known as the retardation, $\Phi(z)$, is given by:

$$\Phi(z) = 2\pi z(k_x - k_y). \qquad 3.2.29$$

Consider the interference of linearly polarised light, at 45º to the *x*-axis, with light from the same source which has propagated along birefringent fibre such that it has accumulated retardation $\Phi(z)$. The normalised electric field is:

$$\mathbf{E}(z,t) = \frac{1}{\sqrt{2}}\left(\hat{\mathbf{i}}E_x e^{i(\omega t - kz)} + \hat{\mathbf{j}}E_y e^{i(\omega t - kz)}\right) + \frac{1}{\sqrt{2}}\left(\hat{\mathbf{i}}E_x e^{i(\omega t - kz)} + \hat{\mathbf{j}}E_y e^{i(\omega t - kz) + \Phi(z)}\right). \qquad 3.2.30$$

Calculating the intensities using $I =< \mathbf{E}^* \cdot \mathbf{E} >$ (where * represents the complex conjugate, · is the scalar product and <…> the time average) the resultant intensity is

$$I(z,t) = \tfrac{1}{2}\{1 + \cos(\Phi(z))\}. \qquad 3.2.31$$

The spatial periodicity of the intensity is known as the beat length, L_B. By inspection:

$$L_B = \frac{1}{k_x - k_y}. \qquad 3.2.32$$

In installed fibres, the beat length is typically ~(10-60) m [60], the exact value depending on the symmetry properties of the fibre, the physical structure of the cable assembly and the geometry of the installation.

In considering the effect of fibre birefringence on the C-OTDR sensor it is important to note that the birefringence is non-reciprocal: light travelling through a section of fibre, being reflected or scattered and passing back through the same section of fibre, undergoes twice the retardation due to the birefringence than that incurred in a one-way trip.

To investigate the effect of birefringence on the C-OTDR signal, the analysis of 3.2.2 is modified to include the retardation; this is valid since it was shown in section 3.2.3 that the many-scatter site case reduced to the two-scatter site analysis with resultant fields replacing the sums over all sites.

It is assumed that the launch pulse is linearly polarised, and can be described by:

$$\mathbf{E}(z,t) = \hat{\mathbf{i}} E_x e^{i(\omega t - kz)} + \hat{\mathbf{j}} E_y e^{i(\omega t - kz + \Phi(z))}. \qquad 3.2.33$$

where E_x and E_y can take on any value. Taking into account the retardation of light from the further scatter site relative to the first, the light scattered from two discrete sites located, either side of a phase disturbance, at z_A and z_B with scatter coefficients R_A and R_B and returned to $z = 0$ is:

$$\begin{aligned}\mathbf{E}(z,t) = R_1\left(\hat{\mathbf{i}} E x e^{i(\omega t - kz_A)} + \hat{\mathbf{j}} E_y e^{i(\omega t - kz_B)}\right)\ldots \\ + R_2\left(\hat{\mathbf{i}} E_x e^{i(\omega t - kz_B + 2\phi_x(t))} + \hat{\mathbf{j}} E_y e^{i(\omega t - kz_B) + 2\phi_y(t) + 2\Phi(z_B - z_A)}\right).\end{aligned} \qquad 3.2.34$$

where ϕ_x and ϕ_y are the x- and y-components of the phase disturbance respectively. For a simple longitudinal strain the two components will be approximately equal, while for a bend-induced strain they may be dissimilar, even out of phase.

The intensity components from each orthogonal component, I_x and I_y, may be calculated separately since they will not interfere at the detector:

$$\begin{aligned} I_x &= E_x{}^2\left(R_A^2 + R_B^2 + R_A R_B \cos\left[2\phi_x(t) + \phi_0\right]\right); \\ I_y &= E_y{}^2\left(R_A^2 + R_B^2 + R_A R_B \cos\left[2\phi_y(t) + \phi_0 + 2\Phi(z_B - z_A)\right]\right). \end{aligned} \qquad 3.2.35$$

The phase bias $\phi_0 = k(z_B - z_A)$ and the birefringence is described by the retardation $\Phi(z_B - z_A)$. Any change to the retardation due to the disturbance is considered to be applied via ϕ_x and ϕ_y rather than as a change of the retardation, Φ.

Assuming that $E_x = E_y = E_0/\sqrt{2}$, combining the two wavelengths gives:

$$I_{Total} = E_0{}^2\left(R_A^2 + R_B^2 + R_A R_B\left\{\cos\left[2\phi_x(t) + \phi_0\right] + \cos\left[2\phi_y(t) + \phi_0 + 2\Phi(z_B - z_A)\right]\right\}\right). \quad 3.2.36$$

The retardation is clearly important in determining the response to a phase disturbance since it can bias the phase of the *y*-component response relative to the *x*-component, either reinforcing or reducing the response. Since the beat length and the resultant scatter site separation $(z_B - z_A)$ may vary with the location along the fibre, the response is likely to have spatial dependence which will vary in time as environmental influences alter the birefringence of the fibre. Using a very short pulse ($<< L_B$), ensuring that $(z_B - z_A) << L_B$ would prevent birefringence affecting the signal, however, since the peak power of the pulse remains constant, there is a cost in terms of reduced backscattered power due to the decrease in the total pulse energy.

The possibility of the phase disturbance being off-centre can be allowed, following a similar approach to that in section 3.2.4, by weighting the scatter constants to the square root of the expected number of scatter sites within the two regions:

$$R_A = R\sqrt{1 + \frac{2z_0}{\Lambda}}; \quad R_B = R\sqrt{1 - \frac{2z_0}{\Lambda}}. \quad 3.2.37$$

Variation of the disturbance location away from $z_0 = 0$ may also alter the effective separation of the resultant scatter sites, changing the retardation between the two. Depending on the relation to the beat length and the correlation between the two components of the phase disturbance, this may either improve or degrade the interference visibility over the resolution bin.

The effect of the birefringence is to reduce the small-signal sensitivity (Equation 3.2.7) by the mixing efficiency, *m*, with $0 \le m \le 1$. When the two components are in orthogonal polarisation states no interference occurs and $m = 0$, when the two beams are in identical states perfect interference occurs and $m = 1$. By assuming that the relative polarisation of the two light waves is random, Stowe *et*

al. [66] that the probability, P, at any arbitrary time that m is greater than a minimum small-signal sensitivity, S_0, is given by:

$$P(S_0) = 1 - S_0^2 . \qquad 3.2.38$$

The effect of the random phase bias, ϕ_0, can be analysed similarly, allowing Stowe *et al.* to derive the probability of a minimum sensitivity S_0 as before, where the random phase bias alters the distribution by defining the maximum sensitivity, obtaining the probability [66]:

$$P'(S_0) = \begin{cases} 1 - \frac{2}{\pi}\left\{\arcsin(S_0) + S_0\sqrt{1 - S_0^2}\right\} & \sin(\phi_0) > S_0 \\ 0 & \sin(\phi_0) \le S_0 \end{cases} . \qquad 3.2.39$$

These equations are plotted in Figure 3.2.7.

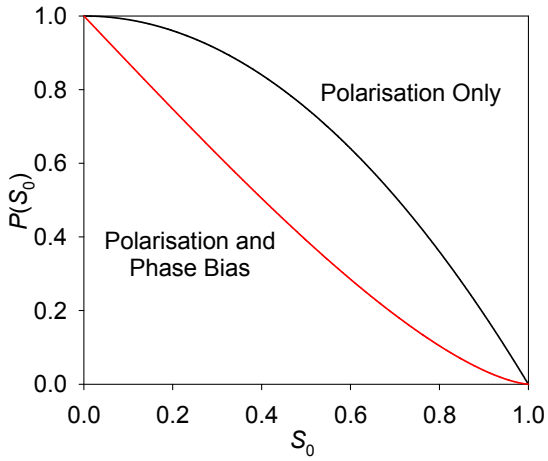

Figure 3.2.7

Probability that the small-signal sensitivity will be at least S_0. The polarisation only line (Black) shows the probability the mixing efficiency is at least S_0. The lower red line shows the probability that the product of the polarisation mixing efficiency and the phase bias gives a minimum sensitivity S_0. The graph shows that the sensitivity will be at least 50 % of the maximum for around 40 % of the time.

To summarise, this brief analysis of the effect of birefringence on the performance of the C-OTDR sensor has suggested that the retardation introduces a random phase bias to the independent signal from one of the two available polarisation states, dependent on the beat length and the effective scatter site separation. The fraction of the light in each orthogonal state is also random, depending on the alignment of the

source relative to the birefringence axes. The randomisation of the birefringence at splices, where the axes are unlikely to be aligned, increases the degrees of freedom available to the statistical distribution that describes the response to a small phase disturbance.

3.2.6. Effect of Wavelength Diversity

In the preceding analysis, the optical wave has been considered to be adequately described by a single optical frequency. In other words, the coherence time has been assumed to be much greater than the duration of the pulse and, additionally, that the same single frequency describes subsequent pulses so that the same backscatter pattern is obtained each time. In the case of a finite line width, or where the optical frequency varies, this can no longer be assumed to be the case since the optical phase between scatter sites will vary, altering the backscatter pattern. It is therefore important to understand the behaviour with varying wavelength in order to specify the line-width required and the effect that a finite line-width may have on the sensor performance.

Considering the division of the pulse into two components, as previously, it is reasonable to envisage each as representing two resultant scatter sites located in the centre of each half pulse, or in the time domain, separated by $\tau / 2$. Where the phase bias between the two, ϕ_0, alters by more than π, the response to an external strain will be considerably modified. The limiting condition is therefore:

$$\pi = 2\pi\Delta\nu\frac{\tau}{2}, \tag{3.2.40}$$

which, following some simple re-arranging, gives:

$$\Delta\nu = \frac{1}{\tau}. \tag{3.2.41}$$

Thus a frequency shift of greater than $1 / \tau$ will lead to a significant change in the backscatter trace. This result, obtained from simple physical arguments, is identical to that obtained by a statistical analysis of the correlation properties of the backscatter trace by Mermelstein *et al.* [63].

In terms of the source coherence, the derived limit is equivalent to demanding a coherence length which exceeds the physical extent of the pulse, and requiring it to remain stable within the same bounds over the multiple pulses from which the phase disturbance is decoded.

3.3. Numerical modelling

3.3.1. Motivation

To validate the analytical model of coherent scattering presented in section 3.2 a numerical model was developed in C++ to generate backscatter traces based on the assumptions used in the analytical analysis.

3.3.2. Modelling of Coherent Backscatter Trace

The simulation was based on an earlier programme by Dr Stuart Russell, with the author developing the original code to allow modelling of two orthogonal polarisation states and simulation of the effect of external phase disturbances on the coherent scatter pattern, generating the results presented here.

The fibre is divided into a large number of elements, with length ~0.1 m, and therefore containing a large number of physical scattering sites. As a result it can be assumed that each element scatters equal energy, and that the light scattered from each element can be described by a single optical wave, of random phase. The forward-propagating pulse and backscattered light is propagated along the fibre element-by-element. The backscattered light from each element containing the forward-propagating pulse is calculated and combined coherently with existing backscattered light in that element, with phase given by the difference in the scatter phases of the current element and its neighbour. This simplification avoids the need to calculate and store a resultant phase for each element; since each phase is random this does not affect the validity of the simulation.

Since equal energy is scattered from each element it is convenient to consider intensities rather than electric fields in the simulation. Using the cosine rule to combine two electric field vectors with magnitudes E_0 and dE, separated by an angle θ, where E_0 is the existing backscatter and dE is the contribution from the current element, gives a resultant from the current fibre element of:

$$E_R^2 = E_0^2 + (dE)^2 - 2E_0 dE\cos(\theta). \qquad 3.3.1$$

Combining the scattered light with the existing backscatter within an element in terms of intensities can therefore be reduced to the simple algorithm:

$$I \to I + dI - 2\sqrt{IdI}\cos(\theta), \qquad 3.3.2$$

where θ is the angle between the field scattered from the element and the existing resultant, I is the existing intensity and dI is the intensity scattered from the current element.

To model the effect of polarisation in the fibre, two independent traces are calculated, representing two orthogonal states. Each uses the same vector of random scatter phases, but one also uses a second vector of random retardations to modify the scattering phase. The independent intensity traces are summed and written to file for subsequent analysis. To model the application of an external phase disturbance to the fibre, the code allows a number of traces to be generated, with the vector of scattering phases modified for each one. A point strain is modelled by a step increase in the phase, which applies to all points beyond the point of strain since these sites have all been modified in their phase relation to the source.

3.3.3. Simulation Results

A simulated trace for the two-polarisation case is shown in Figure 3.3.1 for a 40 m (200 ns) pulse, calculated with the fibre divided into elements of 1 m. The simulated backscatter trace shows reasonable agreement with the character of the experimental trace shown in Figure 3.3.2. The high frequency components in the simulated data are not present in the experimental measurement since the sampling rate of 25 MHz limits the frequency content of the reconstructed data to the Nyquist frequency, 12.5 MHz.

The backscatter statistics obtained from the simulated trace were compared with the predictions in the literature [32]. To do this the loss coefficient in the simulation code was set to zero and traces for a 15000-element fibre calculated, both with a single polarisation state and with two independent orthogonal modes. Because the fibre was lossless each data point could be normalised to the mean, calculated over the entire trace, thus avoiding the need to weight the normalisation based on the loss. Figure 3.3.3 shows histograms of the backscatter value, normalised to the mean and converted to frequency density, plotted along with the theoretical PDF calculated using 3.1.1.

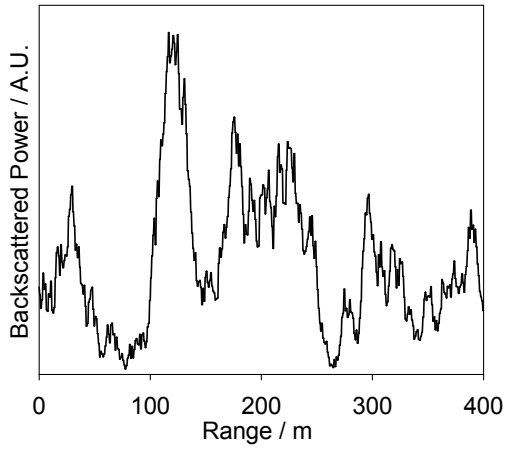

Figure 3.3.1

Simulated backscatter trace for case with two independent polarisation states. The pulse width is 40 m *(200* ns*) and the fibre is divided into elements of 1* m *in length.*

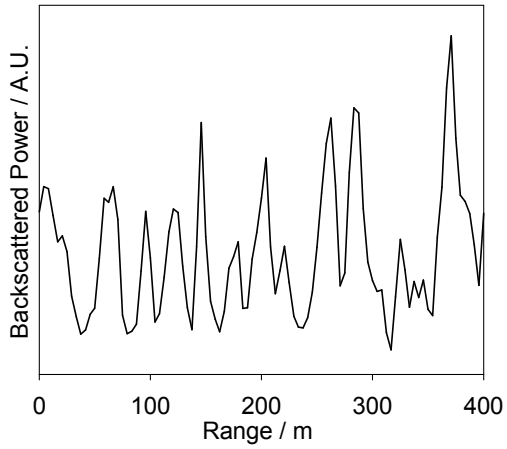

Figure 3.3.2

Experimental backscatter from a 40 m *(200* ns*) pulse, sampled at 4.2* m *intervals (25* MHz*). The source coherence length was > 10* km *in free space).*

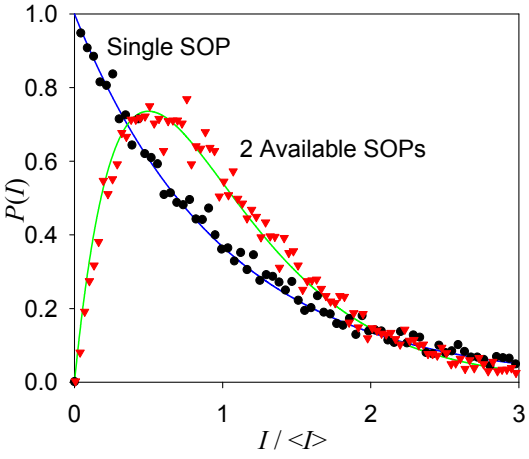

Figure 3.3.3

PDF of obtaining a given intensity in numerical simulation of coherent backscatter and theoretical predictions. The numerical simulations were over 15000 fibre elements giving a total of 30000 samples.

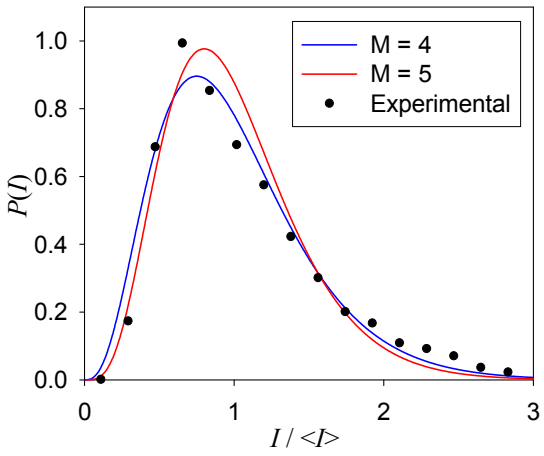

Figure 3.3.4

PDF of experimental backscatter trace. The theoretically predictions for M = 4 and M = 5 are superimposed, both being a reasonable match to the data, showing that more degrees of freedom were available than the expected M = 2.

The simulated data shows excellent agreement with the expected function, confirming that the statistics of the data generated by the numerical model match the expected characteristics. For comparison, data from 7 traces of a 120 m section of fibre, illuminated with a 40 m (200 ns) pulse, derived from a source with line-width less than 30 kHz – equivalent to a coherence length of at least 6.7 km in fibre, were analysed. The round-trip loss, assuming the fibre attenuation to be 0.2 dB / km, was 0.05 dB (~ 2 %), giving negligible broadening of the distribution. The results are shown in Figure 3.3.4, along with theoretical plots for $M = 4$ and $M = 5$. The good agreement with these plots suggests that more degrees of freedom are available to the light than the theory discussed so far suggests. The most likely reasons for this are that noise in the received signal and non-linearity-induced chirp reduced the coherence from that of a perfectly switched, coherent source.

The spectral content of the simulated backscatter trace is shown in Figure 3.3.5, calculated using a 2048-point Fast-Fourier Transform (FFT), using Hanning-windowing and zero-padding. The pulse length was 6 fibre elements, giving a backscatter sample rate of 12 samples per pulse width. The rapid fall-off shows that the majority of the electrical power is within the bandwidth defined by Λ^{-1}, showing that, as for conventional OTDR, this is a reasonable choice of receiver bandwidth.

For comparison, the spectrum of the coherent backscatter pattern was measured experimentally by launching 40 m (195 ns) pulses into a stable fibre of length 3.5 km. The backscatter was sampled at 25 MHz, corresponding to a spatial sample rate of 0.24 m^{-1}. The spectrum was calculated for 9 backscatter traces using a 512-point FFT, and the power spectra were calculated and averaged for each spatial frequency point. The results are plotted in Figure 3.3.6, where the power is in dB relative to arbitrary units. The receiver bandwidth was 20 MHz, which corresponds to a spatial frequency of 0.19 m^{-1}, indicating that the fall-off at lower spatial frequencies is due to the pulse width, not the low-pass effect of the receiver. The fall-off of the experimental data is slower than the simulated data; probably due to the noise spectrum of the receiver, which is approximately white, increasing the power at higher frequencies.

The effect of a point phase disturbance was modelled by comparing an initial trace with a second trace where the scatter phase was increased in a stepwise fashion as shown in the upper graph in Figure 3.3.7, simulating point phase disturbances of 0.1 rad at 100 m, 200 m, 300 m and 400 m. The lower graph in the figure shows the difference

between the two traces. As expected the response differs randomly in direction and magnitude and the spatial resolution is equal to the pulse width.

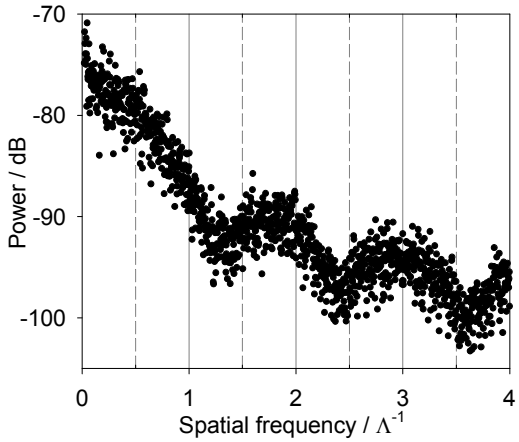

Figure 3.3.5

Spectral content of simulated backscatter trace with two orthogonal polarisation modes, sampled at 12 samples per pulse width. The results show that most of the energy is within a Λ^{-1} *bandwidth.*

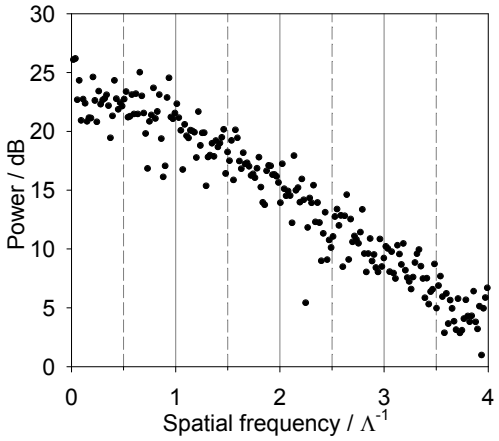

Figure 3.3.6

Experimental spectrum of coherent backscatter pattern from a 40 m *pulse, showing similar behaviour to the simulated data but with slower roll-off with increasing frequency.*

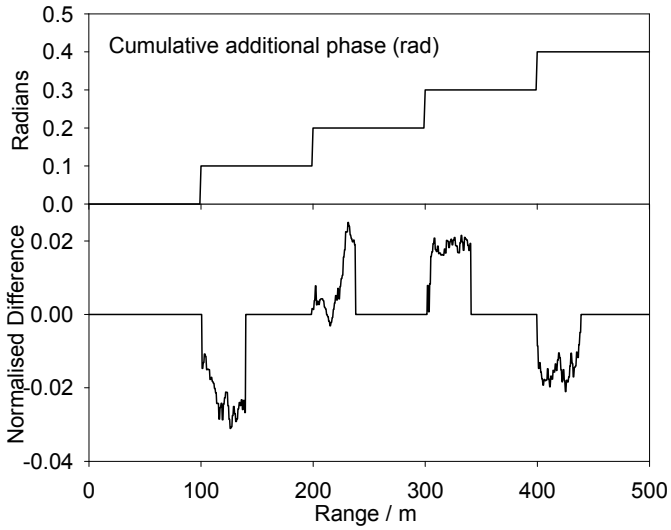

Figure 3.3.7

Top: Modelling application of point phase disturbances by stepped phase modulation. Bottom: difference between initial trace and second trace with point strains of 0.1 rad *located at 100* m*, 200* m*, 300* m *and 400* m*). In the simulation the fibre was divided into 500 elements of 1* m *and the pulse width was 40* m

3.3.4. Conclusions

The assumptions made in the theoretical analysis, in the early parts of this chapter, were used to construct a numerical model of coherent Rayleigh scattering in optical fibres. The backscatter data generated by the numerical model had similar statistics to those predicted, with experimental measurements suggesting that in practice the pulse may be only partially coherent.

The frequency spectrum of the data from numerical modelling was found to have a rapid roll-off, with most of the energy at spatial frequencies below Λ^{-1}, suggesting that a receiver electrical bandwidth equivalent to Λ^{-1} is sufficient to observe the detail of the coherent backscatter trace. The fall-off of experimental data was slower, but demonstrating the same form as the simulated data. Finally the effect of a point phase disturbance was modelled, showing a random-amplitude response as expected, with spatial resolution corresponding to the pulse width.

The good agreement between theoretical analysis, numerical modelling and experimental data shows that a sensor capable of meeting the requirements set out in Section 1.1.4 can be implemented by monitoring the intensity of the coherent backscatter pattern. The good agreement between experimental observations and the numerical model, which is based on the assumptions of the theoretical analysis earlier in the chapter, validates the theoretical analysis, indicating that the behavioural predictions from the theoretical analysis are likely to be accurate.

Chapter 4 Theoretical Sensor Performance

In this chapter, the influence of undesirable noise sources on the C-OTDR sensor is analysed and the resulting limits on performance are discussed. First the noise on the decoded output is analysed, in terms of the optical receiver noise and sensor parameters, such as the sampling rate and filter bandwidths. The receiver noise is then considered, starting at first principles to derive the noise performance of a transimpedance amplifier. Various OTDR architectures are then analysed, and the results applied to the C-OTDR sensor. Finally, the fundamental noise limits due to thermal phase noise in the fibre are considered, developing standard theory to derive the resulting noise on the sensor output.

4.1. C-OTDR Noise Theory

4.1.1. Introduction

While several descriptions of the operation of the C-OTDR sensor are available in the literature [39-42] little has been published on the noise analysis of a sensor of this type. In this section the conversion of receiver noise into noise on the decoded audio signal is analysed, which requires careful consideration of the operations carried out on the raw signal from the receiver and how these affect the noise characteristics.

It is assumed throughout the analysis that the fibre can be treated as a linear medium. The impact of non-linear optical effects on the performance is considered in detail in Chapter 6.

4.1.2. Signal Flow in the C-OTDR Sensor

Consider monitoring a single resolution point of the fibre. The instantaneous signal from that resolution point is the intensity, measured as a voltage at the optical receiver output, backscattered from that part of the fibre. To build up a full picture of the signal, the process must be regularly repeated, allowing the scattered intensity to be sampled in the time domain. Over many samples the time dependence of the signal can be found, allowing it to be reconstructed to give an audio output, or analysed in the digital domain to apply signature recognition algorithms or other complex signal processing. This process is illustrated in Figure 4.1.1.

Pulses are launched into the fibre at rate f_s, which is limited by the length of the fibre, L, as the light needs time to complete a round-trip before the next pulse is launched to avoid cross-talk between bins. Where n is the effective refractive index of the fibre and c is the speed of light in free space, the maximum repetition rate, ignoring the pulse duration, is:

$$f_{s\,Max} = \frac{c}{2nL}. \qquad 4.1.1$$

In practice some additional dwell may be required to allow signal processing, clock synchronisation and so on, to be carried out, reducing the achievable sample rate, however this remains the fundamental limit.

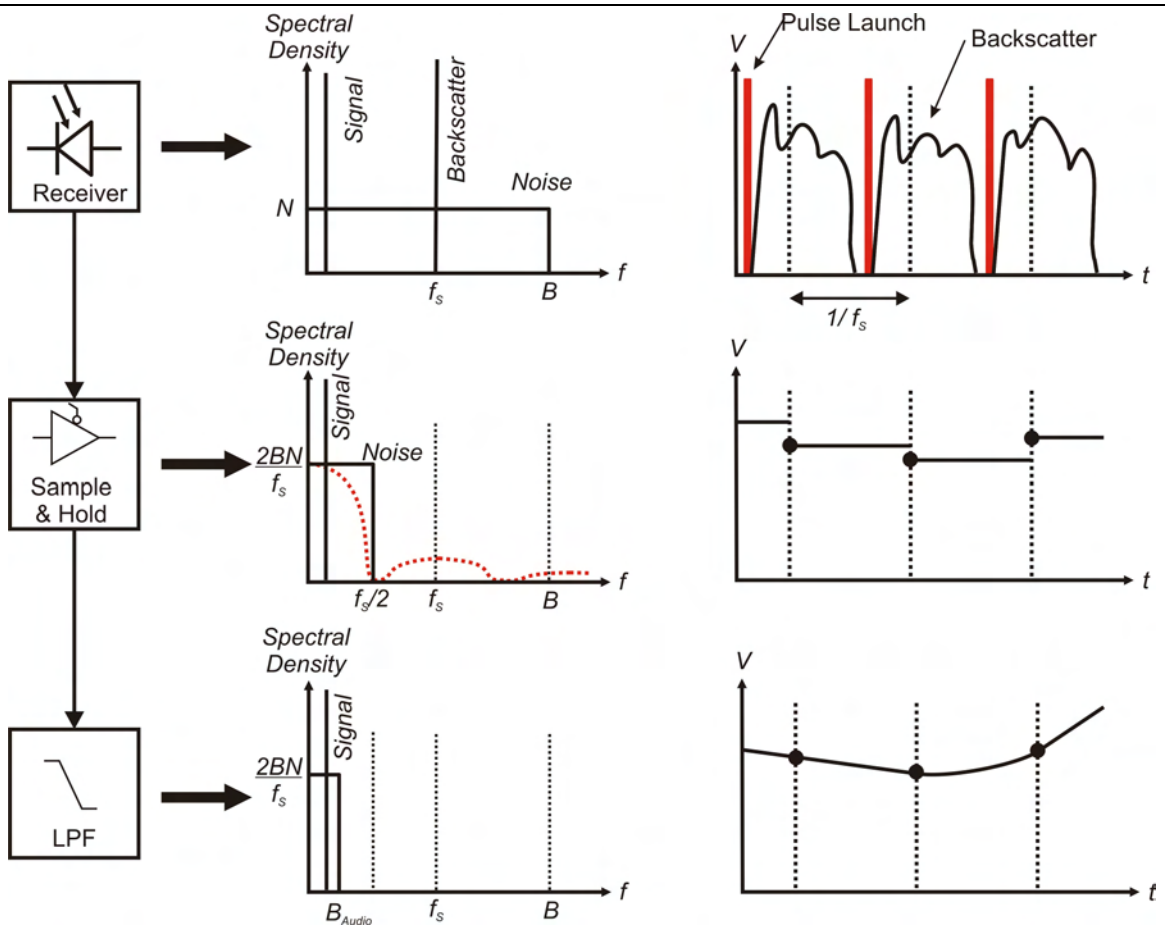

Figure 4.1.1

C-OTDR noise calculation with ideal analogue sample-and-hold amplifier, the low-pass filter limits the audio bandwidth to B_{Audio}

(a) Shows the data flow from optical receiver sampled by the sample-and-hold amplifier and filtered to give the audio output;

(b) Shows the effect of sampling in the frequency domain, in the centre graph the true frequency response of the S&H amplifier is shown in red and the noise-equivalent spectrum in black; and

(c) Shows the conversion of sequential backscatter samples from a single resolution bin into the acoustic signal in the time domain. (Note, any phase delay from the low-pass filter is neglected for clarity)

As discussed in Chapter 2, in order to achieve pulse width-limited spatial resolution, the bandwidth of the receiver, B, has to be sufficiently large to resolve the pulse width. Since the length of fibre under interrogation is inevitably greater than the pulse width, it is invariably the case that $B >> f_s/2$ so the effects of aliasing must be considered in the analysis of the noise performance of the acoustic sensor.

In analysing the noise performance it is therefore necessary to consider the effect of this discrete-time sampling The well-known sampling theorem, formalised by Shannon [67, 68], states that if a signal occupies a bandwidth W then, provided it is sampled at a rate of $2W$, the Nyquist rate, or greater, it can be reconstructed without loss of information using a series of pulses of shape $\mathrm{sinc}(2\pi Wt)$ with their amplitude scaled to the sample values. If the signal contains frequency components outside this bandwidth then aliasing occurs, where the out-of-band components are reconstructed within the bandwidth of interest.

4.1.3. C-OTDR with Ideal Analogue Sampling

To calculate the noise on the decoded signal it is assumed that the receiver noise can be considered to be constant over the period under consideration with a uniform spectral density of N ($= < v^2_{Reciever} > / B$ V^2 / Hz) in the detector electrical bandwidth B and negligible noise outside this band. This is a reasonable description of the noise for analysis purposes. If the noise sources are of constant spectral density and the bandwidth is the 3 dB cut off of a 1st-order filter, then the total noise power at higher frequencies is roughly equivalent to the in-band reduction at power due to the filter roll-off.

The backscatter is sampled at a single point along the fibre for each pulse launched using the sample-and-hold (S&H) amplifier, which for this analysis is assumed to be ideal: adding no noise to the signal, holding without droop, negligible aperture jitter and fast enough response time to resolve any component within the detector bandwidth.

The signal captured by the S&H amplifier is a discrete series of values representing the value of the signal at intervals of $1/f_s$. If this series were reconstructed by low-pass filtering to a bandwidth of $f_s/2$ the result would be as shown in Figure 4.1.1. The frequency components of the receiver noise above $f_s/2$ alias into the sampled signal with the total noise power remaining constant, the spectral density is therefore $2N\frac{B}{f_s}$.

In practice, the acoustic signals of interest may not extend up to $f_s/2$, so it is advantageous to set the low-pass filter cut off to some lower frequency, B_{Audio}. The spectral density of the noise is not changed by this modification, so the total noise is reduced to $NB\frac{B_{Audio}}{f_s/2}$. Finally, in terms of the receiver noise voltage, the noise on the filtered audio signal is:

$$< v_{Audio}^2 >= \frac{2B_{Audio}}{f_s} < v_{Receiver}^2 > . \qquad 4.1.2$$

As will be shown in section 4.2, except for very low light powers, the receiver noise itself depends on the optical power. Furthermore, the nature of the signal from an individual resolution bin along the fibre is non-deterministic. The backscatter power is dependent on the random phase-spacing of the scattering sites and the degree of interference at the detector, while the modulation due to an external disturbance is dependent on the spatial extent of the disturbance and the visibility of the resultant interference modulation. Depending on the particular situation, at the particular point of interest, the decoded signal from a disturbance may vary between the extremes of a small modulation on a DC offset through to 100% modulation. It is therefore impossible to derive an exact equation for the audio SNR as this depends on the nature of the signal, however for comparative purposes SNR_{Audio} can be defined when the interference signal is equal in optical power to the mean optical power expected from range, z, in an incoherent OTDR, $P(z)$:

$$SNR_{Audio} = \frac{P(z)rR_F}{< v_{Audio}^2 >} = \frac{f_s}{2B_{Audio}} \frac{P(z)rR_F}{< v_{Reciever}^2 >} . \qquad 4.1.3$$

where r is the photodiode responsivity and R_F is the receiver transimpedance. By noting that the right-hand factor is simply the receiver SNR for range, z, $SNR_{Rec}(z)$, the audio SNR can be written as:

$$SNR_{Audio} = \frac{f_s}{2B_{Audio}} SNR_{Rec}(z), \qquad 4.1.4$$

confirming the expectation that for optimum performance the receiver should be designed to be as low-noise as possible and the signal sampled at the highest pulse rate possible before filtering the audio signal to allow only the bandwidth of interest to pass.

4.1.4. C-OTDR with Ideal Digital Sampling

The analogue sample-and-hold amplifier and low-pass filter is a suitable method for recovering the signal from a single point on the fibre. However, where it is wished to interrogate multiple points simultaneously the use of digital acquisition is more suitable; allowing parallel processing of many signals without cumbersome analogue electronics. The data flow, for a single audio channel in such a system, is shown in Figure 4.1.2. In terms of noise performance, the difference compared to the analogue method in Section 4.1.3 is the introduction of quantisation noise at the point of conversion.

A typical analogue-to-digital converter (ADC) may have a full-scale range of 5 V and with 12-bit resolution, i.e. the analogue input will be converted to one of 2^{12} digital values. In a q-bit ADC with full-scale input of V_{max} the separation between bits, δ, is

$$\delta = \frac{V_{\max}}{2^q}. \qquad 4.1.5$$

The analogue signal, which is a voltage restricted to the range 0 to V_{max}, is assumed to take any value between these limits, with equal probability. The error, x, between the true analogue signal and the nearest digitised value must lie in the range $-\frac{1}{2}\delta$ to $+\frac{1}{2}\delta$ so the noise, due to quantisation, is:

$$< v_q^2 >= \frac{1}{\delta}\int_{-\frac{1}{2}\delta}^{\frac{1}{2}\delta} x^2 dx = \frac{\delta^2}{12}. \qquad 4.1.6$$

Using 4.1.5 we obtain the quantisation noise in terms of the ADC parameters,

$$< v_q^2 >= \frac{V_{\max}^2}{12 \cdot 2^{2q}}, \qquad 4.1.7$$

where V_{max} is the full-scale deflection of the analogue-to-digital converter (ADC) and q is the effective number of bits (which is usually specified to include any input-referred noise in the ADC). The quantisation noise occupies the full bandwidth of the reconstructed data, $f_s/2$, giving a spectral density N_q, of:

$$N_q = \frac{V_{\max}^2}{6 f_s 2^{2q}}. \qquad 4.1.8$$

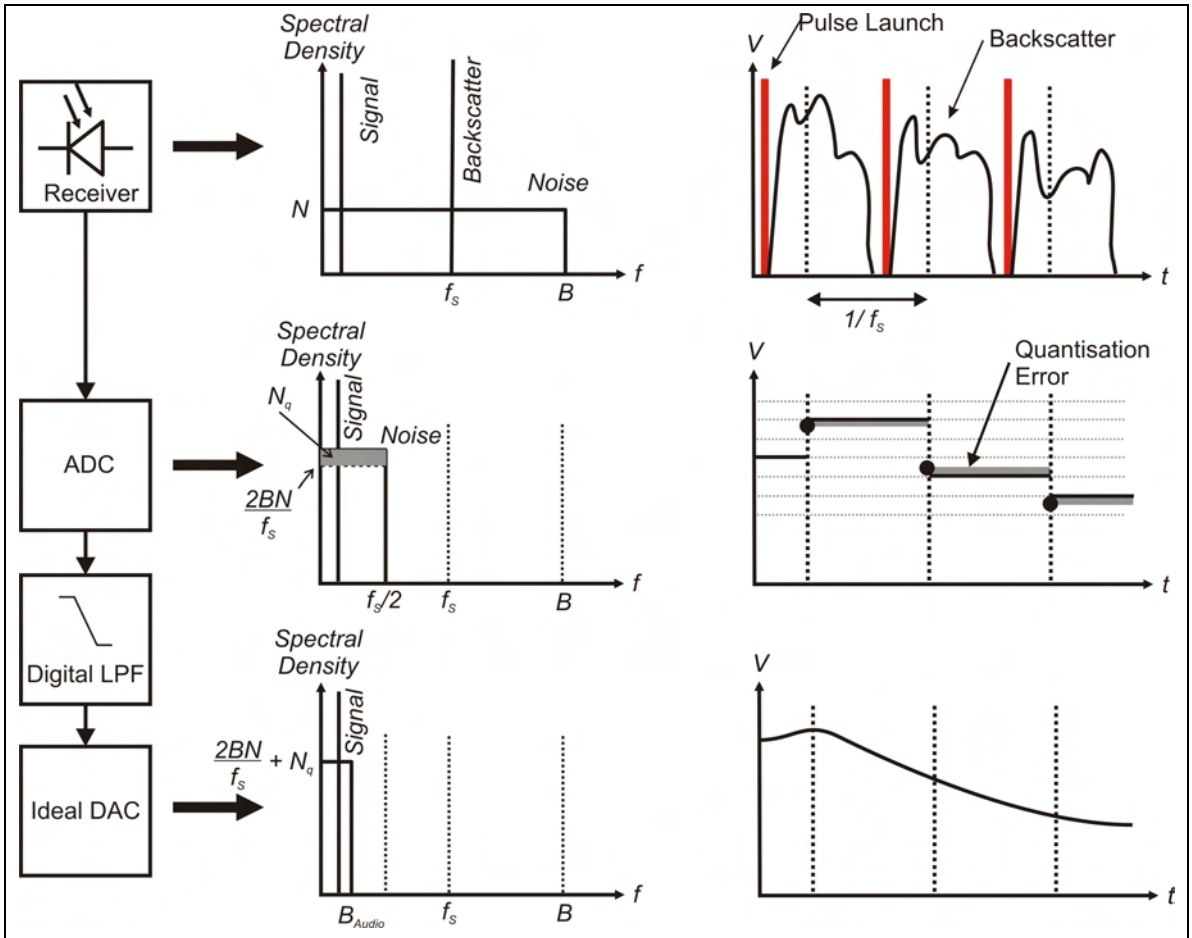

Figure 4.1.2

C-OTDR noise calculation with ideal ADC, the digital low-pass filter limits the bandwidth to B_{Audio}, the DAC is shown for completeness – in reality the data may be processed entirely in the digital domain.

(a) Shows the data flow from receiver to audio output

(b) shows the effect of sampling in the frequency domain – assuming appropriate filtering where required to visualise the spectrum; and

(c) shows the conversion of sequential samples into the acoustic signal from a single resolution bin – note the quantisation error introduced at the ADC. (Note, the phase delay from the low-pass filter is neglected for clarity)

Following the acquisition the receiver noise folds into the recovery bandwidth and, with the addition of quantisation noise, the total noise spectral density is:

$$\frac{2B}{f_s}N + \frac{V_{\max}^2}{6f_s 2^{2q}}. \qquad 4.1.9$$

Once again, low-pass filtering at B_{Audio} reduces the total noise to:

$$< v_{Audio}^2 >= \frac{2B_{Audio}}{f_s}\left(< v_{Reciever}^2 > + \frac{V_{\max}^2}{12 \cdot 2^{2q}} \right). \qquad 4.1.10$$

Writing in terms of the receiver SNR, as before, and using 4.1.7, the audio SNR is:

$$SNR_{Audio} = \frac{f_s}{2B_{Audio}} SNR_{Rec}(z)\left(\frac{< v_{Reciever}^2 >}{< v_{Reciever}^2 > + < v_q^2 >} \right). \qquad 4.1.11$$

For $\left(< v_q^2 >\right) << \left(< v_{Reciever}^2 >\right)$ this reduces to 4.1.4, but, for larger quantisation noises, the audio SNR is degraded; highlighting the importance of choosing an ADC with sufficient dynamic range and speed to allow realisation of an optically-limited sensor.

4.2. Receiver Noise in Conventional OTDR

As shown in Section 4.1 in order to evaluate the overall noise performance of the C-OTDR sensor, the receiver noise must be evaluated. In this section the theory of conventional OTDR noise is developed. The analysis begins with the noise sources in the photo-detector before considering the electronic receiver, in particular the case of the transimpedance amplifier. The noise for various conventional OTDR architectures is then found, and the results applied to the analysis of Section 4.1.

4.2.1. PIN Photodiode Performance

In a PIN photodiode the p and n regions of the p-n junction are separated by a layer of intrinsic semiconductor which contains the depletion region, allowing its dimensions to be controlled more closely than in a plain p-n junction [5]. An incident photon with energy greater than the band-gap can raise an electron into the conduction band giving rise to a photocurrent, I_P, which is related to the incident optical power, P, by:

$$I_P = \frac{\eta e}{h\nu} P . \qquad 4.2.1$$

Where η is the quantum efficiency (i.e. the probability that an incident photon will generate a photo-electron), e is the electronic charge, h is the Planck constant and υ is the optical frequency. The fraction $\frac{\eta e}{h\nu}$ is the responsivity, r, of the photodiode, which is wavelength and temperature dependent – at 1550 nm, at room temperature, a typical value is 0.85 A / W [5].

Photodiodes are often operated under reverse bias, this increases the physical size of the depletion region, reducing the junction capacitance, allowing higher bandwidth and extending the power range over which a linear response can be achieved. These benefits are at the expense of increasing the dark current (the current which flows with no illumination); however, this is only a problem when dealing with very low light levels. With modest reverse bias (~ 5 V) as typically used with InGaAs PIN photodiodes, where the depletion region is already increased by the layer of intrinsic semiconductor, typical dark currents are of the order of 1 nA, and for high-sensitivity applications low-leakage models are available with typical dark currents of the order 0.1 nA [69].

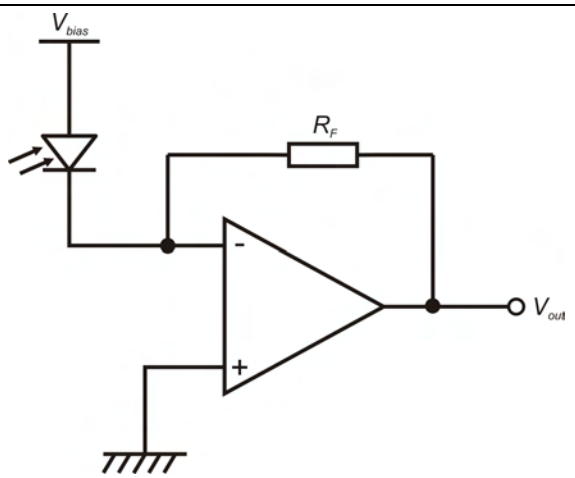

Figure 4.2.1

Simple Transimpedance receiver. The transimpedance feedback resistor, R_F, converts the photocurrent from the diode into a voltage output.

4.2.2. Transimpedance Receiver Noise

Consider the simple optical receiver illustrated in Figure 4.2.1. Assuming that the op-amp input impedance is large compared to R_F then, by noting the inverting input is a virtual earth, by inspection:

$$V_{Out} = I_P R_F \,. \qquad 4.2.2$$

This type of receiver, where the current is converted to a voltage signal by the feedback resistor, is known as a Transimpedance Amplifier (TIA) with the value of the feedback resistor being termed the transimpedance.

The sources of noise that must be considered in analysing the TIA receiver are [5, 70]: thermal noise, in the feedback resistor and photodiode; shot noise (quantum noise), on the photocurrent, the dark current and noise from the op-amp, a combination of thermal noise, shot noise and 1/f noise.

Thermal noise (Johnson noise) occurs in any resistive material due to random thermally-excited carrier motion and is produced by any resistor, regardless of its design or packaging, although these may influence sources of excess noise above the fundamental thermal noise. A resistance R generates an open-circuit thermal noise voltage

$$< v_{Therm}^2 >= 4k_B TBR\,, \qquad 4.2.3$$

where <…> represents time average, k_B is the Boltzmann constant, T is the absolute temperature and B is the bandwidth of the noise measurement. Dividing through by R^2, the current noise is:

$$< i_{Therm}^2 >= \frac{4k_B TB}{R}\,. \qquad 4.2.4$$

As shown in Figure 4.2.2 a real resistor can be modelled as either a voltage source, with an ideal output impedance R, or an ideal resistance, R, with a parallel noise current source [70].

In electrical systems, shot noise occurs due to the discrete nature of electron flow through a potential barrier. The same effect occurs in light due to the quantisation of light into photons, each carrying a discrete quantity of energy, $h\upsilon$.

At an optical power level P the expected rate of photon arrival is $P/h\nu$ s^{-1}, the actual number arriving in a short time interval is described by a Poisson distribution centred on the expected value [5], leading to a current noise:

$$< i_{Shot}^2 >= 2erBP\,. \qquad 4.2.5$$

Note that the noise amplitude increases with the square root of the power, so increasing the power by a factor F reduces the relative amplitude of the shot-noise by a factor of $\sqrt{F}$.

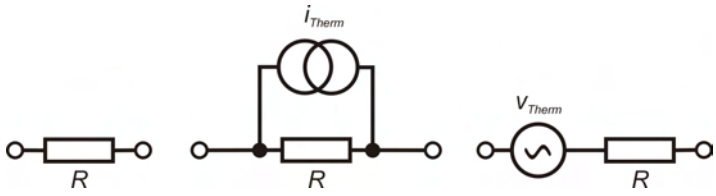

Ideal resistor *Norton Equivalent* *Thévenin equivalent*

Figure 4.2.2

Noise-equivalent models of a real resistor exhibiting thermal noise [70].

In addition to adding an offset to the output, the dark current adds to the total receiver noise by adding additional shot-noise:

$$< i_{Dark}^2 >= 2eBI_{Dark} . \qquad 4.2.6$$

In most cases the dark current is small, in comparison to the signal current, and the contribution to the detector output can be ignored.

1/f noise occurs in active devices due to fluctuations in the carrier diffusion [71]. The spectral density is proportional to 1/f, hence the name. 1/f noise is sometimes called "pink noise" to differentiate it from "white" noise sources where the spectral density does not exhibit frequency dependence. The frequency where the 1/f noise exceeds the thermal noise is known as the corner frequency and varies according to operation conditions and the type of device. The corner frequency in precision bi-polar devices may be ~1 Hz while at the other extreme in very high-frequency MOSFET devices it may be as high at ~100 MHz [70].

The input impedance of a transimpedance amplifier is R_F / A where A is the op-amp open-loop gain. Since A is very large we can assume $A >> R_F$ and calculate the noise current from the diode as though the amplifier input is shorted to ground.

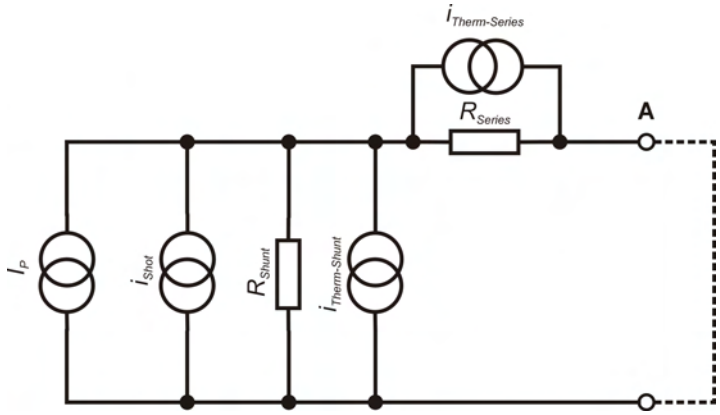

Figure 4.2.3

Noise-equivalent model of photodiode used for the calculations of the noise performance of the transimpedance amplifier..

The diode equivalent circuit for noise calculation is shown in Figure 4.2.3 where it is assumed that the transimpedance amplifier has negligible input impedance, i.e. $R_F / A << R_{Series}$. Only noise-currents passing through point A contribute to the signal, the total noise current i_{Diode} is therefore given by:

$$< i_{Diode}^2 >=< i_{Shot}^2 > + < i_{Datk}^2 > + < i_{Therm-Shunt}^2 > \left(\frac{R_{Shunt}}{R_{Shunt} + R_{Series}} \right)^2 \ldots + < i_{Therm-Series}^2 > \left(\frac{R_{Series}}{R_{Shunt} + R_{Series}} \right)^2 \quad 4.2.7$$

Substituting from 4.2.4 for the thermal noise currents we obtain:

$$< i_{Diode}^2 >=< i_{Shot}^2 > + < i_{Datk}^2 > + 4k_B TB \left[\frac{R_{Shunt}}{(R_{Shunt} + R_{Series})^2} + \frac{R_{Series}}{(R_{Shunt} + R_{Series})^2} \right]. \quad 4.2.8$$

For a typical InGaAs diode [69] R_{Series} = 5 Ω and typical dark currents are ~ 1 nA at ~ 5 V reverse bias, indicating that R_{Shunt} ~ 5 GΩ. Noting that $R_{Series} << R_{Shunt}$ and substituting from 4.2.5 and 4.2.6, the total current noise is given, to a good approximation, by:

$$< i_{Diode}^2 >= 2erBP + 2eBI_{Dark} + \frac{4k_B TB}{R_{Shunt}}. \quad 4.2.9$$

Having analysed the noise sources in the photodiode the transimpedance receiver can be considered as shown in Figure 4.2.4.

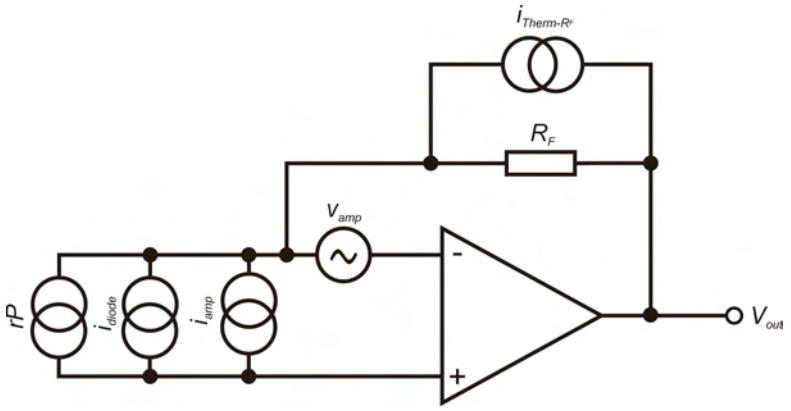

Figure 4.2.4

Noise-equivalent model of transimpedance amplifier. The output signal, V_{Out} = rRFP, the noise contributions are due to the diode, amplifier and thermal noise in the feedback resistor.

The noise voltage at the output is:

$$< v_{Out}^2 >= \left(< i_{Diode}^2 > + < i_{Amp}^2 > + < i_{Therm-R_F}^2 >\right) R_F^2 + < v_{Amp}^2 >, \qquad 4.2.10$$

using 4.2.3 and 4.2.9 this becomes:

$$< v_{Out}^2 >= \left(2erBP + 2eBI_{Dark} + \frac{4k_BTB}{R_{Shunt}} + < i_{Amp}^2 > + \frac{4k_BTB}{R_F} \right) R_F^2 + < v_{Amp}^2 > . \qquad 4.2.11$$

For most photodiodes $R_F << R_{Shunt}$ and the dark current noise is small compared to the feedback resistor thermal noise. FET-input op-amps have negligible RMS input current noise of the order of 10 pA and RMS input voltage noise of the order of 10 μV. The current noise will only be significant where the photocurrent is of the order 10 pA, while, from manipulation of 4.2.3, the input voltage noise will be small in comparison with the thermal noise in the transimpedance resistor where $BR << 6 \times 10^9$ Ω·Hz, whereas for typical OTDR applications the bandwidth may be ~10 MHz and the transimpedance ~100 kΩ $BR \sim 2 \times 10^{12}$ Ω·Hz.

The significant terms of the output noise are therefore the thermal noise in the feedback resistor and shot noise:

$$< v_{Out}^2 >= 2erBPR_F^2 + 4k_BTBR_F . \qquad 4.2.12$$

The electrical signal to noise ratio (*SNR*) is therefore:

$$SNR = \frac{V_{Out}^2}{< v_{Out}^2 >} = \frac{(rP)^2}{2erBP + \frac{4k_B TB}{R_F}}. \qquad 4.2.13$$

The contribution from the thermal noise can be minimised by choosing the largest value of R_F possible while maintaining sufficient bandwidth (as determined by the diode capacitance and op-amp gain-bandwidth product).

The optical power required to give unity SNR can be found from manipulation of 4.2.13:

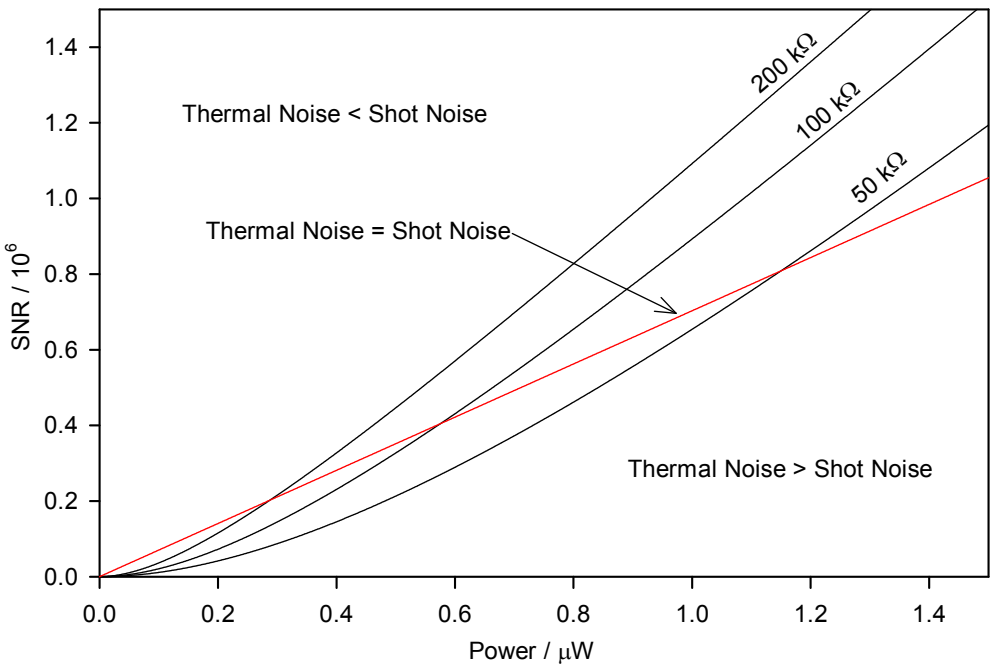

Figure 4.2.5

Theoretical SNR of an ideal transimpedance amplifier as a function of input optical power (note that the SNR is defined in terms of electrical, not optical, powers). The electrical bandwidth is 20 MHz *and a diode responsivity of 0.9* A / W *is assumed. Where possible, the feedback resistance is chosen so that the receiver is operating above the thermal noise threshold indicated by the red line, plotted by noting that when thermal and shot noise are equal, the denominator in* 4.2.13 *becomes 4erBP which is independent of the transimpedance.*

$$P_{SNR=1} = \frac{1}{r}\left(eB + \sqrt{e^2 B^2 + \frac{4k_B TB}{R_F}} \right). \qquad 4.2.14$$

For typical values of B = 20 MHz and R_F = 110 kΩ:

$$eB << \sqrt{\frac{4k_B TB}{R_F}}, \qquad 4.2.15$$

so, to a good approximation:

$$P_{SNR=1} = \frac{1}{r}\sqrt{\frac{4k_B TB}{R_F}}. \qquad 4.2.16$$

For typical values of B = 20 MHz, R_F = 110 kΩ, r = 0.9 and T = 300 K, the power at which the SNR is reduced to unity, $P_{SNR=1}$ = 2 nW.

4.2.3. Noise in Basic OTDR

In the case of a conventional, incoherent OTDR, Figure 4.2.6, the power returned to the receiver, from a range z [16], assuming any internal losses are negligible is:

$$P(z) = \tfrac{1}{2} P_{Launch} \Lambda \alpha_S S \cdot e^{-2\alpha z}, \qquad 4.2.17$$

where P_{Launch} is the pulse power launched into the fibre, Λ is the spatial pulse width, α_S is the scattering loss (typically 4.5 × 10^{-5} m^{-1} or 0.19 dB / km), α is the total attenuation coefficient, typically between 4.6 × 10^{-5} m^{-1} (0.20 dB / km) and 5.6 × 10^{-5} m^{-1} (0.25 dB / km), and S is the capture fraction (typically 0.0063). Combining 4.2.17 with 4.2.16 gives the fibre length at which the SNR is reduced to unity:

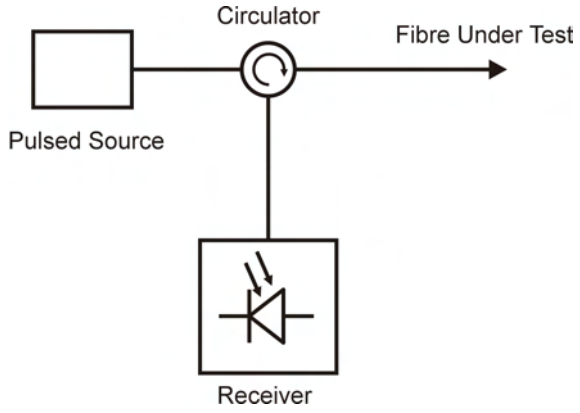

Figure 4.2.6

Layout of an idealised conventional OTDR. Pulses are launched into the fibre and the backscattered light is passed directly to the receiver.

$$z_{SNR=1} = \frac{-1}{2\alpha} \ln\left\{ \frac{2}{rP_{Launch}\Lambda\alpha_S S} \sqrt{\frac{4k_B TB}{R_F}} \right\}. \qquad 4.2.18$$

Finally, the optimum bandwidth of the detector is the minimum required to resolve features in the backscatter pattern as small as the pulse width. The bandwidth thus required, in terms of the group velocity of light in the fibre, $v_g = c/n$ where n is the effective refractive index and c the speed of light in a vacuum, is:

$$B = \frac{v_g}{\Lambda}. \qquad 4.2.19$$

Substituting into 4.2.18 the unity-SNR range in terms of system parameters is:

$$z_{SNR=1} = \frac{-1}{2\alpha} \ln\left\{ \frac{2}{rP_{Launch}\alpha_S S} \sqrt{\frac{\Lambda^3}{v_g} \frac{R_F}{4k_B TB}} \right\}. \qquad 4.2.20$$

The range for unity SNR is plotted as functions of pulse power and transimpedance in Figure 4.2.7.

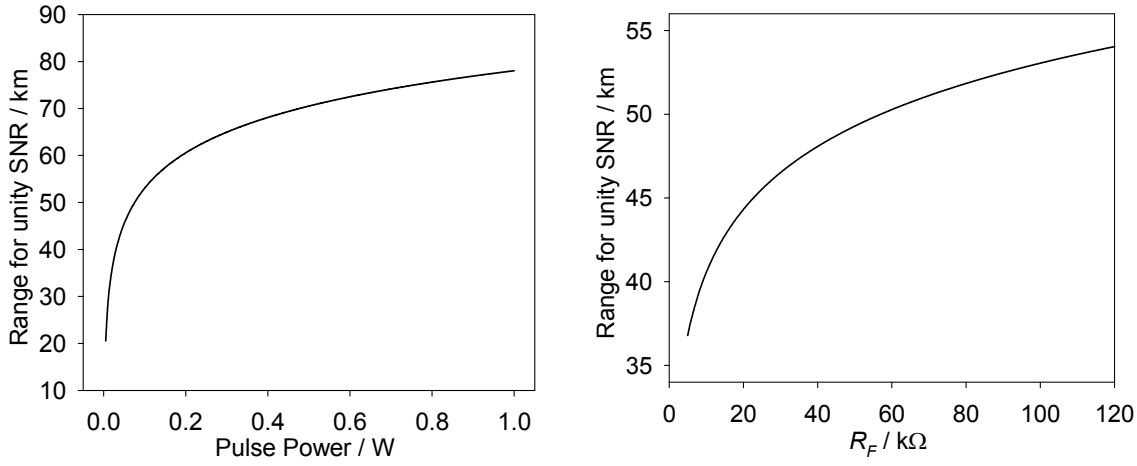

R_F = 100 kΩ $\qquad\qquad$ P_{Launch} = 100 mW

Figure 4.2.7

Theoretical range at which SNR = 1 as a function of pulse power (left) and transimpedance (right) for simple OTDR. In each case the pulse width is 20 m *(100* ns*) and the bandwidth 20* MHz*.*

From this analysis it is found that the maximum operational range can be achieved by maximising the launch power, choosing an efficient photodiode, using the maximum possible transimpedance commensurate with achieving sufficient bandwidth and by

limiting the bandwidth to that required to resolve the chosen spatial resolution as determined by the pulse width. In practice, with current state-of-the-art components, the transimpedance is limited to of the order 100 kΩ by the need to maintain bandwidth, and a small pulse width is frequently desirable to achieve fine spatial resolution. The pulse power can be increased within the limits of the source and, to obtain higher power levels, the pulse can be amplified by means of an optical-fibre amplifier. The analysis above confirms the intuitive result that increasing the pulse power should improve the range indefinitely, however, as will be discussed in Chapter 6, this is not necessarily the case: above certain power levels (~100 mW - 1 W, depending on fibre length) non-linear effects begin to degrade the performance, effectively setting a maximum operational range that can be achieved by limiting the backscattered power, limiting the achievable SNR.

4.2.4. Noise in Conventional OTDR with Pre-Detection Optical Amplifier

As shown in Figure 4.2.7, the electrical SNR from an OTDR, using a given TIA optical receiver, is limited by the backscattered optical power. The SNR for an OTDR can therefore be increased at long ranges by using an optical amplifier to boost the signal power before the receiver [72], as illustrated schematically in Figure 4.2.8.

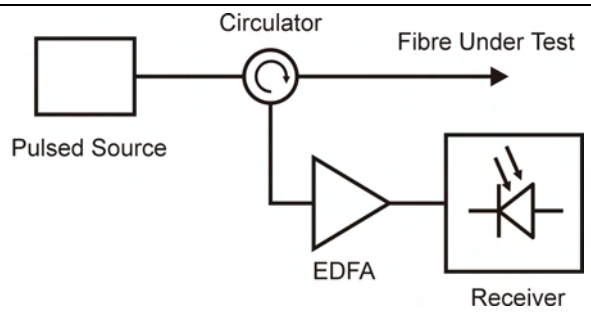

Figure 4.2.8

Simple OTDR with optical pre-amplifier

There are a number of types of optical amplifier, of particular interest here is the Erbium-doped fibre amplifier (EDFA), illustrated in Figure 4.2.9. The absorption of pump light raises electrons into the fast decaying state, E_3, from which they decay, rapidly, into the meta-stable state E_2. A signal photon absorbed by an excited erbium ion can cause an electron in E_2 to fall into the E_1 state, re-emitting the incident photon and stimulating the emission of a second photon of identical energy and phase, thus giving gain. Electrons can also move from E_2 to E_1 spontaneously, emitting photons

which are then amplified – creating amplified spontaneous emission (ASE) noise. It is this that limits the noise performance of the EDFA.

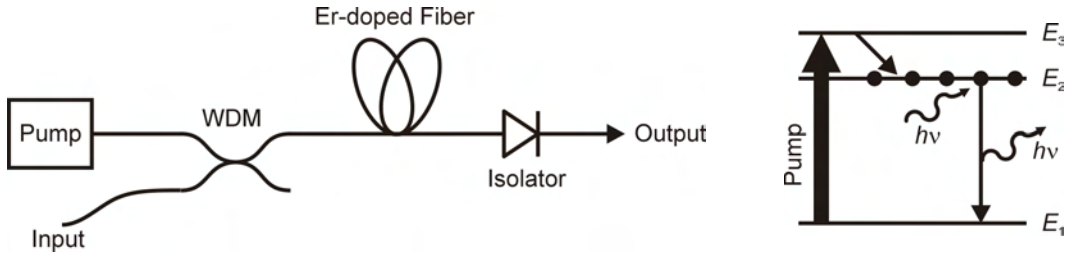

Figure 4.2.9

Configuration of a simple, forward-pumped Erbium-doped fibre amplifier. The pump light, usually at 980 nm *raises electrons into the short-lived state E_3 from which they rapidly fall to the metastable state, E_2, by a radiationless transition, generating a phonon. Decay from the metastable state can be either spontaneous, or stimulated (illustrated) where an incident photon triggers the decay leading to the emission of a second identical photon – thus giving optical gain.*

The optical output of an EDFA can be described as [73]:

$$P_{Out} = GP_S + (G-1)n_{spon}m_t h\upsilon\Delta\nu_f , \qquad 4.2.21$$

where P_S is the input signal power, G is the gain, m_t is the number of polarisation states which are detected: i.e. 1 where the receiver is restricted to a single, linear, polarisation and 2 where light of any polarisation is detected, $\Delta\nu_F$ is the optical bandwidth (normally defined by an optical filter) and n_{spon} is the population inversion factor:

$$n_{spon} = \frac{N_2}{N_2 - N_1}, \qquad 4.2.22$$

where N_1 and N_2 are the numbers of electrons in energy levels E_1 and E_2 respectively.

The first term in 4.2.21 is the amplified signal and the second is the ASE. It is therefore desirable to minimise n_{spon} to improve the noise performance. $n_{spon} = 0$ could be achieved with $N_2 = 0$, however this would leave the amplifier without gain, as the meta-stable excited state, E_2, would be empty. It is more appropriate, therefore, to attempt to maximise the denominator of 4.2.22 by allowing $N_1 = 0$ giving $n_{spon} = 1$, in other words every Erbium ion is in an excited state. Theoretical analysis suggests that this limit can be achieved by strong pumping at 980 nm, giving full population inversion along the whole length of erbium-doped fibre [74]. This has been approached

practically with Yamada *et al.* [75] reporting $n_{spon} = 1.05$ and Laming and Payne [76] measuring $n_{spon} = 0.99 \pm 0.09$ for small input powers. Typically, commercial EDFA modules achieve values in the region $n_{spon} =$ 1.1 to 1.4 (Derived from noise-figure values in Table 5.2 of [77]).

The calculation of the SNR at the output of an EDFA is covered in a number of references [73, 77-79]. In addition to the usual thermal and shot noises in the optical detector, there are contributions from the ASE in the EDFA. The magnitude of the ASE contribution is determined by the EDFA gain, the bandwidth of the optical filter and the electronic bandwidth. There are two components to the electrical noise due to ASE: Signal-ASE beat, where the signal light mixes with the ASE to generate amplitude noise within the electronic pass-band; and ASE-ASE beat where two components of ASE light combine to produce amplitude noise within the electronic bandwidth.

It can be shown [73] that the electrical SNR at the receiver output is:

$$SNR = \frac{P_S^2 r^2}{\underbrace{4r^2 P_S P_{ASE} \frac{B}{\Delta\nu_f}}_{\text{ASE - SIGNAL}} + \underbrace{r^2 P_{ASE}^2 \left(2 - \frac{B}{\Delta\nu_f}\right) \frac{B}{\Delta\nu_f}}_{\text{ASE – ASE}} + \underbrace{2er\left(\frac{1}{G}\{P_S + P_{ASE}\}\right)B}_{\text{SHOT}} + \underbrace{\frac{4k_B TB}{G^2 R_F}}_{\text{THERMAL}}} \qquad 4.2.23$$

where P_S is the signal power and P_{ASE} is the input-equivalent ASE power,

$$P_{ASE} = n_{spon} m_t h\upsilon \Delta\nu_f, \qquad 4.2.24$$

the electrical bandwidth is B and, as earlier, the dark current is neglected since its noise contribution is typically small in comparison to the thermal noise in the feedback resistor, R_F. The amplifier gain, G, includes any loss after the amplifier, i.e. an attenuator to prevent saturation of the TIA.

The effect of the EDFA pre-amplifier on the receiver performance is shown in Figure 4.2.10. At low powers, below ~ 0.3 μW, the SNR is improved since the optical power at the detector is sufficient to negate the thermal noise contribution. As the power increases the SNR from the TIA without EDFA exceeds the optically amplified case, since the SNR is limited by the Signal-ASE beat term, which increases linearly with optical power.

So far, the electrical SNR at the receiver output has been considered in isolation, its relation to hardware "downstream" is now considered. The TIA output is likely to be

captured using an analogue-to-digital converter (ADC). As discussed earlier, the conversion process introduces quantisation noise:

$$< v_q^2 >= \frac{V_{\max}^2}{12 \cdot 2^{2q}}, \qquad 4.2.25$$

where V_{max} is the full-scale input of the analogue-to-digital converter (ADC) and q is the effective number of bits. A typical ADC may have a full-scale range of 5 V and 12-bit resolution, giving an RMS quantisation noise of 0.12 μV. To minimise the effect of this quantisation noise, it is desirable for the acquired signal to use the full dynamic range of the ADC.

The graph on the right of Figure 4.2.10 compares the sampled SNR between cases where the signal light passes directly to the TIA before being amplified electrically by a

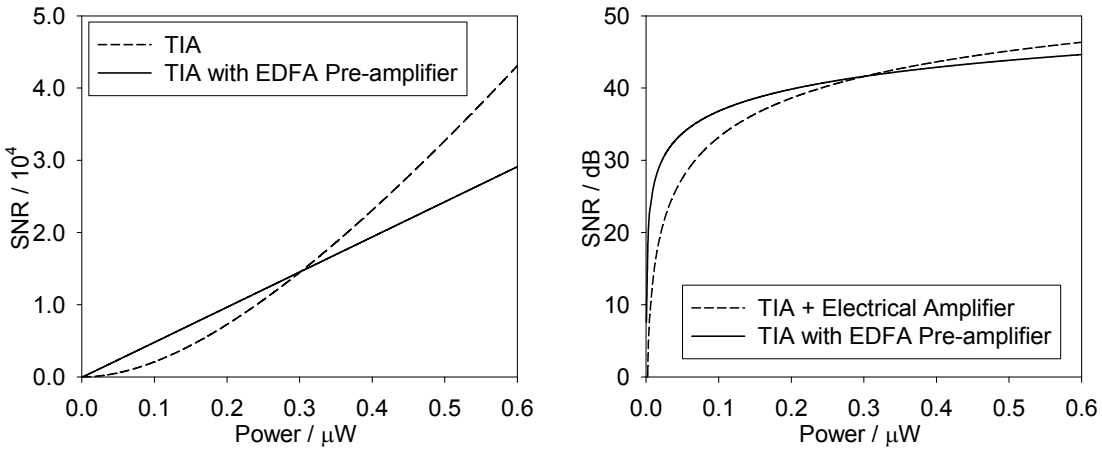

Figure 4.2.10

(left)Electrical SNR at TIA output with and without EDFA pre-amplifier, (right) Comparison of the SNR after sampling with a 12-bit ADC with FSD = 5 V *using a perfect (noiseless) electrical amplifier or an EDFA to give an input of 4.5* V *at 0.2* μW *(the maximum power expected from a 10* m *resolution OTDR with 100* mW *launch power). The benefit of using the EDFA to use the full dynamic range of the ADC is clear at low power levels. In each case the assumed electrical bandwidth is 20* MHz*, the optical filter bandwidth is 12.5* GHz *(0.1* nm*), the transimpedance is 100* kΩ*, the diode responsivity is 0.9* A/W*, n_{spon} = 1, m_t = 2 and the EDFA power gain is 250 (24* dB*) and the electrical voltage gain is 250 (*48 dB*), chosen to use the full scale of the ADC in the power range considered.*

perfect amplifier and where the light is amplified by an EDFA before reaching the TIA, the output of which is sampled directly. In an ideal world the feedback transimpedance would be increased, avoiding the need for amplification, electrical or optical, however this is not normally possible while maintaining the electrical bandwidth required in high-resolution OTDR applications.

To minimise the effect of this quantisation noise, it is desirable for the acquired signal to use the full dynamic range of the ADC. The graph on the right of Figure 4.2.10 compares the sampled SNR between cases where the signal light passes directly to the TIA before being amplified electrically by a perfect amplifier and where the light is amplified by an EDFA before reaching the TIA, the output of which is sampled directly. In an ideal world the feedback transimpedance would be increased, avoiding the need for amplification, electrical or optical, however this is not normally possible while maintaining the electrical bandwidth required in high-resolution OTDR applications.

Finally, as in section 4.2.2, the unity-SNR range is calculated for a simple OTDR where the TIA input is amplified by an EDFA. At low signal powers the noise will be dominated by the ASE-ASE beat and the thermal noise in the feedback transimpedance, allowing us to neglect the other terms in 4.2.23. Thus, at low powers:

$$SNR \approx \frac{P_S^2 r^2}{r^2 P_{ASE}^2 \left(2 - \frac{B}{\Delta\nu_f}\right)\frac{B}{\Delta\nu_f} + \frac{4k_B TB}{G^2 R_F}}, \qquad 4.2.26$$

from which, by putting SNR = 1, and noting that (for all but the most extreme cases) $\frac{B}{\Delta\nu_f} << 1$, it can be obtained that:

$$P_{SNR=1} \approx \sqrt{\frac{2P_{ASE}^2 B}{\Delta\nu_f} + \frac{4k_B TB}{r^2 G^2 R_F}}. \qquad 4.2.27$$

Using 4.2.17 as before, the fibre length at which the SNR is reduced to unity is:

$$z_{SNR=1} = \frac{-1}{2\alpha}\ln\left\{\frac{2}{P_{Launch}\Lambda\alpha_S S}\cdot\left(\frac{2P_{ASE}^2 B}{\Delta\nu_f} + \frac{4k_B TB}{r^2 G^2 R_F}\right)^{\frac{1}{2}}\right\}. \qquad 4.2.28$$

As in section 4.2.2, by writing the required bandwidth in terms of the pulse width, Λ, and group velocity, v_g, we finally obtain:

$$z_{SNR=1} = \frac{-1}{2\alpha} \ln\left\{ \frac{2}{P_{Launch}\alpha_S S} \cdot \sqrt{\frac{v_v}{\Lambda^3}} \cdot \left(\frac{2P_{ASE}^2}{\Delta\nu_f} + \frac{4k_B T}{r^2 G^2 R_F} \right)^{\frac{1}{2}} \right\}, \qquad 4.2.29$$

providing an arbitrary measure of the possible range of operation.

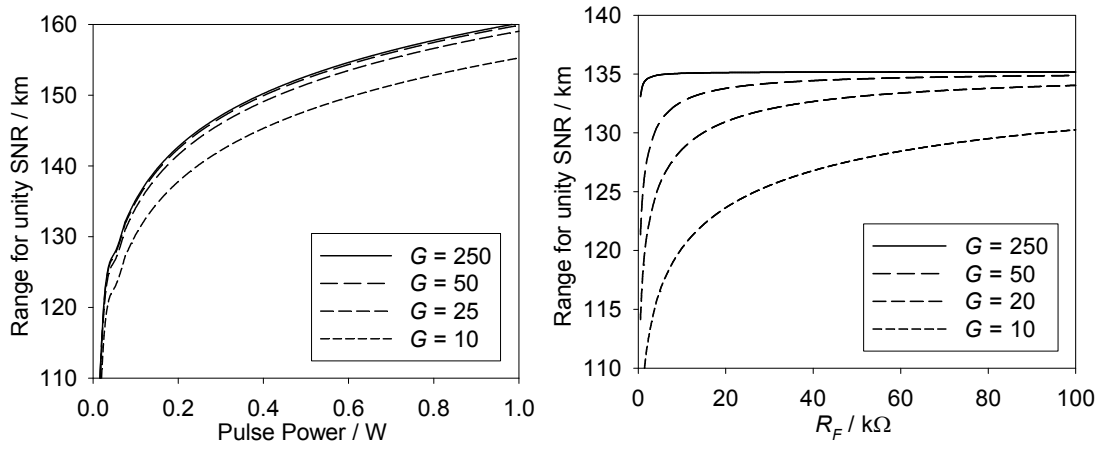

R_F = 100 kΩ P_{Launch} = 100 mW

Figure 4.2.11

Theoretical range at which SNR = 1 as a function of pulse power (left) and transimpedance (right) where the TIA is preceded by an EDFA giving overall gain G. In each case the pulse width is 20 m *(100* ns*) and the bandwidth* 20 MHz

4.2.5. OTDR with Optical Amplification of Launch Pulse

To increase the backscattered power the pulse may be amplified by an EDFA as shown in Figure 4.2.12. For optimum noise performance, the EDFA should be designed to be pumped hard, to obtain near total population inversion. At low duty cycles, as would be expected here, the amplifier is likely to operate in the small-signal regime, giving the same noise characteristics as those discussed for the pre-amplifier in section 4.2.4 above Generally the source power at the launch EDFA input is likely to be significantly greater than the returned backscatter power, which means that the receiver pre-amplifier will dominate the noise performance of the overall system.

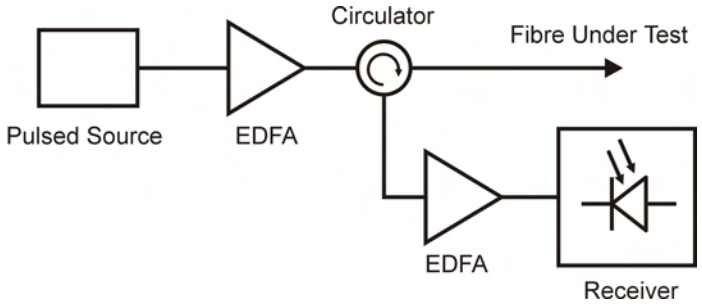

Figure 4.2.12

Simplified OTDR layout with EDFA to increase the launch power in addition to an EDFA pre-amplifier to increase the optical power at the receiver.

4.3. Example OTDR Calculation

To clarify the points made in the previous analysis, the results are applied to an example system, as shown in Figure 4.3.1. The figure shows an OTDR with amplification of the launch pulse and of the backscatter before detection. The backscattered power is calculated assuming a pulse width of 20 m and typical attenuations and gains are indicated where these are significant. Except for these losses the passive components are all considered to be ideal: i.e. the AOMs have infinite extinction ratio and infinitely small rise/fall time and the circulators give infinite isolation. The pre-detection EDFA is considered to contain the required attenuation to reduce the net gain to 10 dB, but is otherwise considered to be identical to the launch amplifier.

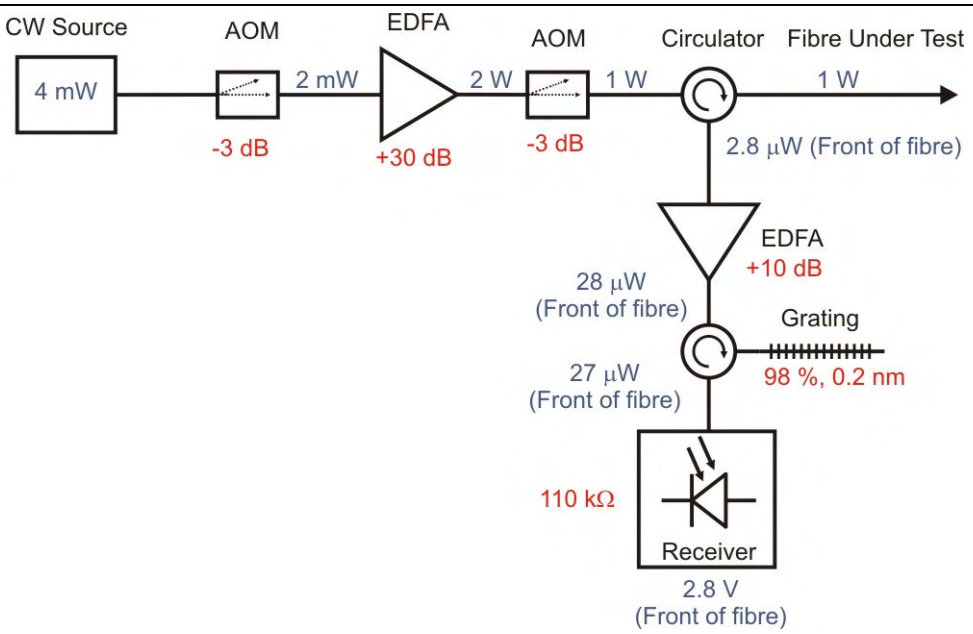

Figure 4.3.1

Example of OTDR analysis with realistic values for analysis. The negligible losses in the circulators (typically ~0.1 dB*) and splice losses (typically ~0.1* dB*) are ignored in the power analysis. The pulse width for the backscatter analysis is 20* m.

The backscattered power from the front of the fibre can be calculated from 4.2.17 to be 2.8 μW. This is approximately 3 orders of magnitude smaller than the power of the pulse at the input of the launch amplifier. Thus the pre-detection amplifier will cause significantly more degradation of the SNR than the ASE from the launch EDFA, justifying the assertion in the previous section that the contribution from the launch EDFA could be neglected.

The SNR at the receiver can be calculated using 4.2.23. The ASE-Signal beat is the largest contribution, with ASE-ASE beat and shot noise being 2 orders of magnitude smaller, even at 40 km. Having found the receiver SNR, it is simple to apply 4.1.4 to find the audio SNR. Assuming the fibre length is 40 km, and ignoring the small delay required to prevent overlap of the pulse with the backscatter from the far end of the fibre, the maximum sample rate is 2.5 kHz, which is assumed to be the rate used. If the signal of interest has components up to 500 Hz and B_{Audio} is set to that value, then the improvement through over-sampling is a factor of 2.5 or 4 dB. The resulting SNR is plotted in Figure 4.3.2.

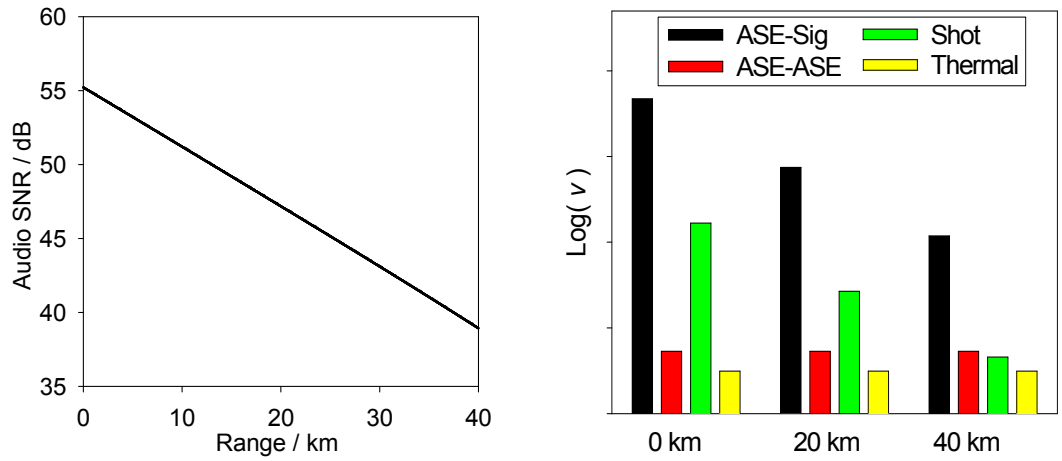

Figure 4.3.2

Left: Audio SNR as a function of range. The audio SNR is increased by 4 dB *relative to the receiver SNR by over-sampling and filtering to* B_{Audio}. *Right: Relative contributions of the different sources of receiver noise (note log scale).*

The average SNR reduction over the 20 km length is 0.41 dB / km, which is less than the signal degradation of 0.8 dB / km. To understand the degradation of the SNR it is necessary to consider the effect of the dominant noise sources: ASE-ASE beat and Signal-ASE beat in the pre-detection EDFA. Recalling 4.2.23, the electrical SNR at the receiver output is given by:

$$SNR(P_S) = \frac{P_S^2 r^2}{\underbrace{4r^2 P_S P_{ASE} \frac{B}{\Delta\nu_f}}_{\text{ASE - SIGNAL}} + \underbrace{r^2 P_{ASE}^2 \left(2 - \frac{B}{\Delta\nu_f}\right)\frac{B}{\Delta\nu_f}}_{\text{ASE}-\text{ASE}} + \underbrace{2er\left(\frac{1}{G}\{P_S + P_{ASE}\}\right)B}_{\text{SHOT}} + \underbrace{\frac{4k_B TB}{G^2 R_F}}_{\text{THERMAL}}} \quad . \tag{4.3.1}$$

As shown in Figure 4.3.2 the ASE-related noise sources dominate, so the receiver SNR may be written, to a good approximation as:

$$SNR(P_S) = \frac{P_S^2}{P_S P_{ASE} X + P_{ASE}^2 Y}$$
$$X = \frac{4B}{\Delta\nu_f}; \quad Y = \left(2 - \frac{B}{\Delta\nu_f}\right)\frac{B}{\Delta\nu_f} \qquad 4.3.2$$

Now making the mapping $P_S \rightarrow \frac{1}{2}P_S$, the SNR becomes:

$$SNR(\tfrac{1}{2}P_S) = \frac{P_S^2}{2P_S P_{ASE} X + 4P_{ASE}^2 Y}, \qquad 4.3.3$$

i.e. the SNR is reduced by a factor *less than 4* due to the reduction of the ASE-Signal beat term scaling with the signal power, or in mathematical terms, where the ASE power is the dominant noise source $SNR\left(\frac{P_S}{k}\right) > \frac{1}{k^2}SNR(P_S)$, hence the differing rates of SNR decay observed. The signal magnitude, of course, will still decay at the expected rate due to fibre attenuation.

4.4. Thermal Phase Noise

In the previous parts of this chapter the limitations of the sensor performance due to system-borne noise limiting the signal level which may be observed. In this section the possibility that the performance is in fact limited by the thermal phase noise in the sensor fibre is considered. The results of analysis in the literature are applied to the specific case of the C-OTDR acoustic sensor, discussing the manners in which the thermal phase noise can degrade the performance, and calculating the magnitude and SNR required for these effects to be observable.

4.4.1. Origin and Spectrum of Thermal Phase Noise

At temperatures above absolute zero, the temperature and density of a material undergo statistical fluctuations, leading to fluctuations in the refractive index. In an optical fibre, these fluctuations will change the phase of light propagating along the fibre, giving a fundamental source of noise which can limit sensor performance in certain situations [80]. The noise contribution in sensors and communications has been extensively studied for many sensor architectures using various approximations for the fibre design and different mathematical modelling techniques [61, 80-82]. In general, at frequencies below ~ 1 GHz the thermal phase noise is an order of magnitude larger than the phase noise from density fluctuations, allowing the latter to be neglected.

In order to obtain an approximation of the thermal phase noise contribution to noise in the C-OTDR acoustic sensing system, it is most simple to apply the results of Glenn [80], derived from basic thermodynamics by analogy with thermal noise in electronic systems. In his analysis Glenn assumes that the fibre core is surrounded by a cladding of infinite extent. While later authors [81, 82] take finite fibre dimensions into account, this nicety is of little value for real-world situations where the fibre will be contained within a cable containing many fibres and various packing components, and located in diverse environments from overhead cabling to being buried many metres underground.

Glenn [80] derives the spectral density of the phase noise due to thermal fluctuations, $<\Phi^2>$, in terms of frequency, f, to be:

$$<\Phi^2> \approx 5.23\times10^{-15} F_2(\xi) \quad \text{rad}^2/\text{m}/\text{Hz}$$
$$F_2 = \frac{\sqrt{2}}{4}\xi^{-\frac{2}{3}}; \quad \xi = \left(60.9\times10^{-6}\right) f \qquad 4.4.1$$

Substituting, this reduces to:

$$< \Phi^2 > \approx \left(3.90 \times 10^{-9}\right) f^{-\frac{3}{2}} \quad \text{rad}^2 / \text{m} / \text{Hz} . \qquad 4.4.2$$

This clearly becomes infinite as the frequency approaches zero, which cannot occur in reality, this is due to the approximations used in the derivation. Using an alternative method Glenn calculates the value at $f = 0$ to be $\left(1.58 \times 10^{-14}\right)$ rad^2 / m / Hz [80]. The overall spectral density is therefore approximated as shown in Figure 4.4.1. Below the "corner frequency" where 4.4.2 becomes equal to the low-frequency value, f_{Corner} = 3.9 kHz, the spectral density is considered to be constant at the $f = 0$ value, and at higher frequencies the frequency-dependent value calculated from 4.4.2 is used.

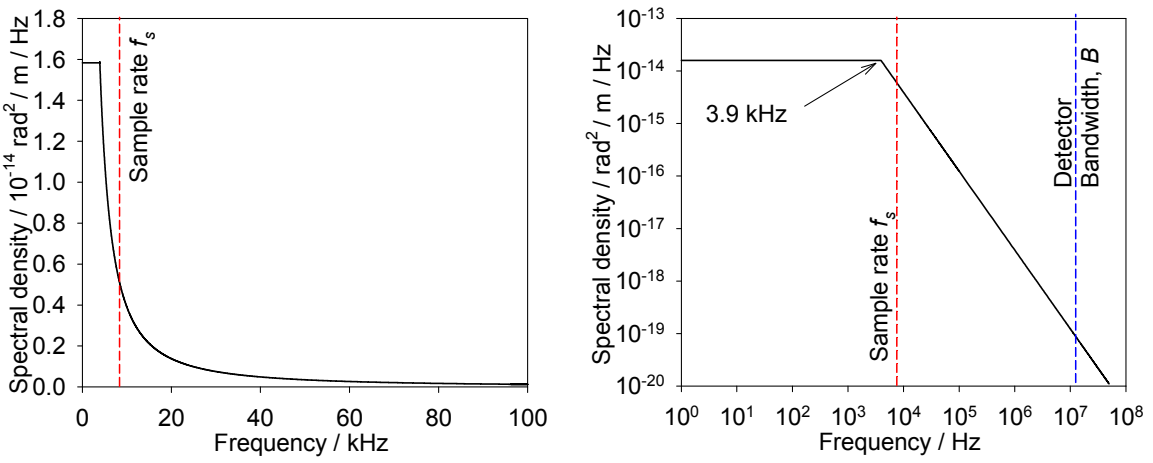

Figure 4.4.1

Thermal phase noise spectral density as a function of frequency in the approximation used in the analysis. The linear plot on the left shows the rapid fall off with increasing frequency, while the Log-Log plot on the right shows the relation between the thermal phase noise spectrum and typical values of the sample rate and detector bandwidth.

4.4.2. Effect of Thermal Phase Noise on C-OTDR

There are three mechanisms by which thermal phase noise can add noise to the C-OTDR signal; these are illustrated in Figure 4.4.2. The first is where different parts of the pulse, experiencing different phase delays as the pulse propagates to the region of interest, generate an apparent phase signal in the region being interrogated. The second is thermal noise generating a phase signal through fluctuations in the fibre within the spatial resolution bin being monitored. The third mechanism is where the change in optical path length, due to the thermal fluctuations of the refractive index, alters the

sampling point from pulse to pulse, generating amplitude noise on the audio signal as the sample point moves along the coherent backscatter interference pattern.

Consider the component of noise arising from the propagation of the pulse along the fibre. It is only necessary to consider the outward propagation since in the return path; any components that will interfere with each other will cover the same fibre

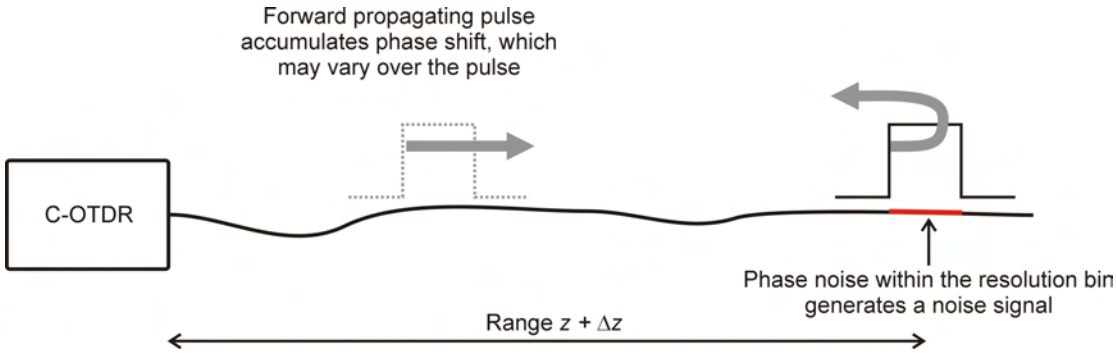

Figure 4.4.2

Effect of thermal phase noise on pulse during propagation. As the pulse propagates along the fibre rapid thermal fluctuations will cause a phase shift which varies across the pulse width, thermal phase fluctuations within the resolution bin (coloured red) generate phase noise which adds to any real signal and fluctuations in the optical path length may change the physical sampling location, giving amplitude noise on the acoustic signal.

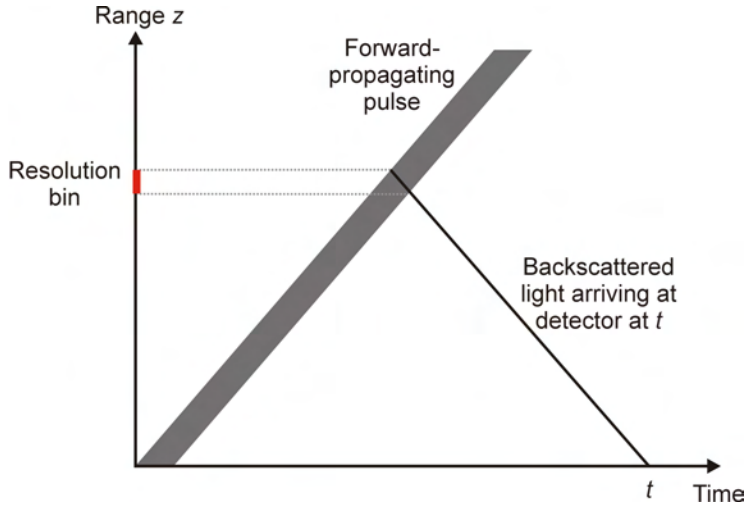

Figure 4.4.3

Propagation of pulse and backscatter along optical fibre. The diagram shows that all light interfering simultaneously at the detector can only accumulate phase noise on the outward journey.

simultaneously, shown graphically in Figure 4.4.3. Furthermore, to add noise to the phase measurement at the resolution bin of interest, during the outward journey the refractive index at a point must change significantly between the moments when leading and trailing edges of the pulse pass that point. This effectively excludes frequencies below the reciprocal of the pulse-width, $1/\Lambda$, which for an optimised design will correspond to the detector bandwidth, B. Therefore, since this noise falls outside the detector bandwidth, no contribution occurs due to accumulated thermal noise as the range increases. This is not the case in CW interferometric systems, which may have a gauge length of several tens of kilometres, where the thermal phase noise builds with total length and limits the overall performance [61, 80, 81, 83].

Now consider the thermal noise of the resolution bin at the point of sampling. The phase noise spectrum "seen" by the receiver is shown on the left in Figure 4.4.4. If the sampling frequency is f_s any frequency components above $\frac{1}{2} f_s$ will alias as shown in the figure.

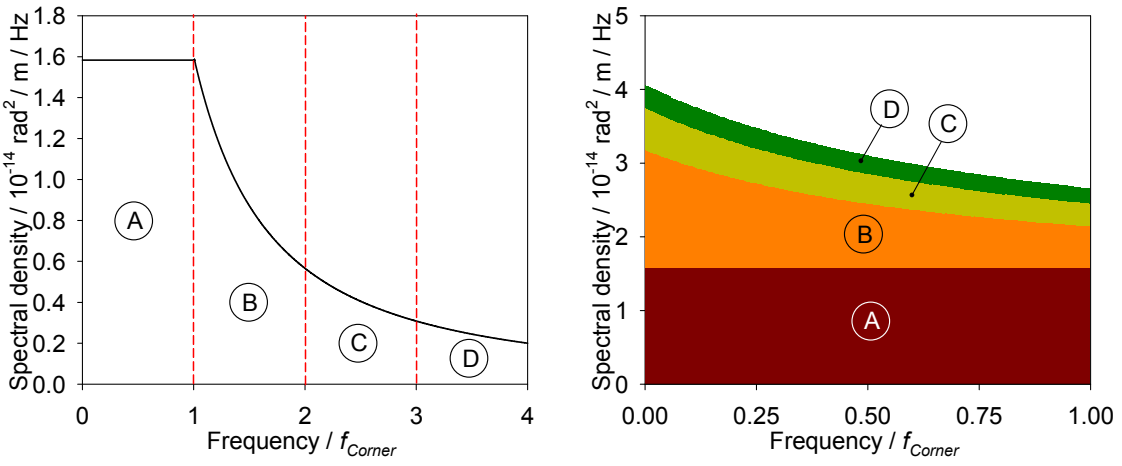

Full-bandwidth spectrum *Spectrum after sampling at $2f_{Corner}$*

Figure 4.4.4

Aliasing of thermal phase noise where the sampling frequency is twice the noise corner frequency, 3.9 kHz*, corresponding to a maximum fibre length of approximately 13* km*. Faster sampling will give a more rapid fall-off with increasing frequency, while for slower sampling the low-frequency spectral density will be increased due to folding of the energy from **A** into the base-band.*

For simplicity, the analysis is for the specific case where the sample rate is 7.8 kHz, i.e. twice the corner frequency of the thermal phase noise, corresponding to a

fibre length of approximately 13 km. The contribution from the section labelled **A** is a constant $\left(1.58\times10^{-14}\right)$ rad^2 / m / Hz. The contribution to the noise spectrum from **B** is:

$$\left(3.90\times10^{-9}\right)\left(f+\tfrac{1}{2}f_s\right)^{-\frac{3}{2}} \quad \text{rad}^2/\text{m}/\text{Hz}, \tag{4.4.3}$$

and from **C**:

$$\left(3.90\times10^{-9}\right)\left(f+f_s\right)^{-\frac{3}{2}} \quad \text{rad}^2/\text{m}/\text{Hz}. \tag{4.4.4}$$

In general, the n^{th} alias contributes:

$$\left(3.90\times10^{-9}\right)\left(f+\tfrac{n}{2}f_s\right)^{-\frac{3}{2}} \quad \text{rad}^2/\text{m}/\text{Hz}. \tag{4.4.5}$$

The total noise spectrum, after sampling, is therefore given by:

$$<\Phi^2_{Samp}>=\left(1.58\times10^{-14}\right)+\left(3.90\times10^{-9}\right)\sum_{n=1}^{2B/f_s}\left\{\left(f+\tfrac{1}{2}nf_s\right)^{-\frac{3}{2}}\right\} \quad \text{rad}^2/\text{m}/\text{Hz}, \tag{4.4.6}$$

where the upper limit $2B/f_s$ is rounded to the nearest integer, with little loss of generality since $B >> f_s$. The first four terms in this equation are plotted in Figure 4.4.4, showing the rapid reduction in significance of the later terms of the summation.

The analysis above considers the particular case where the sampling rate is at twice the corner frequency which was chosen for mathematical simplicity. Lower sampling rates give a shallower fall-off with increasing frequency as the constant contribution below the corner frequency aliases into the signal band, while higher sampling rates give a faster fall-off, particularly above the corner frequency, as the noise spectrum is significantly reduced at the high-end of the base band, meaning any aliased noise is at a lower level. These effects are illustrated in Figure 4.4.5, for sampling at the f_{Corner} and at $4\,f_{Corner}$.

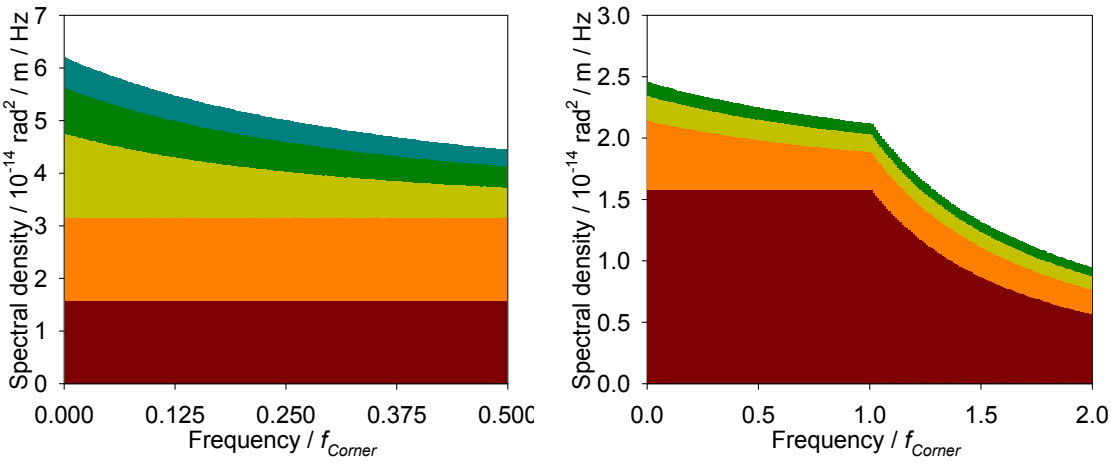

Spectrum after sampling at f_{Corner} *Spectrum after sampling at $4f_{Corner}$*

Figure 4.4.5

Aliasing of thermal phase noise at different sample frequencies, showing the most significant terms in the summation. The shape of the spectrum varies with sample rate due to the folding of the thermal phase noise spectrum into the base-band.

As discussed in Section 4.1, after sampling the signal is low-pass filtered with the cut-off at B_{Audio}. Since, for most applications, $B_{Audio} << f_{Corner}$ the frequency dependence of the spectral density can be ignored and the total noise calculated using the zero-frequency value as the approximate spectral density over the whole audio band. Using the truncated summations as in Figure 4.4.4 and Figure 4.4.5 the total phase noise for a 40 m pulse and 200 Hz audio bandwidth are shown in Figure 4.4.6.

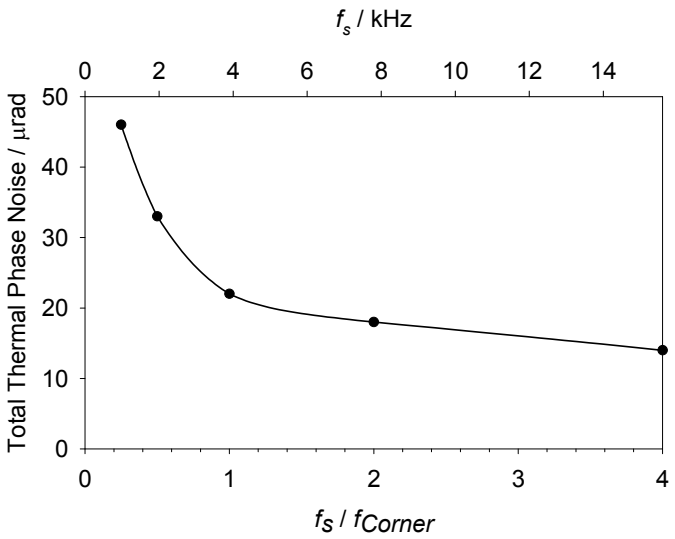

Figure 4.4.6

Graph showing the effect of sample rate, fs, on the total thermal phase noise with a 40 m *pulse after the sampled data is low-pass filtered with a 200* Hz *cut-off frequency.*

The minimum detectable phase change for an interferometer, $d\phi$, can be related to the noise performance of the interrogation optics [61]. The response is a cosine in applied phase: for maximum performance the interferometer will be biased in quadrature, so that for small signals (<< 1 rad) the response is linear. The noise associated with the thermal phase noise can therefore be written, in terms of optical powers:

$$dP = Pd\phi, \tag{4.4.7}$$

where dP is the resulting fluctuation in optical power due to thermal phase noise $d\phi$ and P is the average optical power. The corresponding signal to noise ratio at the receiver output, in terms of the electrical power, is:

$$\frac{P}{dP} = \frac{1}{d\phi}. \tag{4.4.8}$$

For a worst-case thermal phase noise of 50 μrad, the corresponding electrical SNR, assuming that thermal phase noise is the only noise source, is $-20\log\left(50\times10^{-6}\right)$ = 86 dB. In other words, the thermal phase noise from within the resolution bin only becomes an important contribution where the audio SNR is already in excess of approximately 86 dB.

The final mechanism, by which thermal phase noise may create noise on the audio signal, is if the change in optical path length (OPL) due to the refractive index fluctuations cause the sample point, which is at a fixed *time* relative to the launch, to move back and forth along the fibre, generating an amplitude signal as different parts of the coherent backscatter pattern are interrogated. The magnitude of this effect can be estimated by considering the thermal phase noise accumulated over a long length of fibre, integrated over all frequencies:

$$< \phi_{Total}^2 >= \int_0^\infty < \Phi^2 > df = \left(1.58 \times 10^{-14}\right) f_{Corner} + \left(3.90 \times 10^{-9}\right) \int_{f_{Corner}}^\infty f^{-\frac{3}{2}} df \,. \qquad 4.4.9$$

Carrying out the simple integration gives $< \phi_{Total}^2 >= 1.87 \times 10^{-10}$ rad^2 / m.

For a fibre of length 40 km this equates to a RMS phase noise, ϕ_{RMS}, of 2.73 mrad. Since a phase disturbance of 2π represents a change in the OPL of one optical wavelength, the corresponding range uncertainty due to the thermal noise is given by:

$$\Delta z_{RMS} = n\lambda \frac{\phi_{RMS}}{2\pi}, \qquad 4.4.10$$

where n is the refractive index of the core. For light at 1550 nm and a core refractive index of n = 1.44 the range uncertainty is 1 nm. Since the maximum spatial frequency of the coherent backscatter signal is of the order 1 / pulse-width, a range error of the order 1 nm would create a negligible amplitude modulation. Alternatively the error may be considered to be a timing error in the sample aperture, given by the time-of-flight for 1 nm, 5×10^{-18} s; that is many orders of magnitude better than is achieved in practice.

4.4.3. Conclusions

The thermal phase noise generated in the fibre, through which the pulse travels between the point of launch and the resolution bin of interest, does not affect the measured phase signal. The cumulative variation in OPL to the resolution bin is of the order 1 nm, which is insufficient to generate significant amplitude noise, being smaller than the jitter likely in the timing electronics. Finally, the fundamental thermal phase noise within the resolution bin itself is ~ 50 μm for a 40 m pulse, which will only limit the SNR where the audio SNR would otherwise be greater than 86 dB. Audio SNRs > 86 dB are likely to be rare in practice, particularly if an EDFA pre-amplifier is used to obtain long range performance, but limiting front-end performance due to Signal-ASE

beat noise. Furthermore, even if this level of performance could be met, in most conditions environmental noise (acoustic and thermal) is likely to limit practical performance rather than the inherent thermal-phase noise of the fibre.

In conclusion, it is the receiver performance, rather than thermal phase noise in the interrogation fibre, that will limit the sensor performance. This is another advantage of this particular OTDR system over conventional interferometric architectures, where the phase noise is integrated over the whole gauge length and is the dominant noise source in many situations [61]; whereas, in this sensor, the limit is set by the receiver, which must therefore be designed with optimal performance in mind to achieve the full potential of the sensor.

Chapter 5 Initial Field Evaluation

In this chapter the design and construction of a portable sensor for field evaluation purposes is described. A series of field tests designed to test the sensor's response to a variety of stimuli are then reported. Modifications to the optical design to overcome problems identified during these tests are then described. Finally, a series of field tests carried out on deployed telecoms fibre are described, showing the power of the sensor for telecoms cable-protection applications.

5.1. Portable Sensor for Field Trials – FTAS Rev 1

5.1.1. Background

Following the initial investigations using the bench-top experimental system, reported in Chapter 2, a portable sensor system was built (the FTAS Rev 1 demonstration system), to allow field testing of the C-OTDR sensor to investigate its performance in "real world" environments, desirable since the wide range of disturbances and variety of environments encountered by buried fibre are difficult to replicate in the laboratory where the fibre is, be necessity, confined in a small area.

The optics were designed and constructed by the author, as were the majority of the structural components. The sequencer and DDS electronics, along with the sample-and-hold (S&H) boards, were designed by Barry Fleury and other parts were designed and/or built by Dr Stuart Russell and Robert Clarke. The contributions to the major system elements are summarised in the table in Figure 1.5.1.

Item:	Carried out by:
Optics design and construction	JPWH
Control electronics	BF
Power supplies, design and manufacture	JPWH / RJC
RF distribution and switching design and build	RJC / JPWH
Software development	BF (From prior code by ABL and SR)
S&H Board design and manufacture	BF

ABL = Andrew Lewis; BF = Barry Fleury; JPWH = Justin Hayward (Author);
RJC = Robert Clarke; SR = Dr Stuart Russell

Figure 5.1.1

Summary of main contributions to the construction of the FTAS Rev 1 demonstration system.

The unit as initially built, Rev 1.0, was used for extensive testing, after which a number of modifications were made (giving Rev 1.1), before carrying out further testing, including field trials in the USA. The unit was also used for detailed experiments in the laboratory to investigate improvement of the sensor performance with the aim of meeting the requirements set out in Section 1.1.4.

5.1.2. Initial Optical Architecture – Rev 1.0

The optical architecture of the Rev 1.0 demonstration system, which is very similar to that used in the initial experiments described in 1.7, but described here for completeness, is shown in Figure 5.1.2. CW light was generated by a Southampton Photonics HN01 fibre DFB laser, operating at (1550.116 ± 0.050) nm with a specified maximum line-width of 30 kHz, (equivalent to a coherence length of approximately 6 km). The fibre DFB was pumped, using a 975 nm pump diode, giving approximately 90 mW. The source output was measured to be 2.8 mW, indicating pump loss of approximately 3 dB. The source output is pulsed by an AOM (Gooch & Housego M080-2J-F2S) with a specified 10-90 % transition time of 30 ns (0-100 %, 40 ns) and loss of ~3 dB.

The pulse was amplified by a co-pumped EDFA, which was measured to give a small-signal gain of approximately 30 dB and saturated power around 25 mW. With pulsed illumination at ~ 1.4 mW the small-signal gain was achieved for duty cycles below ~0.5 %. A second, identical, AOM allowed the pulse to leave the EDFA while blocking the out-of-pulse ASE. The light was directed to the FUT connector via an optical circulator.

Using the characteristics listed above the pulse power can be estimated to be ~0.7 W, equating to a pulse energy of 0.14 μJ. This was considered satisfactory although, as discussed in the noise analysis of Chapter 4, it was believed that increasing the power would improve the SNR. The possibility of non-linear effects degrading the performance was disregarded since the stimulated scattering processing, Raman and Brillouin, are insignificant for pulse energies below ~3 μJ [35].

The backscattered light was directed by the circulator to an ST connector which could either be connected directly to the receiver or to a second pre-detection EDFA. The pre-detection EDFA was counter-pumped with a measured small-signal gain of 27 dB and the output was filtered using a HiWave FBG (HWT-FBG-1550-95) with 0.34 nm bandwidth. Receiver saturation was avoided by introducing loss between the EDFA and the receiver.

The receiver was a Theoptics TA10, using a 100 μm InGaAs PIN with a 110 kΩ transimpedance amplifier giving a bandwidth of 30 MHz. The receiver output was sampled using the S&H amplifier, designed by Barry Fleury at Radiodetection. The S&H amplifier used an Analog Devices AD783 S&H chip, with a small-signal

bandwidth of 15 MHz, limiting the spatial resolution to ≥ 6.7 m. The S&H device was protected from damage from connector reflections by AC coupling the input and clamping the signal to the power rails with diodes. The S&H device was followed by an active low-pass filter allowing 3 dB bandwidths of 0.5 kHz, 2.0 kHz or 2.7 kHz to be selected using an external switch. An op-amp stage buffered the output and gave 15 dB gain. The output noise was approximately 0.5 μV / √ Hz, small in comparison with the receiver noise.

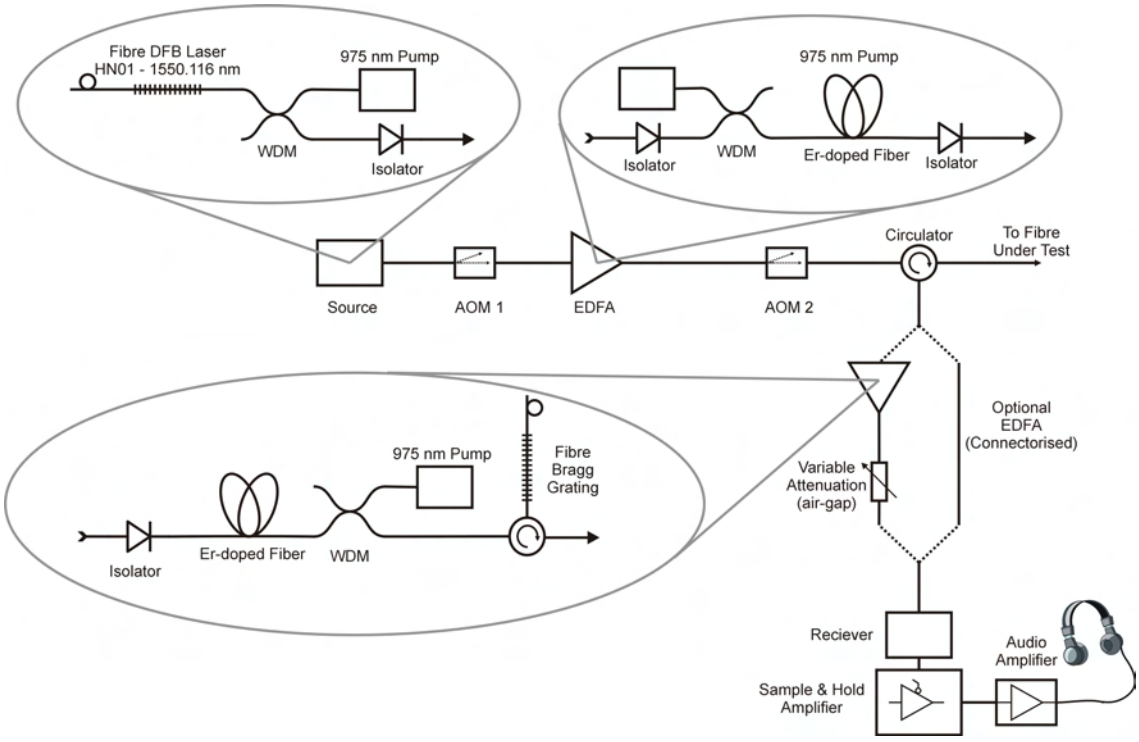

Figure 5.1.2

Optical architecture of the Rev 1.0 demonstration unit. ST connectors on the rear panel allowed the backscattered light to be amplified using the second EDFA or to be routed directly to the receiver. Where the EDFA was used the connector was partially withdrawn to cause loss to allow saturation to be avoided until a variable attenuator was acquired and installed.

5.1.3. Electronic Design

The functions of the control system were to generate RF pulses to drive the AOMs to switch the light from the source and to control the timing of these pulses and to trigger the S&H amplifier.

The author specified the required functionality, summarised by the timing diagram in Figure 5.1.3, and Barry Fleury designed a PCB, containing the components required

to carry out the timing and RF generation functions. The implementation of the electronic control system is shown schematically in Figure 5.1.3. The timing functions were carried out by an FPGA, configurable via the interface with the external PC, which generated pulses to switch the RF drive to the AOMs and to trigger the S&H amplifier.

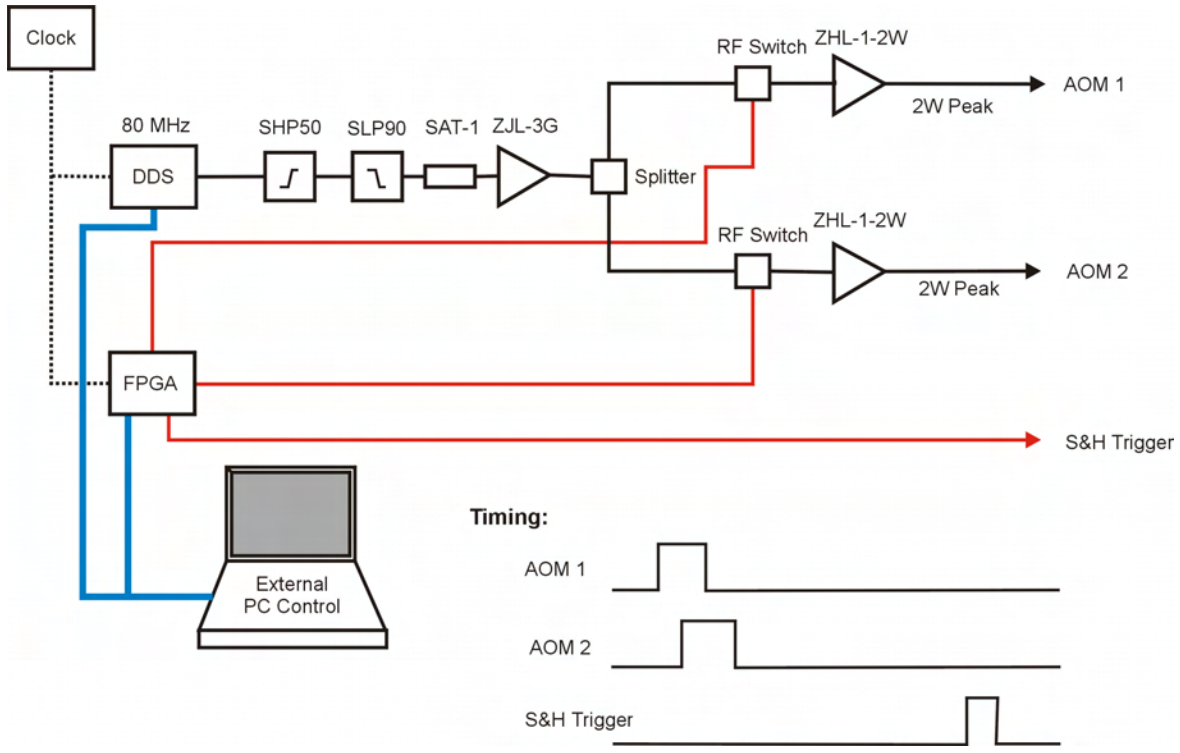

Figure 5.1.3

Control electronics of Rev 1 demonstration system. The FPGA was configured using the external PC to control the timing. The RF, for the AOM drives, was generated using a DDS and manipulated by standard discrete components from Mini-Circuits.

The control pulses generated by the FPGA could be controlled with a resolution of 100 ns and had a minimum width of 100 ns. The jitter on the delay between the AOM 1 pulse, controlling the pulse launch, and the S&H trigger was too small to be measured indicating that it was below 0.1 ns (the accuracy of the Phillips PM6680 timer-counter used for the measurements), and is considered to be several orders of magnitude better.

5.1.4. Packaging

The demonstration unit is shown in Figure 5.1.4. The majority of the optics is contained in the three optics modules comprising the source and two EDFAs, in the white boxes in the front-right of the case. The RF power amplifiers for the AOM drives are mounted on the rear panel allowing local heat-sinking, important since each of the

linear amplifiers generates approximately 10 W of heat which could lead to substantial temperature rise in the box if uncontrolled. The AOMs, detector and S&H boards are mounted on the base on the left-hand side, the rest of the space being filled with power supplies and filtering and the sequencer and DDS board.

Figure 5.1.4

Photograph of the Rev 1.0 demonstration unit, with lid removed. The three optics modules are visible in the front right corner. The RF amplifiers and heat sink are on the right at the rear with the control electronics and power supply filtering on the left-hand side. The fibre leaving the box on the right-hand side is the connection to the FUT which is spliced to avoid connector reflections. The variable attenuator to control the power out of the pre-detection EDFA is visible near the front of the box, between the filter inductors and capacitors on the left and the RF filters on the right.

Considerable care was taken to reduce the system noise as far as possible by taking care in the design of power supplies and avoiding "earth loops". It was found to be particularly important to provide adequate power-supply filtering to the analogue circuits. For critical components, such as the detector and S&H amplifier, totally isolated power supplies were used with "π-section" filters at the supplies and substantial decoupling at the device. Without these measures, the switching noise of the various AC-DC and DC-DC converters used in the power supplies heterodyned together, generating unacceptable levels of audio-frequency noise on the output signal, exceeding that due to the receiver noise.

5.2. Testing in Radiodetection Building

5.2.1. Background

Following the completion of the Rev 1.0 demonstration unit, trials were carried out at Radiodetection's Bristol premises to allow preliminary qualitative evaluation of the system's performance in an environment more akin to those encountered in deployed fibre. The system was used without the pre-detection EDFA as this gave no noise benefit (as discussed in Section 5.4, the EDFA, at this time, was not correctly optimised).

5.2.2. Fibre Layout

Standard 125/9 µm telecoms SMF, with 900 µm coating contained in 3 mm diameter protective jacketing, was routed around the building, passing through a number of separate rooms, as shown Figure 5.2.1. The Rev 1.0 demonstration system was set up in the Control Room, with the audio output passed to headphones and a loud-speaker to allow convenient demonstration to a group. The FUT passed through a number of rooms for different demonstrations, eventually being routed back to the control room to allow the un-used end to be shown in the demonstration, emphasising the need to only access a single end of the fibre.

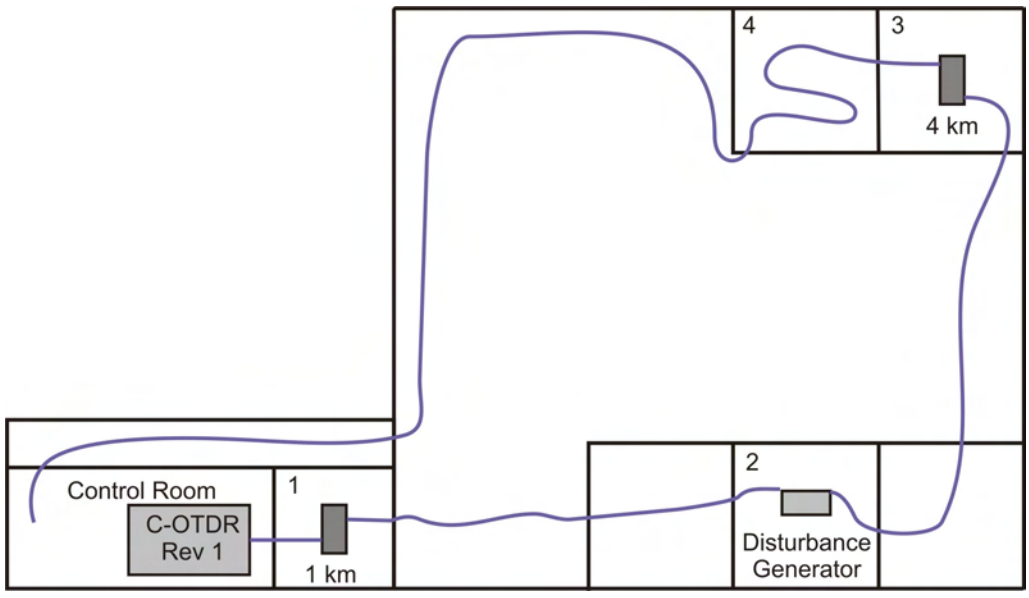

Figure 5.2.1

Schematic fibre layout for evaluation of the Rev 1.0 sensor performance in Radiodetection's Bristol premises.

In Room 1 a 1 km drum of 250 µm acrylate-coated fibre ensured that all farther sections of the fibre were out of the "dead" region caused by the reflection of the pulse from the FUT connector saturating the detector. In Room 2, a length of 250 µm acrylate-coated fibre was routed along a bench, passing over a beam-type disturbance generator, shown in Figure 5.2.2, to apply acoustic–frequency disturbance to the fibre. Room 3 contained a 4 km drum of 250 µm fibre. The jacketed fibre passed through Room 4, being spread over the floor to illustrate possible intrusion sensor applications, before returning to the Control Room, where the fibre end was tied off to prevent unwanted reflections from the fibre end face.

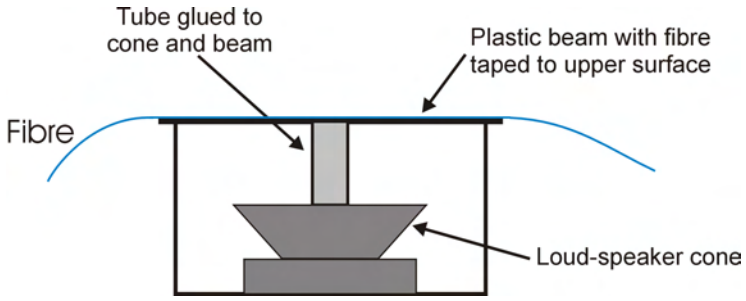

Figure 5.2.2

Disturbance generator using a loud-speaker to deform a plastic beam, with the fibre attached, to apply acoustic-frequency disturbances to the fibre for testing purposes.

5.2.3. Performance evaluation

With the disturbance generator driven by a swept-frequency tone, from ~100 Hz to ~1 kHz, and the S&H amplifier timing set to interrogate Room 2, although barely audible in the room, the decoded audio signal was clearly audible. With a fixed-frequency disturbance applied by the disturbance generator, of sufficiently small size to give a linear response the SNR was measured to be in excess of 40 dB using a PC-based acoustic-frequency spectrum analyser. This result represented an improvement of ~ 10 dB compared to a similar experiment using the bench system, the improvement being gained primarily from reductions in noise in the S&H amplifier and reduction of power supply noise on the analogue electronics.

With no drive applied to the disturbance generator, it was possible to detect intelligible speech from Room 2 when a person spoke loudly near (<1 m) to the disturbance generator. Since this could not be repeated with the disturbance generator removed, it is likely that the speaker cone was acting as a microphone; efficiently

converting the sound to mechanical vibration of the fibre. This shows the potential of the system, as a distributed microphone array, when combined with specifically designed fibre layouts to maximise the mechanical coupling of the sound into the fibre.

The sensitivity to fibre disturbance was demonstrated using the jacketed fibre in room 4 by lightly tapping the outside of the jacket, giving a very strong audible signal, showing the potential of the sensor for intrusion sensing and cable protection applications.

5.3. Testing on Buried Fibre

5.3.1. Background

This section describes a number of tests which were carried out to evaluate the possibility of using the C-OTDR sensor system to relate fibre distances to geographical positions. In addition to gaining a general understanding of the behaviour of the system on buried fibre, we wished to investigate application of the sensor in the scenario where a fibre is damaged by a lightning strike, leaving no evidence of the damage on the surface. The optical distance to the fibre break can be measured using a conventional OTDR, however, locating the geographical position relating to this optical range, relies on the accuracy of the installation records, which often vary from reality by as much a number of kilometres; particularly if other repairs have been carried out and poorly documented. As a result, many hours can be wasted excavating cables to locate the damage: expensive to carry out and costly in terms of lengthy cable down-time.

It was proposed that the C-OTDR acoustic sensor could help solve this problem by using a device to generate an acoustic disturbance at a known physical location, allowing geographic location and optical distance to be related. The system could be used to update records, alongside routine maintenance and, in the event of a failure at an unknown geographic location, rapidly locate the fibre break. The device would be used to generate a disturbance of known characteristics near to the expected geographic location, but closer to the launch end of the fibre, based on the OTDR measurement. The distance from the point of the disturbance to the break can then be measured, allowing the geographic location of the damage to be located, to accuracy of ~10 m, in only a few iterations, hence avoiding the need for extended excavations and reducing cable down-time. To evaluate the feasibility of this proposition, extensive testing was carried out on a cable buried in the garden at Radiodetection's Bristol site, described below.

5.3.2. The Acoustic Signalling Tool

To generate the acoustic disturbance, Barry Fleury built the Acoustic Signalling Tool (AST) - Figure 5.3.1. The device was based on a hammer drill, modified to oscillate a thin rod, approximately 15 mm in diameter, which could be inserted into the ground for good coupling, effectively providing a point source of acoustic-frequency vibration. The motor was powered by two lead-acid batteries, via a power transistor, allowing a potentiometer to adjust the oscillation frequency: optimum performance was

found to be in the range (70 – 90) Hz. The impulsive nature of hammer action meant that a large amount of energy was also present in harmonics of the fundamental frequency – being observable to the 8th harmonic.

Figure 5.3.1

Left: The Acoustic Signalling Tool (AST) Right: Barry Fleury operating the AST in the Radiodetection garden. The grid markers can be seen in the foreground and on the right-hand side.

5.3.3. Experimental Site

The experiments were carried out in the garden at the rear of Radiodetection's R&D facility in Bristol. A fibre cable (standard telecoms SMF with 900 µm diameter coating, within a 3 mm plastic jacket, with Kevlar reinforcing fibres around the fibre) was passed through an existing 100 mm diameter plastic duct, buried at approximately 1 m depth and accessed via two manholes at either end of the 30 m buried length. At the time of the measurements recent rainfall had left the duct at least partially filled with water. The soil at ground level was only slightly moist, dried by warm conditions and sun. The fibre was routed above ground from one of the manholes to the Rev 1.0 demonstration system, located within the building, where it was initially connected to the demonstration system with ST connectors, but was spliced to the FUT connection to avoid problems due to connector reflections of the AOM "ghost" pulses, discussed in the following section. The total fibre length was ~200 m and the loss ~0.2 dB / km.

5.3.4. AOM "Ghost" Pulses

The Rev 1.0 system was initially tested in the laboratory with the FUT spliced to the circulator, performing as expected. However, when the fibre was connectorised and the connection to the FUT was made using ST connectors and a uniter, the performance was degraded and the front few kilometres of the fibre were found to be insensitive, meaning that none of the buried fibre could be interrogated.

Detailed investigation, working with Barry Fleury, showed that this was due to a series of secondary optical "ghost" pulses, of identical width to the intentional pulse, separated by 2.6 μs, with varying power levels, the largest being the eighth at -20 dB relative to the main pulse. Close examination of the optical power and the RF drive to the AOM revealed that, where the ghost pulses occurred an RF signal was also present, but occurring *after* the optical pulse.

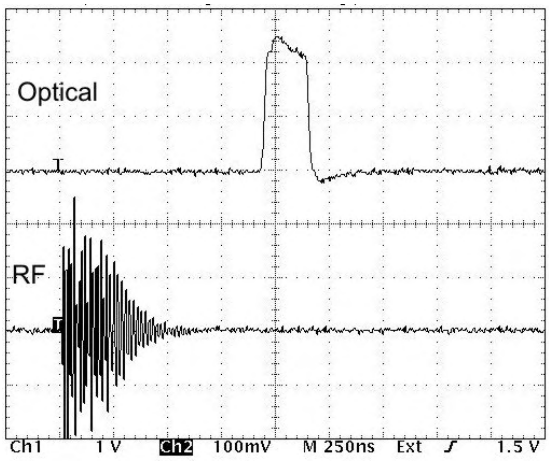

Figure 5.3.2

Oscilloscope trace of the launch pulse (top trace) and the RF (bottom trace) showing the time delay between application of the RF to the AOM and the generation of the optical pulse.

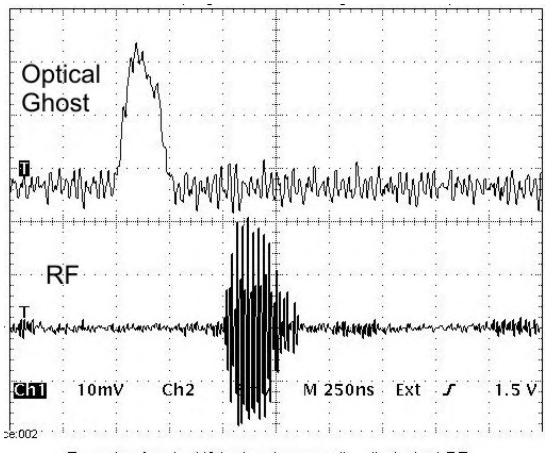

Figure 5.3.3

Oscilloscope trace of the 8th optical "ghost" pulse (top) and the induced RF pulse (bottom) which occurs after the optical pulse, indicating that it is generated by the acoustic reflection.

It was thus concluded, that the ghost pulses were the result of the acoustic wave in the AOM, reflecting from the ends of the active crystal, driving the piezoelectric generating the observed RF signals. A "back of the envelope" calculation, assuming the speed of sound in the Tellurium dioxide (TeO_2) active crystal to be 4000 ms^{-1}, combined with the period of 2.6 μs suggested a crystal size of ~5 mm. Discussions with Gooch & Housego confirmed these suspicions, and subsequently AOMs purchased

were modified, by angling the crystal end-faces in two planes crystals, to ensure that any acoustic reflection was suppressed and did not pass through the optically active area.

For the experiments reported in this section, the problem was overcome by splicing the FUT to the circulator. Following completion of these measurements the FPGA programme was modified to allow the ASE blocking AOM to switch out the 8^{th} ghost pulse – the only one which was significantly larger than the backscatter.

5.3.5. Acoustic Transmission in Soil

The acoustic transmission properties of the ground were investigated by setting the timing such that the 20 m sensitive region was within the buried section of fibre. The centre of the region was located by comparing the response along the buried section and finding the peak and edges. A grid of markers, visible in Figure 5.3.1, was then laid on the grass allowing any location to be quickly related to the sensitive section of the fibre.

For reference, an electrical microphone was pulled into the duct, and located at the centre of the optically sensitive section. The AST was inserted in the soil, directly above the duct, at the centre of the sensitive region, to a depth of (150 ± 20) mm and operated at (91 ± 2) Hz. The signal was analysed by an audio-frequency spectrum analyser and is shown in the top graph of Figure 5.3.4. The harmonics of the fundamental frequency, due to the AST's mode of operation, are clearly visible, as is mains pick-up at 50 Hz, 150 Hz and 200 Hz due to the long length of un-shielded cable.

The signal was then measured using the C-OTDR Rev 1.0 demonstration system, operating with a pulse width of 100 ns (20 m) and a sampling rate of 33 kHz. The pulse power was not measured, but was estimated, using the measured performance of the source and launch EDFA and knowledge of the AOM losses, to be in the range 0.5 W to 1.0W. Assuming the pulse power was 1 W the expected backscattered power from the front end of the fibre is 2.8 μW. The required gain from the EDFA is therefore 7.1 (8.5 dB) in order to give a maximum signal of 2 V at the S&H amplifiers (the maximum without the active filters generating distortion).

The SNR expected at the receiver can therefore be calculated. Assuming that the population inversion is complete in the pre-detection EDFA (which may be an optimistic assumption for a counter-pumped amplifier), the ASE power is 10.8 nW. Using the S&H input bandwidth of 15 MHz, in place of the receiver bandwidth, and transimpedance of 110 kΩ the receiver SNR is 66×10^3 (48 dB), with ASE-Signal beat

dominating. The sample frequency was 33 kHz and the audio filters were set to a cut-off frequency of 500 Hz giving a 15 dB advantage from over-sampling. The expected audio SNR is therefore 63 dB. For a pulse power of 0.5 W the effective EDFA gain can be increased to 14.2 (17 dB) and the audio SNR falls to 60 dB.

The AST was used to generate a (91 ± 2) Hz signal, directly above the cable at the centre of the acoustically sensitive region and at a number of points at varying distances along a line, perpendicular to the cable route (the "latitude"). The AST was inserted to a depth of (150 ± 20) mm in each case, avoiding resting the tip on large stones which would artificially increase the coupling into the soil.

The results are shown in Figure 5.3.4 for latitudes of 0 m, 10 m, 15 m and 20 m. The agreement between the measurement at 0 m latitude and the corresponding measurement with the electronic microphone is excellent, demonstrating the high fidelity of the acoustic signal from the C-OTDR sensor. The background noise level is -70 dBV and, at 0m latitude at the centre of the sensitive region the peak of the fundamental is at -12 dBV, giving an SNR (at 90 Hz) of 58 dB, comparable to the calculated values of between 63 dB and 60 dB, suggesting that the noise background is the noise floor of the C-OTDR sensor, not acoustic background noise in the ground. The measured SNR relates to the specific circumstances during the measurement; however, assuming that the signal amplitude is large enough to generate a phase modulation from fully destructive to fully constructive interference, as is likely to be the case with disturbance close to the fibre, the measured SNR will be the maximum that can be achieved.

The power at the AST fundamental frequency is shown as a function of latitude in Figure 5.3.5. Ignoring the 10 m result, which is anomalous, the attenuation is 1.6 dB / m at measurement frequency of (91 ± 2) Hz. Figure 5.3.6 shows the fall-off per octave with increasing latitude, demonstrating the strong low-pass filtering effect of acoustic transmission in moist soil. This result shows the importance of the lower end of the audio spectrum in the sensor response, particularly where it is desired to observe disturbances situated away from the fibre.

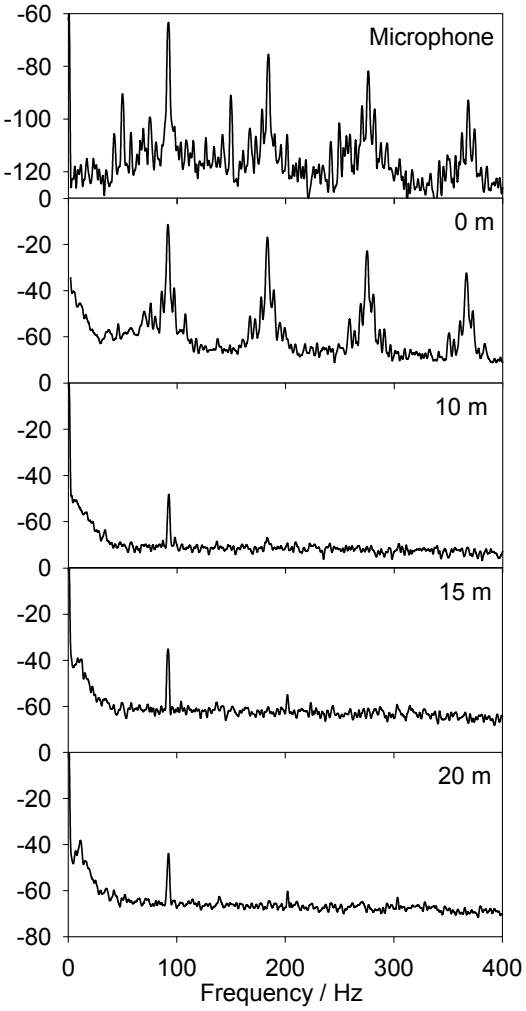

Figure 5.3.4

Spectrum measured by electrical microphone in duct and frequency spectra measured using C-OTDR with the AST located at increasing latitude. The 10 m *result is smaller than expected – suggesting that unusually poor acoustic coupling, or optical "fading" influence the measurement.*

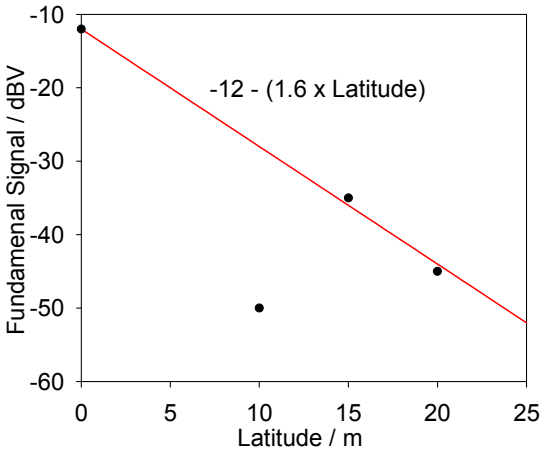

Figure 5.3.5

Attenuation of the fundamental frequency with increasing latitude. Ignoring the anomalous 10 m *result, the acoustic attenuation is 1.6* dB / m *at ~ 90* Hz.

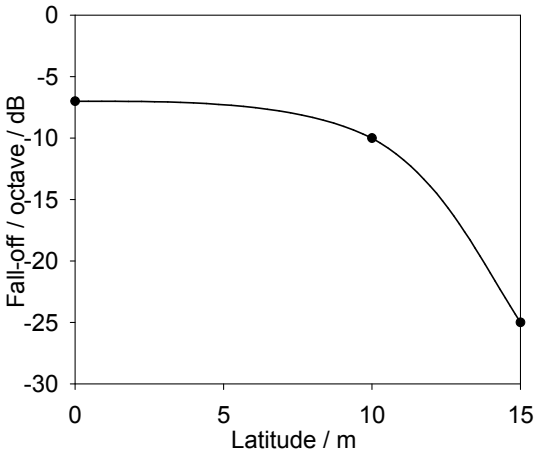

Figure 5.3.6

Low-pass filtering effect of the soil as a function of perpendicular distance from the fibre. The 7 dB / octave *measurement at 0 m latitude describes the spectrum of the disturbance generated by the AST.*

5.3.6. Effect of Buried Artefacts

Further measurements were carried out at a number of locations in order to gain a understanding of how different underground artefacts may affect the acoustic propagation of the AST signal. The AST frequency was reduced to (88 ± 2) Hz to allow operation over a greater fraction of the battery life, with no reduction in the signal size relative to the earlier (91 ± 2) Hz measurements being observed, allowing them to be

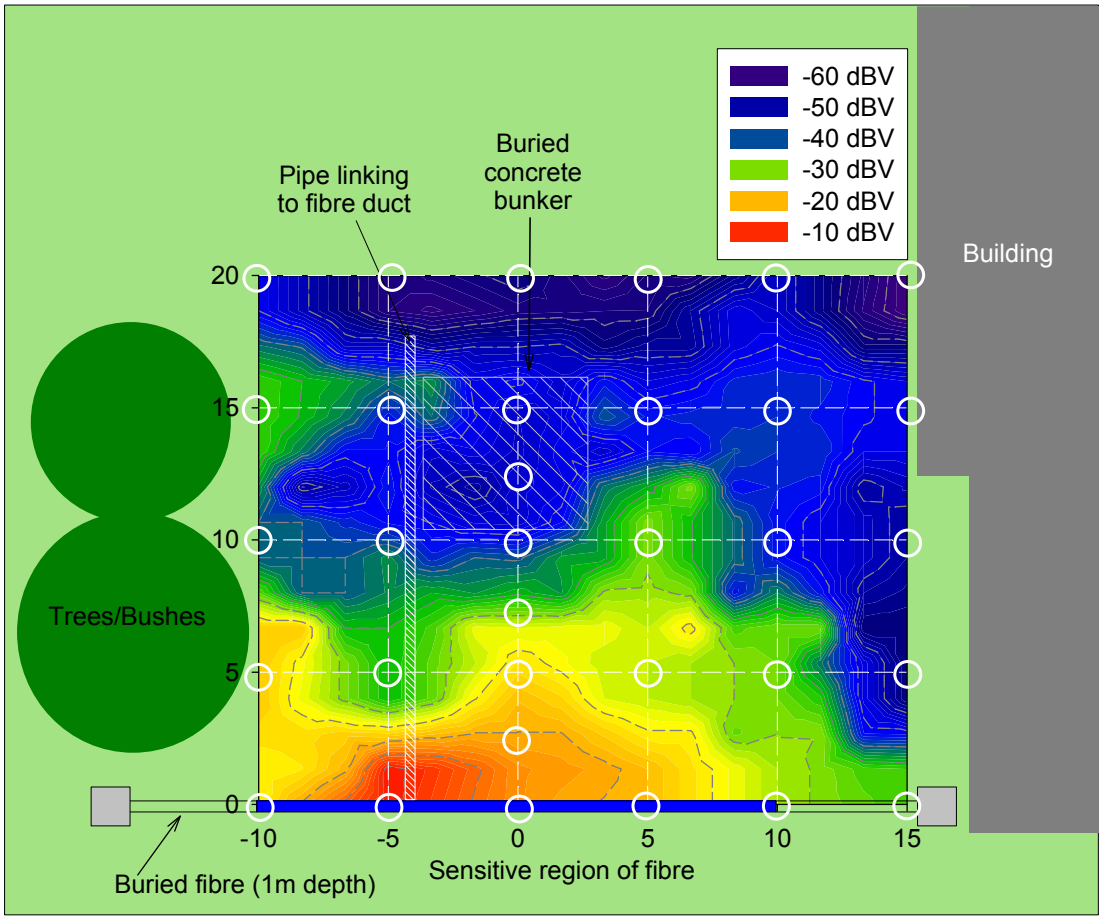

Figure 5.3.7

Results from buried fibre at Radiodetection's Bristol premises showing the variation of signal strength with geographic location of the disturbance. The white circles indicate points where measurements were made, using the AST operating at ~90 Hz *with a rod insertion depth of (150 ± 20)* mm. *The 3* mm *jacketed fibre was contained in a plastic duct approximately 100* mm *diameter buried at a depth of 1* m *as shown. The approximate locations of a second buried pipe and the buried remains of a concrete bunker are shown, along with the main building. The influence of these features on the acoustic signal can be clearly seen in the measured response.*

used in the new data set. As in the previous section, the pulse duration was 100 ns at a sampling rate of 33 kHz.

The results are shown in Figure 5.3.7, with the measurement sites indicated by white circles. Particularly noticeable is the strong coupling at the intersection of the cable duct with the pipe running perpendicular to it and the reduced sensitivity at the location of the buried remains of the concrete bunker, appearing to explain the anomalous result in Figure 5.3.5. The signal strength is also increased at the (-10, 5) sample point, possibly due to roots from the trees increasing the acoustic coupling efficiency.

5.3.7. Conclusions

These preliminary experiments showed that the sensor performed as expected, when operating on buried fibre, obtaining SNRs that were comparable with the theoretical predictions from Chapter 4. When detecting the signal produced with the AST it was found that the terrain, in particular buried artefacts, strongly influences the acoustic coupling to the fibre. For optical-to-geographic mapping applications this may cause problems: for example where a duct carries the acoustic signal along the fibre causing mis-location of a fibre break; however, with suitable precautions these problems should be surmountable, for example by applying a modulation to the acoustic signal and measuring the propagation time from the AST to the fibre. Further experiments carried out in field trials on installed telecommunications fibres (Section 5.5.4 and Chapter 7) confirmed the effectiveness of such a system.

5.4. Revised Optical Architecture – FTAS Rev 1.1

5.4.1. Modifications

During the early testing with the Rev 1.0 demonstration system, it was found that a number of changes were desirable to improve performance. Problems with the AOM operation were identified, requiring a change of architecture to compensate; to attempt to overcome "fading" a polarisation controller was added; to improve the ease of use and stability a variable attenuator was inserted in the pre-detection EDFA path; an additional S&H amplifier was added to allow two points to be interrogated simultaneously; and, while carrying out the modifications, the opportunity was taken to optimise and characterise the two EDFAs. The revised layout, with all the changes incorporated, is shown in Figure 5.4.1.

A problem with the previous architecture was that any significant reflection, from

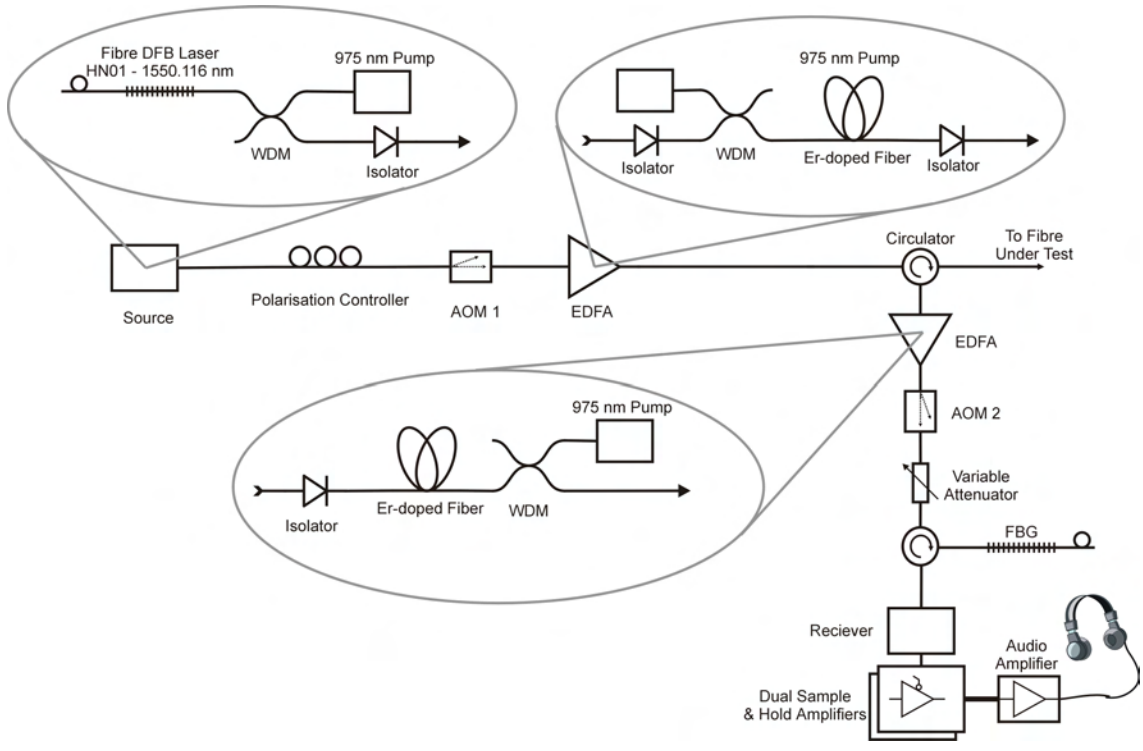

Figure 5.4.1

Optical architecture of the Rev 1.1 demonstration unit. The second AOM is now used to block reflections from connectors or mechanical splices to prevent saturation of the detector, a polarisation controller allows modification of the launch SOP, a variable attenuator allows the optical power reaching the receiver to be controlled, and a second S&H amplifier allows two points to be monitored simultaneously.

imperfect connectors, rotary splices etc, caused the pulse to be reflected at a power level which saturated the receiver, with the resulting recovery time leading to a "dead" spot in the sensitivity. To overcome this, AOM 2 was moved to the location shown in Figure 5.4.1, after the pre-detection EDFA. The FPGA was modified to set the AOM "ON" at all times except where reflections would otherwise saturate the detector, when it was turned "OFF". Having previously confirmed that the EDFA recovery from the pulses was sufficiently rapid to avoid spreading the "dead spot" over many resolution points, the AOM was positioned after the EDFA, along with the variable attenuator, to avoid degrading the EDFA noise performance by reducing the input power.

To allow control over the launch SOP, a General Photonics PolaRITE-II piezoelectric polarisation controller (model PCS-3X-NC-7-C) was incorporated in the launch path, as shown in Figure 5.4.1. A connector was provided on the rear panel to connect an external driver, built by Dr Stuart Russell, which allowed a static SOP to be set manually, or for the SOP to be modulated over the Poincarré sphere [84] at frequencies ~ 1 Hz.

To allow two points to be simultaneously monitored, a spare channel on the FPGA was used to trigger a second S&H amplifier. To allow maximum flexibility, each S&H amplifier had independently selectable cut-off frequencies in the filter stage.

5.4.2. EDFA Characterisation

While re-building the optics, to incorporate the changes discussed in Section 5.4.1, the EDFAs were optimised by varying the length of erbium-doped fibre and characterised. The characterisation apparatus is shown in Figure 5.4.2 and the results are shown in Figure 5.4.3.

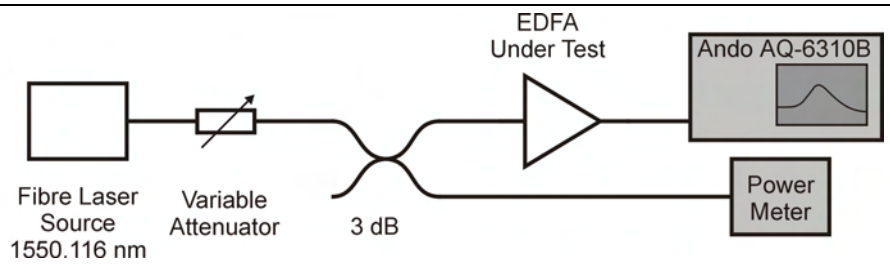

Figure 5.4.2

Characterisation of EDFAs in the Rev 1.1 demonstration unit. The OSA was used to measure the output power so that the ASE contribution to the total optical power could be rejected. The power meter was a Rifocus 555B.

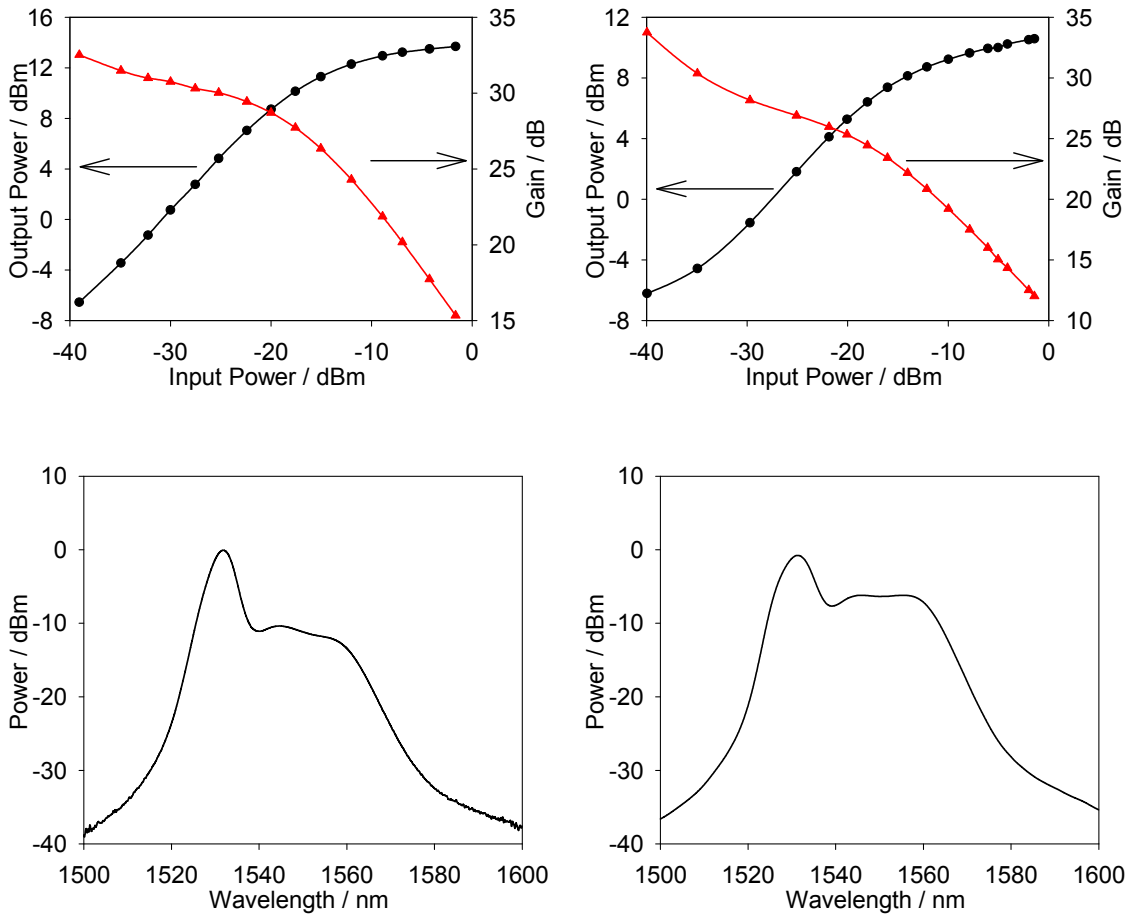

Figure 5.4.3

Top: Gain and output power of FTAS Rev 1.1 demonstration system EDFAs with varying CW input power; and Bottom: ASE spectra with no optical input.

The launch EDFA has a saturated output power [77] of around 14 dBm (25 mW) and small-signal gain of greater than 30 dB. The gain begins to fall more rapidly at around -20 dBm input power indicating the onset of saturation. Assuming the source power reaching the EDFA input is approximately 2 mW, this suggests the amplifier will operate in the small-signal regime for duty cycles of up to 0.5 %. For a 20 m (100 ns) pulse, this is equivalent to a maximum sample rate of 50 kHz, which would only be possible for a fibre shorter than 2 km.

The expected backscattered powers are of the order of -25 dBm, at which powers the pre-detection EDFA gave a gain of 27 dB. At this level the amplifier was still operating in the small-signal regime, ensuring a linear response from the EDFA.

5.5. Field Evaluation of FTAS Rev 1.1

5.5.1. Background

Following on from the trials, described in Sections 5.2 and 5.3, the opportunity arose to test the system in a series of field trials using deployed fibre cable in the USA. The aims were to investigate the system's response to a variety of signals, particularly those relevant to cable-protection applications, in environments typical of installed cables.

5.5.2. Cable Route

The cable route for initial tests was 51.5 km in length. Signals were observed at ranges up to 25 km, although the SNR was lower than desirable and the signal seemed to degrade faster than the expected 0.8 dB / km. The degradation was initially attributed to a number of rotary splices and connectors in the optical path degrading performance through loss and reflection, however, conventional OTDR measurement showed no unexpected attenuation, leaving the rate of degradation for further investigation on return to the ORC. It was therefore decided to disconnect the cable after the connector in the termination building, reducing the total length to 5.0 km, allowing a significant increase in sample rate, with the associated benefit to the audio SNR.

The cable route is shown schematically in Figure 5.5.1. In the control building the optical hardware was located in a quiet room, away from the loud-speakers reproducing the audio signal which caused feedback due to the acoustic sensitivity of the fibre-lasers in the system. The connection to the test cable was using a high-quality ST-ST patch cord. On leaving the control building the fibre passed under a road, just past (Site 1), passing from a depth of approximately 1.2 m at the road edges to around 3.5 m at the centre of the road., The route then passed under a tarmac surfaced car park area where the cable crossed a gas main, roughly perpendicular to the fibre route. Site 2, at an optical distance of 1230 m, was located away from built-up areas, with the fibre buried ~ 1 m deep in 45 mm diameter plastic duct in dry, sandy-clay, soil.

The cable passed under a major road at approximately 3000 m, in a steel duct buried at approximately 6 m at the road edges, reaching around 18 m at the centre below the road surface. The splice losses were measured using an OTDR (Anritsu MW9070B) to be 0.53 dB and 0.03 dB for the fusion and rotary splices respectively, no reflection was observed. The cable then passed around a retail area, passing through a number of man-holes, one of which, Site 3 at 4390 m optical distance, contained

approximately 200 m of coiled cable (provided to allow for repairs). The final part of the route ended at a second building, where the fibre reached a patch panel.

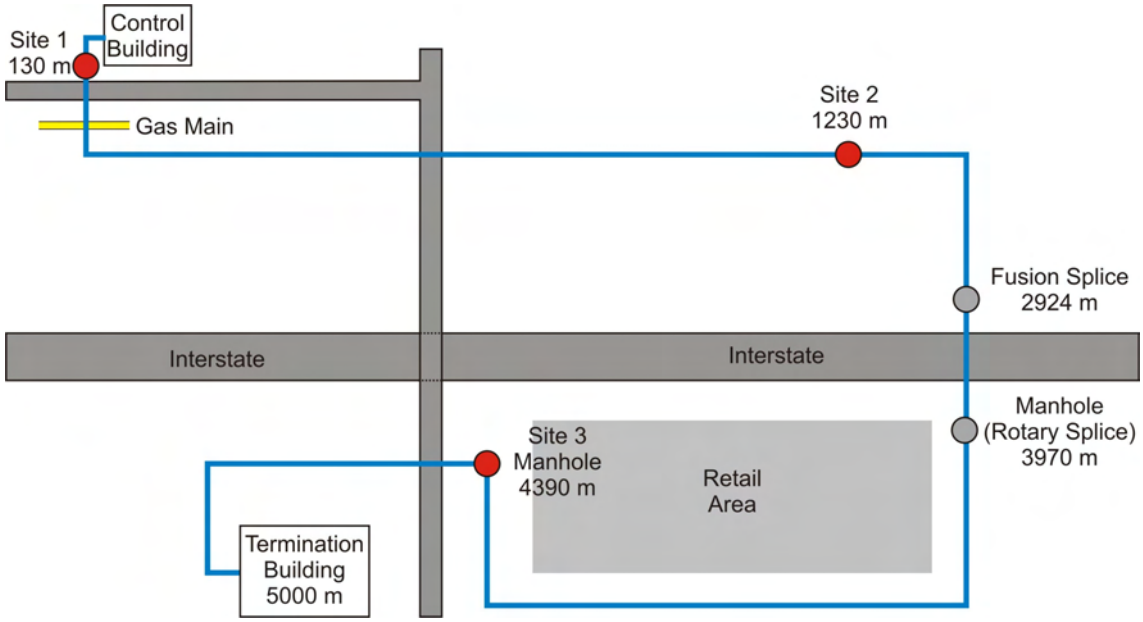

Figure 5.5.1

Schematic cable route for field trials (in blue). The Rev 1.1 demonstration unit was located in the Control building, connected to the cable via an ST patch cord. The test locations are indicated in red along with significant features.

5.5.3. System Parameters and Expected Noise

As in Section 5.3 the launched pulse power was approximately 0.5 W to 1 W, and the pulse length was 20 m, so the SNR expected at the receiver can be calculated. Making the same assumptions as previously and ignoring the effect of scattered ASE from the launch amplifier, the expected receiver SNR for a 1 W pulse is 62×10^3 (48 dB) In this case the sample frequency for the majority of tests was 18 kHz and the audio filters were set to a cut-off frequency of ~ 2 kHz, giving an expected audio SNR at the front of the fibre of 2.3×10^5 (54 dB), lower than in the previous experiments due to the reduced sample rate and increased audio bandwidth. For a 0.5 W pulse, this falls to 52 dB. To give improved performance the audio output was filtered again, using a standard home-audio equaliser, allowing the frequency response to be easily customised for each situation.

5.5.4. AST Tests

The AST (Section 5.3.2) was used to generate a test signal at a variety of locations, giving good SNR in different soil types and when used on hard surfaces, tarmac,

concrete, paving slabs etc, although in these situations the energy reaching the fibre was much reduced due to the reduced coupling from the AST. The optical to geographic mapping principle was demonstrated, by sweeping the sample point bin-by-bin in the region where the signal was expected. Although the AST location could be found in this manner, it could be time consuming on occasions when the installation data was inaccurate – in one case, by in excess of 1 km! To develop the technique for regular use, a more effective method of locating the AST signal would be to filter the data from each location at the AST fundamental and indicate the signal strength at each location, allowing the signal to be located at a glance.

5.5.5. Mechanical Digger Tests

The potential for using the C-OTDR acoustic sensor as a telecommunications fibre protection system was investigated by simulating a typical scenario where cable breakage occurs: unauthorised mechanical excavation. To simulate this occurrence, a test location was chosen (Site 2) and two adjacent resolution bins were monitored in the control building using the two S&H channels. A mechanical digger was driven towards site 2 and instructed to dig immediately adjacent to the cable, which was ~ 1 m deep, in sandy-clay soil, which was moist after recent rainfall.

The approaching digger was clearly audible, causing very large strains as it approached the fibre, causing the interference pattern to pass through many fringes, generating distinctive high-frequency signals. Lowering the digger's out-riggers caused a recognisable "thump" followed by more high-frequency components as they lifted the rear wheels off the ground, redistributing the load pattern on the ground. With the digger positioned above the cable the vibration coupled into the ground due to the engine running could be easily heard and recognised, this was confirmed by switching the engine off and then re-starting, observing the signal fall to the background level whilst the engine was not running and return to the previous level when it was re-started. Finally, the digger began to excavate a trench, immediately adjacent to the cable, giving an audio signal, recognisable as digging, which, again, passed through many interference fringes.

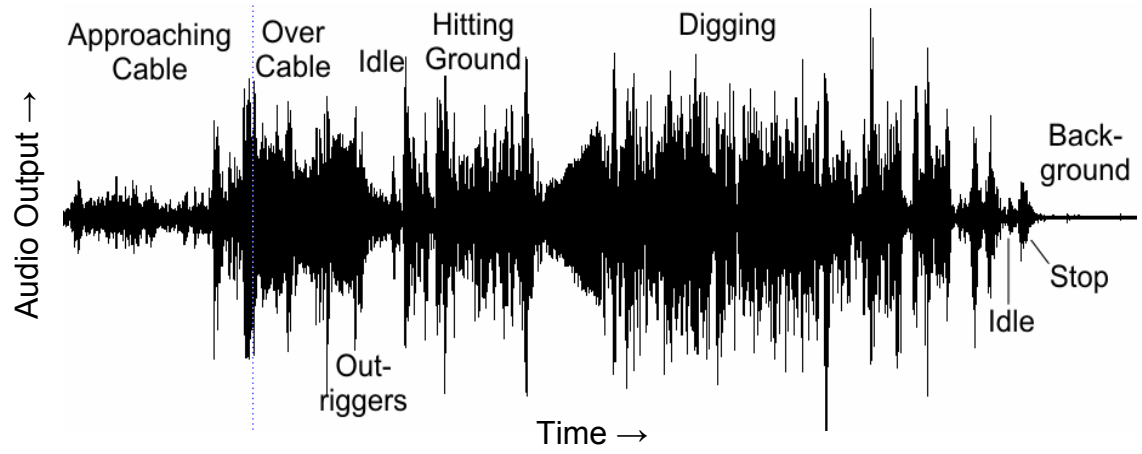

Figure 5.5.2

Audio data recorded from the FTAS Rev 1.1 output. The total elapsed time shown in the plot is 1.5 min. *The changing signals can be seen as the digger approaches the cable, drives above it, lowers the out-riggers before pausing with the engine idling. The operator then hits the ground with the bucket before digging immediately adjacent to the cable. The reduced signal can be seen while the engine idles and the impulse as the engine stops is visible. The low background noise at the end of the trace illustrates the high SNR which was achieved.*

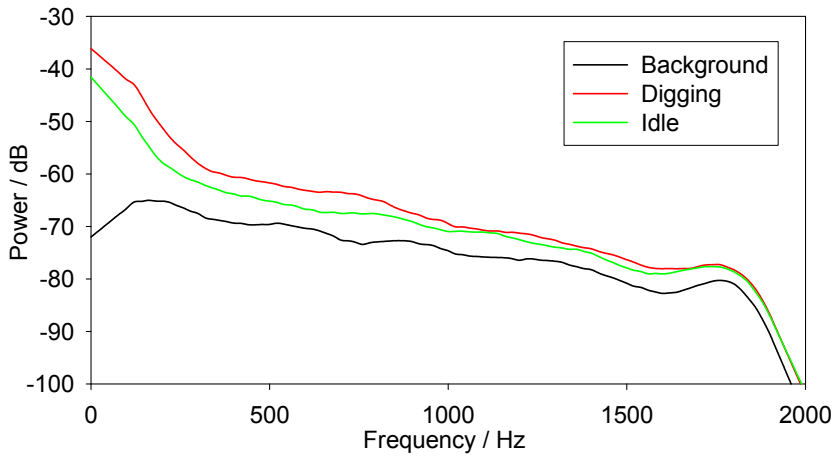

Figure 5.5.3

Audio spectra recorded from FTAS Rev 1.1 output of mechanical digger with engine idling and in process of digging. The audio recording is saturated at the signal peaks; higher powers were present in the recovered audio but could not be recorded with the sound card.

The frequency spectra of the background noise, engine idling and digging are shown in Figure 5.5.3. The background noise includes the fundamental system noise and also the real acoustic noise at the test location, generated by the personnel present at the test site, and vibrations coupled into the ground from surrounding trees and fences etc. The sound card used to record the data also limited the dynamic range that could be recorded.

The RMS power during digging was -8.0 dB (relative to the sound card full-scale input), although the audio data is clipped at its peaks, with SNR, relative to the background noise, of 23.8 dB; although this is limited by the recording equipment – if the signal did not clip in the sound card the SNR could be expected to be > 30 dB, as predicted.

This test demonstrated convincingly that, even with very rudimentary signal processing, the threat of un-authorised excavation could be easily identified, before developing into a significant risk to the cable.

5.5.6. Post-Hole Digger Tests

A second disturbance observed at site 2 was that of a man operating a post-hole digger. Again the audio output was recorded using a lap-top PC via the sound card, limiting the dynamic range of the recording. The RMS signal level from the post-hole digger striking the ground was -7.6 dB (relative to the sound card full scale), with an SNR, relative to the background, of 24.2 dB. The footsteps of the operator were also audible, with an SNR above the background of 6.6 dB. The decoded signal from the post-hole digger, operated above the cable, is shown in Figure 5.5.4. As would be expected the impulse gives broad-band signals extending to high frequencies. The rapid decay of the high-frequency components can be clearly seen in the plot, leaving the lower frequencies at which the ground resonates.

The frequency spectra of these signals are shown in Figure 5.5.5, calculated using an 8192-point FFT using the Adobe Audition software package. The absolute power level is arbitrary, relating to the settings of the sound card used for the recording. The post-hole digger is clearly a larger signal than the footstep, and contains more energy at higher frequencies – as would be expected from the sharp impulse compared to the controlled impact from a typical footstep.

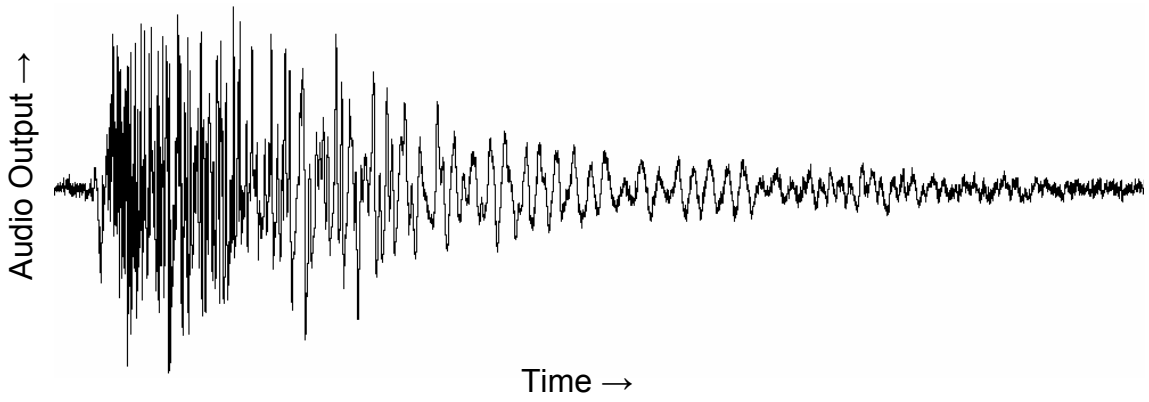

Figure 5.5.4

Audio signal, recoded from the S&H output, of Post-hole digger above the cable, duration 1.5 s. *The rapid decay of the high-frequency components compared to the lower-frequency resonances of the ground is clear in this plot*

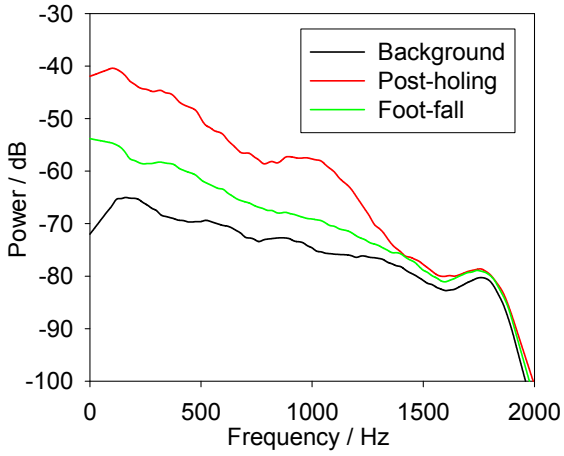

Figure 5.5.5

FTAS Rev 1.1 output audio spectra of post-holing and foot-fall directly above the cable which was buried at a depth of approximately 1 m.

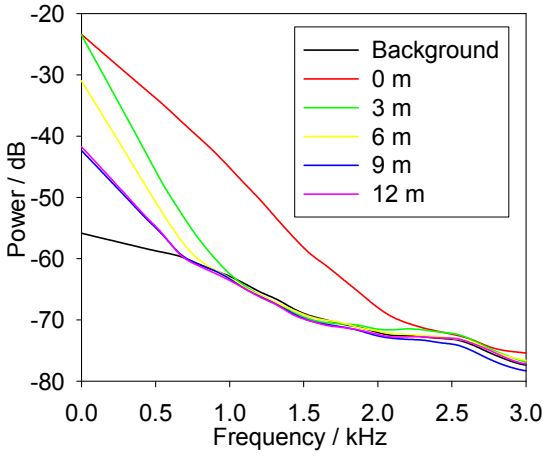

Figure 5.5.6

Audio spectra of post-holing with increasing distance away from the cable route showing the low-pass filtering characteristic of the soil.

To investigate the acoustic propagation properties of the soil the post-holing was repeated, recorded at a higher data rate to observe more of the high-frequency information, above the cable and at various distances perpendicular to the cable route. The spectra of a typical impulse from each is shown in Figure 5.5.6, showing the low-pass filtering effect of the soil, previously observed in the earlier buried-fibre experiments described in Section 5.3. The post-hole digger gave a clear signal at up to

18 m range, however measurements beyond this were not possible since the area was not accessible during the field trials.

The data is shown as a spectrogram in Figure 5.5.7, which clearly shows the rapid attenuation at higher frequencies and the loss of total energy with increasing range. The operator's footsteps can be easily seen between the post-hole digger signals at 0 m and 3 m. It is interesting to note the lack of very-low frequency components in the footsteps, since the energy imparted to the ground is insufficient to cause substantial, low-frequency, displacements, instead causing the ground to vibrate at a characteristic frequency, ~ 100 Hz. The post-hole digger transmits enough energy to the ground to cause significant, semi-permanent deformation, giving the stronger low-frequency components. The impulsive nature of transfer excites the ~100 Hz resonance as well as generating significant high-frequency components > 1 kHz, although these are strongly attenuated as they propagate through the soil.

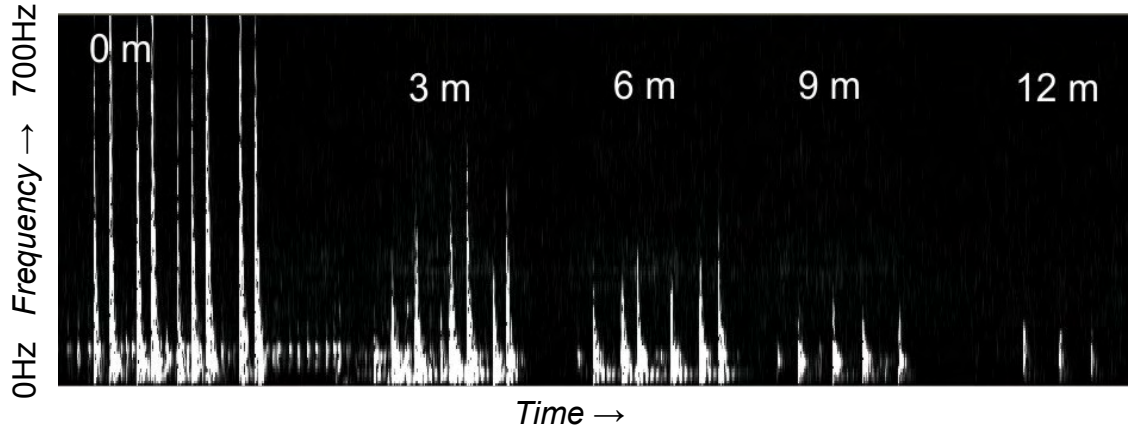

Figure 5.5.7

Spectrogram showing the attenuation and low-pass filtering effect of the ground as the post-hole digger is operated at increasing distances from the cable route. The small signals before the 0 m *digging and between 0* m *and 3* m *are the footsteps of the operator moving between dig locations.*

5.5.7. Fibre Tampering Tests

In addition to the threat from accidental damage, telecommunications networks may be at risk from deliberate damage. Easily accessible sections of cable are particularly vulnerable to this type of threat, for example overhead cables and where the cable passes through manholes. To demonstrate the ease with which such a threat may

be identified a mock intrusion was carried out at the manhole at Site 3 which contained approximately 200 m of coiled fibre.

The C-OTDR audio channels were set to monitor two points within this length and to simulate an attempt to damage the cable, the manhole lid was lifted and dropped to the side and the cable tapped and scuffed using the manhole pulling spike. Each of these actions was clearly audible on each channel, with actions where the cable was contacted giving strong, distinctive signals. Since the time taken to, for example, deliberately cut the cable is very small, it is quite likely that there would be insufficient warning to take preventative actions, however the short warning time may give sufficient notice to re-route important traffic, reducing the impact on network performance as far as possible.

5.5.8. Fading Reduction by Polarisation Control

Polarisation control of the launch pulse was incorporated in the launch path as a measure intended to combat the problem of fading. In the field tests, however, at short ranges the performance was consistent without applying modulation to the SOP. Where regions with apparently reduced sensitivity were encountered, the improvement from adjusting the launch SOP was found to be negligible, suggesting these occurred due to environmental rather than optical effects.

This can be understood based on the theory presented in Chapter 2. Fading occurs when the phase relation of the individual scattering sites is such that the sensitivity is near zero and/or the fibre birefringence is such that the interference of interest is between two orthogonal SOPs, giving no interferometric modulation of the light intensity.

This explanation was confirmed by observing the modulation of the backscatter trace with applied SOP, using an oscilloscope to monitor the backscatter pattern. Changing the launch SOP with the polarisation controller, caused random variation of the amplitude of the various features within the backscatter pattern; however the feature location remained unchanged – showing that the interferometric phase relations are unchanged by modulation of the SOP. Thus, for SOP modulation to reduce fading, the birefringence of one arm of the interferometer must be modulated, which is not practical for a sensor where the interferometer is entirely within the FUT.

5.5.9. Conclusions and Observations

The field trials described above clearly demonstrated the potential power of using the C-OTDR acoustic strain sensor in telecommunications cable protection applications. The sensor was shown to be capable of detecting the strain signals due to mechanical excavation near to the fibre; manual excavation, beyond 12 m away from the fibre; and disturbance of the fibre in a manhole.

The SNRs observed on recorded data were lower than expected from the analysis of Chapter 3 and calculation in Section 5.5.3 and also lower than the SNR observed in section 5.3, even when the reduction due to the reduced sample rate is considered; due to the scattered launch amplifier ASE from the entire fibre. The aims stated in Section 1.1.4 include the ability to operate successfully over an entire link, typically 40 km point-to-point. The SNR at long ranges was not sufficient this trial to achieve this goal, particularly as the signal degradation with range appeared, qualitatively, to be worse than expected based on the reduction of the received backscatter power with range. The relationship between SNR and range was therefore highlighted as required more detailed investigation in the laboratory, with improvement at long ranges required to meet the specification of Section 1.1.4.

The trials of using the AST for geographic-to-optical mapping demonstrated the limitations of locating a signal along the fibre by scanning the sampling point, emphasising the need to develop a more user-friendly interface, allowing information from the whole fibre to be viewed simultaneously, both for fibre protection monitoring and geographical to optical range mapping using the AST.

Chapter 6 Degradation due to Non-Linear Effects

In this chapter formal experiments, showing that the signal reduction with range exceeded the expected rate, are presented and the resulting investigation into the causes of this anomaly is described. Detailed examination of the pulse spectrum at different ranges and powers indicated that non-linear phenomena were responsible for the excess loss, although it was thought that the pulse power was low enough to avoid any non-linear thresholds. A description of the relevant non-linear effects is given and their effect on the C-OTDR sensor discussed. The predictions are then compared with the experimental observations and the critical launch power is derived analytically and compared with experimental results. Finally, the implications for operation in WDM systems are considered. The work in this chapter was carried out primarily by the author - with advice from supervisors.

6.1. Effect of Range and Optical Loss

6.1.1. Background

It was observed during the initial field trials, described in the previous chapter, that the degradation of the sensor performance with optical distance appeared, qualitatively, to be greater than would be expected due to the optical loss alone. Following the field trials, an experiment was devised to test this observation, more quantitatively, by separating the effect of loss from that of the distance propagated along the fibre.

6.1.2. Experimental Method

The experimental arrangement is shown in Figure 6.1.1. The Rev 1.1 demonstration system was used to interrogate a disturbance, created by the usual disturbance generator (described in Chapter 4) operating at 320 Hz to avoid any mains-borne interference at harmonics of 50 Hz, located between drums of 320 m and 700 m of standard 125 µm telecoms SMF with 250 µm acrylate coating. The pulse width was 200 ns (nominally 40 m) and the sampling frequency was 5 kHz. The pre-detection EDFA was used and the variable optical attenuator to prevent detector saturation was not adjusted during the measurements. The demonstration system was connected to the

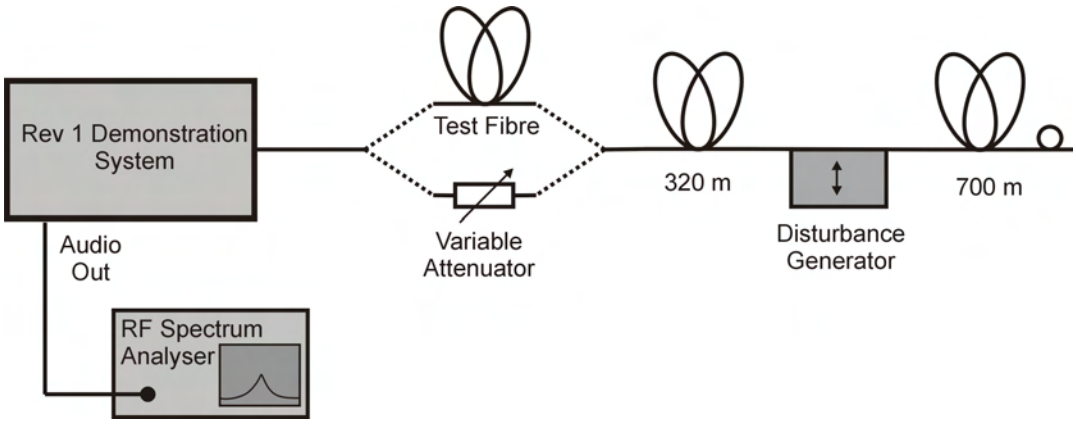

Figure 6.1.1

Experimental arrangement for separating the effect of loss and of optical range on the sensor performance. The Rev 1.0 demonstration system, operating at 40 m *pulse width, at 5* kHz *sample rate, was connected to a fibre, with an acoustic disturbance at 320* Hz*, via a variable attenuator or test fibres of different lengths, allowing the effects of loss and optical propagation to be separated. The audio output was analysed by a Marconi 2382 spectrum analyser operating at 30* Hz *resolution bandwidth.*

disturbed fibre, via either a variable optical attenuator or test fibres of various lengths, making it possible to observe the effect of loss independent of range, and of optical range, along with the associated loss due to fibre attenuation. The audio output from the S&H amplifier was monitored using a Marconi 2382 RF spectrum analyser, operating at 30 Hz bandwidth in "Max Hold" mode – allowing the peak signal to be obtained, thus minimising problems from "fading". The signal size and SNR were measured five times at each loss and four times at each range and the average and standard error was calculated.

In the measurements of the effect of attenuation the attenuator was re-set for each measurement, using a fibre DFB source and power meter, randomising any systematic error from an incorrect attenuator setting. The test fibre lengths were measured using an Anritsu MW98A OTDR.

6.1.3. Results

Considering loss alone, a one-way loss of A dB will result in a reduction in backscattered optical power, at the receiver, of $2A$ dB, which, in terms of electrical power at the audio output, corresponds to $4A$ dB. The results for inserting a loss using the optical attenuator are shown in Figure 6.1.2. In terms of the one-way attenuation, A dB, the best fit for the signal is $((-55\pm1)-(4.1\pm0.4)A)$ dBV and, for the SNR, $((-23\pm1)-(2.9\pm0.4)A)$ dB. The best-fit value of the signal degradation with applied

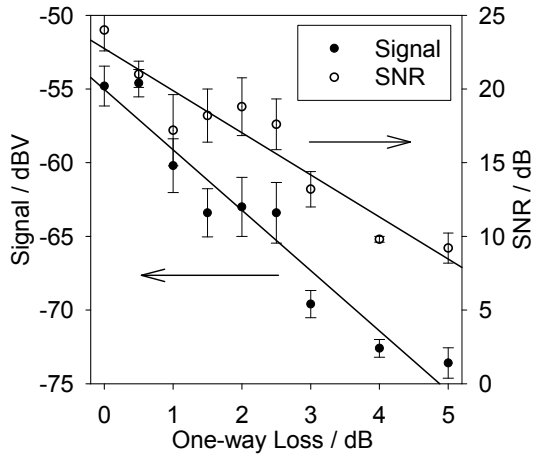

Figure 6.1.2

Effect of attenuation on Signal and SNR. The range is fixed at 320 m.

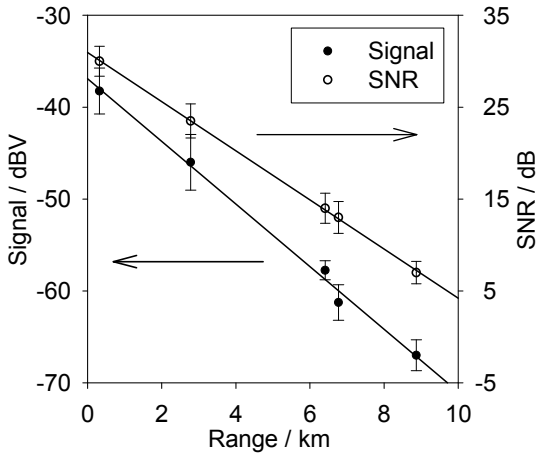

Figure 6.1.3

Effect of range, and associated loss, on signal and SNR at normal launch power.

loss of (4.1 ± 0.4) dB / dB is in excellent agreement with the predicted behaviour. As shown in Chapter 5, Section 5.3, for launch powers ~1 W the SNR falls off slower than the signal due to the domination of ASE-Signal noise. The value of SNR degradation due to loss insertion of (2.9 ± 0.4) dB / dB can therefore be understood: the scaling of the ASE-Signal beat power giving an advantage of approximately 1 dB / dB.

Having measured the effect of loss, different length test fibres were introduced in place of the attenuator to measure the effect of optical range. The results, showing signal magnitude and SNR as a function of optical range, are plotted in Figure 6.1.3. If the fibre loss was the only signal degradation mechanism, then with a total fibre loss of 0.25 dB / km, a range z would reduce the backscatter power by 0.5 dB / km, reducing the audio signal by 1.0 dB / km. The best fit, however, gives the signal at a range z as $((-36.9 \pm 0.8) - (3.4 \pm 0.1)z)$ dBV. The degradation with range of (3.4 ± 0.1) dB / km exceeds the expected value, based on the fibre loss alone, by (2.4 ± 0.1) dB / km. This clearly indicates that the optical loss is not the only factor which reduces the signal amplitude with range. As discussed above, the SNR degradation is expected to be less than the signal reduction, due to the EDFA characteristics, allowing the best-fit SNR degradation of (2.67 ± 0.03) dB / km to be understood.

To gain an indication of whether the launch power affected the degradation, a quick experiment was carried out using a simple attenuator where the fibre is bent around a former, inducing bend loss, which was measured to be approximately 5 dB per kink. The results are shown in Figure 6.1.4 and Figure 6.1.5. With a single kink the signal degradation with range was (1.6 ± 0.2) dB / km, still worse than the expected 0.8 dB / km, but closer to this value than with the un-attenuated launch power. With two kinks, giving a loss of approximately 10 dB, the line of best fit is (0.1 ± 0.4) dB / km, although the fit is very poor, probably since the receiver SNR was very low due to the reduced backscatter power, the result is indicative that the theoretical loss with range can be approached in practice at low powers.

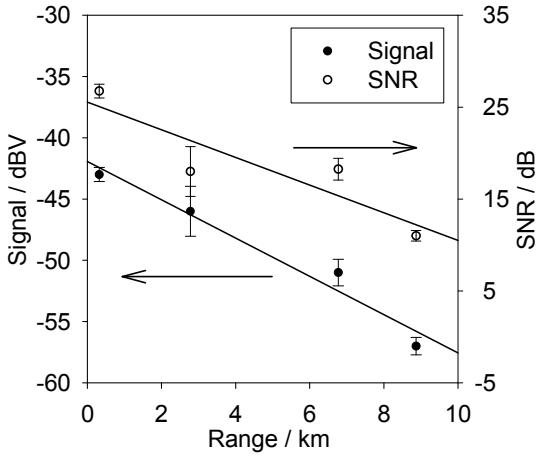

Figure 6.1.4

Effect of range, and associated loss, on signal and SNR with launch power reduced by one fibre kink (~5 dB*)*

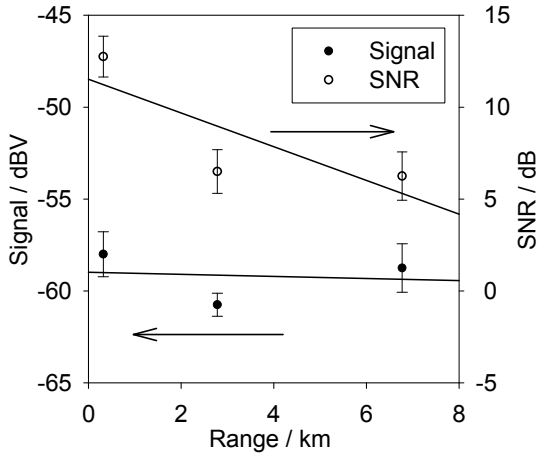

Figure 6.1.5

Effect of range, and associated loss, on signal and SNR with launch power reduced by two fibre kinks (~10 dB*)*

6.1.4. Conclusions

From these results it is clear that the propagation loss is not the only factor influencing the degradation with range. For a fibre attenuation of 0.25 dB / km, if the degradation were due to loss alone, the measured signal reduction with range of (3.4 ± 0.1) dB / km is equivalent to (13.6 ± 0.5) dB / dB compared to the value measured for a "pure" loss of (4.1 ± 0.4) dB / dB, which was itself in agreement with the expected value of 4.0 dB / dB. The results suggest that the optical power usefully involved in the interference is effectively reduced, explaining the signal reduction and degradation of the SNR.

Reducing the launch power appears to reduce the anomalous signal reduction, with better than expected reduction observed with 10 dB attenuation of the launch pulse. The dependence on range and optical power suggests that optical non-linearities may be the cause. As stated in the previous chapter, following Rogers' consideration of the maximum launch power for P-OTDR [35], it was believed that non-linear effects would not be significant for pulses of total energy less than ~ 3 μJ. The pulses launched in the experiments reported here were estimated to be an order of magnitude smaller than this. Thus, this assumption was challenged by these results, leading to the detailed experimental and theoretical analysis of the effect of non-linear phenomena on the C-OTDR sensor described in the rest of this chapter.

6.2. Spectral Evolution

6.2.1. Introduction

Having proved that the signal degradation with range was greater than would be expected from the loss alone (Section 6.1), a number of simple measurements were carried out to attempt to find the cause of this disparity. Two mechanisms are possible to reduce the signal: excess loss, above the expected value; and spectral broadening, reducing the interference visibility. To establish which of these was occurring; the forward-propagating pulse spectrum was measured at varying lengths and launch powers.

6.2.2. Experimental Investigation

The method used to carry out the measurements is shown in Figure 6.2.1. The FTAS Rev 1.1 demonstration system was used to generate 200 ns pulses at a rate of 10 kHz, with a variable attenuator, by OzOptics, allowing the pulse power to be modified. A circulating filter, using a HiWave FBG, removed the in-pulse ASE outside the 0.34 nm bandwidth, with the second AOM in the demonstration unit removing out-of-pulse ASE by temporal gating. The resulting light was directed to an Ando AQ6137B OSA through the test fibre.

The spectrum was measured after various fibre lengths, with a launch power of approximately 640 mW. The results, shown in Figure 6.2.2, show immediately that the spectrum was evolving rapidly as the pulse propagated along the fibre. Sidebands are visible above and below the launch spectrum, even for very short fibre lengths,

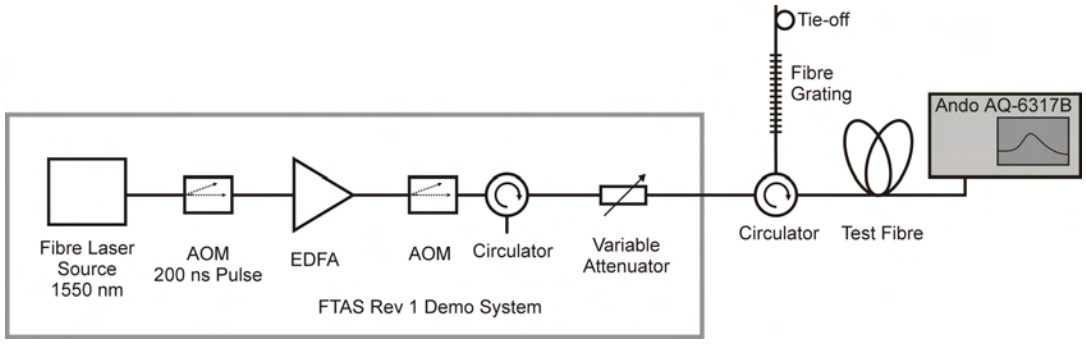

Figure 6.2.1

Experimental set up for investigating self-phase modulation. The fibre grating, by HiWave, had a bandwidth of 0.34 nm*, removing the majority of the ASE from the launch spectrum. The second AOM removed ASE outside the duration of the pulse.*

becoming comparable to the launch at 12 km. The spectrum appears to be symmetric, with the sideband offset increasing with length, although the blue-side is less clear due to the presence of the ASE passed by the circulating filter.

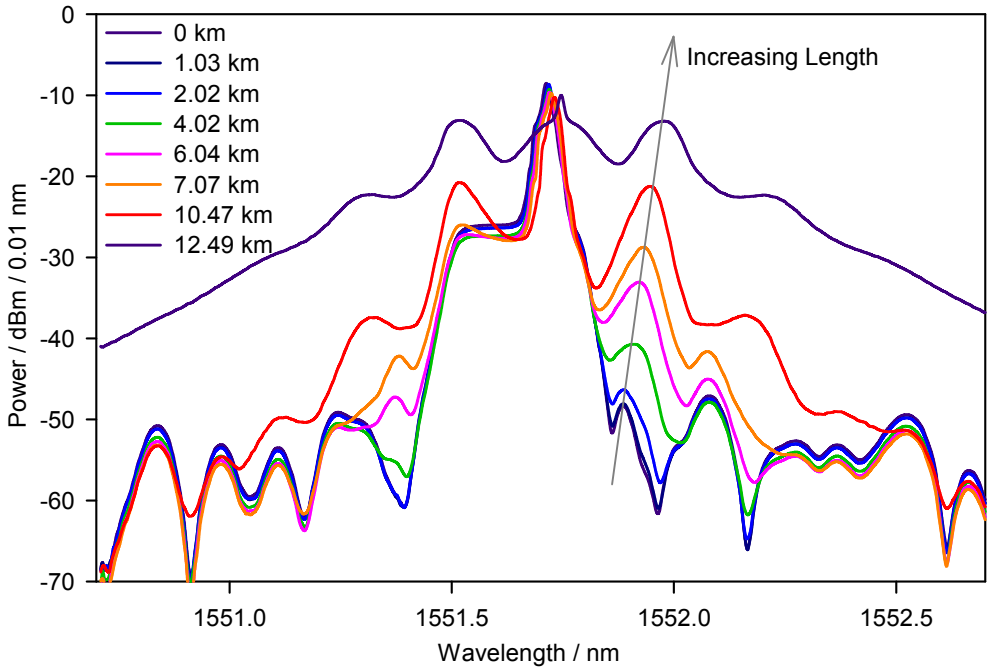

Figure 6.2.2

Pulse spectrum measured at the OSA after different fibre lengths, the resolution was set to 0.01 nm. *The pulse duration was 200* ns *and the power approximately 640* mW. *The laser line is on the red edge of the filter pass band, meaning that detail is more easily visible at longer wavelengths than shorter.*

Figure 6.2.3 shows the spectrum after a fibre length of 12.49 km for a range of launch powers. As the power increases the power in the sidebands increases, as does the sideband spacing from the signal. At higher powers the spectrum is significantly broadened, which would clearly have an effect on the interference visibility, reducing the size of the decoded signal and degrading the SNR

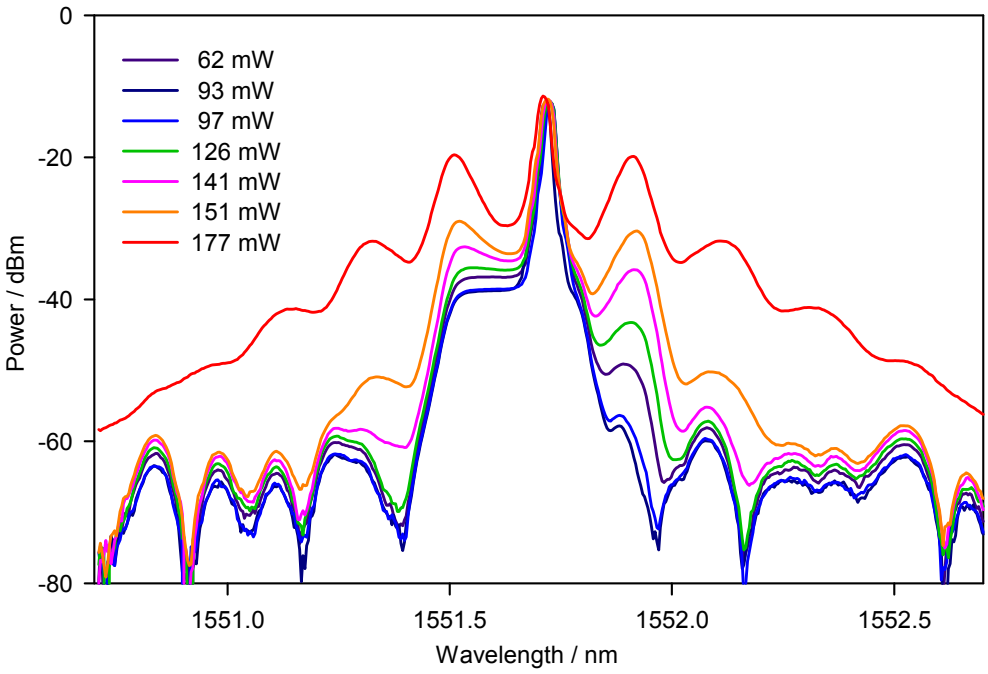

Figure 6.2.3

Pulse spectrum measured at the OSA at different launch powers, the resolution was set to 0.01 nm. *The pulse duration was 200* ns *and the fibre length was 12.49* km. *The pulse powers are calculated using the mean power measured using the OSA's power-meter function and correcting for the duty cycle. For low-duty-cycle measurements such as here (0.2 %) the pulse power can be considered only as an approximate value.*

6.2.3. Conclusion

The results from these simple experiments show that the optical spectrum changes as the pulse propagates along the fibre, which indicates that the propagation of the pulse is not in the linear regime. In the next section the various non-linear effects are discussed, allowing identification of the cause of the evolution, and the required conditions to avoid the sensor performance are considered.

6.3. Non-Linear Effects

In the preceding discussion of the C-OTDR acoustic sensor system in Chapter 3 and Chapter 4 it was tacitly assumed that the fibre transmitting the light behaves as a linear media. This approximation is valid for low optical powers, however as the optical power increases the light begins to interact with the media in a number of ways. As a result it is not possible to improve the SNR indefinitely by launching more powerful pulses, since the non-linear effects, which begin to take place, limit the performance of the sensor.

Interaction with the internal vibration states of the molecules in the medium can lead to Raman scattering [20, 85], increasing the fibre propagation loss and broadening the source spectrum. Light can also interact with macroscopic variations in the density of the medium via phonon interactions, leading to Brillouin scattering [20, 85], again increasing the transmission loss and converting light to new optical wavelengths. These processes may be considered in terms of the mechanical dispersion relation with Raman processes taking place in the optical branch and Brillouin interactions accessing the acoustic branch.

Other non-linear effects occur due to the dependence of the refractive index on the optical power. To a first-order approximation the refractive index can be assumed to be independent of the magnitude of the optical field, but for higher powers the small non-linear components, where the refractive index depends on the power, come into play. Where light of varying power is propagating in the fibre it can undergo self-phase modulation (SPM), where the change in refractive index associated with the change in power causes phase modulation of the light, changing its spectrum [85]. Cross-phase modulation (XPM) occurs due to the same mechanism: where two optical signals are propagating in the medium the refractive index will depend on the total optical power, so power variations at one wavelength will cause a phase modulation of the light at the other wavelength [85].

The non-linearity of the refractive index also leads to four-wave mixing (FWM). Here, light of two frequencies is propagating in the medium; the non-linearity of the medium allows them to mix, generating sidebands which propagate with the initial light [86]. Where phase matching between the pump and generated light occurs, the sidebands can increase in intensity, at the expense of the pump light, causing increased loss at the original frequencies.

In the following sections the conditions for the onset of each of these phenomena are discussed and their effects on the performance of the C-OTDR acoustic sensor are considered.

6.3.1. Stimulated Raman Scattering

Stimulated Raman scattering (SRS), where a parametric interaction between the pump light and the vibrational states of the molecules in the optical medium generates light at anti-Stokes frequencies above and Stokes frequencies below the pump light, leading to excessive attenuation of the pump. The backscattered light from these new waves need not be of concern here since the Stokes spectra are centred approximately 13 THz from the pump, equivalent to approximately 100 nm for a 1550 nm pump, allowing the unwanted backscatter to be easily filtered from the Rayleigh scatter using Bragg grating filters. It is therefore only necessary to consider the reduction in performance due to the increased attenuation of the forward pulse.

Smith [87] derived a simple relation for the critical power, P_{Crit}, where the Stokes light power is equal to the pump power at the fibre end for high-loss (~ 20 dB / km) fibres, which predicts a value of approximately 1.2 W for low-loss (~ 0.2 dB / km) fibres. This condition corresponds to a 3 dB loss of optical power in the Rayleigh backscatter, the rest of the launched light having undergone conversion to Stokes light. Although this result has been applied to low-loss fibres[86, 88], Smith's formulation is not valid for modern low-loss fibres since he ignores pump depletion through Raman scattering, considering only the loss due to the fibre attenuation which dominates in high-loss fibre which is valid only for losses > 4 dB / km [89]. Taking into account pump depletion due to SRS, Auyeung and Yariv [89] calculate the threshold for various fibres, the values, of the order 10 W – 100 W, generally being in agreement with experimental results. The fraction of the pump light converted by SRS varies exponentially with the pump power [89], so reducing the pump power below the threshold quickly reduces the effect of SRS to negligible levels.

Considering the above, it is reasonable to conclude that for moderate pulse powers, ~ 1 W and below, the effects of SRS can be ignored, in agreement with the experimental results of Izumita *et al.* [88].

6.3.2. Stimulated Brillouin Scattering

Stimulated Brillouin scattering (SBS) is a parametric interaction where forward-propagating light is scattered, generating a phonon and backscattered light wave, down-

shifted in frequency due to the loss of energy to the phonon. In silica, at 1550 nm, the downshift is approximately 11 GHz, corresponding to a wavelength shift of ~0.1 nm, with a bandwidth of ~ 20 MHz, although this can be as great as ~ 100 MHz in doped fibre [86]. As a result, the optical power at which SBS begins to effect the propagation of light depends strongly on the bandwidth of the optical signal being transmitted [86, 87, 90].

The occurrence of SBS could degrade the performance of the C-OTDR sensor by two mechanisms: interference at the detector of the Stokes light, which would generate broadband noise, with bandwidth of several tens of megahertz; and at the onset of SBS the majority of the forward light is backscattered, causing excess reduction in receiver SNR with range.

The critical power was first defined by Smith [87], ignoring pump depletion, as the power where there is complete conversion of forward-propagating pump light to backward-propagating Stokes light. This condition can not be achieved in practice since pump depletion inevitably occurs through conversion to Stokes light and fibre attenuation, thus the backscattered power is always less than the input pump power [91]. Nonetheless this definition remains common in the literature [20, 86, 90].

Koyamada *et al.* calculate the critical power for SBS, P_B, of a pulse of duration τ as [88, 90]:

$$P_B = 2 \cdot \frac{21A}{g_B\left(\frac{\tau c}{2n}\right)}, \qquad 6.3.1$$

where g_B is the SBS gain coefficient, A is the effective mode area and c/n is the group velocity of light in the fibre.

The predicted values, from 6.3.1, are shown in Figure 6.3.1 and are in approximate agreement with the experimental data of Fluck *et al.* [92], differing only by a factor of approximately 2 in the range of 20 ns to 100 ns, which could be related to the definition of threshold in the experimental measurements. Using 6.3.1, a pulse of 400 ns duration has a critical power of ~1 W. Because the power scattered by SBS increases rapidly with increasing power, it can be concluded that powers of up to 1 W should not give problems from SBS where the pulse duration is < 400 ns, as is likely to be the case for the C-OTDR sensor.

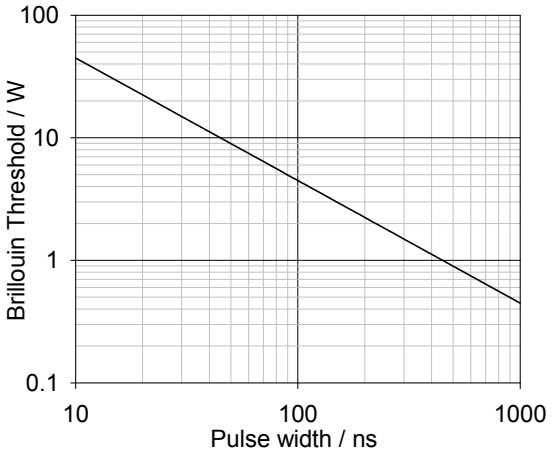

Figure 6.3.1

Brillouin threshold power as a function of pulse width from 6.3.1, assuming standard single-mode fibre with an effective mode area $A = 50 \times 10^{-12}$ m^2*, Brillouin gain coefficient* $g_B = 4.5 \times 10^{-11}$ m / W*, and core refractive index n = 1.44. The threshold is in excess of 1* W *for pulse widths below 400* ns*, corresponding to spatial resolutions of 80* m*, and above and in excess of 10* W *for pulse widths less than 40* ns*, corresponding to 8* m *resolution.*

6.3.3. Self-Phase Modulation

Self-phase modulation (SPM) occurs where the refractive index cannot be regarded as constant with power, instead having the form:

$$n(P) = n_0 + aP\,, \tag{6.3.2}$$

where n_0 is the normal refractive index, P is the optical power and a is the power-dependent component of the refractive index. As a result when a pulse is launched into a fibre, different parts of the pulse experience a different refractive index dependant on the instantaneous power, leading to different parts of the pulse travelling through different optical path lengths. This causes the leading edge of a pulse, where the optical power is lower than at the peak, to be red-shifted while the trailing edge is blue-shifted.

A pulse propagating along a fibre can be described in terms of the normalised envelope of the electric field at the point of launch, $U(0,T)$, where T is the time in the frame of reference, relative to the pulse centre, as [85]:

$$U(L,T) = U(0,T)\exp[i\phi_{NL}(L,T)], \tag{6.3.3}$$

where ϕ_{NL} is the phase shift due to SPM, which is given by:

$$\phi_{NL} = |U(0,T)|^2 \gamma L_{eff} P_0 . \qquad 6.3.4$$

The effective length L_{eff}, which compensates for the pulse attenuation as it propagates along the fibre, is defined in terms of the physical fibre length, L, and the linear attenuation constant, α, as

$$L_{eff} = \frac{1 - e^{-\alpha L}}{\alpha}, \qquad 6.3.5$$

and γ is defined as

$$\gamma = \frac{n_2 \omega_0}{cA}, \qquad 6.3.6$$

where n_2 is the non-linear coefficient, ω_0 is the optical frequency, A is the effective mode area and c is the speed of light in a vacuum.

The chirp due to SPM across the pulse, $\delta\omega(T)$, can be found by differentiation of 6.3.4:

$$\delta\omega(T) = -\frac{\partial}{\partial T}\phi_{NL} = -\gamma L_{eff} P_0 \frac{\partial}{\partial T}|U(0,T)|^2 . \qquad 6.3.7$$

The negative sign is due to the pulse-centred frame of reference. It is clear from this equation that the greatest chirp occurs at the steepest part of the pulse and that the maximum chirp is proportional to the peak power and the effective length. Therefore a pulse with gentle edges and only a short flat peak will obtain moderate chirp over the majority of the pulse, while a steep-sided pulse will obtain a large chirp on its edges, but remain unaltered in the central part where the power is constant.

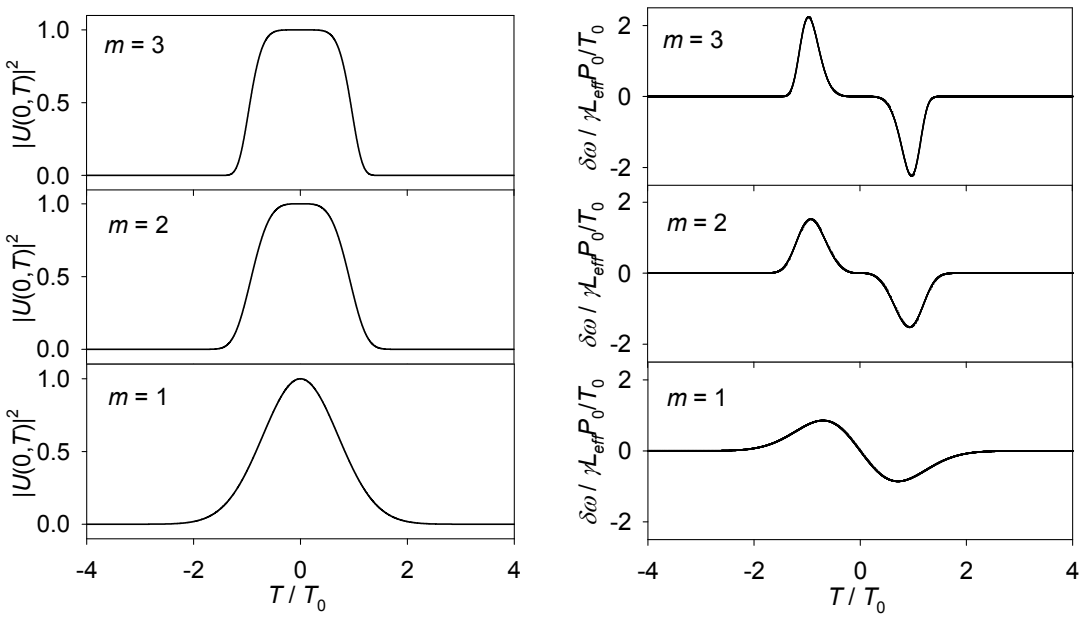

Figure 6.3.2

Left: Gaussian pulses for different values of m and Right: the corresponding chirp due to SPM. As the pulse becomes more rectangular with increasing m, the size of the chirp increases, but affects a reduced fraction of the pulse.

Consider an n^{th}-order Gaussian pulse with $1/e$ pulse-width $2T_0$:

$$\left|U\left(0,T\right)\right|^2 = \exp\left[-\left(\frac{T}{T_0}\right)^{2m}\right]. \tag{6.3.8}$$

Differentiating and substituting into 6.3.7, the chirp is:

$$\delta\omega\left(T\right) = -\frac{\partial}{\partial T}\phi_{NL} = -\gamma\, L_{eff}\, P_0\, \frac{2m}{T_0}\left(\frac{T}{T_0}\right)^{2m-1} \exp\left[-\left(\frac{T}{T_0}\right)^{2m}\right] \tag{6.3.9}$$

The resulting $\delta\omega\left(T\right)$ is shown for different values of *m* in Figure 6.3.2. As expected, the magnitude of the chirp increases with *m* but the fraction of the pulse which is frequency shifted is reduced, emphasising the effect that pulse shape has on the character of the spectral broadening due to SPM.

The peak value of the chirp, $\delta\omega_{\max}$, can be found by maximising 6.3.9 [85]:

$$\delta\omega_{\max} = \frac{m f(m)}{T_0}\gamma L_{eff} P_0;$$

$$f(m) = 2\left(1-\frac{1}{2m}\right)^{1-\frac{1}{2m}} \exp\left[-\left(1-\frac{1}{2m}\right)\right] = \begin{cases} 0.86;\ m=1 \\ 0.76;\ m=2 \\ 0.75;\ m=3 \end{cases} \qquad 6.3.10$$

For a 1 W pulse with m = 3, T_0 = 100 ns, with long fibre, so L_{eff} = 22 km, having a typical value of γ = 2 W^{-1} km^{-1} [85] this gives a peak frequency shift of 160 MHz, equivalent to 1.3 pm (at 1550 nm).

It can be shown that a frequency shift of $\Delta\nu_c = 1/\tau$, where τ is the pulse duration, is sufficient to change the signal from coherent Rayleigh scattering such that the backscatter trace is uncorrelated [63]. The critical power for SPM, P_{SPM}, may therefore be defined as that where the peak chirp amplitude is equal to the de-correlation frequency:

$$P_{SPM} = \frac{\pi}{m f(m)\gamma L_{eff}} \qquad 6.3.11$$

The values of critical power calculated for m = 3 may be pessimistic because only a small fraction of the pulse is chirped meaning that the majority of the light remains monochromatic; the chirped portion effectively generates noise from interference with itself and the un-chirped component. The result is a reduction in SNR at the receiver roughly in proportion to the fraction of the pulse that remains un-chirped. Similarly, the result for the m = 1 case may be optimistic, since chirp is present on nearly the whole pulse, which will produce interference noise, reducing the SNR, although the Rayleigh backscatter trace remains stable.

In practice the pulse is unlikely to be Gaussian, and where it is amplified by an EDFA it is likely to be asymmetric with the rising edge having a larger power gradient than the falling edge. The pulse shape is also likely to be related to its width: a short pulse, where the pulse length is comparable to the rise/fall time of the optical switching device, will be more similar to the m = 1 case than a long pulse, with a relatively long plateau which will be more similar to the m = 3 case.

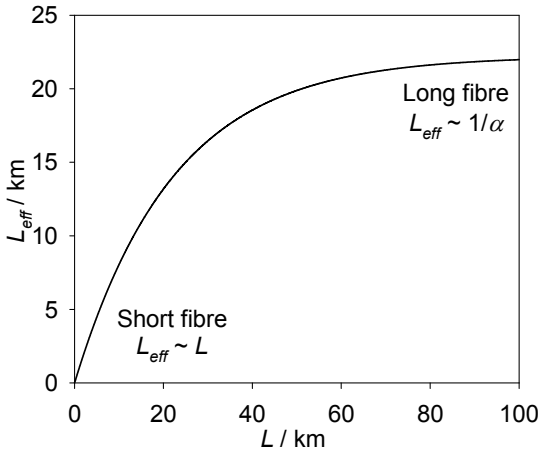

Figure 6.3.3

Non-linear effective length, Leff, as a function of the physical fibre length L. The fibre loss is taken as $\alpha = 4.5 \times 10\text{-}5$ m^{-1} *(0.2* dB / km*). For short fibres, where the total loss is small, Leff is approximately equal to L, for longer fibres the Leff approaches* $1/\alpha = 22$ km.

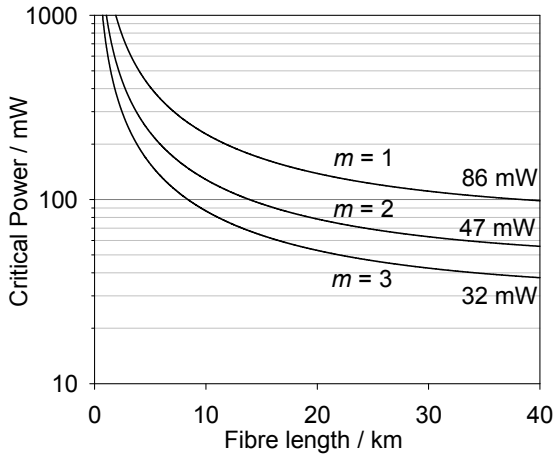

Figure 6.3.4

Critical powers for SPM, for Gaussian pulses with different m, calculated using 6.3.11. *The asymptotic values for long fibres are shown on the right hand side. These critical powers can only be considered indicative since the fraction of the pulse affected by SPM changes with m,*

A better approximation to the pulse shape is shown in Figure 6.3.5, where the full-width at half maximum (FWHM) is τ and the rise and fall time is t_r. In this case the peak gradient of the envelope is simply $1 / t_r$ so 6.3.11 becomes:

$$P_{SPM} = \frac{2\pi t_r}{\tau \gamma L_{eff}} . \qquad 6.3.12$$

The pulse width appears on the denominator because a wider pulse requires a smaller frequency deviation to decorrelate the coherent backscatter pattern. As with the Gaussian case, a long rise time increases the critical power, but at the expense of a greater fraction of the pulse undergoing chirp, $2t_r / \tau$. The critical power is plotted as a function of fibre length in Figure 6.3.6. Substituting typical values for a 1 W pulse from an AOM of t_r = 40 ns the peak frequency shift is 175 MHz, or 1.4 pm, close to that for the m = 3 Gaussian case.

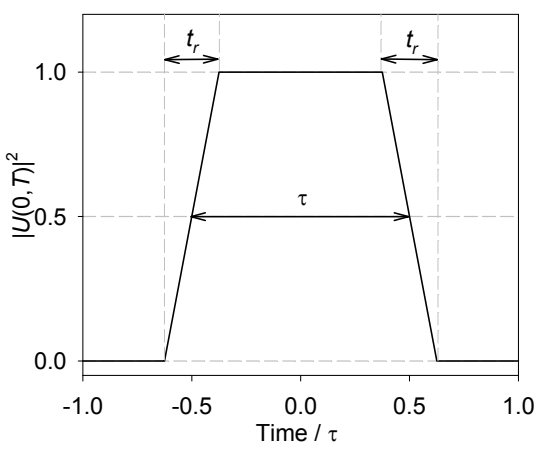

Figure 6.3.5

Improved approximation for the pulse shape for considering the effect of SPM. The FWHM is τ and the equal rise and fall times are tr. Typical pulse widths are 50 ns *to 400* ns. *When the AOMs are used to generate the pulses typical rise and fall times are approximately 10* ns *to 30* ns.

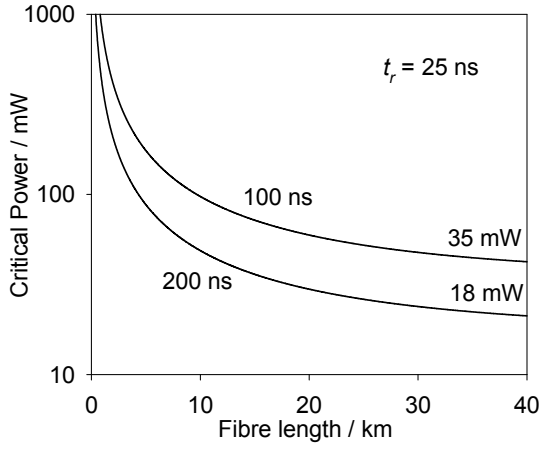

Figure 6.3.6

Critical power due to SPM for trapezoidal pulses of width 100 ns *and 200* ns *with* $t_r = 25$ ns. *The critical power is higher for the shorter pulse since the degree of chirp to* decorrelate *the trace is smaller than for the shorter pulse; however, this may be offset by the chirp affecting a smaller fraction of the pulse.*

6.3.4. Four-Wave Mixing

Four-wave mixing (FWM) occurs where co-propagating light, of two (or more) wavelengths, mixes via the non-linear refractive index to generate sidebands which co-propagate with the initial light, causing attenuation as energy is transferred to the new frequencies. The total power transferred to the new frequencies is proportional to the product of the powers of the initial light waves and physical parameters of the fibre and is significant only for channels separated by approximately 80 GHz or less [86]. For DWDM optical communications FWM limits the power in each channel to ~ 1 mW, independent of the number of channels since only the two nearest channels take part in the interaction [86].

In the C-OTDR sensor, where it operates on a dedicated fibre the pulse may interact with the ASE from the fibre DFB and the launch EDFA which amplifies the pulse. Using the results of Chraplyvy [86], that the critical power for DWM communications channels is 1 mW per channel, where the channel of interest interacts

with the two channels above and below its own frequency, then by dividing the total ASE power into two components, above and below the pulse frequency, the condition for avoiding FWM can be written:

$$\left(1\times10^{-3}\right)^3 \le P_{Pulse}\times\left(\frac{GP_{ASE}}{2}\right)^2. \qquad 6.3.13$$

Where GP_{ASE} is the ASE power launched into the fibre where G is the gain of the launch EDFA and P_{ASE} is defined in Chapter 4 as:

$$P_{ASE} = n_{spon} m_t h\upsilon \Delta\nu_f. \qquad 6.3.14$$

In this case the optical bandwidth $\Delta\nu_f$ is the total bandwidth of the FWM interaction, which is ~80 GHz [86], giving $P_{ASE} = 20\,\text{nW}$. Assuming a modest EDFA gain of only 200 (23 dB) this still sets the pulse power to avoid FWM as:

$$P_{Pulse} \le 250\,\text{W}. \qquad 6.3.15$$

Thus as the pulse powers expected here, where the sensor is operated on a dedicated fibre, FWM will not occur between the pulse with the ASE from the launch EDFA.

6.4. Comparison of Theory and Experiment

The previous section outlined the non-linear effects which are candidates for causing the observed spectral evolution and showing theoretically that SPM will limit the launch power possible without performance degradation. In this section the theoretical discussion is compared with the experimental results presented earlier in the chapter.

6.4.1. Non-Linear Scattering

In section 6.3.1 it was stated that SRS would not be significant for pulse powers below ~1 W. The observed spectral evolution in Figure 6.2.2 and Figure 6.2.3 confirms this assertion: the sidebands are too close to the signal wavelength to be stimulated Raman scattering which generates broad-band sidebands at around 100 nm from the pump light.

Brillouin scattering is a better candidate: however, the Brillouin shift, which is approximately 11 GHz (0.1 nm) in silica [14], should remain constant, whereas the sidebands observed in Section 6.2 vary with launch power. Furthermore, Stimulated Brillouin scattering generates only a red-shifted Stokes line and spontaneous Brillouin scattering is ~ 20 dB weaker than Rayleigh scattering, meaning that for 40 m pulses the Brillouin scattering would be expected to be around 70 dB weaker than the forward-propagating pulse.

To confirm the elimination of Brillouin scattering as the cause of the spectral evolution, and to verify the theoretical SBS threshold 6.3.1, a simple measurement was made of the CW SBS threshold. The FTAS Rev 1.0 demonstration system was used to generate CW light at 1550 nm, which was launched into 44 km of standard single-mode fibre, as shown in Figure 6.4.1. The launch power was measured by connecting the system output to a power meter (Rifocus 555B) via an ST patch-cord, allowing the connection to the Optical Spectrum Analyser (OSA) to remain un-broken since this was less repeatable due to using a bare-fibre adapter. The launched power could be varied using the variable attenuator within the demonstration system. The end of the test fibre was tied in a knot of approximately 6 mm in diameter to ensure that there was no reflection from the fibre end-face, which was broken rather than cleaved to increase the return loss. The EDFA was saturated due to the CW input at ~ 2 mW, giving a good SNR: measurements with the OSA showed the ASE spectral density to be approximately 30 dB below the signal.

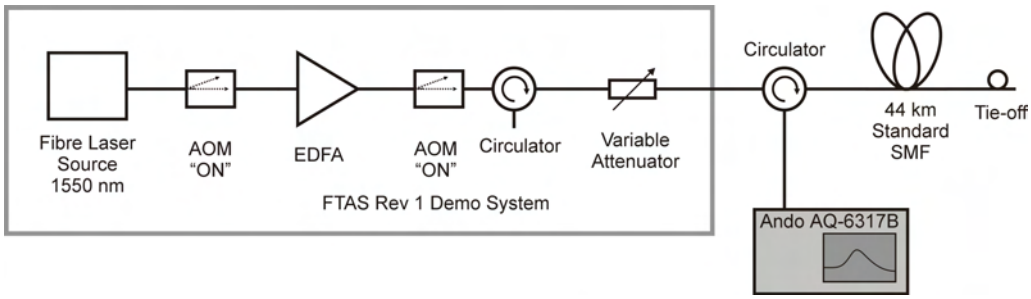

Figure 6.4.1

Experimental set up for monitoring the onset of Brillouin scattering with CW illumination. Measurement of the backscatter power using the Ando AQ-6310B spectrum analyser allowed the relative powers scattered by Rayleigh and Brillouin mechanisms to be measured.

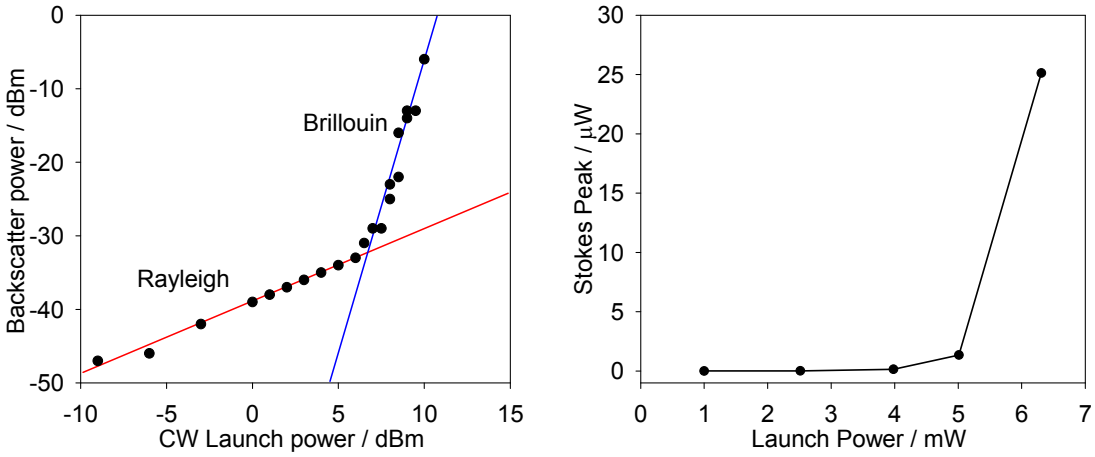

Figure 6.4.2

Experimental data showing (left) the total backscattered power as a function of CW launch power, demonstrating the onset of Brillouin scattering in 44 km *of standard SM fibre at 1550* nm*. The corner power is approximately 7* dBm *(5* mW*), this compares well with the predicted value from* 6.3.1 *using* $\tau c/n = 44$ km *of 2.1* mW*. The transition between regimes is very rapid: a 5* dB *change in launch power can modify the backscattered power by over 30* dB*; (right) the Stokes power from CW illumination at 1550* nm *of 44* km *of single-mode fibre. The sharp threshold at ~ 5* mW *is clearly visible.*

The experimental results are illustrated in Figure 6.4.2. Using the OSA it was found that the backscattered Stokes power was equal to the Rayleigh backscattered power for an input power of 7.0 dBm (5.0 mW) and that, at powers of 9.5 dBm

(8.9 mW) and above, there was complete conversion to the Stokes wavelength. As expected the Stokes shift was found to be independent of the launch power, and was measured to be (0.091 ± 0.002) nm with the launched light centred at 1549.88 nm, corresponding to a frequency shift of (11.4 ± 0.2) GHz, which is in agreement with published values for silica fibres [14]. The power at which Brillouin scattering becomes significant is comparable to the value predicted in Section 6.3.2 of 2 mW and the rapid increase in backscattered power confirms that, as expected, the Stokes power increases very rapidly above the Brillouin threshold. These results confirm the prediction of 6.3.1 that, with pulses shorter than 400 ns, SBS should not cause any degradation at powers below 1 W.

6.4.2. Four-Wave Mixing and Self-Phase Modulation

The experimental measurements have shown that the non-linear scattering mechanisms SRS and SBS are not responsible for the observed evolution of the pulse spectrum. The remaining phenomena are FWM and SPM.

FWM can be eliminated since it leads to the generation of sidebands through non-linear mixing of the signal with light at other frequencies within a 160 GHz bandwidth. In the experiments carried out, the only light, other than the pulse, was the residual ASE from the fibre laser and from the launch EDFA. Mixing between the pulse light and the ASE would lead to generation of broadband sidebands, rather than the narrow sidebands at approximately 0.2 nm from the pulse observed in Figure 6.2.2 and Figure 6.2.3.

This leaves SPM, predicted in Section 6.3.3 to have the lowest power threshold to affect the sensor performance. The predicted behaviour of chirping the pulse, with the magnitude increasing with range and power, is matched by the experimental results of in Figure 6.2.2 and Figure 6.2.3. However, the predicted shift from Section 6.3.3, for a pulse with the rise-time determined by the AOM, is of the order 1 pm, compared with the observed shift which is of the order 0.1 nm. The most probable cause of this disparity is that the launch EDFA increases the steepness of the rising and falling edges of the pulse, as a result of the power-dependence of the gain, measured in Chapter 5.

6.4.3. The Effect of Spectral Broadening

The theoretical analysis in Section 6.3 indicated that the maximum launch power is limited by SPM of the propagating pulse. The analysis relied on the results of Mermelstein *et al.* [63] that a frequency shift of $1/\tau$, where τ is the pulse width, is

sufficient to de-correlate, i.e. to substantially change, the backscatter trace. Similarly, the simple analysis in Chapter 2 indicated that the effect would be to vary the phase bias, giving sinusoidal variation with period $2/\tau$.

To confirm these results, the simple experiment shown in Figure 6.4.3 was carried out. For convenience, a later experimental implementation of the C-OTDR sensor, the FTAS Rev 3 demonstration system (which will be described in detail in Chapter 6) was used to make these measurements. Pulses of 200 ns duration (40 m length) of approximately 100 mW, which passed through an AOM (Gooch & Housego M080-2J-F2S), were launched, via a circulator, into a 2 km length of acoustically isolated fibre. The backscattered light returned from the circulator was routed to the pre-detection EDFA and receiver in the Rev 3 system. The internal acquisition system was used to record the backscatter intensity at four locations on the fibre. The AOM was driven at frequencies from (70 - 90) MHz using a Marconi 2031 RF signal generator with the output amplified to 2 W using a Mini-Circuits ZHL-1-2W linear amplifier.

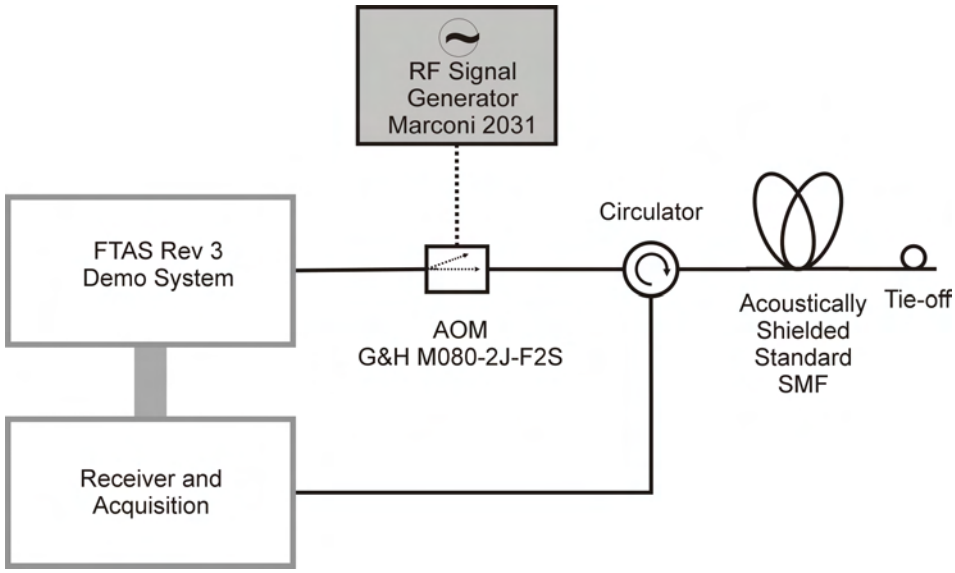

Figure 6.4.3

Experimental arrangement for measuring the frequency deviation required to modify the backscatter trace.

Before carrying out the experiment, the loss of the AOM was measured, as a function of frequency, using CW light from a 1550 nm fibre DFB source and a Rifocus 555B power meter. With the frequency detuned by Δf MHz, relative to the designed

operational frequency of 80 MHz, the one-way loss, in dB, was found by fitting a quadratic to the measured data points, to be:

$$\text{Loss} = (2.99 \pm 0.04) + (0.0273 \pm .0007)(\Delta f)^2 . \qquad 6.4.1$$

This is plotted, along with the measured data, in Figure 6.4.4.

The measurements were carried out by using the Rev 3 acquisition system to sample the backscatter from four separate points on the fibre, at a rate of 4 kHz, while the frequency generator was varied from 70 MHz to 90 MHz in 1 MHz steps at intervals of approximately 2 s. The signal at each AOM frequency was then averaged (typically over 8000 samples) and compensated for two-way loss, allowing the backscatter intensity to be plotted as a function of AOM frequency, shown in Figure 6.4.5.

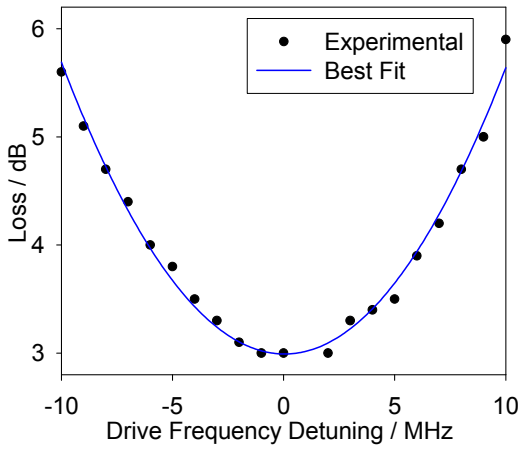

Figure 6.4.4

Measurement of AOM loss as the frequency is varied, showing the experimental data and the best fit.

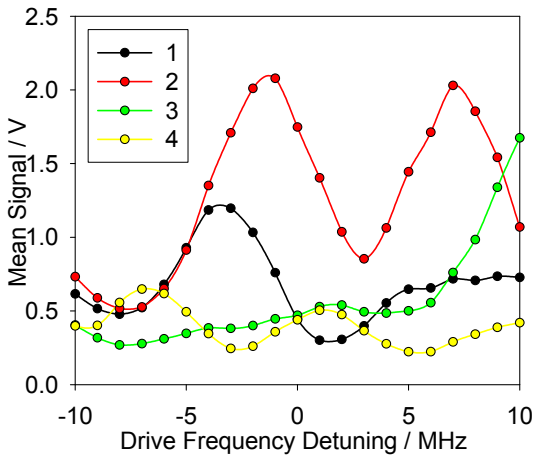

Figure 6.4.5

Backscatter signal as a function of AOM drive frequency, compensated for the AOM loss. The uncertainty is ~ 10-4 V.

The experimental results shown in Figure 6.4.5 confirm the expected result: traces 1, 2 and 4 show a periodicity of 10 MHz, while trace 3 appears to show no interference, suggesting that the fibre birefringence reduced the interference visibility to near zero. The predicted $1/\tau$ frequency shift is 5 MHz, matching the experimental peak-minima separation well. The experiment could not be repeated with shorter pulses because the electronic matching on the AOM had insufficient bandwidth to operate at detuning greater than 10 MHz.

6.5. Measurement of Critical Power for SPM

6.5.1. Introduction

The theoretical analysis and experimental results of Sections 6.3 and 6.4, indicate that the overall performance of the C-OTDR sensor is limited by the occurrence of SPM, limiting the maximum launched pulse power and, in turn, limiting the receiver SNR. Having confirmed that SPM was impairing the performance at long ranges and high launch powers, a number of measurements were carried out to allow determination of the optimum launch power, since the best noise performance is obtained by balancing the benefits of increased launch power with the degradation due to SPM.

6.5.2. Experimental Measurements

The experiment shown in Figure 6.5.1 was carried out to measure the effect of the SPM-induced spectral degradation on pulse interference. The Rev 1.1 demonstration system was used to generate 200 ns pulses, which were launched into the test fibre. The pulse power was adjusted using the variable attenuator, which, for convenience of carrying out the measurements, was located between source and AOM. Locating the attenuator here meant that the SNR at the EDFA output would decrease with increasing attenuation; however, sufficient SNR remained at all powers for the degradation of interference visibility to be un-observable. The launched power was found by using the Ando AQ6310B OSA to measure the average power and correcting for the duty cycle to obtain the pulse power.

A 3 dB coupler split the light into the two arms of an interferometer, formed by the reflections from the cleaved fibre ends, with a manual polarisation controller located in one of the arms. The remaining port was connected to a photodiode and TIA receiver. The receiver input fibre was bent to provide loss to prevent saturation of the receiver. The receiver output was monitored using an oscilloscope and the polarisation controller was adjusted to maximise the interference visibility [65], which is defined, in terms of the maximum and minimum receiver outputs V_{max} and V_{min}, (which are proportional to the optical power) as:

$$\text{Visibility} = \frac{V_{\max} - V_{\min}}{V_{\max} + V_{\min}}. \qquad 6.5.1$$

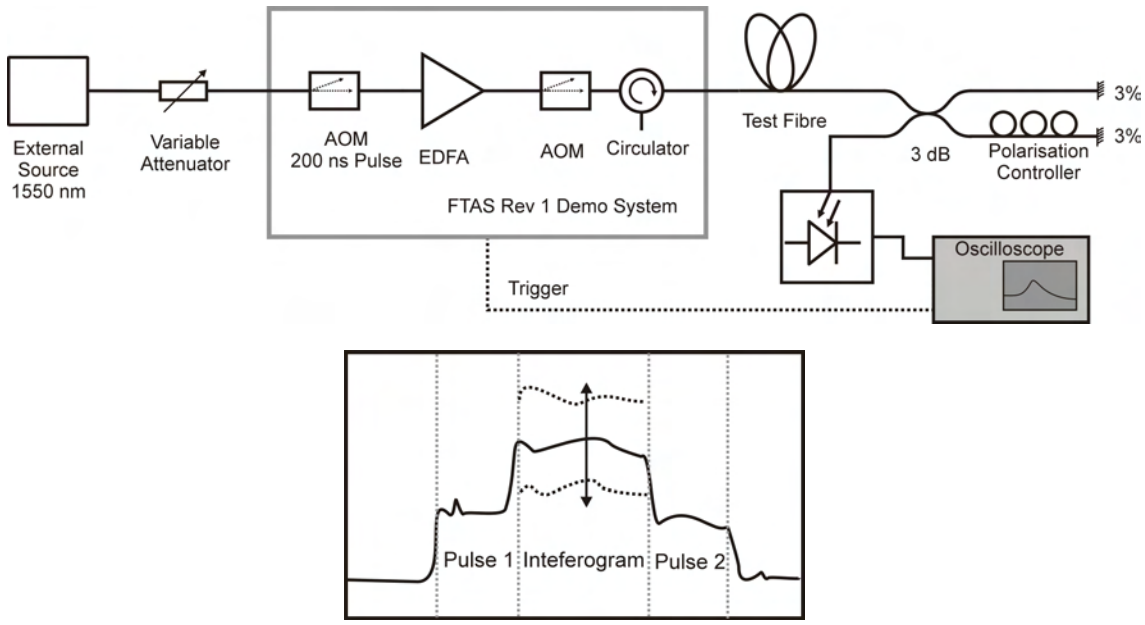

Figure 6.5.1

Experimental arrangement for investigating the reduction in interference visibility due to SPM. The pulse power was varied using the variable attenuator and the polarisation controller was adjusted to maximise the interference depth. The environmental noise in the laboratory gave sufficient phase disturbance that the interference passed through many fringes.

No external stimulus was necessary to modulate the interference: the environmental noise in the laboratory created sufficient phase disturbance for the interference signal to pass through many fringes.

Measurements were carried out using two optical sources: an HN01 fibre DFB laser by SPI, with centre wavelength 1550.116 nm and maximum line-width 30 kHz; and an Agere D2525P25 solid-state DFB laser, centred at 1557.36 nm with a typical line-width of 2 MHz (maximum 10 MHz).

The results are shown in Figure 6.5.2. The power at which the interference is reduced to 50 % can be estimated by interpolation between the data points above and below the 50 % line. With the narrow-line-width fibre-laser source, the interference depth falls to 50 % at pulse powers of 190 mW and 162 mW for the 12.45 km and 43.23 km fibres respectively. With the solid-state DFB laser the 50 % powers are 180 mW and 153 mW. At both fibre lengths the powers for 50 % interference depth are reduced by approximately 10 mW for the solid-state laser with the wider line-width

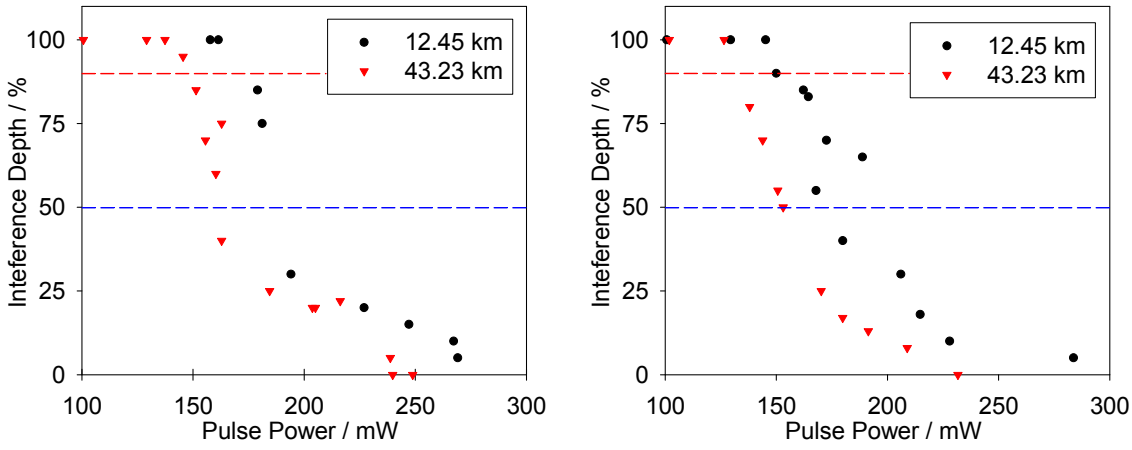

SPI HN01 fibre laser: line-width < 30 kHz *Solid-state laser: line-width < 10* MHz

Figure 6.5.2

Experimental measurement of the interference depth as a function of pulse power for fibres of different lengths. The dashed blue and red lines indicate 50 % and 90 % respectively.

compared to the fibre laser. This would be expected because less SPM-induced chirp is required to broaden the spectrum sufficiently to modify the coherent backscatter pattern.

The 90 % point, indicated by the red line on the graphs, can be found similarly. With the fibre laser the interference depth falls to 90 % at 175 mW and150 mW for the 12.45 km and 43.23 km fibres respectively; with the solid-state DFB these are reduced to 150 mW and 132 mW, approximately 20 mW lower than with the fibre laser.

The predicted powers, for the onset of degradation by SPM, assuming a Super-Gaussian pulse with $m = 1$, are 192 mW for a 12.45 km fibre and 96 mW for a 43.23 km fibre. For a trapezoidal pulse, with FWHM of 200 ns and rise time of 25 ns, the predicted values are 41 mW and 21 mW, for the 12.45 km and 43.23 km fibres respectively. The measured results agree reasonably well with the predicted power, calculated using the $m = 1$ Super-Gaussian for the short fibre, but for the longer fibre the measured power level is around 50 % greater than predicted. For both fibre lengths the critical power predicted by the trapezoidal pulse model is significantly lower than the measured power.

The theoretical description of SPM suggests that the critical power should be inversely proportional to the effective length. From the data, obtained using the fibre

laser, the product of critical power and effective length is 1.7 W·km for the 12.45 km fibre and 2.9 W·km for the 45.23 km fibre; suggesting either that the model is inaccurate, or that the power measurements are non-linear.

6.5.3. Discussion

The experimental results show that significant degradation does not occur in long fibres until the power exceeds around 150 % of the predicted critical power. Possible reasons for this are inaccurate measurement of the launch power, which could not be improved upon in the time available, and the effect of pulse shape varying the temporal fraction of the pulse which is chirped significantly.

The definition of the critical power, used in the derivation in Section 6.3.3, was that power where any part of the pulse is chirped sufficiently to generate a $1/\tau$ frequency shift. This definition takes no account of the fraction of the pulse which undergoes chirp, and which fraction does not exceed the decorrelation frequency. Consider, for example, a near-perfect square pulse: the "edges" will be massively red-shifted, however this accounts for only a tiny fraction of the total optical power, meaning that the resulting SPM causes little degradation of the interference pattern. Perhaps explaining the large frequency shifts observed in Section 6.2, which it was postulated (in Section 6.4.2) were due to sharpening of the pulse edges by the launch EDFA, at powers where the interference remains satisfactory. Furthermore, in practice, some degradation due to SPM may be compensated for by the increase in backscatter power giving noise benefit at the pre-detection EDFA.

The approach taken, in practice, has been to choose initial launch conditions based on the experimental results and theoretical analysis above, and to optimise the launch power iteratively, starting from those values, for the particular situation of interest. This qualitative approach means that other factors, not considered in the analyses, for example: strong acoustic background noise with the signal of interest, fibres with high loss, etc, are allowed for in the final setting, whereas to include these analytically would require extensive investigation of the specific FUT and complex algorithms.

6.6. Limits on Noise Performance

6.6.1. Summary of Non-Linear Thresholds

The evolution of the pulse spectrum has been studied as a function of fibre length and launch power. The results show that, as was predicted in the theoretical analysis, the signal degradation is dominated by SPM, with stimulated scattering processes not being observed in the pulse length and power regimes of interest. A simple experiment confirmed that a frequency shift comparable to $1/\tau$ is sufficient to cause a significant change to the backscatter pattern, preventing correct operation of the C-OTDR sensor if the shift frequencies is within, or above, the frequency band of interest. This indicates that the spectral broadening from SPM will degrade the signal and SNR, as was observed in Section 6.1.

The theoretical limits on launch power due to the various non-linear phenomena discussed are illustrated in Figure 6.6.1. For fibres longer than 1 or 2 kilometres the maximum launch power is limited by SPM. Since the effect of SPM is dependent on pulse shape, in practice the powers calculated above will be a guide to the approximate optimum launch power, with optimisation being needed to give the best performance in a real situation.

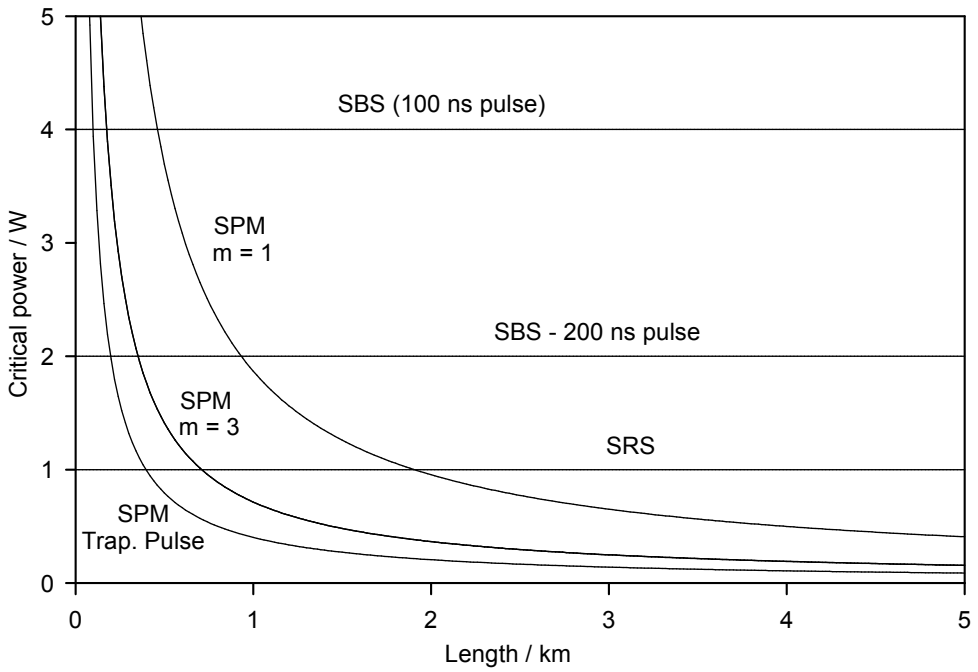

Figure 6.6.1

Summary of theoretical launch power limits due to onset of non-linear phenomena for C-OTDR operating on a dedicated fibre. For very short fibres the limit is set by the onset of SRS, while for longer fibres pulse broadening by SPM sets the maximum launch power – the specific point depending on the pulse shape, the graph showing the limit for Gaussian pulses with m = 1 and 3 and a trapezoidal pulse 200 ns *duration with rise and fall times of 25* ns. *The SBS threshold is lower for longer pulses, however 200* ns *is the longest likely to be used in practice.*

6.6.2. Noise Contributions

Having found that the maximum pulse launch power for a given situation is limited by the need to avoid degradation due to non-linear effects, the noise contributions and audio SNRs for three cases of different fibre lengths, using the maximum launch power from above, are plotted in Figure 6.6.2, for 20 m resolution. The signal in each case is considered to be sampled using an ADC with a full-scale input of 5 V with the EDFA gain set to attain this level at the front of the fibre with a 110 kΩ TIA receiver, assumed to have a bandwidth of 20 MHz.

For a 2 km cable the launch power is assumed to be 1 W and the maximum sample rate of 50 kHz is assumed. To achieve the required output level to use the full dynamic range of the ADC the EDFA gain is 12.5 dB. The figure clearly shows that the most significant noise contribution is ASE-Signal beat from the pre-detection EDFA, with ASE-ASE beat making a lesser contribution. The shot noise and thermal noise in the TIA are negligible. The SNR falls off from 68.4 dB at the front of the fibre at a rate of 0.4 dB / km.

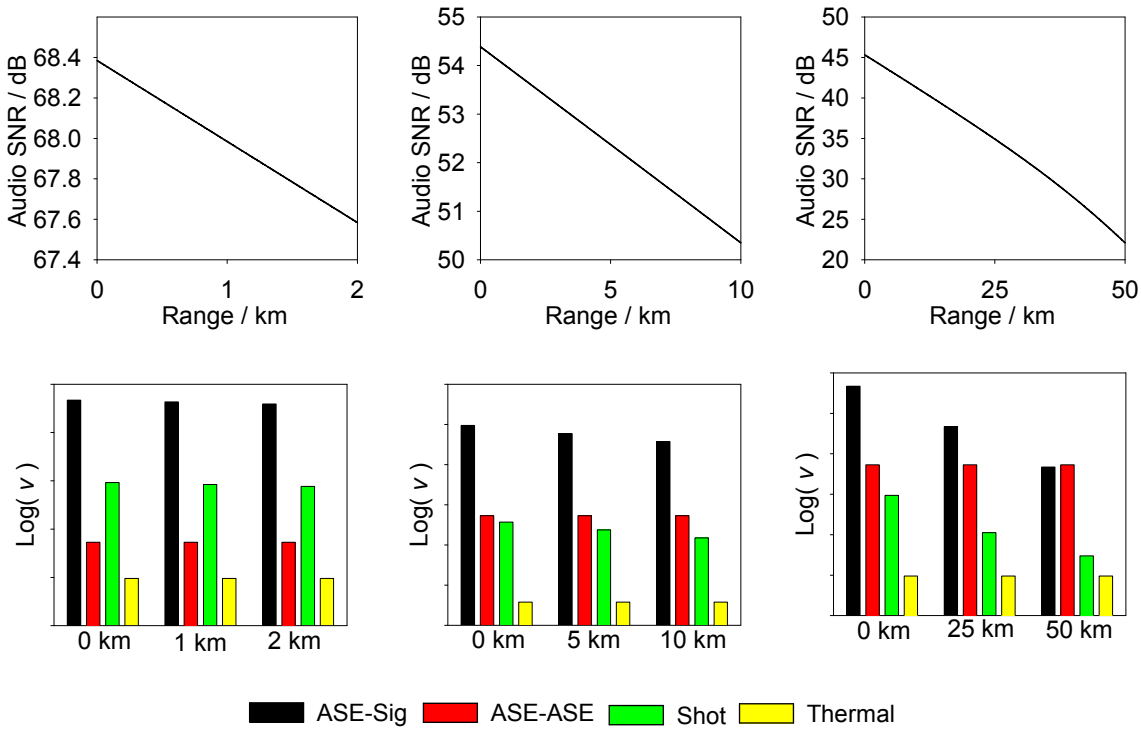

f_s = 50 kHz; P = 1 W; G = 17.8 = 12.5 dB

f_s = 10 kHz; P = 200 mW; G = 89 = 19.5 dB

f_s = 2.5 kHz; P = 100 mW; G = 178 = 22.5 dB

The pulse duration is 100 ns *(20* m*); the gain at the pre-detection EDFA, G, is chosen to match an ADC with full-scale input of 5* V *using a TIA with 110* kΩ *transimpedance and 20* MHz *bandwidth. The launch power is the maximum possible avoiding degradation from nonlinear effects taken from Figure 6.6.1.*

Figure 6.6.2

Noise performance with the sample rate and launch power limited by the fibre length.

Top: Audio SNR as a function of range for different fibre lengths assuming 500 Hz *audio bandwidth.*

Bottom: Relative contribution from different noise sources for difference fibre lengths.

For the case of a 10 km cable, the launch power is reduced to 200 mW and the sample rate is reduced to 10 kHz. To achieve the required TIA output level the EDFA gain is 19.5 dB. The figure clearly shows that the most significant noise contribution is ASE-Signal beat from the pre-detection EDFA. The ASE-ASE beat noise, shot noise and TIA thermal noise remain negligible. The SNR falls off from 54.4 dB at the front of the fibre at a rate of 0.4 dB / km.

In the case of the longest fibre, 50 km, the pulse power is lowered to 100 mW and the maximum possible sample rate is 2.5 kHz and the required EDFA gain is increased to 22.5 dB. The dominant noise source is the Signal-ASE beat at the front end of the fibre, with ASE-ASE beat becoming significant towards the end of the fibre. The mean SNR fall off is 0.46 dB / km although this is more rapid at long ranges due to the ASE-ASE beat noise becoming significant. The variation with fibre length of the SNR, at the front end of the fibre, is due to the need to reduce the launch power to operate at longer ranges to avoid SPM, coupled with the reduction of the sample rate set by the round-trip time-of-flight for the fibre.

This analysis does not consider any degradation other than that due the reduction of backscattered power due to optical loss in the fibre. In practice the SNR may fall off faster than predicted above, as optimum performance will be obtained by balancing increasing the launch power with the resulting degradation of performance with range due to spectral broadening from SPM. Thus the experimental optimum launch power may return a faster SNR degradation in range, along with a better SNR at the fibre front end and no change in the far-end SNR.

An alternative scenario is where only the front section of the fibre is of interest: in this case the optimum launch power will that for a fibre of length equivalent to the range of interest. At longer ranges the launch power must be reduced, but if the early parts of the fibre are not of interest, the pre-detection EDFA gain may be increased, improving the SNR at long ranges at the expense of receiver saturation for the nearer sections of fibre.

In conclusion, while the analysis in this chapter has analysed the important noise sources and the effect that varying the many operational parameters has on the noise performance, there is no single prescriptive equation for the optimum conditions; instead the theory allows the operator understand how to optimise the parameters for the vast array of potential situations in which the sensor may be used.

6.7. Operation in WDM Systems

6.7.1. C-OTDR – Communications Interaction

For some applications, particularly in telecommunications networks where a spare fibre is not available, it may be desirable to operate the C-OTDR sensor on a single WDM channel of an active communications fibre. To evaluate whether this is feasible the possible mechanisms through which the C-OTDR pulse and the communications traffic may interact must be considered.

FWM (Section 6.3.4) could lead to generation of sidebands; however, as discussed earlier, this can be avoided by leaving the WDM channels either side of that used for the sensor unlit. The second mechanism is Cross-Phase Modulation (XPM), which is analogous to SPM, however here the change in refractive index due to light at one wavelength also causes phase modulation to the light at another wavelength.

Where the sensor shares the fibre with communications traffic, degradation of the performance will occur due to XPM as discussed above, and due to interference via FWM. Unlike the XPM case however, FWM will allow the C-OTDR pulse to cause interference to the adjacent communications channels. Provided the nearest-neighbour channels are left unused, however, FWM should not cause a significant problem since XPM will be the dominant mechanism of degradation.

6.7.2. XPM with C-OTDR Sharing a Fibre with Communications Traffic

Consider the simple case of finding the non-linear phase on channel 0 due only to the light in channel 1. Ignoring SPM the non-linear phase due to XPM, ϕ_{XPM}, is:

$$\phi_{XPM} = \left|U_1(0,T)\right|^2 \gamma L_{eff} P_1, \qquad 6.7.1$$

where $\left|U_1(0,T)\right|^2$ is the normalised power envelope of channel one and P_1 is the peak power.

Assuming channel 1 is an active communications channel running at a data rate of f_d b / s, transmitting a bit sequence 0 1 0 1 0 1 0 1 0 1… the signal can be approximated, to first order, as a sinusoid of frequency f_d / 2:

$$\left|U_1(0,T)\right|^2 = \tfrac{1}{2} P_1\left[1+\sin(\pi f_d T)\right]. \qquad 6.7.2$$

Differentiating, as for 6.3.9, the chirp is:

$$\delta\omega(T) = -\frac{\partial}{\partial T}\phi_{XPM} = \tfrac{1}{2}\pi\gamma L_{eff} f_d P_1 \cos(\pi f_d T). \qquad 6.7.3$$

For a typical SONET compliant optical link at 2.488 Gb / s, f_d = 1.244 GHz and typical average optical powers are 4.5 dBm [93]. Assuming 100 % extinction (compared to a typical value of 9 dB [93]) this corresponds to a peak optical power P_1 = 5.6 mW. Taking a typical value of γ = 2 W^{-1} km^{-1} [85] and assuming a long fibre of loss 0.2 dB / km giving L_{eff} = 22 km, the peak chirp generated is 0.5 GHz or 5 pm. This does not pose a problem by causing the C-OTDR pulse to interfere with other channels as the ITU channel spacing is 100 GHz. However, it is considerably larger than the frequency shift needed to alter the coherent backscatter trace, which is given by the reciprocal of the pulse width [63]. Furthermore, since there are likely to be many data cycles in each pulse (a typical pulse width of 200 ns would contain nearly 500 bits at 2.488 Gb / s) the whole pulse will be influenced whereas in SPM only the pulse edges are affected.

Clearly XPM has the potential to seriously degrade the C-OTDR performance when used on a live communications fibre. To estimate the degree of degradation it is necessary to consider the form of the signal generating the phase modulation more carefully. The assumption of a 0 1 0 1 0 1 0 1 0 1… bit sequence is very crude. In reality the bit sequence is likely to be random: each bit has an equal probability of being valued 0 or 1, regardless of the bits preceding it, meaning that long sequences of identical bits may occur [94]. Most coding algorithms limit the number of consecutive identical bits, and insert additional non-data bits into the data stream to accomplish this and balance the content over a pre-determined time interval.

The data pattern in SONET systems, as often used in fibre communications, is well approximated by a long (~ 2^{23} bit, ~ 8 Mbyte) pseudo-random bit sequence (PRBS). Illustrated in Figure 6.7.1, the power spectrum of a PRBS with a bit rate f_b is a series of discrete lines at intervals of 1 / (bit rate × sequence length) scaled in amplitude by $\mathrm{sinc}^2(\pi f / f_d)$, giving nulls at harmonics of the data rate [94]. Applying rules that

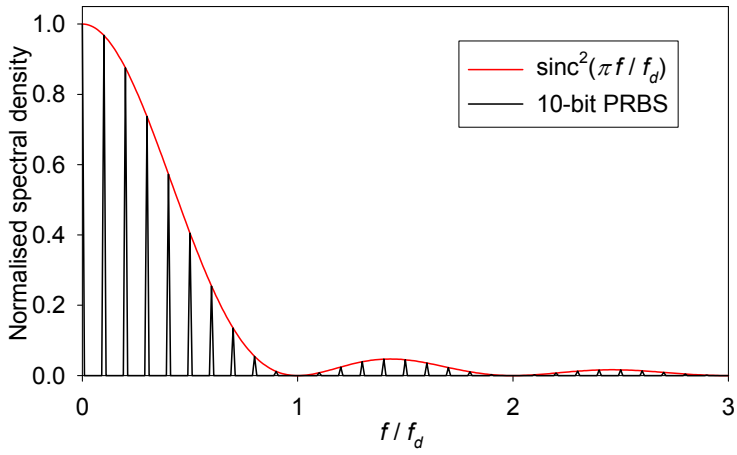

Figure 6.7.1

Spectral envelope for PRBS, normalised to the peak spectral density (in red), with the discrete spectrum for a 10-bit PRBS shown in black. As the length of the sequence increases the lines become closer, until for a non-repeating sequence the spectrum becomes a continuum.

restrict the maximum number of consecutive identical bits will cause a roll-off of the spectrum at low frequency, but with a line at DC remaining to give the DC offset (since optical power can only be positive), however this detail is neglected in the analysis which follows since the effect is likely to be insignificant since it will apply to only a small fraction of the bandwidth of interest.

For very long PRBS patterns, or real random data, as the sequence length becomes very long, the line spacing becomes very small relative to f_b, then the spectral density, $N(f)$, can be approximated as a continuum, with peak spectral density N_d:

$$N(f) = N_d \operatorname{sinc}^2\left(\frac{\pi f}{f_d}\right). \qquad 6.7.4$$

To find the value of the peak spectral density, the spectral density is integrated over all frequencies and the result defined to be equal to the average optical power P_d:

$$P_d = \int_0^\infty N(f)df = N_d \int_0^\infty \operatorname{sinc}^2\left(\frac{\pi f}{f_d}\right)df \,. \qquad 6.7.5$$

The integral can be carried out by making the substitution $X = \frac{\pi f}{f_d}$ and using the standard integral $\int_0^\infty \mathrm{sinc}^2(x)dx = \frac{\pi}{2}$, giving the result:

$$N_d = \frac{2P_d}{f_d}. \qquad 6.7.6$$

The spectral density of the resulting non-linear phase can therefore be written as:

$$\Phi_{XPM}(f) = 2\gamma L_{eff} \frac{2P_d}{f_d} \mathrm{sinc}^2\left(\frac{\pi f}{f_d}\right). \qquad 6.7.7$$

This is the spectrum of the phase noise generated on the fibre at any arbitrary position due to the signal in the data channel. Therefore noise will be generated in the acoustic signal due to the change of phase in the resolution bin being interrogated. As with thermal noise discussed in Chapter 3, only phase noise within the detector bandwidth, B, will be detected, and since $B << f_d$ the frequency dependence of the spectrum may be negated as, for $x << 1$, $\mathrm{sinc}(x) \approx 1$. This may be an overestimate since the roll-off at low frequency due to any maximum number of consecutive bit rules is ignored, however it will serve as an order of magnitude estimate.

The RMS phase noise in the detector bandwidth is given by:

$$\phi_{XPM} = \sqrt{B(\Phi(f=0))^2}. \qquad 6.7.8$$

When sampled at a rate f_s, the phase noise will alias into a bandwidth of f_s / 2, and when low-pass filtered to frequencies below B_{audio} the total RMS phase noise will be:

$$\phi_{XPM} = \frac{2B_{audio}}{f_s}\sqrt{B(\Phi(f=0))^2}, \qquad 6.7.9$$

which, by making appropriate substitutions, becomes:

$$\phi_{XPM} = 6\gamma L_{eff} P_d \frac{B_{audio}\sqrt{B}}{f_d f_s}. \qquad 6.7.10$$

Assuming γ = 2 W^{-1} km^{-1}, L_{eff} = 22 km, P_d = 3 mW, f_d = 2.488 GHz, B_{audio} = 200 Hz, B = 20 MHz and f_s = 4 kHz, the RMS phase noise is 0.02 μrad, corresponding to an SNR limit of 156 dB. This result is surprisingly small, however this is because since the bit rate is very large (~ Gb / s) the majority of the phase noise is much faster than the

bandwidth of the optical receiver. For comparison, the total noise over all frequencies is $2\gamma L_{eff} P_d = 0.26\,\text{rad}$, and the noise in the detector bandwidth is 0.9 μrad.

6.7.3. Conclusion

The considerations of FWM and XPM discussed above suggest that XPM limits the performance by causing spectral broadening of the interrogation pulse, which is broadened by frequency chirps in the GHz range. Since the bit duration is much smaller than the C-OTDR pulse length, this chirp is likely to affect a significant proportion of the pulse, severely reducing the interference visibility, probably to near zero, at all optical ranges. The analysis also shows that if operation of the sensor was attempted, the C-OTDR pulse would not cause degradation of the performance of the communications channel in the fibre, which is critical for operation on a "live" fibre. The XPM shift on the communications channel from the C-OTDR pulse is significantly smaller than the shift from SPM due to the high data rates and associated power gradients at bit-state transitions. FWM can be avoided by suitable selection of wavelengths to separate the data channels and the C-OTDR by more than the bandwidth of the FWM process.

Chapter 7 Further Experimental Investigations

In this chapter a revised experimental system, incorporating changes to improve optical design, based on the work described in Chapters 5 and 6, and using digital signal processing, is described. Following the description of the design, the experimental optimisation of the signal processing and optical launch power is discussed. Brief results, from tests carried out on a deployed fibre, are presented, including trials of long-range operation. Following this latter experiment, a noise analysis is carried out explaining the benefits obtained in the experiment and how they can be incorporated into the optical design. A further, revised, optical arrangement is then described, incorporating this development. Finally, detailed experiments aimed at testing the theoretical spatial response predicted in Chapter 3, in order to optimise the spatial sampling pitch are described. Comparison of the results with the theory shows that modifications are required to the theory to explain the experimental findings.

7.1. Improved Sensor Design – FTAS Rev 2

7.1.1. Background

The experimental work described in Chapters 5 and 6 suggested a number of ways of improving the performance of the sensor system. The Rev 2 demonstration system was constructed to allow testing of improvements to the optical design and to begin developing a system where the acquisition and signal analysis was carried out in the digital domain, allowing software analysis of the independent audio signals from each of the spatial resolution bins over the entire length of the fibre. The system was split into two independent units: one containing the optics and timing functions, the other the control PC and signal processing equipment.

The author was actively involved in the design, testing and evaluation of the system, carrying out a number of experiments to characterise the performance of the demonstration system and its individual components. As summarised, in the table of Figure 1.5.1, the optics and superstructure was constructed by Dr Stuart Russell, with some assistance from the author; the dedicated PC and acquisition system was built by Robert Clarke; the software was written by Barry Fleury, along with the control electronics; and the TIAs were designed by Andrew Lewis.

Item:	**Carried out by:**
Design and construction of optics	JPWH, SR, RJC
Implementation of control electronics	BF
TIAs – design and build	ABL
Software / GUI	BF
Control PC and Acquisition Hardware	RJC / SR

ABL = Andrew Lewis; BF = Barry Fleury; JPWH = Justin Hayward (Author);
RJC = Robert Clarke; SR = Dr Stuart Russell

Figure 7.1.1

Summary of main contributions to the design and construction of the FTAS Rev 2 demonstration system.

Figure 7.1.2

Rev 2 demonstration system: (left) optics module and (right) DSP and control module.

7.1.2. Experimental Features

The optical architecture, shown in Figure 7.1.3, incorporated a number of experimental features aimed at investigating means of improving performance or reducing complexity.

One problem observed with the Rev 1 system was "fading", where the random distribution of the scattering sites leads to reduction in sensitivity at one or more resolution points [66]. The problem was found to be most pronounced in situations where a quasi-point disturbance acts on a fibre in an environment where the acoustic disturbance is rapidly damped, preventing the vibration from spreading across more than one resolution bin. As described in Chapter 5, control of the state of polarisation (SOP) of the launch pulse was found to be only partially successful in mitigating this effect. Clearly, the existence of one or more insensitive regions is problematic for fibre protection and perimeter security applications, so it was considered important to investigate possible means of overcome this drawback.

To investigate a possible means to overcome this problem, the new architecture was designed to operate at two optical wavelengths; separated sufficiently in optical frequency that no correlation should exist between the coherent backscatter traces from each wavelength. The results of Stowe *et al.* [66] discussed in Chapter 3 suggest that "fading" will remain above 10 % of the peak value for 87 % of the time. Thus with two statistically independent sensors the sensitivity of one of the sensors is expected to remain at least 10 % of the peak value for 98 % of the time, significantly improving the probability of retaining working sensitivity.

The fibre laser source, requiring a pump laser, WDM and isolator in addition to the laser itself, formed a significant number of the components used in the Rev 1 optical design. Considerable reduction in component count, and thus complexity, could be obtained if semiconductor DFB lasers could be used as the optical source as well as reducing the space required for the sources and reducing the acoustic sensitivity of the optics assembly. Semiconductor lasers, however, generally have line-widths which are several orders of magnitude larger than those that can be obtained with fibre lasers. Increasing line-width was expected to add noise to the C-OTDR sensor, however the exact increase is difficult to calculate, especially since the greater power obtained from solid state lasers allows the noise performance of the launch EDFA to be improved. Given the large potential savings in complexity and the related economic benefits, the design therefore included both fibre lasers and semiconductor DFB lasers, allowing a direct comparison to be made in an operational sensor.

7.1.3. Details of Rev 2 Optical Architecture

As shown in Figure 7.1.3, the four sources, two fibre lasers and two solid state DFB lasers, are connected to the launch AOM by a network of two WDMs and a 3 dB coupler. The solid state sources, Fitel FOL15DCWB-B-*-WM (* specifies the wavelength), have a specified maximum line-width of 2 MHz and are capable of producing 20 mW CW. The fibre lasers, Southampton Photonics HN02 (line-width < 30 kHz, signal to ASE ratio > 50 dB), were reverse pumped at 980 nm, at approximately 100 mW. With the pump laser driven at the maximum current of 150 mA, the output powers were measured using an Ando AQ6317B OSA to be 7.72 dBm for the 1523.68 nm channel and 9.45 dBm for the 1550.12 nm channel, with signal to ASE ratios of 75 dB and 80 dB respectively. The 1550.12 nm source matched the power of the 1532.68 nm source with the pump current reduced to 120 mA, reducing the signal to ASE ratio to 76 dB. Software-controlled switching allowed each laser to be controlled separately, allowing operation using fibre lasers only, semiconductor DFB lasers only, or one of each.

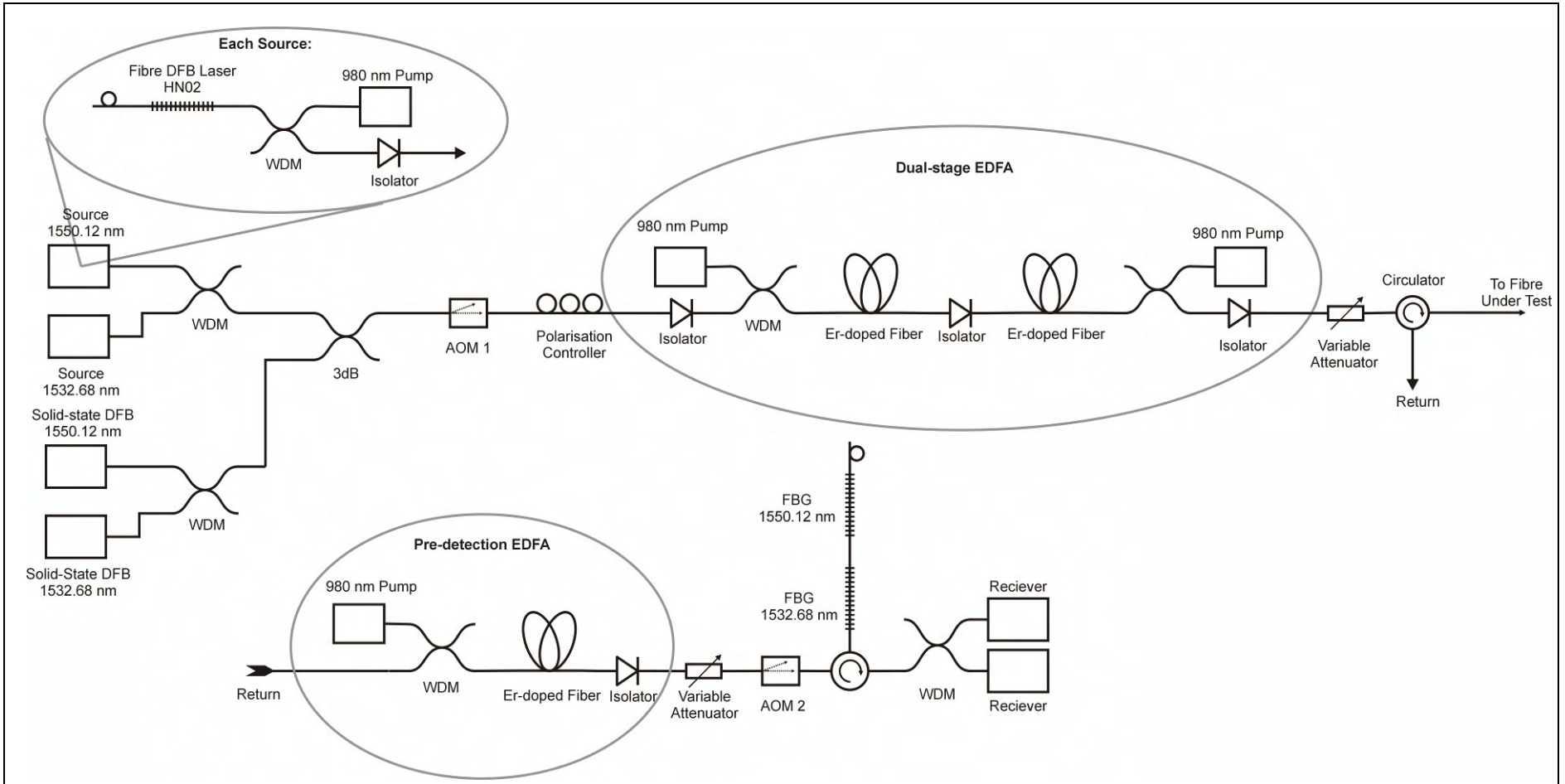

Figure 7.1.3

Optical architecture of the Rev 2.0 demonstration system, as originally built. Extensive testing was carried out with the unit in this form before modifications were made following component failures and further developmental research.

The CW light from the sources is switched using an AOM by Gooch & Housego, a modified M080-2J-F2S, having angled faces on the active crystal to prevent the ghost pulses observed in the Rev 1 unit, giving 10-90 % rise and fall times of 30 ns. The pulse passes through a General Photonics PolaRITE-II piezoelectric polarisation controller (model PCS-3X-NC-7-C), as in the Rev 1.1 system; however, this was not actually enabled, due to the limited improvement gained by SOP control with the Rev 1.1 system in the field trials, described in Chapter 5.

The pulses are amplified by a dual stage EDFA. The first stage is co-pumped and uses a short (~4 m) length of Erbium-doped fibre, ensuring near-perfect population inversion, thus minimising the ASE power. The second stage uses a longer length of Erbium-doped fibre (~10 m) in counter-pumped configuration, giving high saturated output power. The front-end saturation is less important in the second stage, since the signal has already been amplified by the first stage, defining the noise performance. To allow the detrimental effects of SPM to be avoided the pulse power is controlled by a variable attenuator (OzOptics DD-100-MC), which allowed the attenuation to be controlled via the PC, meaning that the power to be easily optimised for different situations. Attenuating the EDFA output is the most suitable means of controlling the launch power, as it allows the power to be varied predictably and without potential noise penalty. Reducing the source power, or EDFA pump powers, would reduce the signal to ASE ratio of the launch pulse, potentially degrading the sensor performance.

The backscattered light, returned via the circulator, is amplified by a single-stage co-pumped EDFA, the output of which is attenuated by a second variable attenuator. An AOM (Gooch & Housego M080-2J-F2S) removes the reflection of the launch pulse from the FUT connector, and from any reflective connectors or mechanical splices in the FUT, which could saturate the receiver, causing a “dead spot” as it recovers. The light is filtered by a circulating filter using two FBGs (SPI FBG06) with 3 dB bandwidth of 0.2 nm and in-band reflectivity of 99.9 %.

The light at each wavelength is then separated by a WDM and passed to two independent receivers. The photodiodes (Epitaxx 06050658-006) have a responsivity of 0.96 A / W at 1550 nm. The TIA has a 110 kΩ transimpedance and bandwidth of 20 MHz with a settling time of 60 ns, corresponding to 6 m. Both the TIAs are mounted in the DSP & Control box, along with the acquisition hardware, allowing the

acquisition card and the TIAs to share an isolated, common ground, avoiding noise from "Earth loops".

7.1.4. Optical Characterisation

The performance of the launch EDFA was measured, by the method described in Chapter 6, using an Ando AQ6317B OSA and an Exfo FOT-90A power meter. The pump lasers for the first and second stages were driven at 203 mA and 220 mA respectively, giving a saturated output power [77] of approximately 17 dBm (50 mW). The saturated output power is only 3 dB larger than for the single-stage amplifier used in the Rev 1.1. However, the benefit from the dual-stage design is not through increasing the launch power (which is limited by the need to avoid non-linear degradation as discussed in the previous chapter) but in the improvement of noise performance obtained by using a short initial stage, ensuring near-perfect population inversion, maximising the signal-to-ASE ratio.

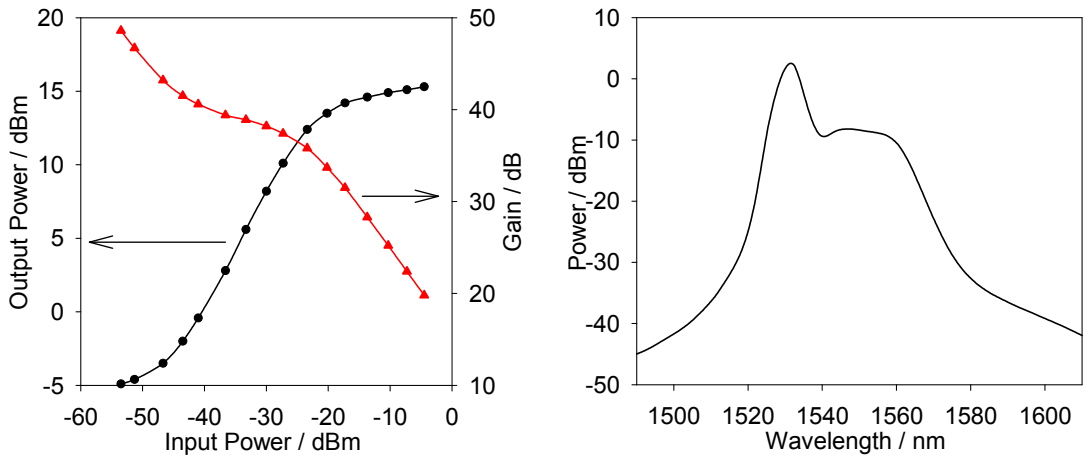

Figure 7.1.4

Left: Gain and output power of the Rev 2 demonstration system dual-stage launch EDFA with varying CW input power and Right: ASE spectrum with no optical input.

By applying approximately 60 dB external attenuation and using the 110 kΩ TIA the performance with pulsed input was measured. With a pulse of width 97 ns, period 40 μs, the pulse power was measured to be approximately 17 W at 1532.68 nm and 10 W at 1550.12 nm.

7.1.5. Control Electronics

In addition to the RF switching functions required in the previous system, the control system was now required to generate appropriate control signals for the ADC card, controlling the acquisition process. The control electronics are illustrated, schematically, in Figure 7.1.5 and the details are discussed below.

The system is controlled by software running on the PC, within the DSP & Control box, which connects to the acquisition card via the PCI bus and controls the FPGA and DDS via the parallel port. The FPGA is required to generate pulses to control the launch AOM, the blanking AOM and the trigger and clock signals for the ADC card. It is crucial that the ADC clock remains synchronous with the launch pulse, since any variation in the delay between launch and the clock edges, which define the sample locations, will cause amplitude noise on the decoded audio signal. Barry Fleury designed a PCB containing the FPGA, clock and DDSs to fulfil these criteria. The RF splitter, switches and power amplifiers were standard components, manufactured by Mini-Circuits.

The ADC card (ICS-652) has two, DC-coupled, channels with input bandwidth from DC to 43 MHz (-3 dB point). The maximum sample rate is 65 MHz and the ADC resolution is 14 bits. The Signal / (Noise + Distortion) ratio is 70 dB, i.e. an effective bit depth of 11.6. The input range is -1.2 V (0000) to +1.2 V (3FFF), so, in order to minimise the contribution of quantisation noise, the receivers incorporate a stable reference and an adder to offset the output by -1.0 V, making use of a greater fraction of the ADC dynamic range than would be possible with a zero-offset signal, where negative half of the input range would be wasted.

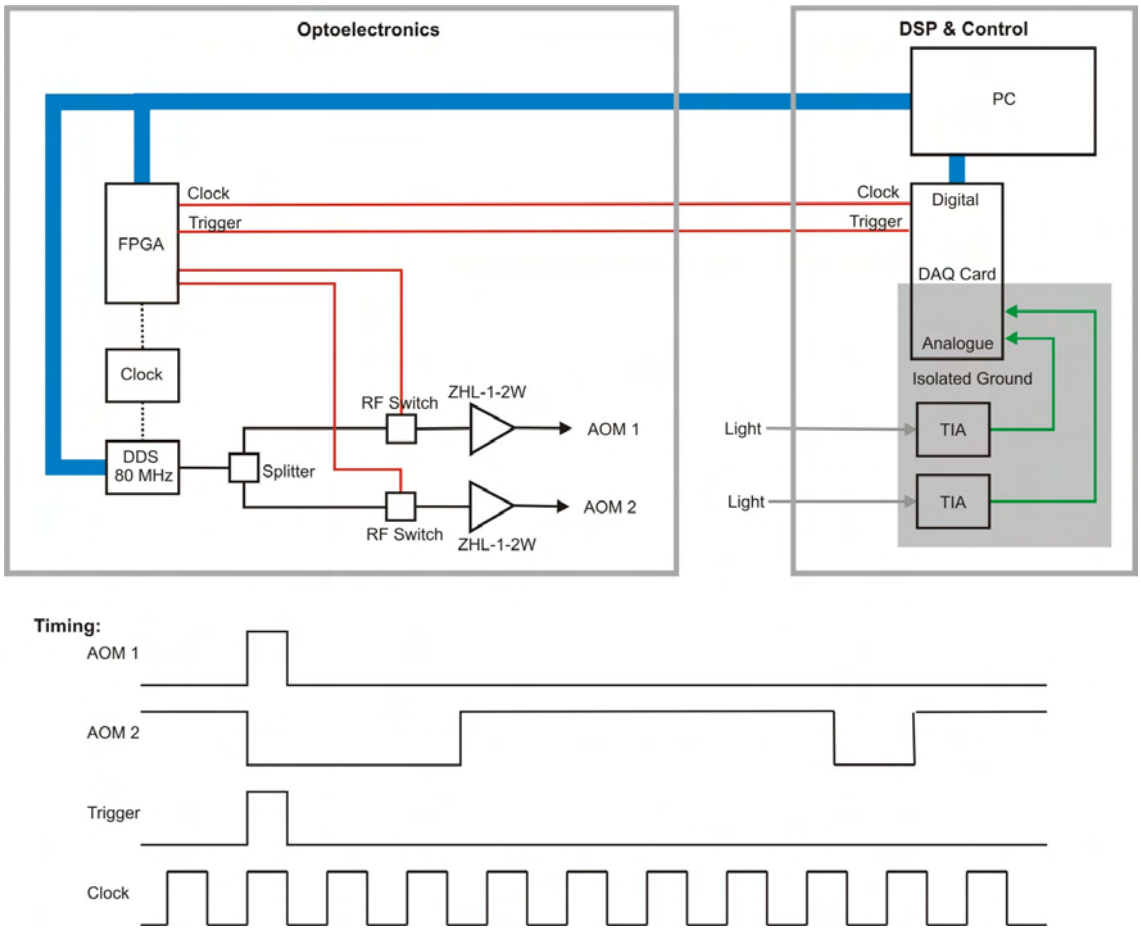

Figure 7.1.5

Schematic diagram of the control hardware for the FTAS Rev 2 demonstration system. The analogue ground is isolated from the PC ground to avoid "Earth loops" causing additional noise. As drawn the ADC, which is triggered on the rising edge of the sample clock, corresponds to a sample pitch on the FUT equal to the spatial extent of the pulse. The clock must remain synchronous with the launch of the pulse; otherwise amplitude noise will be generated as the sample point moves along the coherent backscatter trace.

7.1.6. Signal Processing

The acoustic signal from each resolution bin was to be monitored simultaneously and displayed as part of a histogram, representing the magnitude of the signal along the fibre. A purpose-built PC was to be used to carry out the control functions and the signal processing. Although it was known that this would limit the total number of bins that could be simultaneously processed, for experimental purposes the flexibility of

signal processing in C++ code, running on a PC, out-weighed the increased processing power possible using DSP hardware.

The data flow for the signal from a single resolution bin is illustrated in Figure 7.1.6. The sample from the ADC, representing the resolution bin of interest, passes to a digital high-pass filter, the cut off frequency being chosen to reject as much of the low-frequency environmental noise as possible while retaining the useful components of the signal of interest. The second filter defines the noise bandwidth, B_{audio} and the audio signal, which can be output via the PC sound card. The data then passes to a third filter, which is arbitrarily shaped, to allow the histogram selectivity to be modified. For general purposes this will be another low-pass filter at some audio frequency, or may be optimised for a specific application, for example for monitoring traffic it may have a low cut-off at a few tens of hertz, or for locating a known disturbance, such as the AST, it may be a narrow-band filter at the known disturbance frequency.

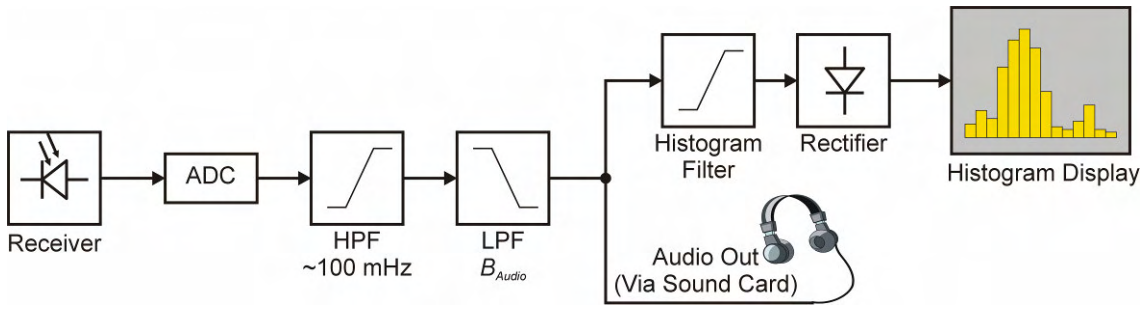

Figure 7.1.6

Data flow for a single resolution bin in the Rev 2 demonstration system. The HPF removes slow thermal drift and very-low frequency environmental noise. The anti-aliasing LPF reduces the bandwidth to the required audio bandwidth, defining the noise performance. The histogram filter allows the response to be shaped to emphasise specific signals. The rectifier determines the signal magnitude and feeds the data to the correct resolution bin on the histogram display.

As discussed in Section 7.1.2, it was intended to develop an algorithm to combine the data from two optical channels to reduce the probability of fading; however, this was not implemented, since the fibre length and sample rate was already limited by the available processing power with only the signal processing described above.

The information is output through the graphical user interface (GUI) in the form of a histogram, with each bar representing the signal from a single spatial sample point. Considering a single resolution bin, the filtered audio data is rectified and the signal

added to the current histogram value. At the same time a decay constant is applied to the histogram, reducing the bar amplitude by a defined fraction each cycle. The result is that the histogram displays a combination of the size and duration of a disturbance: a short intense disturbance will give a similar sized peak output to that from a moderately sized continuous signal. Provision is made in the GUI to vary the rate of decay and the relative weighting of any new signal to optimise the performance in different situations. A typical histogram display from an installed fibre is shown in Figure 7.1.7. The software included the provision for defining alarm thresholds for alerting the user to suspicious signals; the final objective being to develop a geographically-based display showing the cable route, or protected perimeter, and highlighting the location of signals requiring further investigation.

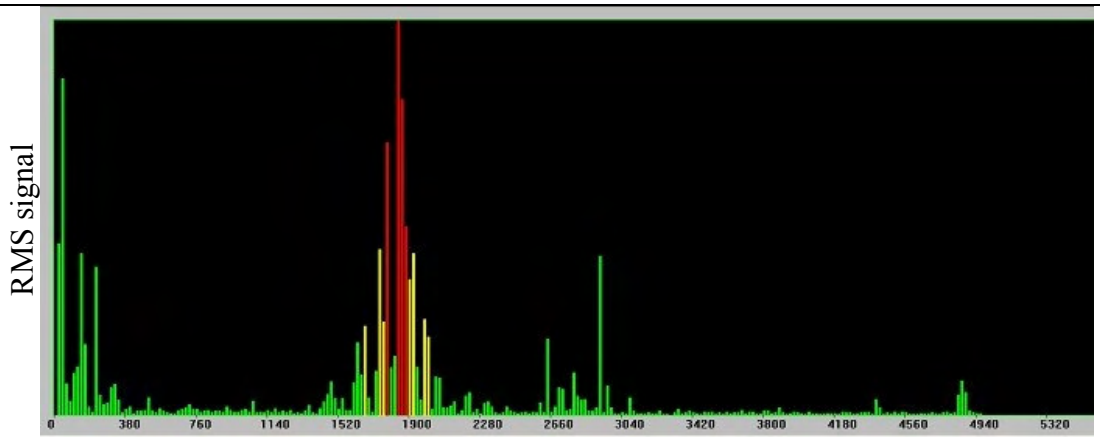

Figure 7.1.7

Typical histogram display from an installed fibre, showing the sophisticated GUI developed by Barry Fleury. The upper plot is a small section of the fibre, the whole of which is shown in the lower plot. The red and yellow marks show the alarm thresholds for a "warning" and "alarm" respectively. The coloured bars on the histogram are where an alarm threshold has been exceeded and is either unacknowledged or remains above the threshold.

7.2. Performance Optimisation

7.2.1. Comparison of Fibre Lasers and Semiconductor DFB Lasers

As explained in the previous section, there would be technical and economic benefits if the fibre-laser sources could be replaced with semiconductor lasers. To investigate this possibility, the design included fibre laser sources and solid-state semiconductor lasers to allow direct comparison of the performance with each. The performance with the 1550.12 nm fibre laser was compared with the performance with the semiconductor laser at the same wavelength, with the drive current set to deliver the same optical power into the launch EDFA ensuring that the source type was the only variable. With the latter, the audio signal and histogram SNR were significantly degraded with additional white noise across the spectrum.

This is the result of the larger spectral line-width of the semiconductor source: <2 MHz compared to <30 kHz for the fibre lasers. It was shown experimentally, in Section 6.4.3, that varying the optical frequency of the pulse causes the backscatter intensity from a single point to vary as a sinusoid, with period $2/\tau$ where τ is the pulse duration. Because of this variation in the coherent backscatter intensity with frequency, a source of finite line-width will generate an intensity noise on the coherent backscatter signal, as shown in Figure 7.2.1.

The RMS slope of the backscatter response is $\frac{\pi\tau}{2\sqrt{2}}$ to a frequency shift. Thus, for

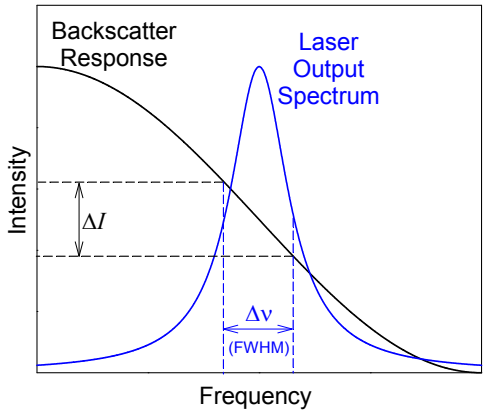

Figure 7.2.1

Conversion of finite line-width, $\Delta\nu$, to intensity noise, ΔI, by the variation in coherent backscatter intensity with frequency.

a FWHM line-width of $\Delta\nu$ the RMS intensity noise is approximately:

$$\Delta I_{RMS} = \frac{\pi\tau}{2\sqrt{2}}\Delta\nu . \qquad 7.2.1$$

The limit on the electrical due to this effect is $\sim\left(\frac{1}{\Delta I_{RMS}}\right)^2$, so, noting that $2\sqrt{2} \approx \pi$ the limit on SNR, due to finite source line-width, is:

$$SNR \sim \frac{1}{(\tau\Delta\nu)^2} . \qquad 7.2.2$$

For a pulse of duration 100 ns (20 m) this gives a limiting SNR of 50 dB for the fibre laser, assuming a line-width of 30 kHz (the specified maximum) and 14 dB for the semiconductor lasers, assuming a 2 MHz line-width (the typical value). These SNR estimates are likely to be conservative, since the lasers will emit more light close to the centre wavelength than at the edges. A more sophisticated analysis would integrate the noise over the laser spectrum; however, the general behaviour is likely to remain similar to this simple analysis.

These considerations also explain the observations in Chapter 6, section 6.5, that, with a broader source, the critical power due to SPM was ~20 mW lower than with the narrow fibre laser source, since the spectrum was already broader, requiring less broadening by SPM to reach the critical condition.

As a result of these observations, it was decided to discontinue experiments with the semiconductor laser sources, the increased complexity of the fibre lasers being justified by the better performance.

7.2.2. Measurement of SPM Threshold

It was shown in the previous chapter that to obtain optimum performance the pulse power must be chosen to avoid excessive spectral broadening by SPM. To allow determination of the correct attenuator settings, for the revised design, the intra-pulse interference experiment was repeated with the Rev 2 demonstration system, using the revised experimental architecture shown in Figure 7.2.2. The attenuator, after the test fibre, attenuated the light sufficiently so that no significant evolution occurred due to SPM within the arms of the interferometer. Two further variable attenuators were built

into each arm of the interferometer, allowing the output from each to be balanced to ensure that 100 % interference visibility could be achieved.

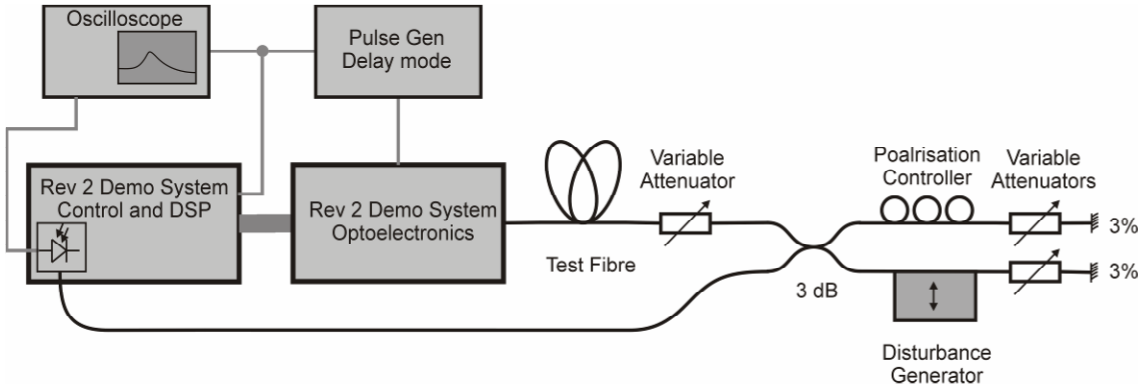

Figure 7.2.2

Improved experimental layout for investigation of interference degradation from self-phase modulation with the Rev 2 system. The pulse generator provided a delayed trigger pulse for the oscilloscope. The attenuator, after the test fibre, allowed the power to be reduced, thus eliminating spectral evolution within the interferometer fibre. Additional attenuators, in each arm of the interferometer, allowed the power reflected from each arm to be balanced.

The power launched into the fibre was controlled using the variable attenuator in the launch stage of the demonstration system. The pulse power was measured, with no applied attenuation, using the demonstration system's receiver and an external attenuation of 60 dB, to be approximately 8 W, although the uncertainty in this measurement is large, perhaps as much as 3 dB, due to instability of the external attenuation and possible overshoot in the receiver.

The interference visibility is plotted as a function of the calculated launch power in Figure 7.2.3 along for fibre lengths of 1.8 km, 26 km and 48 km. Reading from the graph, the visibility falls to 90 % at powers of approximately 5000 mW, 600 mW and 300 mW respectively. The analysis in Chapter 6 shows that the critical power should be inversely proportional to the effective length, so the 90 % powers are plotted in Figure 7.2.4 against the reciprocal of the effective length. The good fit confirms that the critical power is inversely proportional to the effective length.

The measured critical powers are a factor of approximately 4 larger than those measured using the Rev 1.0 demonstration unit. This is possibly because the dual-stage launch EDFA generates a differently shaped pulse than that in the Rev 1 system,

allowing higher powers without degradation; however, experimental error in the pulse power measurements is also possible. The measurements could have been improved by building a low-transimpedance, high-speed TIA and, using a stable attenuator, measuring the pulse power and shape, however this was not possible due to time constraints.

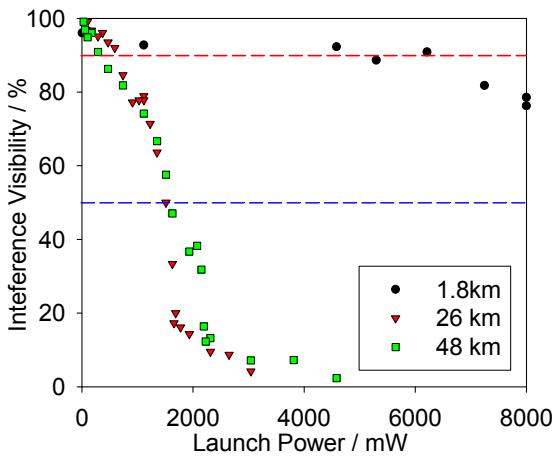

Figure 7.2.3

Experimental results showing the effect of launch power on interference visibility for fibres of length 1.8 km*, 26* km *and 48* km *with 200* ns *pulses. The 50 % values are approximately equal for 26* km *and 48* km *however the shape of the decay varies.*

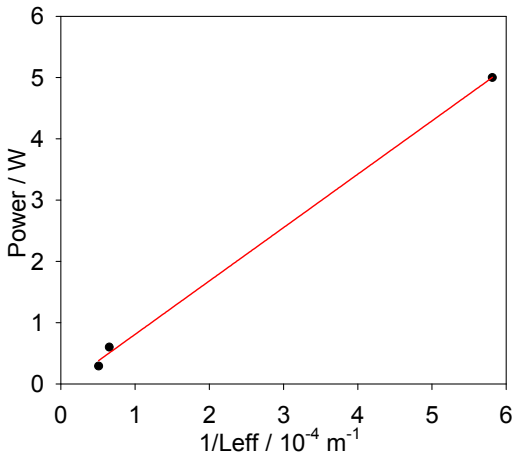

Figure 7.2.4

Experimental values of the launch power where the visibility is reduced to 90 % plotted against the reciprocal of the effective length, showing the length dependence expected from the theoretical analysis.

7.2.3. Launch Power Optimisation

In practice, when optimising the launch power, the data measured in the previous section was used as a guide to a suitable starting point from where adjustments were made, increasing and reducing the launch power iteratively until the best performance was obtained at the region of interest. Small differences may occur because the measurements above do not consider the benefit conferred by the increased backscatter power increasing the receiver SNR.

7.2.4. Filter Optimisation

As described in Section 7.1.6, a digital high-pass filter was incorporated into the data path to remove the low-frequency environmental noise. To optimise the filter characteristics the frequency content of the noise and the signals of interest must be

considered. The approximate frequency range of various signals is illustrated in Figure 7.2.5, based on the observations in Chapter 5 and measurements in the literature. Significant energy is often present at low frequencies, particularly for signals from heavy plant which has sufficient weight to cause permanent deformation of the ground in addition to impulsive vibration.

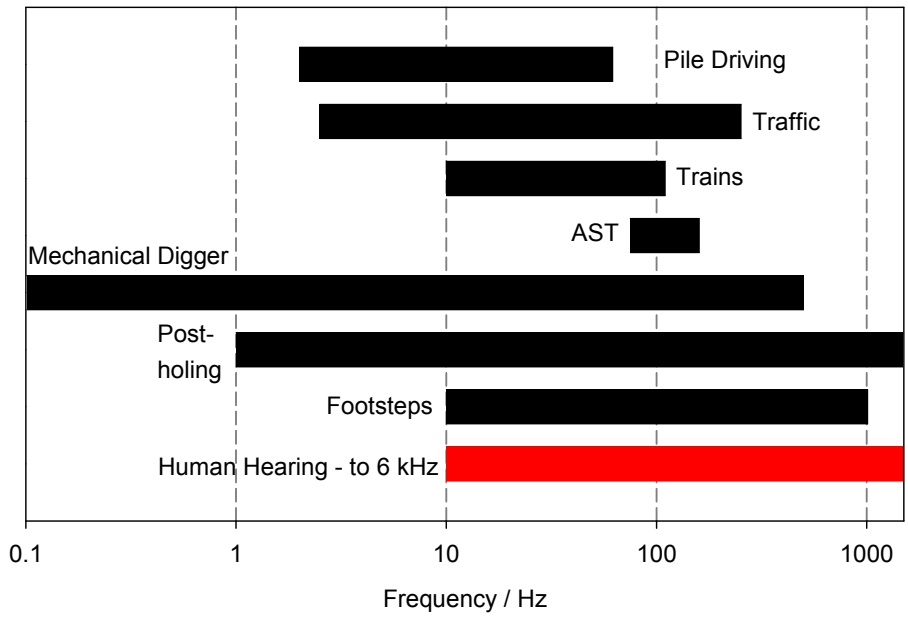

Figure 7.2.5

Frequency content of ground-borne signals from Chapter 5 and typical values for trains, pile driving [95] *and road traffic* [96].

The results of the experiments using the AST, described in Chapter 5, showed that the attenuation of the ground increases with frequency, meaning that the background noise spectrum is likely to be weighted towards low frequencies. Practical experimentation showed that the optimum filter cut-off was ~100 mHz, giving significant noise attenuation, removing almost all the noise from the slow environmental evolution of the backscatter trace, while allowing the signals of interest to pass without significant attenuation.

7.3. Field Evaluation of Rev 2 System

7.3.1. Background

To investigate the capabilities of the Rev 2 demonstration system in a typical telecommunications environment, extensive field trials were carried out on installed fibres in the USA. The aims were to prove the ability to observe the signals along an entire fibre simultaneously, allowing areas of interest to be investigated; to demonstrate the response to a greater variety of real threats to telecommunications fibres; and to show the power of the AST-based approach to geographic fault location and correlating optical distances to geographical location for improved cable route documentation.

7.3.2. Cable Route

The testing was carried out using the same cable as for the earlier tests using the Rev 1 system shown in Chapter 4, Section 4.5, providing a 5 km length for short-range testing. Where testing at longer ranges was required, this cable was patched to an additional cable at the termination building which added an additional 49 km giving a total length of 54 km. This second cable ran for approximately 10 km in relatively un-populated areas, then following a major interstate for of the order of 10 km. The remainder was through built-up "down-town" areas, generally under roads with frequent manhole access.

During the on-site system optimisation, it was noted that the audio noise appeared to be lower on the short, 5 km, route, even when all other parameters remained unchanged. It was realised that this was due to a problem with the revised optical architecture which had been overlooked. Since the ASE from the launch amplifier is not blocked, Rayleigh scattering of the ASE takes place over the entire fibre length, effectively reducing the signal to ASE ratio of the light scattered from the front of the fibre by a factor of Λ/L_{scat} , where Λ is the pulse width and L_{scat} is the effective scattering length, taking into account the fibre attenuation over the fibre. When the Rev 1 system was modified and the second AOM was relocated to block reflections that saturate the detector, a quick test was carried out to check that the noise was not increased, but this was done on a fibre of length ~6 km, where the total scattered ASE power is significantly less than from a 50 km fibre. From equation 1.4.1, the back-scattered power reaching the receiver from a pulse of width *dz* at range *z* is:

$$dP(z) = \tfrac{1}{2}\alpha_s S P_0 e^{-2\alpha z} dz \,. \qquad 7.3.1$$

Integrating from $z = 0$ to L the total scattered power is:

$$P = \tfrac{1}{2}\alpha_s S P_0 L_{Scat}, \qquad 7.3.2$$

where the effective scattering length is given by:

$$L_{scat}(L) = \int_0^L e^{-2\alpha z}\, dz = \frac{1 - e^{-2\alpha L}}{2\alpha}. \qquad 7.3.3$$

For short fibres, where the scattered ASE power remains less than the ASE power at the front end of the pre-detection amplifier, no SNR degradation occurs; however, for longer fibres, where the scattered ASE power is larger than the front end noise of the pre-detection amplifier, the SNR will be reduced; hence the observed degradation on the 54 km cable.

7.3.3. Geographic-to-Optical Mapping with AST

A number of improvements had been made to the AST, after the measurements reported in Chapter 2, to improve its performance for mapping geographic location to optical range. To enable location of the acoustic signal, even when strongly attenuated by the ground, in the presence of strong acoustic background noise or at long ranges with reduced audio SNR, the AST was frequency-locked to a crystal oscillator allowing the histogram display to make use of a narrow (1 Hz) band-pass filter, to remove other signals, allowing the AST to be easily seen without ambiguity. The long stake on the AST was replaced by an aluminium plate, (200 × 150) mm, with a sheet of 6 mm thick rubber fixed to the underside, giving much improved coupling to the ground, particularly on hard surfaces such as roads and paving slabs. The modified AST is shown in Figure 7.3.1: the striped tape on the rotating head is monitored by an optical sensor and appropriate electronics for the crystal-locking circuit, designed by Andrew Lewis. The frequency when locked was set to 80 Hz, giving a good level of energy transfer to the soil and allowing operation down to a low level of battery charge.

With the 1 Hz filter applied to the histogram input, the AST was easily located in the acoustic noise present on the cable, without prior knowledge of its location. In one test, the AST was operated at the point, at ~ 3 km range, where the cable passes under the interstate. With the AST located approximately 3 m from the carriageway, despite the large, continuous, acoustic signals from the busy road, with most of their energy in the 0 Hz to 100 Hz band, with the 1 Hz band-pass filter at the histogram input, the AST signal was clearly visible, of the order 30 dB above the acoustic background noise.

Figure 7.3.1

Main Picture: Operating the AST above the fibre route at Site 2. Inset: The modified AST's internal construction – the striped tape is for the frequency-

Vertical scale: 0 Hz *to 500* Hz

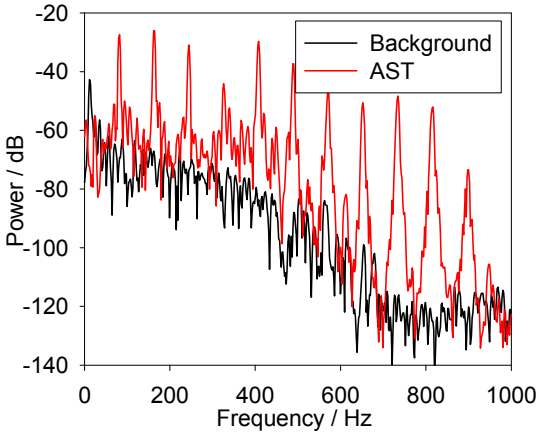

Figure 7.3.2

Response to AST at 130 m *range on grass at 20* m *resolution, 4* kHz *sample rate.*

The audio output obtained from interrogation of the 5 km fibre with the modified AST located on grass at Site 1, range 130 m, is shown in Figure 7.3.2. The sampling rate was 4 kHz, limited by the processing power required to apply the filters etc, not the round-trip time for the 5 km fibre length. The spectrograph illustrates the stability achieved by crystal-locking while the lower graph shows the 4096-point FFT of the spectra with and without the AST operational, generated using digital data from the demonstration system. The FFT bin width is ~1 Hz so the spectrum in Figure 7.3.2 is close to the histogram performance with the 1 Hz band-pass filter.

Assuming the power of the launch pulse to be 200 mW, the power expected to be backscattered from the front of the fibre is 0.57 µW, requiring attenuation to reduce the pre-detection EDAF gain to 33 (15 dB) to avoid saturating the TIA. The expected SNR at the receiver output is therefore 42 dB. The sampled data is recorded immediately after the high-pass filter, but with no other processing applied so there is no improvement from over-sampling, meaning that the expected audio SNR is 42 dB.

The audio SNR in Figure 7.3.2, taking into account the whole noise spectrum, is ~ 36 dB, which compares well to the predicted figure, particularly as some reduction from the backscattering of the launch EDFA ASE from the whole fibre and acoustic background noise would be expected.

7.3.4. Telecommunications Protection Evaluation

Tests were arranged to prove the sensor's ability to detect threats to the cable from a variety of sources typically placing installed telecommunications cables at risk. In addition to repeating the tests with the mechanical digger, the response to a horizontal borer and a trenching machine ("Ditch-Witch") was demonstrated at a range of ~1 km. The acoustic signals from each of these operations were easily observed, and the re-constructed audio appeared sufficiently different in each case that a suitable signal-recognition system could separate them.

The horizontal borer and the trencher were both operated along a route parallel to the cable, allowing the progress to be observed on the histogram display as the cutting head moved along successive resolution bins. The horizontal borer was particularly interesting since, approximately every 2 m, additional rods are inserted, during which time the rotation is stopped, giving very little signal, the impact of the new rod meeting the existing rod is easily observed, as is the resumption of rotation when the machine re-starts.

7.3.5. Long-Range Operation

To investigate the operation of the C-OTDR sensor at long optical ranges, where tests with the Rev 1 system had shown poor performance, and in different acoustic environments, the AST was used at various points along the 54 km cable route, being detectable at ranges approaching 50 km, showing the improvement made since the trials with the Rev 1.1 system described in Chapter 5 where no signals were observable at these ranges. To enhance the performance at long ranges, the return attenuator was adjusted to increase the effective gain of the pre-detection EDFA stage, with the blanking AOM shut for the near end of the fibre to prevent receiver saturation. The light returned was further increased by operating at 50 m pulse length. The sampling rate was 1 kHz, limited by the processing power, the round-trip time setting the absolute maximum rate as 1.8 kHz.

As usual, the spatial sampling pitch was equal to the pulse width, 50 m. The theory of Chapter 2 indicates that the sensitivity decreases as a disturbance location moves

away from the centre of a resolution bin, having FWHM of 87 % of the pulse width. Ignoring any blurring effect of the detector, for a 50 m pulse this predicts a region of fibre between the sample points with sensitivity less than half the peak value of 7 m in length. The TIA settling time was equivalent to 6 m, suggesting that a minimum sensitivity of half the peak value would be maintained over the whole fibre so long as acoustic transmission carried the disturbance over a few metres of fibre, as would be expected for buried fibre. In practice, however, it was found that the sensitivity appeared to fall to near zero when the disturbance was between sample points, suggesting the need for further investigation. The problem was overcome by sampling at a pitch of 25 m; instead of 50 m as would usually be the case. Because of the large number of sampling points required, this meant that the total length of fibre which could be monitored was significantly reduced due to the limitations of the signal processing hardware.

Assuming a launch pulse power of 100 mW, the light returned from a range of 40 km is 17.8 nW, requiring a net EDFA gain of 1160 (30 dB) to give a 2 V signal. Using the known system parameters and assuming a full population inversion in the pre-detection EDFA, the expected SNR at the receiver is 29 dB. For the audio bandwidth of 500 Hz, there is no over-sampling advantage from the 1 kHz sampling rate, so the expected audio SNR is also 29 dB. By comparison, if it was also desired to operate at the front of the fibre, the pre-detection EDFA gain would be reduced to 28.5 (15 dB) to give a 2 V signal from the front of the fibre, giving an SNR at 40 km of 12.4 dB.

The recorded data is shown in Figure 7.3.3. The spectrograph on the left shows the stability of the frequency-controlled signal and the presence of a large number of harmonics. There is also a signal at non-harmonic frequencies, probably as a result of operating the AST on a hard surface, where the coupling is poorly matched, giving non-linear components in the vibration. The peak at the 80 Hz fundamental is ~42 dB above the background level. Considering the noise over the whole bandwidth, assuming the AST signal is entirely contained within a single FFT bin, this corresponds to an SNR of 24 dB. This is 5 dB lower than expected, probably due to the scattering of ASE from the launch amplifier from the whole fibre and acoustic background noise.

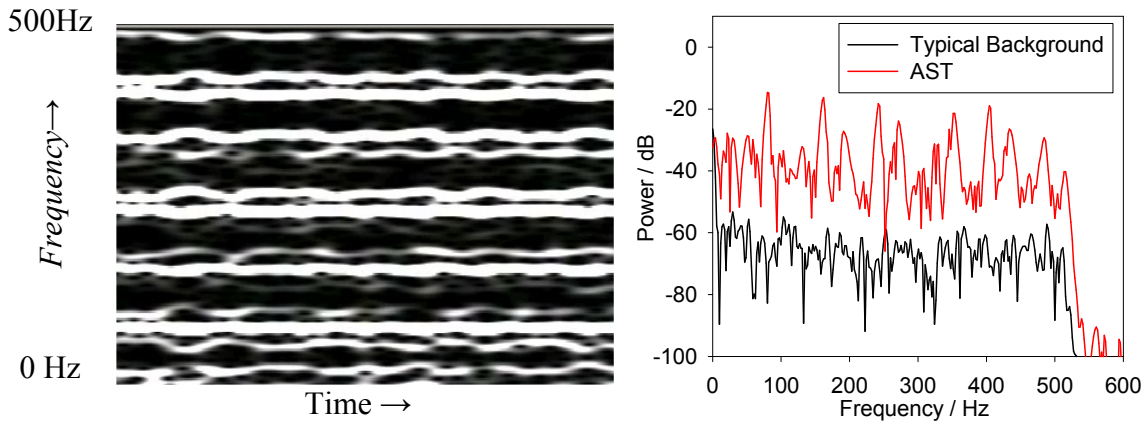

Figure 7.3.3

FTAS Rev 2 audio output from disturbance generated by the AST at a range of 43.1 km, *operating at 50 m spatial resolution and 1* kHz *sample rate, with the EDFA gain increased to improve long-range performance at the expense of saturating the receiver at the front of the fibre. The presence of a number of additional frequencies is probably the result of non-linear coupling into the soil due to the hard surface.*

7.4. Asymmetric Split Detection for Long Cables

7.4.1. Introduction

Having shown, experimentally, that the operation of the sensor at long ranges can be improved by increasing the pre-detection EDFA gain and blocking the light from the front of the fibre, it was realised that this benefit, in the long-range performance of the C-OTDR sensor, can be obtained, without affecting the short-range performance, by using an asymmetric coupler to direct the amplified returned light to two identical receivers as shown in Figure 7.4.1. For high light levels the signal from the weaker branch is used and for lower light levels the stronger branch is used, effectively increasing the dynamic range available. Asymmetric optical splitting is more effective than using receivers with different transimpedance, because the best receiver performance is always obtained for the highest transimpedance possible while maintaining the desired bandwidth.

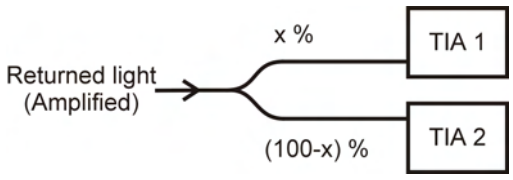

Figure 7.4.1

Increasing dynamic range by splitting light using asymmetric coupler. The light from each branch passes to one of two identical transimpedance amplifiers, TIA 1 and TIA 2.

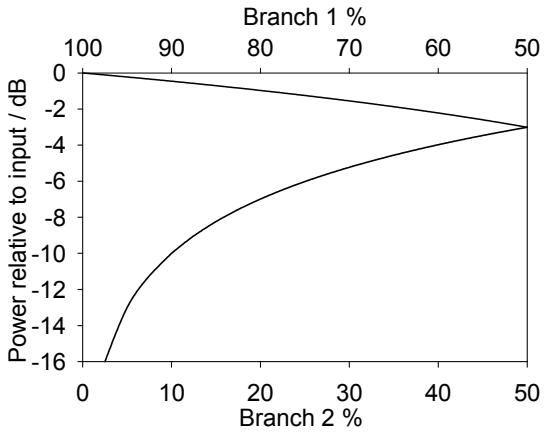

Figure 7.4.2

Power from each branch relative to input

7.4.2. Choice of Change-Over Point

Firstly, consider the case of long cables, shown in Figure 7.4.3, where it is desired to give the best possible performance at long ranges, while remaining operational over the entire fibre. Defining the splitting ratio, R, as:

$$R = 10\log\left(\frac{100-x}{x}\right)\text{dB}, \qquad 7.4.1$$

the best overall performance is obtained when the two-way loss in the first section is equal to this ratio. Moving either side of this point either saturates one of the detectors

or wastes dynamic range. The maximum changeover range, in kilometres, is therefore given by:

$$z_{ch}\big|_{\max} = \frac{R}{2\alpha_{dB}}(\text{km}), \tag{7.4.2}$$

where α_{dB} is the fibre attenuation in dB / km. For the example shown in Figure 7.4.3, with a 90/10 % coupler where R = 9.5 dB and attenuation of 0.2 dB / km, the maximum switchover range is 23.75 km.

For shorter cables, to make maximum use of the additional dynamic range afforded by using two receivers, the change-over point between the two branches should be at the point where the far-end operational dynamic range is equal in both detectors, as shown in Figure 7.4.4. By simple geometry, this occurs when:

$$2\alpha_{dB}\left(L - z_{ch}\right) = R, \tag{7.4.3}$$

where L is the cable length in kilometres. Rearranging, we obtain the changeover range as a function of the splitting ratio of the asymmetric coupler and the cable length:

$$z_{ch}\left(L, R\right) = L - \frac{R}{2\alpha_{dB}}(\text{km}). \tag{7.4.4}$$

Clearly, it is meaningless to change between detectors at negative ranges, so for lengths less than $\frac{R}{2\alpha_{dB}}$ just one receiver should be used, furthermore, as calculated in 7.4.2, there is no benefit in changing between detectors beyond $\frac{R}{2\alpha_{dB}}$. Combining these arguments, and considering a 90/10 % coupler, the optimal changeover point is as plotted in Figure 7.4.5.

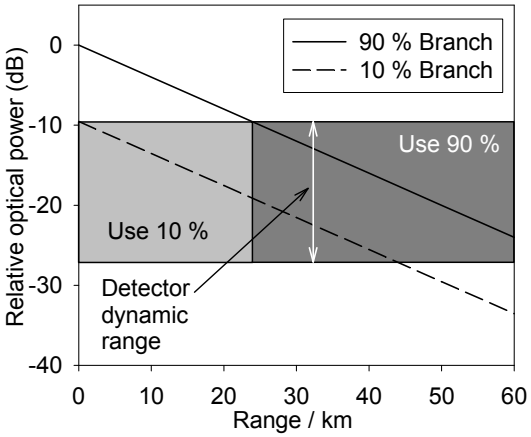

Length > *48* km

Figure 7.4.3

Illustration of branch switching for long cables assuming branches of 10 % and 90 % and a one-way fibre loss of 0.2 dB / km.

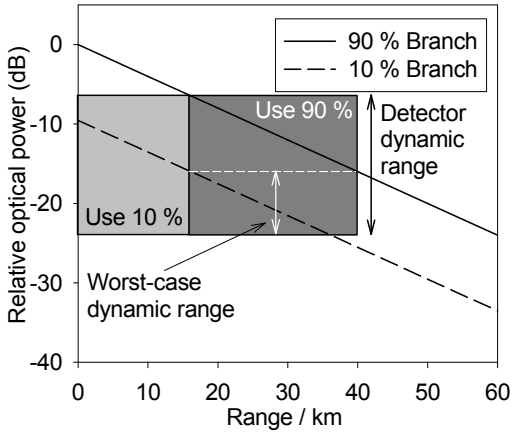

24 km < *Length* < *48* km

Figure 7.4.4

Illustration of branch switching the short-cable case: the switchover point is defined as the range that gives equal reduction of performance at the far end of the receivers' range.

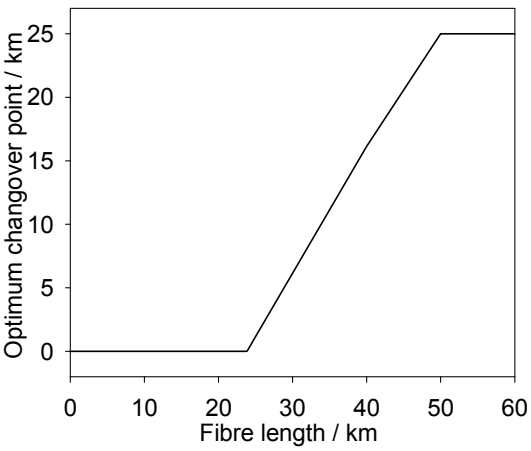

Figure 7.4.5

Optimum changeover range for 10 % and 90 % split, with fibre loss of 0.2 dB / km. *There is no benefit in changing earlier as either the 90 % receiver will be saturated or the 10 % receiver will be under-illuminated.*

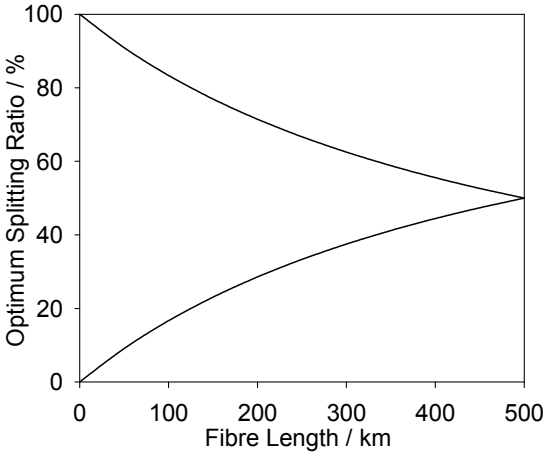

Figure 7.4.6

Optimum splitting ratio as function of fibre length. The range limit due to the dynamic range of the receivers is ignored, although in practice this is the main limitation on performance.

7.4.3. Optimum Splitting Ratio

In the examples above, the splitting ratio has been considered fixed and the optimum changeover point for different cable lengths has been calculated, without considering optimising the splitting ratio for the coupler. Where it is possible to fix the splitting ratio, for a specific length, the best performance is obtained where the degradation at the far end of each detector's range of operation is equal. For the optimum splitting ratio, this will set the changeover point at the centre of the cable, where the two-way loss is $\alpha_{dB} L$. The optimum splitting ratio is therefore $R = \alpha_{dB} L$ dB, plotted in Figure 7.4.6 assuming a fibre attenuation of 0.2 dB / km. For a 50 km fibre, the optimum splitting ratio is R = 10 dB, equivalent to a 81/9 % coupler, close to the 90/10 % chosen in Section 7.4.2.

7.4.4. SNR with Split Detection Scheme

The benefit of the split detection scheme is shown in the plot of SNR as a function of range, in Figure 7.4.7. The splitting ratio is simply incorporated into the theory, from Chapter 3, by modifying the EDFA gain by the branch transmission factor. The calculation is for a pulse width of 20 m, at a power of 100 mW. An ADC maximum input signal of 2.4 V is assumed, which (ignoring interference effects) sets the overall gain for the EDFA to be 19 dB at the front of the fibre. Assuming a 90/10 % ratio as before, the gain for the far section is 28.5 dB.

Figure 7.4.8 shows the relative contributions from the different noise sources when operating at a range of 60 km with, and without, the split detection scheme; showing that, with simple detection, the thermal noise begins to exceed the ASE-related noise sources, whereas, with the split detection scheme, the thermal noise is approximately equal to the ASE-related noises at 60 km.

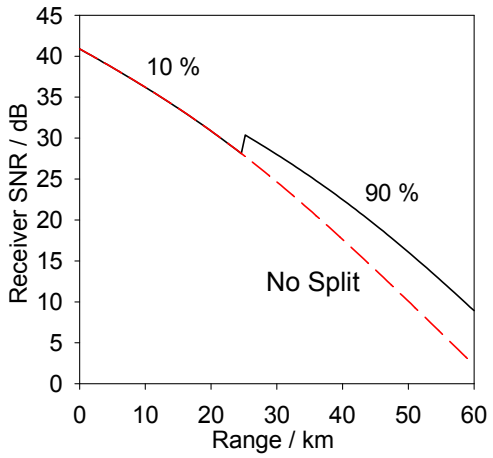

Figure 7.4.7

Calculated SNR for long fibre with 90/10 % split detection, showing the advantage gained at long ranges. An ADC maximum input of 2.4 V *is assumed and the EDFA gain is set to the maximum possible without exceeding this value, assuming the signal returned is equal to that from a conventional OTDR. The maximum range for a given minimum SNR is increased by ~10* km.

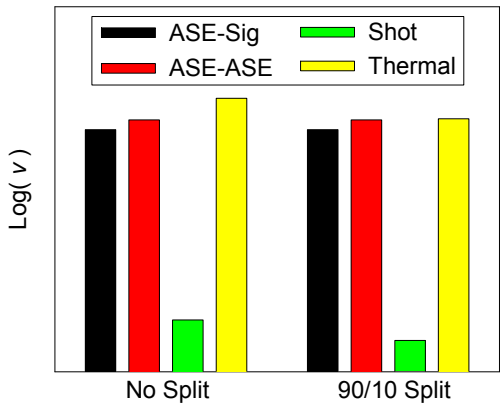

Figure 7.4.8

Relative receiver noise contributions at 60 km *with (left) an EDFA gain of 19* dB *and a single detector and (right) contributions with an EDFA gain of 29* dB *using the 90 % branch of 90/10 % split detection scheme The increased light reaching the receiver in the split case reduces the relative contributions from shot and thermal noises at the receiver.*

7.5. FTAS Rev 3

The Rev 3 demonstration system was constructed to build on the improvements made with the Rev 2 system, improving on the processing ability, with a more powerful PC, and incorporating minor changes and omissions in the optics. The split detection scheme, discussed in the previous section, was incorporated and an ASE blocking AOM was included to improve performance on long fibres following the observations of ASE build-up during the field trials using the Rev 2 system. The PC, was based on a commercial server system, which was modified to accept the optical receiver module by Robert Clarke.

Item:	Carried out by:
Optics design and manufacture	SR / JPWH / RJC
Control electronics design and manufacture	BF
RF Electronics design	ABL
TIAs & laser driver design	ABL
Software	BF
Control PC and Acquisition Hardware	Commercial / RJC

ABL = Andrew Lewis; BF = Barry Fleury; JPWH = Justin Hayward (Author);
RJC = Robert Clarke; SR = Dr Stuart Russell

Figure 7.5.1

Summary of main contributions to the construction of the FTAS Rev 3 demonstration system.

7.5.1. Optical Architecture

As shown in Figure 7.5.3, the optical architecture is very similar to the Rev 2 design. The differences are that the second stage of the launch EDFA is co-pumped, giving lower gain but improved noise performance, an ASE blocking AOM (AOM 2) is included to prevent the degradation of the noise performance due to ASE scattering from long fibres observed with the Rev 2 system and the inclusion of 90/10 % couplers at the receivers, as described in the previous section, to improve performance at long ranges without compromising the front-end performance.

The layout of the optics enclosure is shown in Figure 7.5.2. The optical components are mounted on the vertical boards and the pump lasers are normally

attached to the rear panel of the box. The acoustically-isolated, temperature-controlled fibre-laser housing is visible on the left hand side, above the AOMs and the control electronics and power supply unit (PSU) can be seen on the right-hand side of the case. The receivers were mounted in the DSP and Control box, electrically isolated with a separate ground along with the analogue side of the ADC card. The receiver assembly is shown in the right-hand side of Figure 7.5.2.

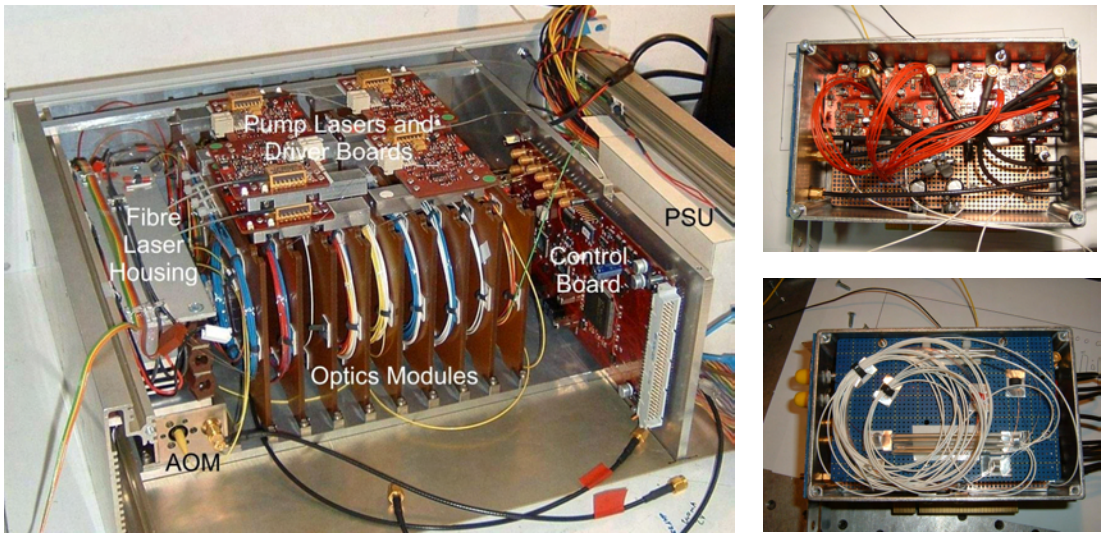

Figure 7.5.2

Left: Rev 3 optics module before mounting the pump laser boards on the rear panel.

Right: Receiver module electronics, top, and optics, bottom.

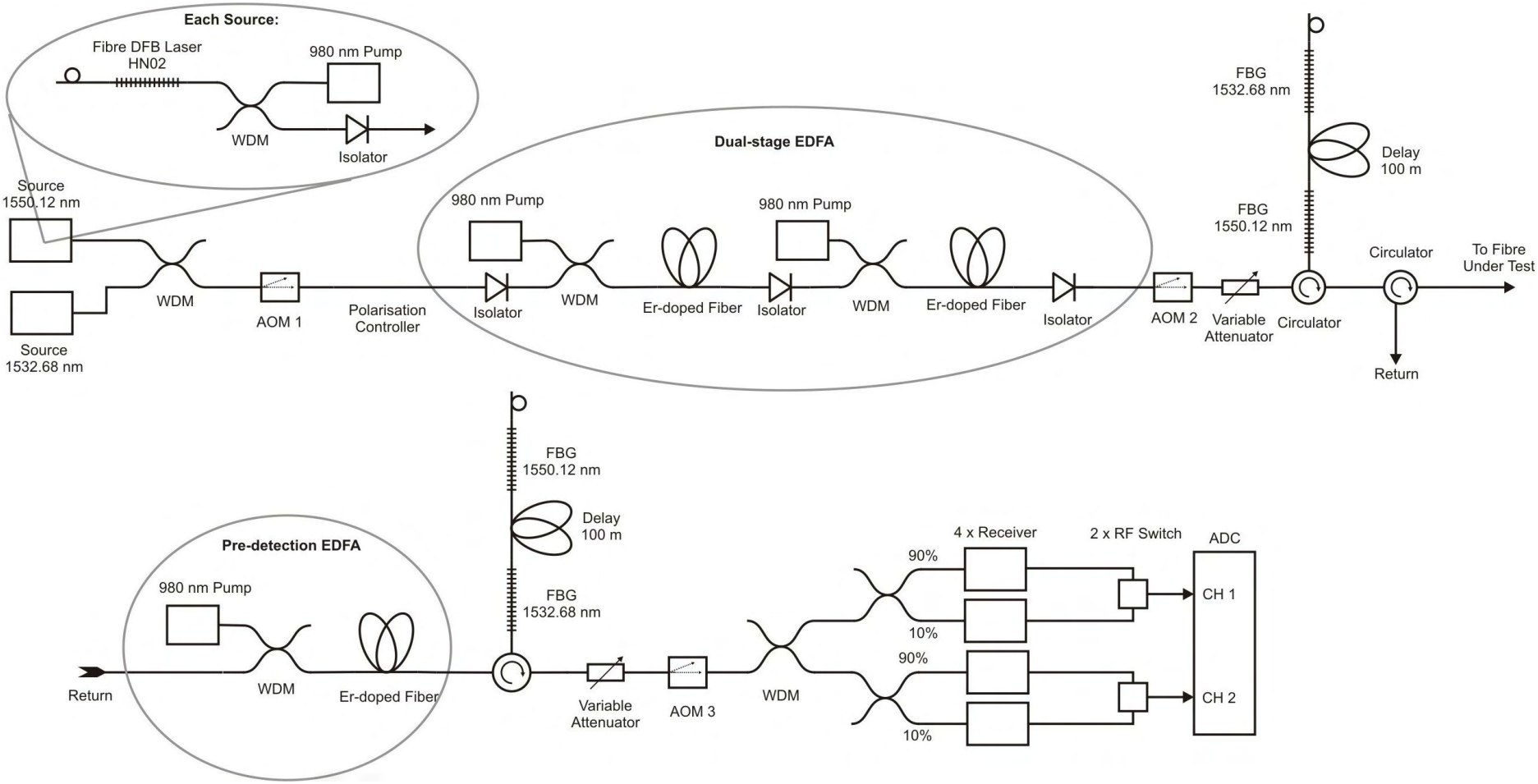

Figure 7.5.3

Optical architecture of the Rev 3 demonstration system.

7.5.2. Electronic Design and Signal Processing

The control electronics and signal processing is very similar to that of the Rev 2 demonstration unit, described in section 7.1. Minor modifications to the control architecture were required for the additional AOM and the RF switching for the split detection. The RF design was also extensively modified by Andrew Lewis to allow the use of class B RF amplifiers, significantly reducing the heat dissipation which was difficult to manage in the previous design.

7.5.3. Specimen Results

The FTAS Rev 3 demonstration system was used in a number of field trials, most of which were a repetition of the type of experiments described in Chapter 5 for Radiodetection's purposes. Although some sample results from these trials are given here, the most significant work carried out using Rev 3 system, for the preparation of this thesis, was the measurement of the spatial response of the sensor presented in section 7.6 and the initial experiments attempting to measure fibre extension by correlation of the backscatter traces reported in the addendum to Chapter 8.

Figure 7.5.4 shows the sensor response from a standard 3 mm patch-cord-style cable, buried at a depth of approximately 200 mm, in dry, sandy soil, at an optical range of 120 m. The sample rate was 4 kHz and the signal is band-limited to the Nyquist frequency, 2 kHz. The acoustic background, shown in the lower line of the frequency spectrum, has a broad-band feature at around 400 Hz and another, smaller feature, at 800 Hz. This is probably the result of acoustic background noise in the ground and in the temporary building containing the sensor, which had other pieces of equipment with noisy fans, the vibration of which could be transmitted to the fibre laser, even with the care taken to minimising the mechanical transmission path between the case and laser. It is also possible that these artefacts were due to a "bug" in the FPGA programming, leading to the sample point timing varying with respect to the launch timing, giving amplitude noise as the sample point moves along the coherent backscatter pattern.

The upper spectrum is from signal obtained from a person stamping their foot above the cable. The signal can be clearly seen in the spectrograph, two heavy stamps followed by three lighter, two heavy and one light. The heavier stamps generated a broader frequency spectrum, probably due to the phase disturbance being large-enough to give a non-linear response. It can be seen that the background signal at 400 Hz has an interesting character, with clear components at 400 Hz and 450 Hz.

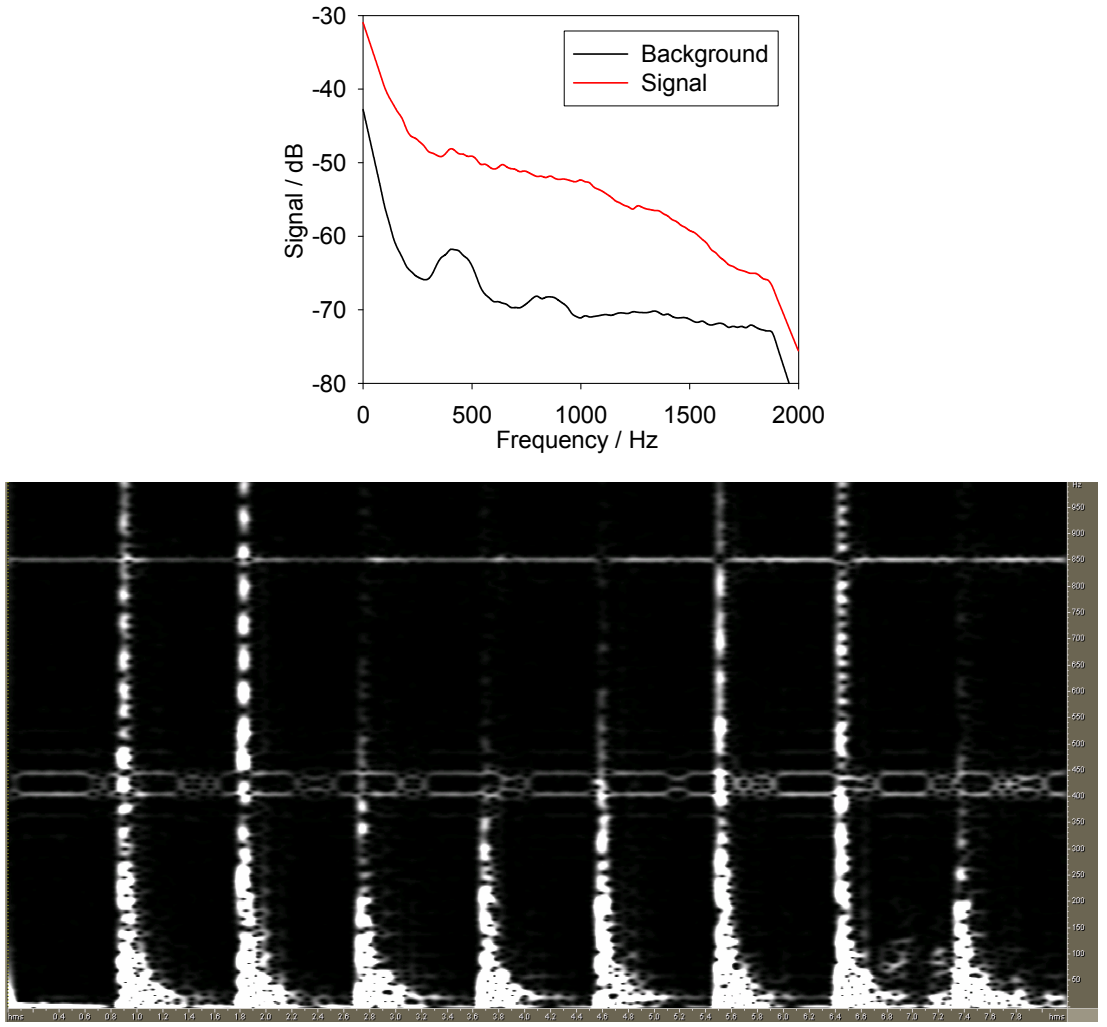

Figure 7.5.4

Response to impulsive disturbance above a cable buried approximately 200 mm *deep in sandy soil at an optical range of 120* m*. The spectrograph (bottom) shows the broad frequency content at the moment of impact, with the spectral width falling as the resulting vibration decays. The FFT power spectrum (top) shows the background and peak spectra. The artefacts at ~400* Hz *and ~800* Hz *are likely to be acoustically borne since the measurements were carried out in a noisy environment.*

7.6. Spatial Response – Optimum Sample Pitch

7.6.1. Motivation

Having made the qualitative observation, in Section 7.3.5, that where longer pulse-widths are used to increase the optical power returned to the receiver, in situations where the spread of the acoustic disturbance limits the length of disturbed fibre, the sensitivity appears to become very small at certain locations on the fibre. This problem could be overcome using a wide pulse, say 40 m, but sampling twice within this interval, with a sample pitch of 20 m. This observation was unexpected since the theory, developed in Chapter 2, suggested that the response from sampling at a given point would have a FWHM width of 87 % of the pulse width, so for a 40 m pulse the sensitivity would fall to half the peak over a physical region only 5.2 m long, insufficiently small to fully damp disturbances above a buried fibre. To investigate this observation more thoroughly and in order to select the optimum sampling pitch, measurements of the response to a quasi-point disturbance were made in controlled conditions in the laboratory.

7.6.2. Experimental Design

The experimental layout for measuring the variation of response over distance is shown in Figure 7.6.1. A 49 m length of standard 125 μm SMF patch-cord, with 3 mm diameter plastic jacket and Kevlar reinforcement, was wound onto two drums. The fibre between the two drums, passed through two tubular supports and over a disturbance generator. The disturbance generator, shown in Chapter 4, consists of a loud-speaker cone, connected to a 1 mm thick plastic beam via a rigid tube, causing deflection of the beam when a signal is applied to the cone. The fibre cable was taped to this beam to effectively and consistently transmit the disturbance to the fibre.

The tubular supports were 140 mm and 190 mm long with an internal diameter of 4.5 mm and restrained the fibre, such that no vibration could be seen or felt beyond the tube ends. The Kevlar reinforcing threads within the cable would further damp any vibration of the outer jacket. The supports were positioned to give a free fibre length between the tube ends of 500 mm; ensuring sufficient fibre was deflected to generate sufficient cumulative phase disturbance to give a good signal. The disturbance generator was located 100 mm off-centre to ensure that the fibre was not inadvertently excited at even harmonics of the drive frequency, with anti-nodes at the centre.

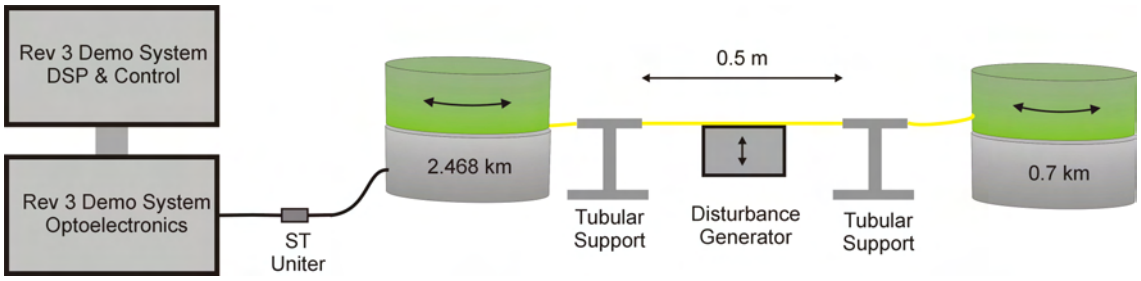

Figure 7.6.1

Experimental architecture for measuring the spatial response of the sensor. With the ST connectors separated the drums could be rotated, hence applying different sections of fibre to the disturbance generator allowing the response to be mapped.

Drums of 250 µm-coated, standard telecoms 125 µm SMF, were spliced at either end of the test fibre, having lengths of 2468 m and 700 m, and attached to the test fibre drums, allowing each assembly to be mounted on a vertical shaft, enabling the disturbed section of fibre to be easily varied by rotating the drums after separating the ST uniter. To aid accurate movement, the test fibre was marked at 500 mm intervals and the marks aligned with the support tubes..

If the splices caused partial reflection of the launch pulse, the measurements would have been distorted. To ensure this was not the case, the splices were examined using a conventional OTDR: the losses were << 1 dB and they gave no observable reflection.

The fibre was interrogated using the Rev 3 demonstration unit, operating at a sample rate of 4 kHz and pulse lengths of 10 m, 20 m and 40 m, with the data recorded from the resolution bin closest to the centre of the test fibre. The optimum signal was found to occur for a disturbance frequency of 80 kHz. The signal level was chosen to be within the linear regime, where the signal does not pass through interference fringes, requiring the disturbance generator to be driven at 1.0 V peak-to-peak. The signal was recorded for 2 min at each fibre location, allowing the effects of "fading" and acoustic noise in the laboratory to be minimised by averaging. The signal recordings were then converted to Windows Wave (*.wav) files, allowing sophisticated analysis to be carried out using the Adobe Audition software package. First, an (80 ± 5) Hz 10^{th} order band-pass filter removed any out-of-band signals from acoustic noise in the laboratory. The RMS power was then calculated with a 10 s window, and averaged over the whole 2 min data set.

7.6.3. Results

The experimental results are shown in Figure 7.6.2 for pulse lengths of 10 m, 20 m and 40 m. In each case, the experimental data is superimposed with the theoretical response, derived in Chapter 3, convolved with an approximated detector response, which is assumed to be a top-hat function with width equal to the settling time of the detector, equivalent to 5 m. The data was manually centred so that the peak lies at 0 m and the theoretical response is scaled to fit the experimental data envelope as well as possible.

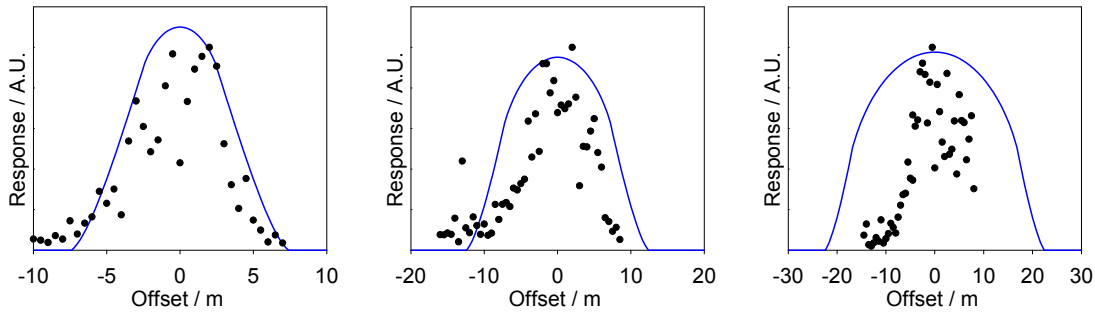

10 m *pulse* *20* m *pulse* *40* m *pulse*

Figure 7.6.2

Experimental results showing the measured RMS amplitude spatial response over at pulse lengths of 10 m*, 20* m *and 40* m*. The Blue lines are the predicted response, assuming a 20* MHz *detector, scaled to the experimental data.*

The results at 10 m pulse length show approximately the expected shape, although the left-hand tail is stronger than the theory would suggest. The spread of data in the central region suggests that the averaging time was insufficient to fully compensate for the effects of "fading"; however, the edges match the theoretical curve reasonably well. The extended tail on the left hand side is probably the result of asymmetry in the impulse response of the receiver, giving a slower response for falling edges than rising, which would be more significant for the short pulse widths than for the measurements at longer pulse lengths.

The results with a 20 m pulse are shown in the centre of Figure 7.6.2. Here the peak is narrower than predicted by the theoretical analysis and again the amplitude of the signal appears to retain "fading" noise after averaging. The results at 40 m are incomplete due to the available sampling point being off-centre on the test fibre, meaning that it was only possible to interrogate a useful range of ~ 25 m, although the

results available seem to suggest that the response falls off more quickly than would be expected.

7.6.4. Discussion

The experimental results appear to indicate that the response falls off faster then predicted for longer pulse lengths, 20 m and above, in agreement with the qualitative observations made in field trials. A possible reason for this reduction in sensitivity, for longer pulses, is that the fibre birefringence modulates the SOP over the pulse width.

In Chapter 3 the effect of the fibre birefringence was described using the results of Stowe *et al.* [66], giving the probability of achieving a certain sensitivity assuming that the birefringence between the two resultant scattering sites is random. This assumption is valid where long lengths of fibre are involved, as is normally the case in a conventional interferometer. In the C-OTDR sensor, however, the interferometer length is defined by the separation of the resultant scattering sites, which must always lie within the pulse length, Λ, setting the maximum possible interferometer length to the two-way propagation length, 2Λ. Therefore to explain the observed spatial resolution performance an alternative model is proposed for the case when the beat length is of the order of the pulse length or smaller.

Rewriting the intensity at the receiver, derived in Chapter 3 (3.2.36), using the identity $\cos(A)+\cos(B)=2\cos\left(\frac{A+B}{2}\right)\cos\left(\frac{A-B}{2}\right)$ gives the total detector intensity as:

$$I_{Total} = E_0{}^2\left(\begin{array}{r} R_A^2 + R_B^2 + 2R_AR_B\cos\left[\phi_x(t)+\phi_y(t)+\phi_0+\Phi(z_B-z_A)\right]\ldots \\ +\cos\left[\phi_x(t)-\phi_y(t)2\phi_y(t)-2\Phi(z_B-z_A)\right]\end{array}\right). \qquad 7.6.1$$

Now for simplicity, assume that $\phi_x(t)=\phi_y(t)=\phi(t)$, allowing 7.6.1 to be rewritten as:

$$I_{Total} = E_0{}^2\left\{R_A^2 + R_B^2 + 2R_AR_B\cos\left(2\phi(t)+\phi_0'\right)\cos\left(\Phi(z_B-z_A)\right)\right\}. \qquad 7.6.2$$

where $\phi_0' = \phi_0 + \Phi(z_A - z_B)$, which is admissible with no loss of generality, since although the retardation is quasi-deterministic, the phase ϕ_0 is truly random so ϕ_0' will remain random.

Recalling, from Chapter 3, that the retardation can be written in terms of the beat length, L_B, and the spatial separation of the resultant scattering sites, the received intensity may be written as:

$$I_{Total} = {E_0}^2 \left\{ R_A^2 + R_B^2 + 2R_A R_B \cos\left(2\phi(t) + \phi_0'\right) \cos\left(\frac{2\pi}{L_B} \left[z_B - z_A \right] \right) \right\} . \qquad 7.6.3$$

As in Chapter 3, the small-signal sensitivity is obtained from the 1st-order Taylor expansion as:

$$S = 2{E_0}^2 R_A R_B \sin\left(\phi_0'\right) \cos\left(\frac{2\pi}{L_B} \left[z_B - z_A \right] \right), \qquad 7.6.4$$

showing that the sensitivity is reduced by the cosine of the retardation.

To calculate the resulting spatial response, the same method as applied in Chapter 2 can be used. The relative amplitude reflectivities are assumed to be proportional to the square root of the fraction of the pulse energy either side of the disturbance:

$$R_A = R\sqrt{1 + \frac{2z_0}{\Lambda}}; \quad R_B = R\sqrt{1 - \frac{2z_0}{\Lambda}} . \qquad 7.6.5$$

The most likely location for the resultant scattering site is at the centre of the pulse fraction, by geometry:

$$< z_A >= \frac{1}{2}\left(\frac{\Lambda}{2} - z_0 \right); \quad < z_B >= \frac{1}{2}\left(\frac{\Lambda}{2} + z_0 \right), \qquad 7.6.6$$

from which simple manipulation gives the expected separation,

$$< z_B > - < z_A >= z_0 . \qquad 7.6.7$$

Substituting into 7.6.3 the intensity becomes:

$$I_{Total} = 2R^2 {E_0}^2 \left\{ 1 + \sqrt{1 + \frac{2z_0}{\Lambda}} \sqrt{1 - \frac{2z_0}{\Lambda}} \cos\left(2\phi(t) + \phi_0'\right) \cos\left(\frac{2\pi}{L_B} z_0 \right) \right\} . \qquad 7.6.8$$

To calculate the interference visibility, $V = \dfrac{I_{Max} - I_{Min}}{I_{Max} + I_{Min}}$, inspection of 7.6.8 gives the maximum and minimum intensities respectively:

$$I_{Max} = 2R^2 {E_0}^2 \left\{1 + \sqrt{1 - \left(\frac{2z_0}{\Lambda}\right)^2} \left|\cos\left(\frac{2\pi}{L_B} z_0\right)\right|\right\};$$
$$I_{Min} = 2R^2 {E_0}^2 \left\{1 - \sqrt{1 - \left(\frac{2z_0}{\Lambda}\right)^2} \left|\cos\left(\frac{2\pi}{L_B} z_0\right)\right|\right\}. \quad 7.6.9$$

Inserting into the definition of the visibility obtains the result:

$$V(z_0) = \sqrt{1 - \left(\frac{2z_0}{\Lambda}\right)^2} \left|\cos\left(\frac{2\pi}{L_B} z_0\right)\right|. \quad 7.6.10$$

The beat length of fibre depends on the inherent birefringence, due to asymmetry of the fibre geometry, and the bending-induced birefringence [57] related to the layout of the fibre and, where contained in a cable, the cable geometry. Coiled fibre typically has beat lengths of the order 10 m to 25 m and typical installed fibre 10 m to 60 m [60], depending on fibre type. Equation 7.6.10 is plotted in Figure 7.6.3 for a pulse width of 20 m and beat lengths of 50 m, 25 m and 10 m.

The predicted response, smoothed with a top-hat filter of 5 m width to approximate the response of a detector of 20 MHz bandwidth, is plotted along with the experimental data in Figure 7.6.4. The best fit is occurs for the 50 m beat length, within the range of beat lengths observed in [60] for deployed fibre, and comparable with measurements made in our laboratory.

These results indicate that fibre birefringence-related fading is almost certainly the cause of the narrowed response observed experimentally. However, the analysis still retains an approximation, which may not be valid for pulse lengths which are comparable to the beat length. The model assumes that the scatter from all the sites within the pulse can be described by the scatter from two resultant scattering sites, scattering light with a single phase and a single state of polarisation (SOP). When light is scattered from a large number of scattering sites, however, each one will scatter light which passes through different cumulative birefringence, meaning that the light from a finite section of fibre cannot be described by a single SOP, instead the light will be spread over a range of polarisations and must be described by the resultant SOP and the degree of polarisation (DOP). Therefore, detailed consideration of this effect and of the statistical distribution of birefringence in the fibre is required to refine the model of spatial response further.

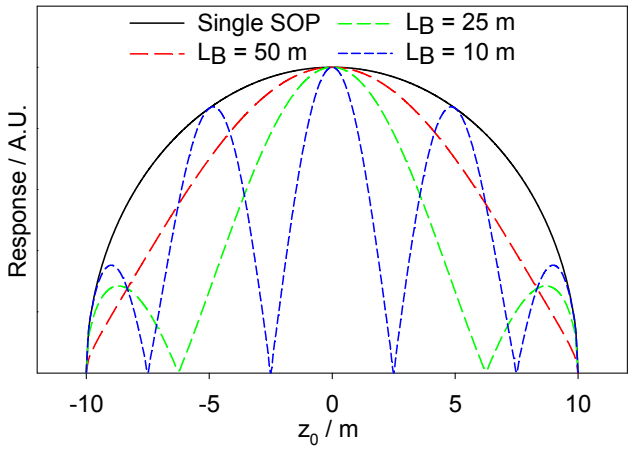

Figure 7.6.3

Response predicted by 7.6.10, ignoring any detector effects, for the single-polarisation case from Chapter 3, equivalent to infinite beat length, and for fibre with beat lengths of 10 m*, 25* m *and 50* m.

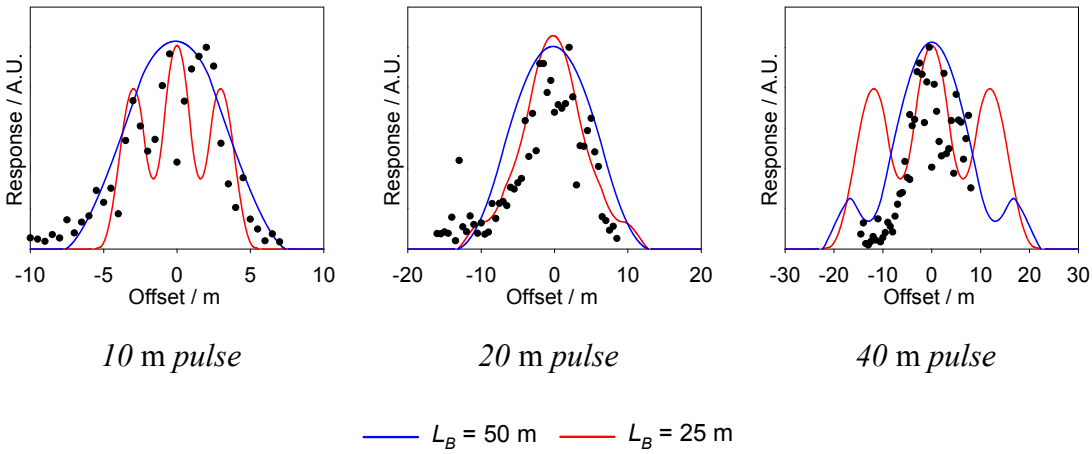

10 m *pulse* *20* m *pulse* *40* m *pulse*

Figure 7.6.4

Experimental results with theoretical responses for beat lengths of 25 m *and 50* m *superimposed, smoothed by a 5* m *wide top-hat filter to model the effect of the finite impulse response of the detector, which has a rise-time equivalent to 5* m.

7.6.5. Conclusions

The analysis and experimental results presented above show that the effects of polarisation and birefringence must be considered when analysing the spatial response of the C-OTDR sensor. The experimental results show that, for pulse widths greater than 20 m, the analyses of Chapter 3 and Shatalin *et al.* [40] no longer apply. It has been proposed that this is because, the birefringence cannot be treated as a random statistical variable, as considered by Stowe *et al.* [66], since where the interferometer length is comparable to the beat length, the variation in birefringence is quasi deterministic.

An analysis of the effect of birefringence has been carried out, showing that the effect of de-randomisation of the birefringence is the reduction of the sensitivity FWHM, as observed in the experiments. As discussed, the model could be further enhanced by considering how scattering from many points alters the DOP of the scattered light; however, this analysis is left for the future.

In terms of optimisation of the C-OTDR sensor, where operation at long ranges requires the use of pulses longer than 20 m, the theoretical and experimental results indicate that it is prudent to sample the backscatter at a pitch of less than a pulse width. From the results with a 40 m pulse, shown in Figure 7.6.4, a sample pitch of half the pulse width appears necessary; ensuring that, even in a situation a quasi-point disturbance, the sensitivity is only reduced to half the peak value at the edge of each resolution bin.

Chapter 8 Conclusions and Future Work

In this chapter the conclusions which can be drawn from the current work are presented and the potential avenues for continuing research are discussed, highlighting the areas where further development may be possible and the available benefits.

8.1. Conclusions

A thorough investigation has been carried out into the C-OTDR sensor, concentrating on applications in telecommunications cable protection. The sensor operation was analysed, using a simple model of coherent scattering that assumed that scattering from many sites can be modelled as scattering from a single, resultant, site. The validity of this model was confirmed by numerical modelling and comparison of its predictions with more complex analyses in the literature.

The noise performance of the sensor was then analysed, showing that the performance of the optical receiver limits the overall performance of the sensor. Consideration of the fundamental thermal noise in the sensing fibre showed that, unlike in a conventional interferometer, it is unlikely to limit the performance in normal situations.

Field trials proved the sensor was suitable for cable protection applications. During the field trials, detection of footsteps above buried fibre was demonstrated at a range of 1 km with 20 m resolution, obtaining SNRs comparable to those obtained at 2 km by Juarez *et al.* [38] where the spatial resolution was 1000 m. Despite this high level of performance, the degradation of SNR with increasing range was larger than predicted by the noise analysis. Experimental and theoretical investigation showed that the source of this unexpected reduction in performance was broadening of the pulse line-width by self-phase modulation (SPM), allowing SNR improvements to be obtained by optimisation of the launch power.

With the pulse power modified to avoid SPM, operation on a deployed cable, at 50 km range with 50 m resolution, was demonstrated. Following observations during these tests, experimental investigation showed that the spatial response differed from that predicted by the earlier analysis and a revised analysis was produced, taking the fibre birefringence into account, showing good agreement with the experimental data.

The performance observed in field trials has shown that the sensor which has been developed is capable of meeting the requirements for cable protection applications described in Section 1.1.4. Furthermore, on the basis of the field trials and laboratory tests, it has been shown that the performance of the sensor, whose evolution has been described in this thesis, is superior that achieved by other sensors of this type, with longer operational range and superior spatial resolution, summarised in Figure 8.1.1.

These advantages have been obtained by careful analysis of the factors which limit the performance and by optimising the design of each element of the experimental systems.

Sensor	Maximum operational range	Minimum spatial resolution	Practicality
FTAS C-OTDR	50 km	10 m	Fully portable, self-contained unit
Taylor *et al.* [38, 42]	14 km	1000 m	Some field trials reported
Shatalin *et al.* [39, 40]	11 km	10 m	Lab experiments

Figure 8.1.1

Comparison of the sensor described in this thesis to other similar sensors reported in the literature by Taylor et al. at Texas A&M University and Shatalin et al.

8.2. Future Work

Although the sensor has been developed sufficiently to meet the requirements set out in Section 1.1.4, a number of areas for future work have been identified where the sensor performance may be improved or optimised for different applications, and where the theoretical description of the sensor operation can be made more complete.

8.2.1. Developing model of spatial sensitivity to include finite DOP

In the previous chapter, the effect of fibre birefringence on the spatial response of the sensor was analysed, making the assumption that the backscatter from a large number of scattering sites can be described in terms of a scattering from a single, resultant scatter site, giving a single polarisation state. To develop this model further, the effect of scattering from many sites on the degree of polarisation (DOP) of the scattered light must be considered, and how this affects the influence of the fibre birefringence on the analysis.

To test the theory, more sophisticated experiments may be useful. By measuring the spatial response on high-birefringence fibre the effect of polarisation should be eliminated, allowing the simple model, with no consideration of the polarisation of the light, to be confirmed. Measurement of the spatial response on SMF could then be carried out, along with measurements of the beat length and DOP of the scattered light, to confirm the improved model whilst taking these factors into account.

8.2.2. Optimising Pulse shape

The shape of the pulse power envelope affects two aspects of the performance of the C-OTDR sensor: the spatial response function (analysed in Chapter 2) and the maximum pulse power without degradation from SPM (as discussed in Chapter 6). A more detailed analysis of the influence of the pulse shape on the degradation due to SPM would allow the optimum shape, enabling the maximum launch power, to be derived. A compromise is likely to be required, however, in order to maintain acceptable spatial resolution, while maximising the pulse energy to maximise the receiver SNR.

If the analysis of pulse shaping indicated that significant gains were available a practical means of controlling the power envelope would have to be developed. A number of possible methods are available. It may be possible to control the power of the RF drive to the AOM to determine the loss, either actively or perhaps by a

customised matching circuit ensuring the required response. Any technique of this type would need to be inherently stable to prevent causing amplitude noise on the pulse, which would translate into noise on the decoded audio signal. This envelope control may act on the pulse entering the launch EDFA, or it may be easier to shape the pulse after amplification. An alternative approach may be to attempt to design the EDFA so that it inherently generates a pulse of the required shape, although this may be difficult to achieve while maintaining the required noise performance.

8.2.3. Development of Combination Algorithm

As discussed in Chapter 7, the likelihood of fading reducing the sensitivity at a given resolution bin is substantially decreased where the signal from more than one independent wavelength is considered. Each independent sensor is effectively a randomly biased interferometer, with small-signal sensitivity $S = \sin(\phi_0)$, where ϕ_0 is the random phase bias. As a result, each sensor may have either positive or negative sensitivity, with equal probability. Thus, in order to combine the signals from two, or more, independent sensors an algorithm must be developed to determine the correct sign of the summation. Combining signals coherently, as is the case here, confers a SNR advantage as the audio noise of the independent sensors will be uncorrelated.

Where the same section of fibre is interrogated by each sensor the signal from each must be either in phase or exact anti-phase. Where the sensors operate on different sections of fibre, however, an acoustic phase delay, Ω, may exist between the perturbation acting on each fibre. The effect is to reduce the signal improvement by a factor of $\cos\left(\frac{\Omega}{2}\right)$. Assuming that the optimum sense can be chosen for the combination, the largest effective value of Ω will be $\pi/2$, so for the worst-case scenario of combining two signals in quadrature the signal improvement will be a factor of $\sqrt{2}$. Since the noise amplitude, which combines with random phase, will also be increased by $\sqrt{2}$ there will be no overall improvement in SNR. However, the likelihood of fading will be significantly reduced. The application of a suitable combination algorithm, in the specific application of providing a perimeter security sensor is discussed in more detail in the following section.

As an alternative to developing an algorithm for optimising the combination, the possibility of combining the signals at the histogram stage may be considered. While

this would give the same advantages of fading avoidance as the technique described above, it does not give the SNR improvement which comes from combining the audio signals coherently.

8.2.4. Multi-Wrap Cable Layout for Protection of Short Perimeters

For security applications it may be desirable to monitor a short perimeter, up to a few kilometres in circumference. In such situations there may be benefit available from passing the cable around the perimeter a number of times, as shown in Figure 8.2.1. Where the cable is laid specifically for the purpose, it could be arranged in a spiral allowing disturbances to be tracked as they move toward or away from the protected area. Alternatively the cable may be laid along the same route a number of times, or routed along a number of fibres within the same cable around the perimeter. In this case no additional spatial information is gained, but by linking optical bins relating to the same geographic position and summing the audio signal from each, an improvement in SNR can be obtained.

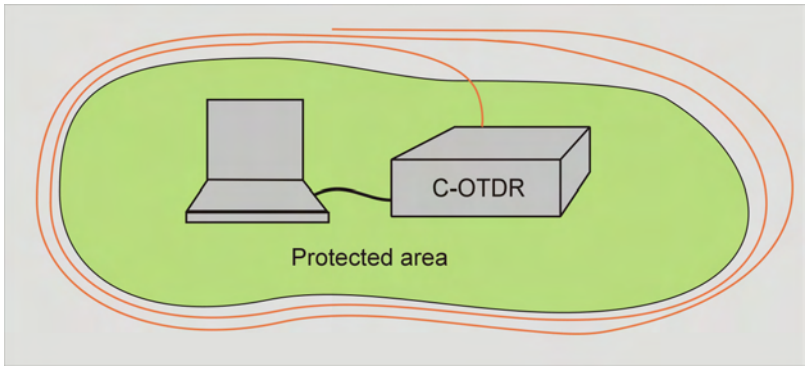

Figure 8.2.1

Perimeter protection with fibre looped around the same physical path many times to improve SNR. The greater the number of loops the more improvement from signal addition through SNR improvement and reduction of the likelihood of fading, but at a cost of reduced sample rate.

The audio signal at a point is combined by summing the signal from each loop as it passes through the geographic point of interest. Assuming that the same acoustic disturbance perturbs all the fibres, depending on the particular section of fibre the audio signals from each point will vary in amplitude and may either be in phase with each other, or 180° out of phase. It is therefore a relatively simple matter to combine the signals correctly in order to sum the signal, thus reducing the relative noise level.

If there are m loops then, since the signal combines coherently, the signal magnitude will be increased by a factor of m, and the noise magnitude, which combines with random phase, will be increased by a factor of $\sqrt{m}$. The audio SNR is therefore improved by a factor of m, or $10\log(m)$ dB.

From the analysis of Chapter 4, the audio noise can be expressed as:

$$< v_{Audio}^2 >= \frac{A}{f_s}; \qquad A = 2B_{Audio}\left(< v_{Reciever}^2 > + \frac{V_{\max}^2}{12 \cdot 2^{2q}} \right). \tag{8.2.1}$$

Since the audio signal level remains unchanged, then the SNR is proportional to the sample frequency, f_s. The maximum sample rate is limited by the total fibre length, writing in terms of the perimeter length L_p and the number of loops m, we obtain the maximum sample rate:

$$f_{s\,Max} = \frac{v_g}{2mL_p}, \tag{8.2.2}$$

where v_g is the group velocity in the fibre. The audio SNR at all points is therefore proportional to $1/m$, balancing the benefit from signal combining, implying that a multi-wrap configuration, as shown in Figure 8.2.1, gives no benefit. However, combining signals from a number of optical ranges allows the effect of "fading", where the birefringence of the fibre reduces the interference visibility to (or near to) zero. Assuming the probability that a single bin is in a faded state is p_f then the probability that all the traces are faded simultaneously is p_f^m, which rapidly becomes negligibly small, making use multiple loops desirable.

The above assumes that the signal and noise from each point are equal for each loop around the perimeter where the fibre is very short this is a reasonable approximation, but for longer perimeters where the loss becomes significant (>~5 km) the reduction of signal and SNR must be considered.

For a loss coefficient of α, the two-way loss, μ, of a loop of length, L_p, is given by:

$$\mu = e^{2l_P}. \tag{8.2.3}$$

If the electrical signal amplitude from a single loop is V_0, then the signal from the i^{th} loop has magnitude:

$$V_i = \mu^i V_0 . \qquad 8.2.4$$

The combined signal from *m* loops is therefore given by:

$$V_{Tot} = \sum_{i=0}^{m-1} V_i = V_0 \sum_{i=0}^{m-1} \mu^i = V_0 \frac{1-\mu^m}{1-\mu} . \qquad 8.2.5$$

Similarly, if the electrical noise from a single loop has RMS amplitude v_0 then, assuming that Signal-ASE noise dominated, as indicated in Chapter 4, then the noise contribution due to the i^{th} loop can be written as:

$$v_i = \mu^i v_0 . \qquad 8.2.6$$

Noting that the noise does not combine coherently, the total noise is:

$$< v_{Tot}^2 >= \sum_{i=0}^{m-1} \left(v_i\right)^2 =< v_0^2 > \sum_{i=0}^{m-1} \left(\mu^2\right)^i = < v_0^2 > \frac{1-\mu^{2m}}{1-\mu^2} . \qquad 8.2.7$$

So, from 8.2.5 and 8.2.7, the signal to noise ratio of the combined data is given by:

$$SNR = \frac{V_{Tot}^2}{< v_{Tot}^2 >} = \frac{V_0^2 \left(\frac{1-\mu^m}{1-\mu}\right)^2}{< v_0^2 > \frac{1-\mu^{2m}}{1-\mu^2}} . \qquad 8.2.8$$

Expanding, and writing in terms of the SNR obtained from a single loop, SNR_1, this becomes:

$$SNR = SNR_1 \frac{\left(1-\mu^m\right)^2 \left(1-\mu^2\right)}{\left(1-\mu\right)^2 \left(1-\mu^{2m}\right)} . \qquad 8.2.9$$

This is plotted for various loop lengths in Figure 8.2.2, showing the reduction in improvement from averaging as the additional signals become noisier. Where the sample rate is limited solely by the total length of fibre, there is therefore no benefit in using multiple loops except to combat the problem of fading. In practice, however, with short cables the maximum achievable sampling rate may be limited by the rate achievable by the sampling system. In this case, a multi-wrap configuration can benefit the SNR by increasing the effective duty cycle, giving the performance illustrated in Figure 8.2.3.

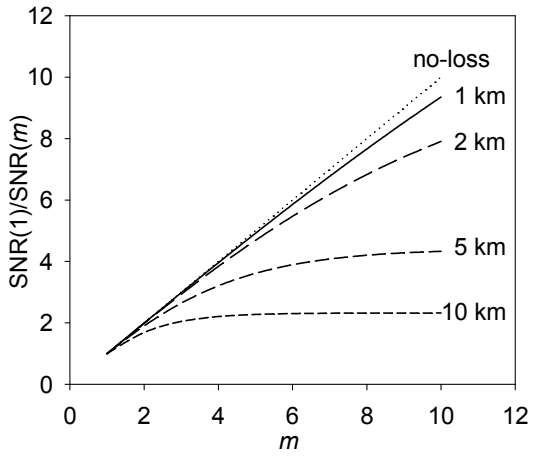

Figure 8.2.2

SNR benefit from combining data from many loops of different length at fixed sample rate, ignoring fading, but taking into account the cable loss of 0.2 dB / km *and assuming that ASE-Signal beat dominates the receiver noise.*

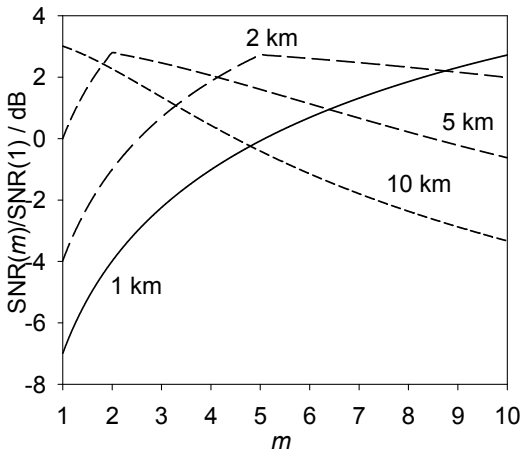

Figure 8.2.3

SNR benefit from combining data from many loops with maximum sample rate of 20 kHz*, relative to the ideal case with unlimited sample rate. The cable loss is taken as 0.2* dB / km *and ASE-Signal beat noise assumed to dominate.*

In conclusion, it is likely to be of benefit to use a multi-wrap cable configuration to improve the SNR where the cable route is shorter than the length corresponding to the hardware-limited maximum sample rate, and also to prevent loss of signal due to fading.

8.2.5. Related Research

The research presented in this thesis, aimed at developing a sensor for audio-frequency strains and disturbances, has developed expertise in the characteristics of coherent Rayleigh scattering, and the factors which influence its characteristics. In addition to the C-OTDR sensor described, this knowledge may be applicable to the development of other technologies.

One possible application of the assembled knowledge of coherent scattering and the high-performance data acquisition systems which have been produced is in developing a novel strain measurement technology, using the coherent backscatter pattern as a unique identifier for a section of fibre, allowing its range to be monitored to high resolution through correlation techniques. Some detailed analysis, numerical simulation and preliminary experimental investigation has already been carried out into this technique by the author, and were presented at OFS-17, [53].

At this stage, having analysed the limitations from the onset of optical non-linearity and optimisation of the receiver noise, there may be merit in revisiting the techniques discussed in Chapter 2. The self-heterodyne C-OTDR would be very sensitive to spectral broadening due to SPM, so improved performance may be obtainable by optimisation of the pulse power. The main limitation, however, was demodulation in the presence of strong amplitude modulation of the carrier. It may be possible to overcome this problem by carrying out the demodulation in the digital domain after high-speed sampling. Before proceeding with such developments, a detailed analysis of the sensor operation and the contribution of noise from different sources, such as carried out for the C-OTDR sensor in Chapters 2 and 3, should be carried out for the self-heterodyne system.

References

1. Whitehouse, P. and D. Thomas, eds. *The Great Western Railway - 150 Glorious Years*. 1985, David & Charles: London.
2. Gowar, J., *Optical Communication Systems*. 2nd ed. 1993, New York: Prentice Hall.
3. Goubaou, G. and F. Schwering, *On the Guided Propagation of Electromagnetic Wave Beams.* IRE Transactions on Antennas and Propagation, 1961. **AP-9**(2): p. 248-256.
4. Gambling, W.A., *Lasers and Optical Electronics.* The Radio and Electronic Engineer, 1975. **45**(10): p. 537-542.
5. Senior, J.M., *Optical Fiber Communications, Principles and Practice*. 2nd ed. 1992, Harlow: Prentice Hall.
6. Dunlop, J. and D.G. Smith, *Telecommunications Engineering*. 3rd ed. 1994, London: Chapman & Hall / Stanley Thornes.
7. Glaesemann, G.S. *Advancements in Mechanical Strength and Reliability of Optical Fibers*. in *Reliability of Optical Fibers and Optical Fiber Systems*. 1999. Boston, Massachusetts: SPIE.
8. Lisle, S.V. *The History, Prevention and Impact of Fiber Cable Failures*. in *National Fiber Optic Engineers Conference*. 1993. San Antonio.
9. Keck, D.B., *Optical fiber spans 30 years.* Lightwave Magazine, 2000(July).
10. Russell, S., K.R.C. Brady, and J.P. Dakin, *Real-time location of multiple time-varying strain disturbances, acting over a 40-km fiber section, using a novel dual-Sagnac interferometer.* Journal of Lightwave Technology, 2001. **19**(2): p. 205-213.
11. Russell, S.J., K.R.C. Brady, and J.P. Dakin. *An improved 40 km dual-wavelength, dual-Sagnac sensor, with enhanced signal processing allowing real-time location of multiple time-varying strain disturbances*. in *OFS-14*. 2000. Florence.
12. Russell, S.J. and J.P. Dakin, *Location of time-varying strain disturbances over a 40 km fibre section, using a dual-Sagnac interferometer with a single source and detector.* Proceedings of the SPIE 1999. **3746**: p. 580-583.
13. Hills, P.C., P.J. Samson, and I. Webster, *Optical fibres are intrinsically safe: reviewing the myth.* Journal of Electrical and Electronics Engineering, Australia, 1990. **10**(3): p. 207-220.
14. Measures, R.M., *Structural Monitoring with Fiber Optic Technology*. 2001, San Diego: Academic Press.
15. Vali, V. and R.W. Shorthill, *Fiber ring interferometer.* Applied Optics, 1976. **15**(5): p. 1099-1100.
16. Barnoski, M.K. and S.M. Jensen, *Fiber waveguides: a novel technique for investigating attenuation characteristics.* Applied Optics, 1976. **15**(9): p. 2112-2115.

17. Culshaw, B., *Optical Fiber Sensor Technologies: Opportunities and - Perhaps - Pitfalls.* Journal of Lightwave Technology, 2004. **22**(1): p. 39-50.
18. Tapanes, E.E., J.R. Goode, and J. Katsifolis, *Apparatus and method for monitoring a structure using a counter-propagating signal method for locating events*, U.p. office, Editor. 2003, FFT Pty Ltd: US.
19. Chtcherbakov, A.A., P.L. Swart, and S.J. Spammer, *Mach-Zehnder and modified Sagnac-distributed fiber-optic impact sensor.* Applied Optics, 1998. **37**(16): p. 34323437.
20. Buck, J., *Fundamentals of Optical Fibers*. Wiley series in pure and applied optics, ed. J. Goodman. 1995, New York: Wiley.
21. Gauglitz, G. and J.P. Dakin, *Spectroscopic Analysis*, in *Handbook of Optoelectronics*, J.P. Dakin and R. Brown, Editors. Awaiting Publication, Institute of Physics Publishing: Bristol.
22. Brinkmeyer, E., *Backscattering in Single-Mode Fibres.* Electronics Letters, 1980. **16**(9): p. 329-330.
23. Hartog, A.H. and M.P. Gold, *On the Theory of Backscattering in Single-Mode Optical Fibers.* Journal of Lightwave Technology, 1984. **LT-2**(2): p. 76-82.
24. Aoyama, K., K. Nakagawa, and T. Itoh, *Optical Time Domain Reflectometry in a Single-Mode Fiber.* IEEE Journal of Quantum Electronics, 1981. **17**(6): p. 862-868.
25. Healey, P., *OTDR in monomode fibres at 1.3 μm using a semiconductor laser.* Electronics Letters, 1981. **17**(2): p. 62-64.
26. Healey, P., *Review of Long Wavelength Single-Mode Optical Fiber Reflectometry Techniques.* Journal of Lightwave Technology, 1985. **3**(4): p. 876-886.
27. Healey, P., *Instrumentation principles for optical time-domain reflectometry.* Journal of Physics E: Scientific Instruments, 1986. **19**(5): p. 334-341.
28. Tateda, M. and T. Horiguchi, *Advances in Optical Time-Domain Reflectometry.* Journal of Lightwave Technology, 1989. **7**(8): p. 1217-1224.
29. Healey, P. and D.J. Malyon, *OTDR in single-mode fiber at 1.5μm using heterodyne detection.* Electronics Letters, 1982. **18**(20): p. 862-863.
30. King, J.P., D.F. Smth, K. Richards, P. Timson, R.E. Epworth, and S. Wright, *Development of a Coherent OTDR Instrument.* Journal of Lightwave Technology, 1987. **5**(4): p. 616-623.
31. Healey, P., *Fading in heterodyne OTDR.* Electronics Letters, 1984. **20**(1): p. 30-32.
32. Healey, P., *Statistics of Rayleigh backscatter from a single-mode optical fibre.* Electronics Letters, 1985. **21**(6): p. 226-228.
33. Izumita, H., Y. Koyamada, S. Furukawa, and I. Sankawa, *Fading Noise Reduction in Coherent OTDR.* IEEE Photonics Technology Letters, 1992. **4**(2): p. 201-203.
34. Rogers, A.J., *Polarisation Optical Time Domain Reflectometry.* Electronics Letters, 1980. **16**(13): p. 489-490.
35. Rogers, A.J., *Polarization-optical time domain reflectometry: a technique for the measurement of field distributions.* Applied Optics, 1981. **20**(6): p. 1060-1074.

36. Ross, J.N., *Birefringence measurement in optical fibers by polarization-optical time-domain reflectometry.* Applied Optics, 1982. **21**(19): p. 3489-3495.
37. Rogers, A.J., S.V. Shatalin, and S.E. Kanellopoulos. *Distributed Measurement of Fluid Pressure via Optical-fibre Backscatter Polarimetry*. in *OFS-17*. 2005. Brugges: SPIE.
38. Juarez, J.C., E.W. Maier, N. Choi, and H.F. Taylor, *Distributed Fiber-Optic Intrusion Sensor System.* Journal of Lightwave Technology, 2005. **23**(6): p. 2081-2087.
39. Juskaitis, R., M. M, V.T. Potapov, and S.V. Shatalin, *Inteferometry with Rayleigh backscattering in a single-mode optical fiber.* Optics Letters, 1994. **19**(3): p. 225-227.
40. Shatalin, S.V., V.N. Treschikov, and A.J. Rogers, *Inteferometric optical time-domain reflectometry for distributed optical-fiber sensing.* Applied Optics, 1998. **37**(24): p. 5600-5604.
41. Taylor, H.F. and C.E. Lee, *Apparatus and method for fiber optic intrusion sensing*, U.P. Office, Editor. 1993, Texas A&M University: USA.
42. Park, J. and H.F. Taylor, *Fiber optic intrusion sensor using coherent optical time domain reflectometer.* Japanese Journal of Applied Physics, 2003. **42**(6A): p. 3481-3482.
43. Posey, R., G.A. Johnson, and S.T. Vohra, *Strain sensing based on coherent Rayleigh scattering in an optical fibre.* Electronics Letters, 2000. **36**(20): p. 1688-1689.
44. Dakin, J.P. and C. Lamb, *A sensing method employing a fibre optic sensor system*, UK, Editor. 1988, The Plessey Company plc: UK.
45. Wooler, J.P.F. and R.I. Crickmore. *Fibre optic sensors for seismic intruder detection*. in *OFS-17*. 2005. Bruges, Belgium: SPIE.
46. Juskaitis, R., A.M. Mamedov, V.T. Potapov, and S.V. Shatalin, *Distributed interferometric fiber sensor system.* Optics Letters, 1992. **17**(22): p. 1623-1625.
47. Kersey, A.D., *A Review of Recent Developments in Fiber Optic Sensor Technology.* Optical Fiber Technology, 1996. **2**: p. 291-317.
48. Dakin, J.P., D.J. Pratt, G.W. Bibby, and J.N. Ross, *Distributed optical fibre Raman temperature sensor using a semiconductor light source and detector.* Electronics Letters, 1985. **21**(13): p. 569-570.
49. Ohno, H., H. Naruse, M. Kihara, and A. Shimada, *Industrial Applications of the BOTDR Optical Fiber Strain Sensor.* Optical Fiber Technology, 2001. **7**(1): p. 45-64.
50. Ogawa, O., T. Kato, and M. Kamikatano, *Technique for Measuring the Dynamic Strain on an Optical Fiber Based on Brillouin Ring Amplification.* Journal of Lightwave Technology, 1999. **17**(2): p. 234-242.
51. Hotate, K. and S.S.L. Ong, *Distributed Dynamic Strain Measurement Using a Correlation-Based Brillouin Sensing System.* IEEE Photonics Technology Letters, 2003. **15**(2): p. 272-274.
52. Alasaarela, I., P. Karioja, and H. Kopola, *Comparison of distributed fiber optic sensing methods for location and quantitiy information measurements.* Optical Engineering, 2002. **41**(1): p. 181-189.

53. Hayward, J.P.W., S.J. Russell, and J.P. Dakin. *Direct monitoring of fiber extension by correlation-based coherent optical time-domain reflectometry*. in *OFS-17*. 2005. Bruges, Belgium: SPIE.
54. Mini-Circuits, *RF/IF Designer's Handbook*. 1992.
55. Phillips-Semiconductor, *SA614 Datasheet*. 1997.
56. Betts, J.A., *Signal Processing, Modulation and Noise*. 1970: Hodder & Stoughton.
57. Ulrich, R., S.C. Rashleigh, and W. Eickhoff, *Bending-induced birefringence in single-mode fibers.* Optics Letters, 1980. **5**(6): p. 273-275.
58. Gere, J., M, *Mechanics of Materials*. 5th ed. 2001: Brooks / Cole.
59. Boudet, J., *Acoustic strain sensing using optical fibre and Polarimetric Optical Time Domain Reflectometry, Tripartite final year project report*. 2002, ORC, University of Southampton / Ecole Superieure d'Ingeniuers en Electronique et Electrotechnique de Paris.
60. Galtorossa, A., L. Palmieri, A. Pizzinat, M. Schiano, and T. Tambosso, *Measurement of Local Beat Length and Differential Group Delay in Installed Single-Mode Fibres.* Journal of Lightwave Technology, 2000. **18**(10): p. 1389-1394.
61. Kirkendall, C.K. and A. Dandridge, *Overview of high-performance fibre-optic sensing.* Journal of Physics D: Applied Physics, 2004. **37**(18): p. R197-R216.
62. Eickhoff, W., *Multiple-scattering noise in single-mode fibers.* Optics Letters, 1982. **7**(1): p. 46-48.
63. Mermelstein, M.D., R. Posey, G.A. Johnson, and S.T. Vohra, *Rayleigh scattering optical frequency correlation in a single-mode optical fiber.* Optics Letters, 2001. **26**(2): p. 58-60.
64. Choi, N., J.C. Juarez, and H.F. Taylor, *Distributed fiber-optic pressure/seismic sensor for low-cost monitoring of long perimeters.* Proceedings of the SPIE, 2003. **5090**: p. 134-141.
65. Hecht, E., *Optics*. 3rd ed. 1998: Addison-Wesley.
66. Stowe, D.W., D.R. Moore, and R.G. Priest, *Polarization Fading in Fiber Interferometric Sensors.* IEEE Journal of Quantum Electronics, 1982. **18**(10): p. 1644-1647.
67. Shannon, C.E., *Communication in the Presence of Noise.* Proceedings of the IRE, 1949. **37**(1): p. 10-21.
68. Shannon, C.E., *Communication in the Presence of Noise.* Proceedings of the IEEE, 1998. **86**(2): p. 447-457.
69. JDS-Uniphase, *Product Bulletin, EPM-6xx Series Photodiodes*. 2004.
70. Isrealsohn, J., *Noise 101*, in *EDN*. 2004. p. 41-47.
71. Storey, N., *Electronics - A Systems Approach*. 1992, Wokingham: Addison-Wesley.
72. Blank, L.C. and D.M. Spirit, *OTDR Performance Enhancement Through Erbium Fibre Amplification.* Electronics Letters, 1989. **25**(25): p. 1693-1694.
73. Iizuka, K., *Elements of Photonics*. Vol. 2. 2002, New York: Wiley.
74. Giles, C.R. and E. Desurvire, *Modeling Erbium-Doped Fiber Amplifiers.* Journal of Lightwave Technology, 1991. **9**(2): p. 271-283.

75. Yamada, M., M. Shimizu, M. Okayasu, T. Takeshita, M. Horiguchi, Y. Tachikawa, and E. Sugita, *Noise Characteristics of Er^{3+}-Doped Fiber Amplifiers Pumped by 0.98 and 1.48 μm Laser Diodes.* IEEE Photonics Technology Letters, 1990. **2**(3): p. 205-207.
76. Laming, R.I. and D.N. Payne, *Noise Characteristics of Erbium-Doped Fiber Amplifier Pumped at 980 nm.* IEEE Photonics Technology Letters, 1990. **2**(6): p. 418-421.
77. Desurvire, E., *Erbium-Doped Fibre Amplifiers: Principles and Applications*. 1997, New York: Wiley.
78. Yamamoto, Y. and K. Inoue, *Noise in Amplifiers.* Journal of Lightwave Technology, 2003. **21**(11): p. 2895-2915.
79. Haus, H.A., *The Noise Figure of Optical Amplifiers.* IEEE Photonics Technology Letters, 1998. **10**(11): p. 1602-1604.
80. Glenn, W.H., *Noise in Interferometric Optical Systems: An Optical Nyquist Theorem.* IEEE Journal of Quantum Electronics, 1989. **25**(6): p. 1218-1224.
81. Wanser, K.H., *Fundamental Phase Noise Limit in Optical Fibres due to Temperature Fluctuations.* Electronics Letters, 1992. **28**(1): p. 53-54.
82. Blotekjaer, K., *Thermal Noise in Optical Fibers and Its Influence On Long-Distance Coherent Communication Systems.* Journal of Lightwave Technology, 1992. **10**(1): p. 36-41.
83. Shupe, D.M., *Thermally induced nonreciprocity in the fiber-optic interferometer.* Applied Optics, 1980. **19**(5): p. 654-655.
84. Shurcliff, W.A., *Polarized light - production and use*. 1962, Harvard: Harvard University Press.
85. Agrawal, G.P., *Nonlinear Fiber Optics*. 3 ed. 2001: Academic Press.
86. Chraplyvy, A.R., *Limitations on Lightwave Communications Imposed by Optical-Fiber Nonlinearities.* Journal of Lightwave Technology, 1990. **8**(10): p. 1548-1557.
87. Smith, R.G., *Optical Power Handling Capacity of Low Loss Optical Fibers as Determined by Stimulated Raman and Brillouin Scattering.* Applied Optics, 1972. **11**(11): p. 2489-2492.
88. Izumita, H., Y. Koyamada, S. Furukawa, and I. Sankawa, *The Performance Limit of Coherent OTDR Enhanced with Optical Fiber Amplifiers due to Optical Nonlinear Phenomena.* Journal of Lightwave Technology, 1994. **12**(7): p. 1230-1238.
89. Auyeung, J. and A. Yariv, *Spontaneous and Stimulated Raman Scattering in Long Low Loss Fibers.* IEEE Journal of Quantum Electronics, 1978. **14**(5): p. 347-352.
90. Koyamada, Y., H. Nakamoto, and N. Ohta, *High performance coherent OTDR enhanced with erbium doped fiber amplifiers.* Journal of Optical Communications, 1992. **13**(4): p. 127-133.
91. Ruffin, A.B. *Stimulated Brillouin Scattering: An Overview of Measurements, System Impairments, and Applications*. in *NIST-SOFM*. 2004. Boulder, Colarado, USA: NIST.

92. Fluck, R., R.B. Wilcox, D.F. Browning, and P. F. *Stimulated Brillouin scattering thresholds for square pulses in polarizing fiber*. in *Lasers and Electro-Optics, Conference on (CLEO 2000)*. 2000. San Francisco: IEEE.
93. Agilent_Technologies, *Agilent AFKC-xxxx Pluggable DWDM Transceiver for operation at up to 2.7 Gb/s - Data Sheet 5989-1067EN*. 2004.
94. Redd, J. and C. Lyon, *Spectral content of NRZ test patterns*, in *EDN*. September 2004. p. 67-72.
95. Kim, D.S. and J.S. Lee, *Propagation and attenuation characteristics of various ground vibrations.* Soil Dynamics and Earthquake Engineering, 2000. **19**(2): p. 115-126.
96. Hao, H. and T.C. Ang, *Analytical modelling of traffic-induced ground vibrations".* Journal of Engineering Mechanics, 1998. **124**(8): p. 921-928.